VALIDITY OF THE POINT SOURCE ASSUMPTION OF A ROTOR FOR FARFIELD ACOUSTIC MEASUREMENTS WITH AND WITHOUT SHIELDING

A Thesis
Presented to
The Academic Faculty

by

Nurkan Turkdogru

In Partial Fulfillment
of the Requirements for the Degree
Doctor of Philosophy in the
School of Aerospace Engineering

Georgia Institute of Technology
December 2010

VALIDITY OF THE POINT SOURCE ASSUMPTION OF A ROTOR FOR FARFIELD ACOUSTIC MEASUREMENTS WITH AND WITHOUT SHIELDING

Approved by:

Dr. Krishan K. Ahuja, Committee Chair
School of Aerospace Engineering
Georgia Institute of Technology

Dr. Krishan K. Ahuja, Advisor
School of Aerospace Engineering
Georgia Institute of Technology

Dr. Lakshmi Sankar
School of Aerospace Engineering
Georgia Institute of Technology

Dr. Richard J. Gaeta
School of Mechanical and Aerospace Engineering
Oklahoma State University

Dr. Jechiel Jagoda
School of Aerospace Engineering
Georgia Institute of Technology

Dr. Charlotte E. Whitfield
Aeroacoustics Branch
NASA Langley Research Center

Date Approved: December 2010

To my family

ACKNOWLEDGEMENTS

First of all, I would like to thank my advisor, Prof. Krishan K. Ahuja, for his guidance, encouragement and endless patience throughout this research. I'm grateful for his insightful discussions and sharing invaluable knowledge that I will carry with me in my future endeavors.

I would like to thank my surrogate advisor Dr. Richard J. Gaeta for spending his time and effort to fill Prof. Ahuja's place when he was abroad, his constructive comments during this work and serving on my thesis committee. I'm grateful to Prof. Jechiel Jagoda who served on my committee for providing part of my financial support and his sincere help in solving the most extraordinary problems I had. I would also like to thank Prof. Lakshmi Sankar who served in my committee, for encouraging me to explore what I found interesting, and directing me to work with Prof. Ahuja. I would also like to thank to Dr. Charlotte E. Whitfield for serving on my thesis committee and many insightful comments.

I want to acknowledge the valuable assistance of Adam Churney and other students at GTRI/ATAS. Thanks to Christine Shapiro and GTRI administrative staff for their kind help. The understanding and kindness at GTRI to me who was raised in a different culture with a different language than theirs is greatly appreciated.

Special thanks go to GTRI's Robert G. Shackelford Graduate Fellowship program for their financial support. Part of this work was also funded by NASA's URETI and PAVE programs.

Finally, thanks to my family, for their support and prayers during this period of my life.

TABLE OF CONTENTS

LIST OF TABLES

LIST OF FIGURES

NOMENCLATURE

α = Measurement Angle for Geometric Far Field Experiments

ρ = Density of Ambient Air

ϕ = Azimuthal Angle for Shielding Experiments

θ = Polar Angle for Shielding Experiments

ω = Angular Velocity

BPF = Blade Passing Frequency

c = Speed of Sound

d = Rotor Tip Clearance

D = Rotor Diameter

D_D = Duct Inner Diameter

D_{OD} = Duct Outer Diameter

f = Frequency

ISL = Inverse Square Law

k = Wave Number

L = Rectangular Plate / Duct Length

n = Number of Point Sources

n_B = Number of Rotor Blades

p = Acoustic Pressure

PS = Point Source

R = Measurement Distance from Observer to Receiver

R_I = Measurement Distance from Observer to Image of Receiver

R_l = Characteristic Distance Associated with Edge Diffraction

SPL = Sound Pressure Level

SPL_n = Normalized Sound Pressure Level ($SPL-SPL_{Reference}$)

ΔSPL = Shielding Amount ($SPL_{Shielded}-SPL_{Unshielded}$)

V = Velocity Potential

V_d = Diffracted Velocity Potential

V_g = Geometric Velocity Potential

V_s = Shielded Velocity Potential

V_u = Unshielded Velocity Potential

W = Rectangular Plate Width

W = Sound Power

ΔdB_T = Error range in SPL due to Temperature

ΔdB_P = Error range in SPL due to Atmospheric Pressure

ΔdB_T = Error range in SPL due to Humidity Rate

SUMMARY

The investigation described in this thesis had two main objectives:

1. To determine the distance at which microphones should be placed for rotor noise measurements so that the rotor can be treated as a point sound source, thus enabling the use of Inverse Square Law (ISL) for the purpose of prediction of rotor noise at different distances and for comparing data from different experiments.

2. To determine validity of representing a full rotor by a point sound source for the purpose of calculating shielding of rotor noise.

In this research, the requirements for microphones to be in the geometric farfield for ducted and unducted rotors have been established. The approach is to acquire acoustic data at various geometric locations relative to the source. This is performed for different rotor configurations and compared with the ISL. This thesis produced a measurement requirement that satisfies the ISL. It is presented in terms of rotor diameter and/or duct length. If this requirement is met then data for rotors with different dimensions acquired at any anechoic facility may be compared. Furthermore, the present work defines the shortest distance where farfield microphone should be placed for accurate extrapolation of the data to the rotor noise of a full-scale system by the ISL.

The second part of the thesis involves acoustic shielding - a noise reduction concept. Acoustic shielding in the present context consists of using part of the vehicle (e.g., wing, body, ducts) to shield the noise source (propeller or fan) from observers. Designers of such vehicles require accurate models for acoustic shielding. The present research is also the first ever work that seeks to answer the question of whether rotor noise from a propeller or a fan can really be approximated by a point source (monopole) as is done in many theoretical calculations and laboratory settings when characterizing the effectiveness of acoustic shields.

The effect of sound scattered and diffracted by the shield placed around or near the actual source of rotor noise is investigated and compared with data acquired using a point source. Shielding configurations consists of rectangular plates and ducts of various lengths. The predictions are made with an existing theory of a point source shielded by a rectangular semi infinite barrier.

The propeller sources are assumed to be made up of many point sources distributed over the propeller disk instead of a single point source. To understand how much difference is made in noise shielding results the following simulations were compared:

1. Case 1: Noise emanating from a single point monopole source of a given acoustic power located at the center of the propeller hub;

2. Case 2: Noise emanating from a collection of point monopole sources, which have the total power equal to that of produced by the single point source at the hub center, distributed either at the tip of the rotor or in a few other manners.

All measurements are made in an anechoic chamber. The findings of this work can be summarized as follows:

1. Minimum measurement distance that satisfies the ISL in terms of rotor diameter is determined for both open and ducted rotors. It was found that the measurement distance should be more than 10 diameters for open rotors and 25 diameters for ducted rotors to satisfy the geometric far-field conditions. Interpreting the results according to the duct length parameter showed that the microphones should be placed at a distance greater than 15 duct lengths.

2. Through the experimental data it is concluded that the point source theory is not always adequate in estimating the noise shielding.

3. Through the calculation of the shielding obtained by a point source and collection of point sources it is concluded that using a single point source at the center to simulate the rotor is very likely to lead to wrong conclusions.

4. Both the calculations and experiments show that as the frequency decreases less shielding is obtained.

5. It is observed that the amount of shielding is quite sensitive to the precision with which the sources are placed with respect to the shield surface.

Finally, it should be mentioned that to the author's knowledge, no other studies exist that document the measurement distance for the microphones to be in the geometric far field for rotor noise. Likewise, this is the first study of validation of the point source assumption for a rotor for shielding studies.

CHAPTER I

INTRODUCTION

Measuring the farfield noise levels of full-scale rotor systems is not trivial and can be costly. Researchers prefer to perform small-scale experiments in the laboratory so that they can extrapolate the model-scale results to larger scales. Typically Inverse Square Law (ISL), commonly referred as $1/R^2$ law, is used to extrapolate the sound pressure levels (SPLs) obtained from model-scale experiments at relatively small distances to predict noise at much larger distances for larger scale systems [1]. ISL is also used to compare rotor noise data acquired in one facility at one distance with that acquired in another facility at a different distance to account for the effect of distance. The assumption underlying the ISL is that the source itself can be treated as a point sound source. At what distance from a rotor system it can be treated as a point source has never been established.

Treating large aerospace systems as a point source is common for a number of other aeroacoustic problems also, for example, many theoretical models of shielding by hard surfaces assume the source to be a point monopole source. If one is interested in shielding the noise of a rotor system by interposing a hard surface between the rotor and the observer, can the rotor system really be considered to be a monopole?

Exploring the validity of point source assumption alluded to above for a rotor for farfield acoustic measurements with and without shielding forms the backbone of the present work.

The ground run up static engine noise is typically measured at microphones located at a distance of 150 ft from near the exit of the engines. In the earlier days when the nozzle dimensions were smaller, this distance was an adequate farfield distance. It is argued in the current work that for the modern high bypass ratio engines where the fan nozzle can be as big as 100 inches and even larger for the ultra high bypass ratio engines of the future, this distance may provide erroneous answers unless due account is taken of the source location or unless the microphone radius is increased considerably so that the noise measurements

are made in the true geometric farfield.

Similar to the modern large fans, the current propellers are quite large and future propellers are expected to be as large as 18 ft in diameter. To estimate the noise of these propellers in the farfield either ground testing will be carried out for the full-scale propeller or acoustic data from small-scale propellers will be extrapolated by using the ISL. The latter case is a more convenient solution.

The ISL simply says that the mean square pressure is inversely proportional to the square of the distance from the source. This means that the sound pressure level decreases 6 dB for each doubling of the measurement distance. If the amplitude of a sound source in free space follows the ISL as the source to receiver distance is increased in any direction then the sound source is considered a point source and it is said that the observer is in the acoustic farfield. For the distances large enough compared to the wavelength of the sound, sound pressure and particle velocity are in phase and ISL is satisfied. In the acoustic farfield, the type of the sound source is unimportant. Similarly, geometric farfield is defined where the effect of source characteristic length is negligible compared to the distance to observer regardless of the source type (e.g., jet, fan, etc.). If the SPL as a function of distance in any direction follows the ISL for the sound source then the observer is said to be located in the geometric farfield [2]. Data acquired in the laboratory meeting this requirement, can be extrapolated to large distances with confidence.

To determine the limits of geometric farfield for acquiring accurate farfield noise of model-scale open or ducted rotors, the plots of SPL at various frequencies are typically obtained in an anechoic chamber as a function of distance in different directions with respect to duct inlet axis. Microphone is typically traversed all the way close to the wedge tips. If the intensity conforms to the ISL, which provides a 6 dB decrease in sound per doubling of the distance, the microphone is considered to be in the geometric farfield of the open or ducted rotor, or for that matter the full aero-engine. It implies that the acoustic interference produced by sources distributed over a finite region of the open or ducted rotor flow do not affect the ISL at distances beyond which this law is followed.

A point source can be any of the simple sources described in classical acoustic theory

developed by Lord Rayleigh which are monopole, dipole and quadrupole sources. These elementary solutions of the equations of motion of small disturbances to a gas at rest, describe the radiation at a single point each having different generation mechanisms. A rotor source, just like any other noise source, is described by a combination of these single sources generated continuously over an area [3].

A brief summary of the rotor noise generation mechanisms would provide a better understanding of the importance of acquiring data at the correct geometric farfield. Superposition of various noise generation mechanisms of a rotor results in a complicated signature of sound propagating to the farfield. The characteristic spectrum of rotor noise is composed of a number of discrete frequency peaks usually occurring at the fundamental blade passing frequency (BPF) and its harmonics, superimposed on a broad spectrum. Broadband noise is dominant at low tip speeds where at higher tip speeds spectrum is characterized by discrete tones [4].

Noise from rotating machinery can be classified as interaction noise and self noise [5].

Interaction noise is generated by unsteady sources due to periodic or random variation of loading on the blades. Unsteady sources result from the rotating blade element encountering a time varying disturbance in the rotating blade frame of reference. As the loading on the blade varies during revolution, generally due to the potential reaction of the blades to local alternating angle of attack, a periodic noise occurs at BPF and its harmonics. Another way of generation of blade loading pulse is through a local distortion induced by and drawn into the rotor. The blades chop through the distortion at several revolutions so the unsteady loading noise can appear at BPF and its harmonics. However, as conditions change, the location of the distortion and, as a result, the amplitude and phase of the unsteady loading noise change. These changes broaden the noise spectrum.

Self noise is generated by the flow over the blades themselves and does not require unsteady inflow. This type of noise, produced by the sources appear constant in time to an observer on the rotating blade, is generally due to the viscous flow over the blades. Distribution of the self noise sources can be monopole, e.g, thickness noise, dipole, e.g., steady loading noise, or quadrupole. Thickness noise is the periodic transverse displacement

of air by the volume of a passing blade element whereas steady loading noise is a combination of thrust and torque (or lift and drag) components, which result from the pressure field that surrounds each blade as a consequence of its motion, both of them appearing at the BPF of the rotor. Loading is an important mechanism at low to moderate speeds. When the flow over the blade section is transonic, nonlinear effects become significant so the rotor noise can be modeled as quadrupole sources distributed within the volume surrounding the blades [6].

When the source is blocked by a structure, and noise shielding is produced, the mechanisms processing the sound waves get more complicated. The basic acoustical phenomena that take place when a noise source is shielded by a barrier are refraction, scattering, and diffraction. In this study, the refracting effect of the local flow field is neglected and it is assumed that no sound is transmitted through the barrier. So the focus will be only on scattering and diffraction. Diffraction and scattering occur when a sound wave encounters a discontinuity, such as an obstacle or an inhomogeneity in the medium, on its path. This generates another group of sound waves spreading out from the discontinuity in a variety of directions [7]. Diffraction may be considered as a subset of scattering. Some mechanisms might be explained by scattering but do not involve diffraction such as in the case of a sound beam reflecting from a rough surface. Diffraction is the reason one can hear another person who is out of sight around the corner or behind a tree. The sound strikes on the corner and scatters around all directions. The waves propagating direct from the source interferes with the scattered waves producing maxima and minima, even nulls at the receiver [8].

The most important condition for diffraction to take place is the constructive or destructive interference of the waves. This causes the amplitude and phase distortion of the sound field. Diffraction mechanism can simply be explained by Huygens-Fresnel theorem. According to this theorem, each element of a wavefront is considered as the center of a secondary disturbance which gives rise to spherical waves. These spherical waves propagate and mutually interfere with each other to form the new wavefront, as a result diffracted waves are generated [9]. In other words, after a wavefront comes across an obstacle, diffraction is the interference of all propagating waves that are not blocked along all possible paths

between the source and the receiver.

Most analytical models of shielding by hard surfaces assume the source to be a point monopole source. This assumption may not work with realistic sources such as a rotor or a jet or jet surface interactions. The aim of this work is to establish how well this assumption might work for an open rotor when placed above a rectangular shield. If we consider a duct for a ducted rotor to be a shield at frequencies below the cut-on of the higher-order modes in the duct, will this assumption hold? However, it is obvious that noise from a rotor has a different directivity pattern than a monopole. So the amplitude and the phase of the rays striking on different edges of the shield will not be the same for a rotor source as they are for a point source. How does this affect the diffraction pattern and the farfield noise as a result? Is the point source assumption which is often used in many available shielding prediction models, a good assumption in terms of reasonable prediction of shielding of the rotor noise in the farfield? The goal is to clarify the differences between the point source and rotor source conditions in terms of shielding for an aeroacoustic engineer to develop more effective designs. To the author's knowledge, the present research is the first ever work that seeks to answer the question of whether rotor noise from a propeller or a fan can really be approximated by a point source as is done in many theoretical calculations when characterizing the effectiveness of acoustic shields.

In summary, this thesis has two main objectives. These are:

1. To determine the distance at which microphones should be placed for rotor noise measurements so that the rotor can be treated as a point sound source, thus enabling the use of ISL for the purpose of prediction of rotor noise at different distances and for comparing data from different experiments.

2. To determine validity of representing a full rotor by a point sound source for the purpose of calculating shielding of rotor noise.

CHAPTER II

PREVIOUS RELATED RESEARCH

A large amount of research has been performed that is relevant to the present work. Table 1 summarizes the key research investigations of geometric farfield limits for jet noise. Tables 2 - 6, focusing on rotor noise, lists the relevant theoretical, computational and experimental research conducted by several researchers on diffraction and acoustic shielding. The information given includes the type of the noise source and the structure that shields the source, categorizes whether the work is theoretical, computational or experimental, and emphasizes the frequency range. It also explains whether the solution is given for farfield or near field and whether the effect of free stream velocity is considered. Each work indicated in these tables are summarized in the following sections.

2.1 Geometric Farfield for Rotors

The ISL is a fundamental law in the field of acoustics and yet little attention to its limitations has been paid by most researchers. For example, modeled the radiation of noise to the farfield from the fan inlet and aft ducts using finite element technique [9]. For his computational work the author chose the farfield boundary to be located 10 diameters away from the source based on the dimensions of Aeroacoustic Propulsion Laboratory at Lewis Research Center.

Although several authors have worked on experimental determination of the geometric farfield for jet noise, similar determination for rotor noise has never been documented. Because of the relevance of the research on geometrical farfield of jet noise, which emanates from a distributed set of sources, the related work is reviewed below. Koch et al [10], shows results for three round jets with exit diameters of 25 mm, 51 mm and 76 mm operated under unheated subsonic conditions. Based on analytical and experimental results this work shows that while for high frequency sound (Strouhal number ≥ 0.2) 8 nozzle diameters is enough to be in the geometric farfield, for low frequency sound (Strouhal number ≤ 0.2)

Table 1: Summary of research on geometric farfield limits.

	Title	Author	Source Type	Configuration	Frequency Description	R/D finding for low frequencies	R/D finding for high frequencies
	Designing Clean Jet Noise Facilities and Making Accurate Jet Noise Measurements	Ahuja [1]	Jet Noise	Round Nozzle	N/A	N/A	N/A
	Experimental and Analytical Determination of Geometric Farfield for Round Jets	Koch et al. [10]	Jet Noise	Round Nozzle	$St.no^a > 0.2$; $St.no < 0.2$	50	8
	Potential Errors Introduced in the Use of Static Engine Noise Data not Acquired in Geometric farfield	Ahuja et al. [11]	Jet Noise	Round Nozzle Rectangular Nozzle	$240 - 48k$ Hz	50	N/A

[a]Abbreviation for Strouhal Number

Table 2: Summary of most recent research on rotor noise shielding by aircraft components. (Y indicates "yes", N indicates "no")

	Title	Author	Source Type	Configuration	Research Type	Farfield	Near Field	Frequency Range
	The Theory of Sound	Rayleigh [12]	N/A	N/A	Analytical	N/A	N/A	N/A
	Vorlesungen uber Mathematische Optik	Kirchhoff [13]	N/A	N/A	Analytical	N/A	N/A	N/A
	Mathematische Theorie der Diffraction	Sommerfeld [14]	N/A	N/A	Analytical	N/A	N/A	N/A
	Diffraction at a Straight Edge	MacDonald [15]	N/A	N/A	Analytical	Y	Y	N/A
	Diffraction of Sound Around a Circular Disk	Primakoff [16]	N/A	N/A	Analytical	Y	Y	N/A
	Noise Reduction by Screens	Maekawa [17]	Point Source	An infinite plane wall on the ground	Experimental, Analytical	Y	N	N/A
	Electromagnetic and Acoustic Scattering by Simple Shapes	Bowman et al. [18]	Monopole Dipole Plane Wave	N/A	Analytical	Y	Y	N/A

Table 3: Summary of most recent research on rotor noise shielding by aircraft components. (Y indicates "yes", N indicates "no")

	Title	Author	Source Type	Configuration	Research Type	Farfield	Near Field	Frequency Range
	Noise Shielding for Aircraft	Broadbent [19]	N/A	N/A	Analytical	Y	Y	N/A
	Evaluation of Approximate Methods for the Prediction of Noise Shielding by Airframe Components	Ahtye et al. [20]	Point Source	PS shielded by rectangular & cylindrical shapes	Experimental, Analytical, Computational	Anechoic Chamber	N	$1 - 20$ kHz
	One Hundred Years of Diffraction Theory	Keller [21]	N/A	N/A	N/A	Y	Y	N/A
	High Speed Turboprop Aeroacoustic Study (Single Rotation) Volume 1: Model Development	Whitfield et al. [22]	Propeller	Propeller, Fuselage, and Wings	Experimental, Analytical, Computational	Y	Y	N/A
	High Speed Turboprop Aeroacoustic Study (Counterrotation) Volume 1: Model Development	Whitfield et al. [23]	Propeller	Propeller, Fuselage, and Wings	Experimental, Analytical, Computational	Y	Y	N/A
	Unified Aeroacoustics Analysis for High Speed Turboprop Aerodynamics and Noise Development of Theory for Noise Shielding	Amiet [24]	Point Source	Wing mounted Propeller	Analytical	$kr < 10$ exact; $kr > 10$ appr.	Y	N/A
	Unified Aeroacoustics Analysis for High Speed Turboprop Aerodynamics and Noise Application of Theory for BL,W,N, and Wing Shielding	Hanson et al. [25]	Propeller	Wing mounted Propeller	Computational	N	Y	N/A

Table 4: Summary of most recent research on rotor noise shielding by aircraft components - Continued. (Y indicates "yes", N indicates "no")

	Title	Author	Source Type	Configuration	Research Type	Farfield	Near Field	Frequency Range
	A Computer Program for Predicting Ducted Fan Engine Noise	Dunn et al. [26]	Ducted Fan Engine	N/A	Computational	Y	Y	N/A
	Inlet Noise Reduction by Shielding for the Blended Wing Body Airplane	Clark et al. [27]	Point Source	PS inside a nacelle located on the blended wing	Experimental	Anechoic Chamber	N	$2-4k$ Hz
	Aircraft Engine Noise Scattering - A Discontinuous Spectral Element Approach	Stanescu et al. [28]	Engine	Nacelle w/ and w/o Wing	Computational	Y	Y	N/A
	Large Scale Frequency Domain Numerical Simulation of Aircraft Engine Tone Noise Radiation and Scattering	Stanescu et al. [29]	Engine	Nacelle w/ and w/o Wing	Computational	Y	Y	N/A
	Computation of Engine Noise Propagation and Scattering off an Aircraft	Xu et al. [30]	Engine	Nacelle w/ and w/o Wing	Experimental, Computational	Y	Y	N/A
	Aeroacoustic Scattering via the Equivalent Source Method	Dunn et al. [31]	Spinning Sources	Commercial Transport; Blended Wing Body	Analytical, Computational	Y	Y	N/A

Table 5: Summary of most recent research on rotor noise shielding by aircraft components - Continued. (Y indicates "yes", N indicates "no")

	Title	Author	Source Type	Configuration	Research Type	Farfield	Near Field	Frequency Range
	Investigation of Acoustical Shielding by a Wedge Shaped Airframe	Gerhold et al. [32]	PS comp. of four impinging jets	PS inside a nacelle located on the blended wing	Experimental, Computational	Anechoic Chamber	N	$6k - 40k$ Hz
	ROSAS Wind Tunnel Test Campaign Dedicated to Unconventional Aircraft Concepts Study	Ricouard et al. [33]	Fan Noise Simulator	Fan noise simulator in a nacelle located on aircraft	Experimental, Analytical, Computational	Anechoic Chamber	N	$500 - 63k$ Hz
	Aeroacoustic Noise Prediction Using the Fast Scattering Code	Tinetti et al. [34]	Spinning Sources	Commercial Transport	Analytical, Computational	Y	Y	N/A
	Noise Prediction Studies for Blended Wing Body Using the Fast Scattering Code	Riemann et al. [35]	Point Source	PS inside a Nacelle located on the blended wing	Experimental, Computational	N/A	N/A	N/A
	Noise Scattering by the Blended Wing Body Airplane - Measurements an Prediction	Riemann et al. [36]	Point Source	PS inside a Nacelle located on the blended wing	Experimental, Computational	N/A	N/A	up to 450 Hz
	Engine Liner Optimization Using Fast Scattering Code	Riemann et al. [37]	Point Source	PS inside a Nacelle located on the blended wing	Experimental, Computational	N/A	N/A	40 Hz - 630 Hz

Table 6: Summary of most recent research on rotor noise shielding by aircraft components - Continued. (Y indicates "yes", N indicates "no")

	Title	Author	Source Type	Configuration	Research Type	Farfield	Near Field	Frequency Range
	Aft Fan Noise Shielding by a Lifting Surface: Analytical, Numerical and Experimental Results	Chappius et al. [38]	Fan Noise Simulator	Simulator shielded by a rectangular wing	Experimental, Analytical, Computational	Anechoic Chamber	N/A	N/A
	Low Frequency Acoustic Shielding by the Silent Aircraft Airframe	Agarwal et al. [39]	Point Sorce	PS above the real aircraft configuration	Experimental, Analytical, Computational	Anechoic Chamber	N	1250 Hz
	Ray Tracing Approach to Calculate Acoustic Shielding by a Flying Wing Airframe	Agarwal et al. [40]	Point Sorce	PS above the real aircraft configuration	Experimental, Analytical, Computational	Anechoic Chamber	N	up to $4k$Hz
	Initial Integration of Noise Prediction Tools for Acoustic Scattering Effects	Nark et al. [41]	N/A	N/A	Computational	Y	Y	N/A
	Scattering High Frequency Duct Noise by Full Scale Hybrid Wing Body Configurations	Tinetti et al. [42]	Spinning Sources	Blended Wing Body, Hybrid Wing Body	Experimental, Computational	Y	Y	up to 1100 Hz
	Prediction of Jet Noise Shielding	Papamoschou [43]	Jet	N/A	Experimental, Analytical, Computational	N	Y	N/A

the geometric farfield is reached at a measurement radius of at least 50 nozzle diameters because of its extended source distribution. Ahuja et al [11], performed a more extensive work including round nozzle, round nozzle equipped with two tabs, round convergent nozzle, Mach 1.7 convergent-divergent nozzle, and a rectangular nozzle. A typical plot of SPL vs. microphone distance that compares ISL with experimental data for jet noise from a conical round nozzle is shown in Figure 1. Their work concludes that while at frequencies above 600 Hz all nozzles meet the geometric farfield for R/D greater than about 30, to acquire accurate data for all polar directions at all frequencies at least 50 diameters is necessary to make measurements in the true geometric field.

2.2 Diffraction and Acoustic Shielding

The diffraction phenomenon was first studied for light waves and electromagnetic waves by the researchers. Rayleigh [12] was one of the first to give an exact solution for the scattering of an electromagnetic wave by a perfectly conducting circular cylinder. His solution used separation of variables, and was an infinite series of products of trigonometric functions multiplied by Bessel or Hankel functions of the radial coordinate. Kirchhoff [13] was one of those who described the diffraction phenomenon through wave theory of light and used the wave equation or Maxwells equations to solve the problem analytically. He developed a method for the case of diffraction through a hole in a thin plate. However, this solution was incomplete because it did not satisfy the boundary conditions on the surface.

Keller [21], published a review that summarizes the history of the theoretical work performed on diffraction until 1983. The following information on the first half of the 20th century is based on this review paper. Several researchers worked on solving the problems of diffraction from geometrically shaped surfaces using Rayleighs solution for small values of kr where r is a typical length in the problem and k is the wave number. Some of these surfaces represent a sphere, a parabolic cylinder, a strip or complementary slit, a circular disk or a complementary hole, and a semi-infinite circular cone. In his review of diffraction theory, Keller [21] mentions that the large kr case was studied by Sommerfeld [14] on the problem of scattering of a plane or spherical wave by a semi-infinite half-plane. Sommerfeld

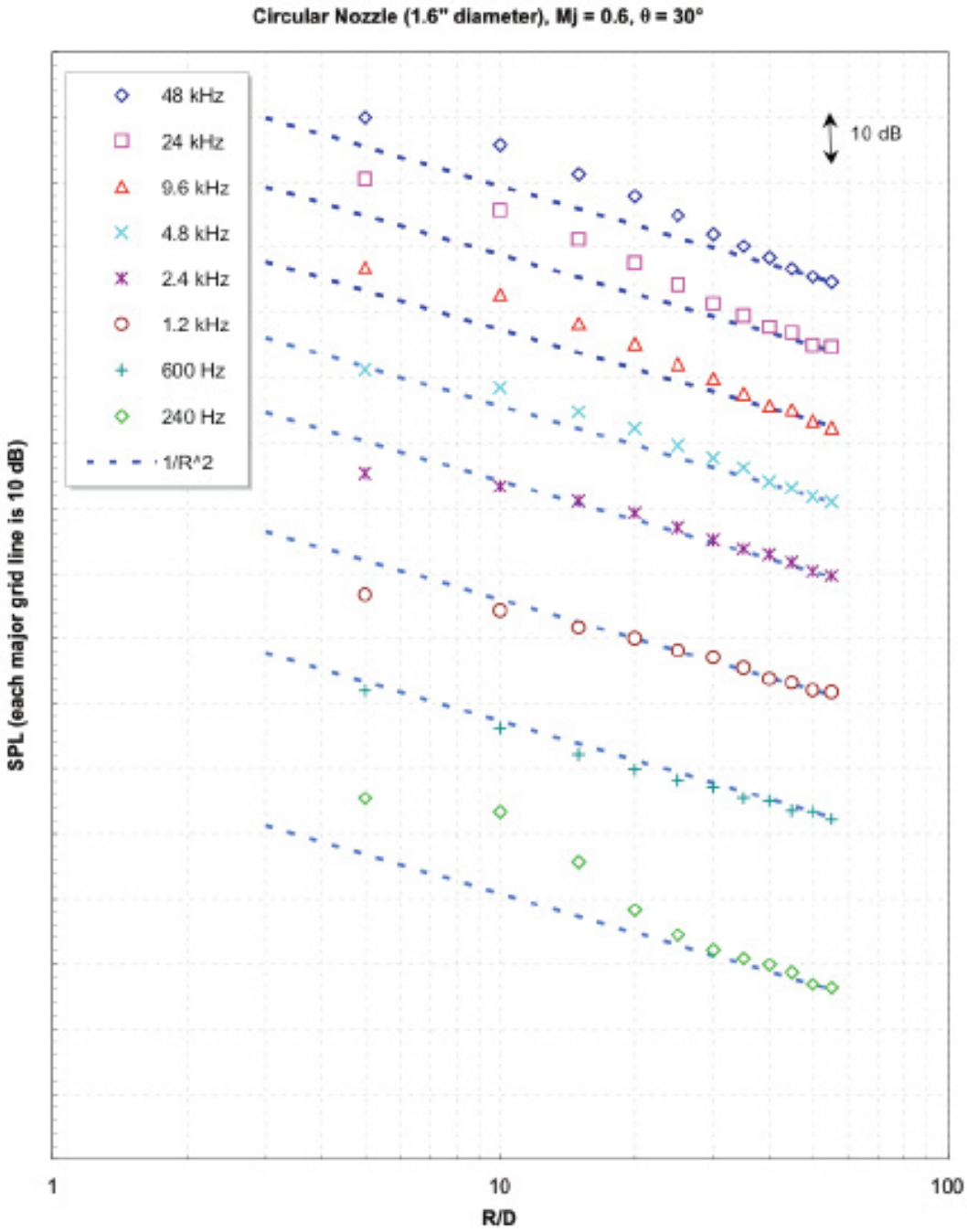

Figure 1: SPL vs. Microphone Distance for jet noise from a conical round nozzle of $D = 1.6''$ at $\theta = 30^o$ [11].

[14] realized that Fresnel integrals revealed the diffraction effects very clearly. So instead of separation of variables which did not give a solution that is directly useful for analyzing diffraction phenomena, he proposed a method in terms of Fresnel integrals which could be evaluated easily for all parameter values. Keller [21] points out that Sommerfelds method was mostly used to solve scattering by a wedge which is important for real life applications, and this problem was solved by MacDonald [15]. Among many of his works on diffraction theory, MacDonald solved the problem of diffraction at a straight edge for a monopole source in a way that does not involve the use of special analytical functions.

Primakoff et al [16] worked on determining the shielding effect of a baffle on propeller noise that resulted in an exact solution. The baffle was represented by a thin circular disk and the propeller by a point source on the axis of symmetry. For the diffraction problems exact solutions exist only for some cases where there is high degree of symmetry for the shield and the source and their configuration with respect to each other. Other cases are solved based on approximations. Maekawa [17] presented a method for calculating the free field shielding effect of a semi-infinite plane screen erected on the ground for the purpose of noise reduction. His method, which didn't need any computer aid, included the ground reflection.

Bowman et al [44], presented a solution for shielding by a semi-infinite half plane based on edge phenomenon and diffraction effects. This closed-form solution was an approximation that was represented in terms of Fresnel integral. They extended the mathematical expression previously developed by MacDonald [15] for monopole sources, for dipole sources with no restrictions on source location. Broadbent [19], reviewed the methods for calculating effect of noise shielding produced by aircraft airframe and also discussed the refraction by the flow field on the basis of ray theory. The importance of frequency and directivity on shielding in terms of source distribution and position was highlighted. The author commented that it is important to know the true source distributions over an area, implying that a single monopole assumption is inadequate. The area covering the source distribution is a function of direction and distance to the shield. The author also commented that since the directivity of the noise sources of the aircraft engine changed with the frequency, the

frequency range needed to be broken down into components.

Ahtye et al [20], performed anechoic chamber measurements of the shielding of a point source, generating tonal and broadband noise, by simple geometrical shapes (rectangular plates, circular cylinder and rectangular plate attached to the cylinder to simulate a wing body combination). For all cases, the predictions were made by the superposition of asymptotic closed form solutions for shielding by semi-infinite plane barrier which was previously presented by Bowman et al. The measured data from both the rectangular and cylindrical shields was compared with these predictions. In Figure 2, the shielding ($\Delta SPL = SPL_{shielded} - SPL_{unshielded}$) by a rectangular shield of [0.5 m x 2 m] are plotted as a function of the traverse angle θ. Figure 2(a) shows the shielding for a tone at 1 KHz. In Figure 2(b) pink noise was used instead of tonal noise, and, again, shielding at 1 kHz is shown. In this case the configuration is symmetric which causes the contributions from the right and left visual edges at small angles to be comparable. The constructive and destructive interference of the wave from the these two edges determine the diffraction pattern seen in this figure over the entire range of θ rather than top and bottom edges that are at larger distances to the point source.

Although the exact solutions for the shielding of a point source by both rectangular plate and circular (infinitely long) cylinders exist, shielding calculations for cylinders are very complex. So Ahtye et al, used the calculations for rectangular plate (whose width is the same as the diameter of the cylinder), to also approximate the cylindrical shielding. An example of the comparisons of theory based on a rectangular shield and experimental results of a cylindrical shield is given in Figure 3. Figure 3(b) shows that the approximation gives good results.

Whitfield et al [22] investigated installation effects on the sound field generated by a single rotation propeller. To estimate the unsteady loading imposed on the propeller by wing and fuselage, they developed mathematical models of the velocity fields induced at the propeller disk by interactions of these fields. Authors used a chordwise compact propeller unsteady-loading noise model together with these unsteady blade loadings to predict unsteady-loading noise caused by the installation effects. Later, Whitfield et al [23] extended

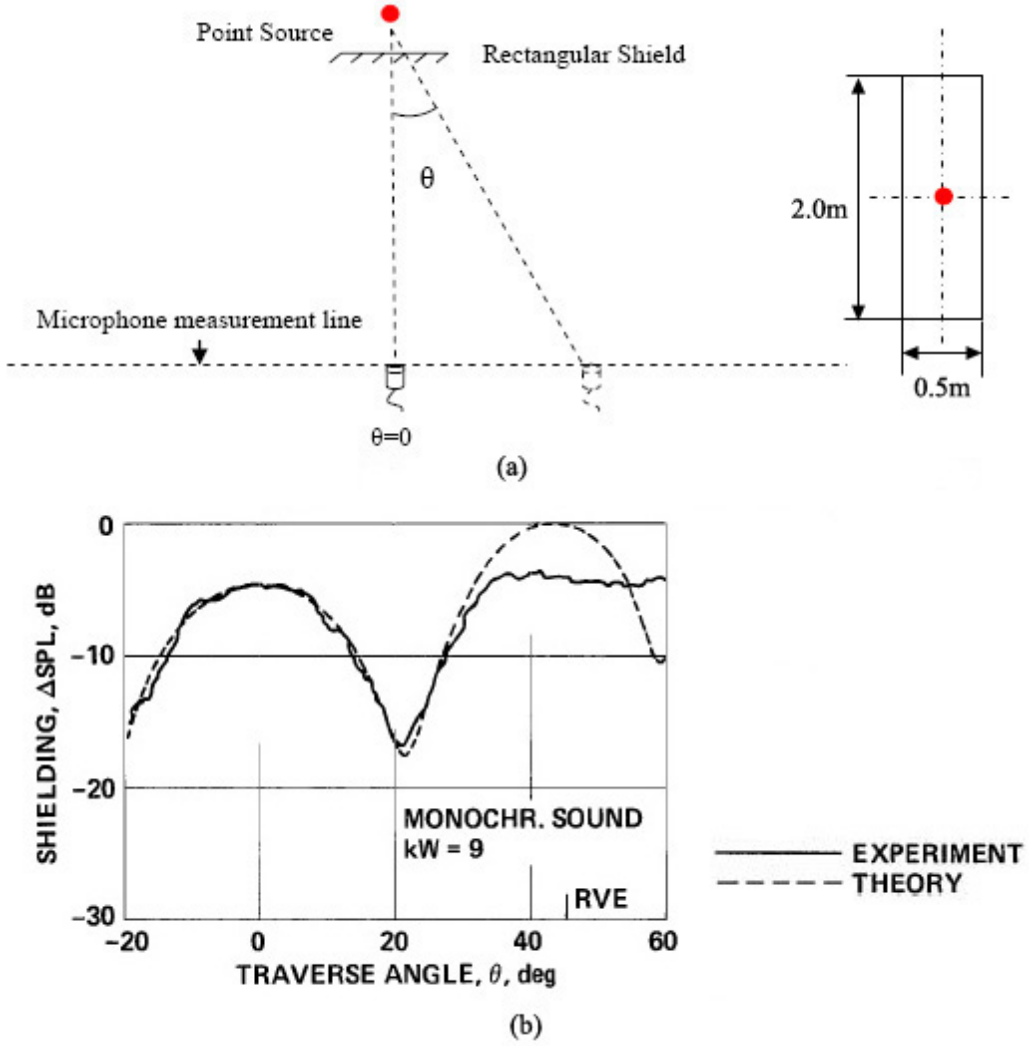

Figure 2: Comparison of experimental and theoretical shielding at 1 kHz for a rectangular plate (Source to shield distance is 0.25 m.) [20], (a) test configuration, (b) shielding by a rectangular plate, $f = 1$ kHz.

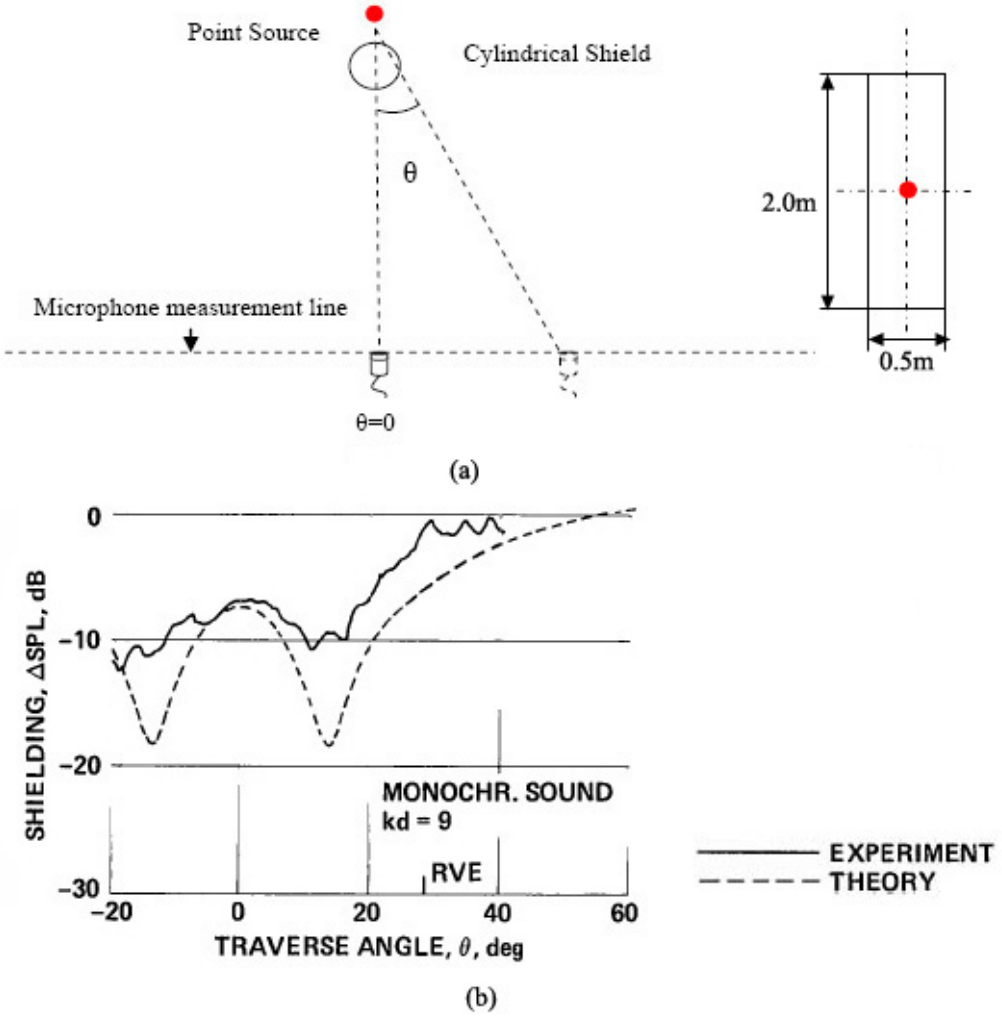

Figure 3: Comparison of experimental data for shielding by a cylindrical barrier and theoretical shielding at 1 kHz for a rectangular plate with 0.5 m width (Source to shield distance is 1 m.) [20], (a) test configuration, (b) shielding by a cylindrical barrier, $f = 1$ kHz.

this work for counterrotating high speed turboprop designs. In addition to the fuselage and the wing, the effect of a mounting pylon upstream of the forward rotor was investigated.

Since most of the theories related with diffraction phenomenon were first investigated as optics or electromagnetics problems, the mean flow concept which is important for aeroacoustics applications were not considered. Amiet [24], extended Sommerfeld's [14] solution for diffraction of sound by a half plane at no mean flow condition, to the case where half plane is immersed into uniform flow. A propeller source mounted on an airplane wing was simulated by a point source for the evaluation of the shielding benefit. The case of diffraction with mean flow was reduced to the ordinary wave equation by a combination of Galilean and Lorenz transforms. So the problem with mean flow was reduced to the problem with no mean flow. Through the same transformations, solution for the effect of the sweep was also obtained. Solutions for the trailing and leading edges of the wing were found to be different due to the different source types at two edges. The author mathematically showed that the behavior of the sound fields normalized by incident wave for two different source types (monopole and plane wave) would give the same directivity pattern. Under the high frequency and farfield assumption for the source, he concluded that, if the two diffraction patterns from different sources were normalized by the wave amplitude incident on the edge the results would be equal. This meant that the diffraction pattern did not depend on the general source directivity but only on the ray striking the edge. Hanson et al [25], applied the theory given by Amiet [24] on the actual airplane geometry. A propeller mounted on an airplane wing was chosen to be the source. The shielding amount of noise propagating to the fuselage wall for an observer at the window level of the airplane, when the sound from propeller was blocked by the wing, was investigated. Since the theory was developed under the point source assumption, to compensate this fact for the propeller source, authors presented the results in a special way. They computed the ratio of sound pressure at the observer to the assumed sound pressure for the ray incident on the wing leading edge at an equal observer radius. The geometry and the results of their calculations at several harmonics of the blade passing frequency for Mach 0.15 is given in Figure 4(b). Wing shielding correction given in dBs as the ordinate represents the amount of shielding achieved by the

wing. To obtain the noise levels at the observer, these shielding amounts given should be added to the calculated noise. Comparing of the results at different Mach numbers, the authors concluded that wing shielding has a stronger effect at high Mach numbers, and frequency has a stronger effect at the low Mach numbers.

Dunn [26] developed a ducted fan noise prediction program, called 'Thin duct, Boundary Integral Equation Method, 3 Dimensional' (TBIEM3D). The author used boundary integral equation method (BIEM), to compute the scattering of fan generated noise by a finite length, infinitesimally thin circular cylinder in a uniform flow field. He modeled fan noise by a collection of spinning thrust dipoles and calculated circumferential modal coefficients of the acoustic pressure.

All these theories developed needed to be verified by experimental data. Several researchers performed laboratory tests simulating the rotor noise sources by a monopole source. Clark and Gerhold [27], performed anechoic chamber tests for fan noise shielded by a blended wing body airplane. They tested a 3-engine nacelle configuration shielded by the blended wing body of subsonic transport aircraft by using a high frequency point source inside the nacelle to represent engine noise. The configuration is shown in Figure 5. Comparing the noise levels above and below the wing, it was observed that significant shielding of inlet noise (up to 20 dB) occurred, however in the aft direction almost no shielding was obtained. The greatest amount of shielding was seen at the third harmonic so authors concluded that the wing shielding mechanism works best for relatively high frequencies. The experimental data obtained by this work was compared with the analytical model developed by Gerhold et al [32], in terms of sound scattering and installation effects of engine noise. Computational model of the shielding mechanism has been developed using two models. One is the 3D Boundary Integral Equation Method (TBIEM3D), which estimates the incident sound from the engine noise source or the point source in a nacelle in this case. The other is the equivalent source method (ESM) which determines the scattering by the wedge to synthesize the sound field in the vicinity of the airfoil. The difference of these two estimates gave the noise shielding. Figure 6 is a comparison of experimental and analytical results for the noise scattered by the airframe at 6300 Hz. The ordinate of the

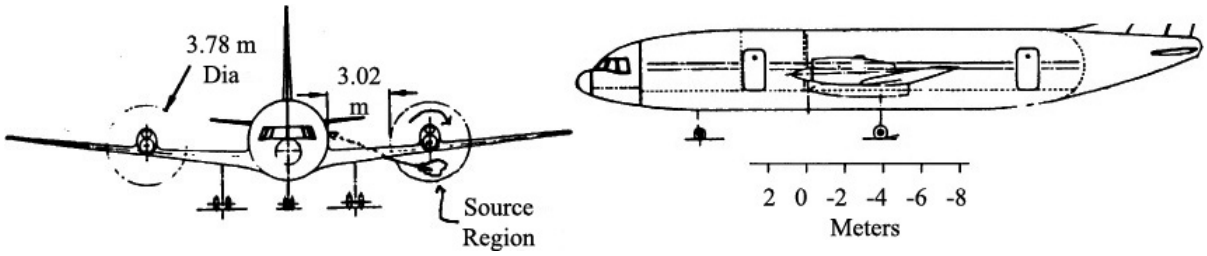

(a)

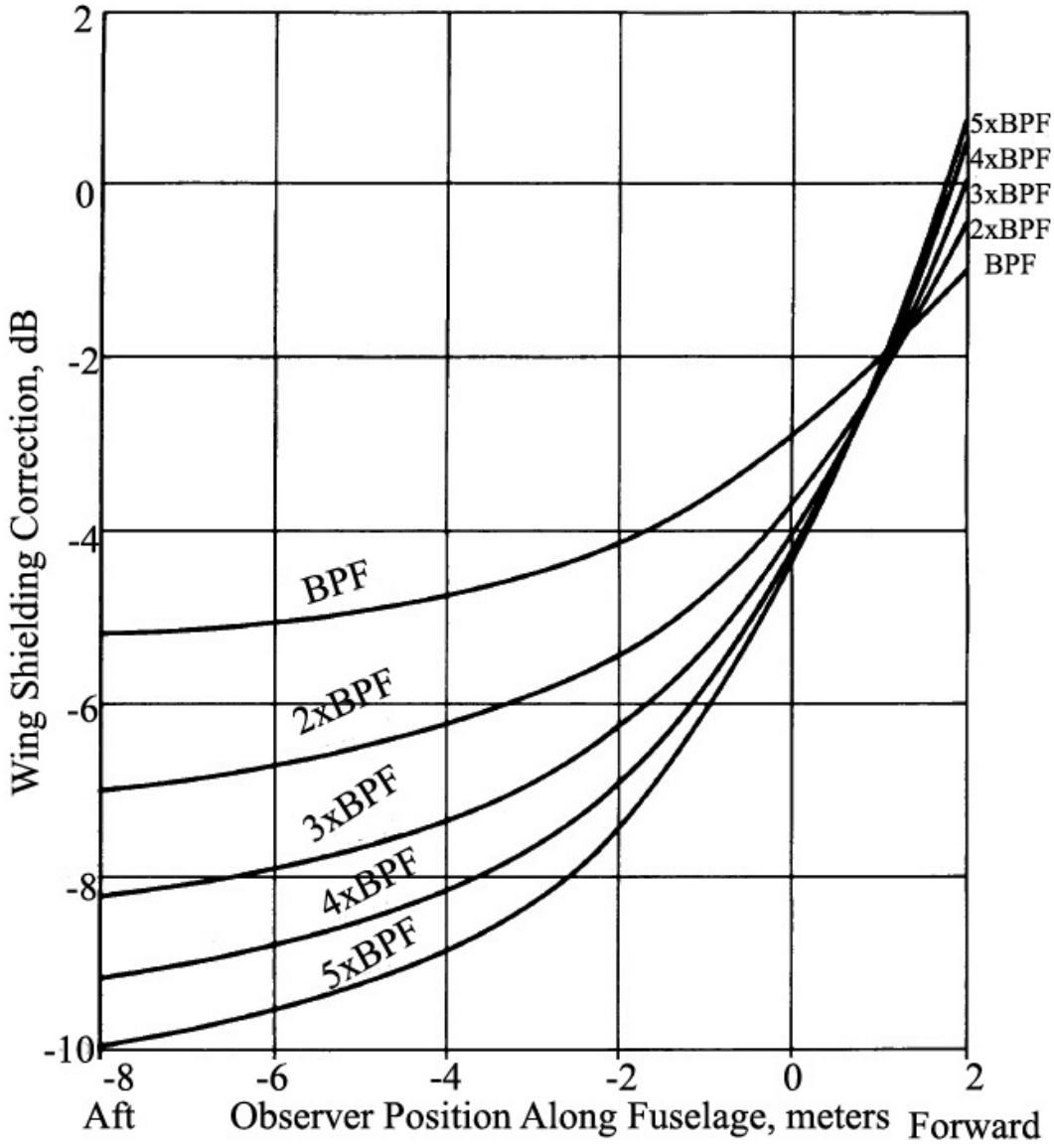

(b)

Figure 4: Noise reduction due to wing shielding at 0.15 Mach number, (a) aircraft geometry, (b) shielding amount for first five harmonics of the blade passing frequency as a function of the observer [25].

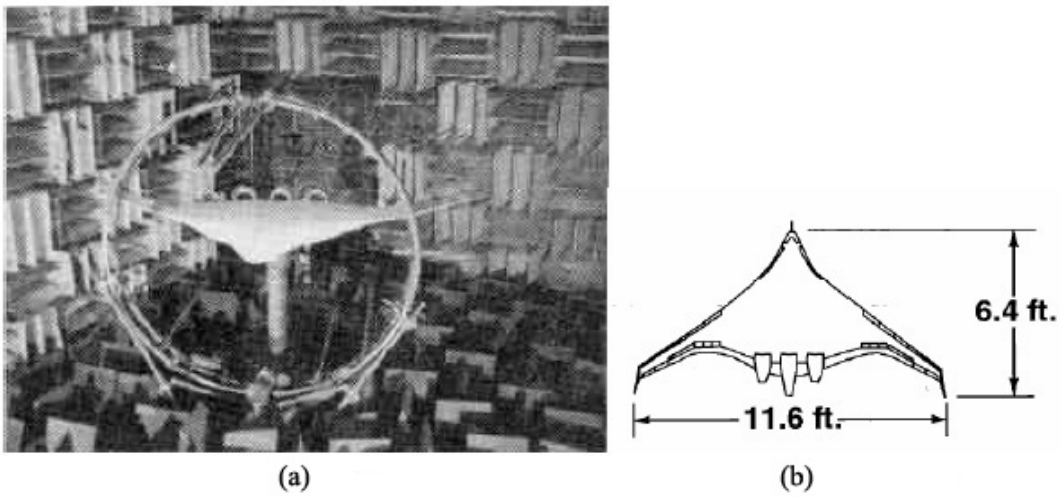

Figure 5: Test configuration [27], (a) photographic view, (b) main aircraft dimensions.

contour plots of SPL represents the measurement direction and the abscissa represents the measurement distance to the noise source. Experimental results agreed well with the analytical calculations. It was seen that about 90^o azimuth noise is increased. According to the authors, this was due to reflection of aft radiated sound by the sloping rear surface of the airframe. Besides these, in general, from the results of both computation and experiment, authors concluded that scattering and diffraction of sound were sensitive to the location of the source and to the shape of the airframe.

Stanescu et al [28], developed a computation method in the time-domain for sound radiation from aircraft engine sources to the far-field that accounts for the effects of nonuniform flow around the aircraft and scattering of sound by fuselage and wings. The modeling was performed based on Discontinuous Galerkin spectral element method. Later, authors solved this problem in the frequency domain by the solution of the linearized full-potential equation [29] . Xu et al [30] simulated the radiation of the dominant spinning mode from the engine and its reflection and scattering by the fuselage and the wing under flight conditions by both time and frequency approaches. Then, the simulations were compared with the experimental noise data. Authors showed that both methods predicted the noise field trends well.

Dunn et al [31] also developed a computational method that employs the equivalent

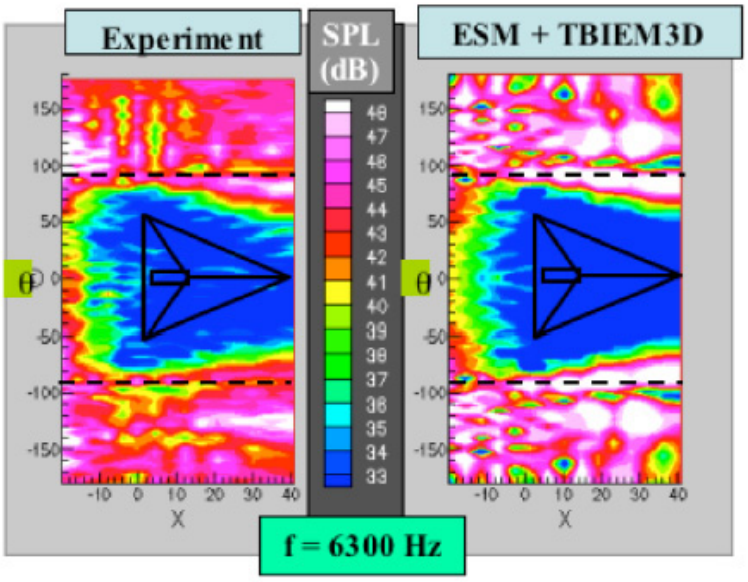

Figure 6: Noise scattered by the airframe - Comparison of experimental and analytical results, $f = 6300$ Hz [32].

source method (ESM) for solving an exterior Helmholtz equation boundary value problem. The computer program, named the Fast Scattering Code (FSC), predicted the scattering of incident engine noise by an airframe in a uniform flow field by implementing ESM. A collection of simple point multipoles (monopoles, dipoles, etc.) in uniform motion formed the incident sound and this sound field was scattered from the airframe/nacelle configuration. The code also simulated the spinning modes generated by engine rotor/stator interaction by a collection of spinning point multipoles. Authors showed that the FSC could simulate the spinning mode duct acoustics properly through the modal analysis study using the scaled GE90 nacelle.

Ricouard et al [33], conducted a parametrical study to explore the installation effects for fan and jet noise. The authors were investigating the effects of source spatial distributions for jet noise, directivity and positioning for the fan tones on shielding by airframe surfaces. These installation effects that create scattering, refraction and diffraction mechanisms were validated by a theoretical point source method of the diffraction effect under semi-infinite planes developed by Maekawa [17]. The experiments performed showed that the experiments did not work for jet noise (Figure 7(a)) but worked reasonably well for fan noise (Figure

7(b)).

Tinetti et al [34] extended the theoretical formulation of the FSC to include the effects of non-uniform flows under conditions where spatial derivatives of the flow variables can be neglected. The authors showed that FSC could calculate the non-uniform flow over simple shapes in isolation. Calculations for the 2.68% scale model of a commercial transport where the incident acoustic field was modeled by spinning monopoles placed inside the nacelles is shown in Figure 8. The asymmetric field surrounding a fuselage/wing/nacelles assembly is clearly seen when the nacelles contain acoustic sources spinning in the same direction.

Reimann et al presented a series of work comparing the acoustic and aerodynamic data obtained at NASA Langley Research Center Anechoic Research Facility from testing of a 3% scale model blended wing body configurations with nacelles, with the FSC. Authors concluded that FSC could successfully predict the acoustic behavior of a source and nacelle combination in the diffraction zone surrounding the configuration [35]. Then they extended their calculations to explore the effects of background flow and acoustic treatment on the nacelle inner walls and showed the benefits of acoustic treatment for a fully lined nacelle [36]. Later, they validated the reliability of FSC for predicting the scattered acoustic field in the presence of lined surfaces and power of its usage for engine liner optimization [37].

Chappius et al [38] studied aft fan noise shielding by the aircraft horizontal plane. The analytical approach, that predicted diffraction of a point source by a rigid half plane, was applied, independently, to the two edges of a rectangular strip of finite chord. Then the corresponding contributions were summed up in the farfield. Authors performed acoustic measurements using a noise simulator to simulate aft fan noise with its modal content and concluded that the monopole source was insufficient for noise shielding predictions because of the importance of directivity of the noise source. Authors proposed the noise source model given in Figure 9 to define fan noise modes. The model was made of an array of phase shifted monopoles to include the directivity effect lacking in the prediction methods.

Agarwal and Dowling [39], used boundary element method to evaluate acoustic shielding at low frequencies. Instead of the diffraction theories based on acoustic scattering from a semi-infinite half plane, the acoustic estimates were obtained from the finite simple 2D

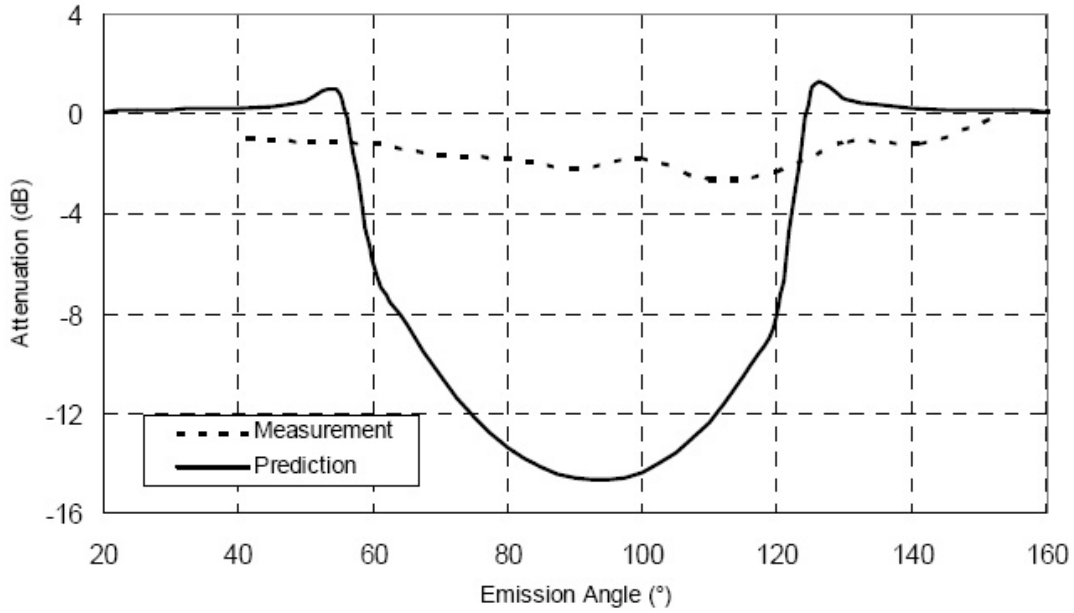

(a)

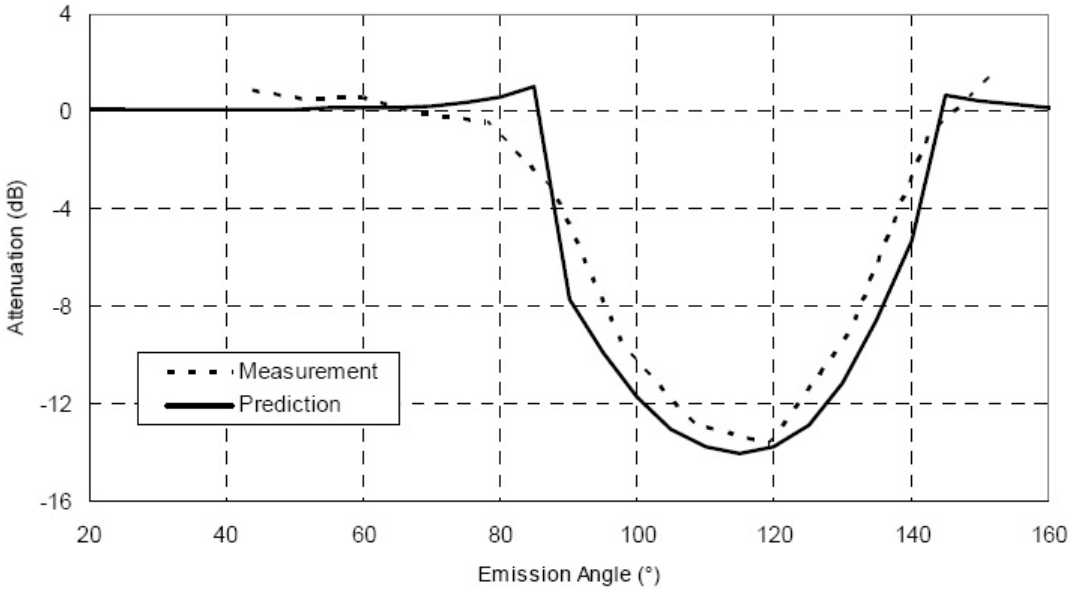

(b)

Figure 7: Comparison of prediction and measurements [33], (a) jet noise shielding, (b) fan noise shielding.

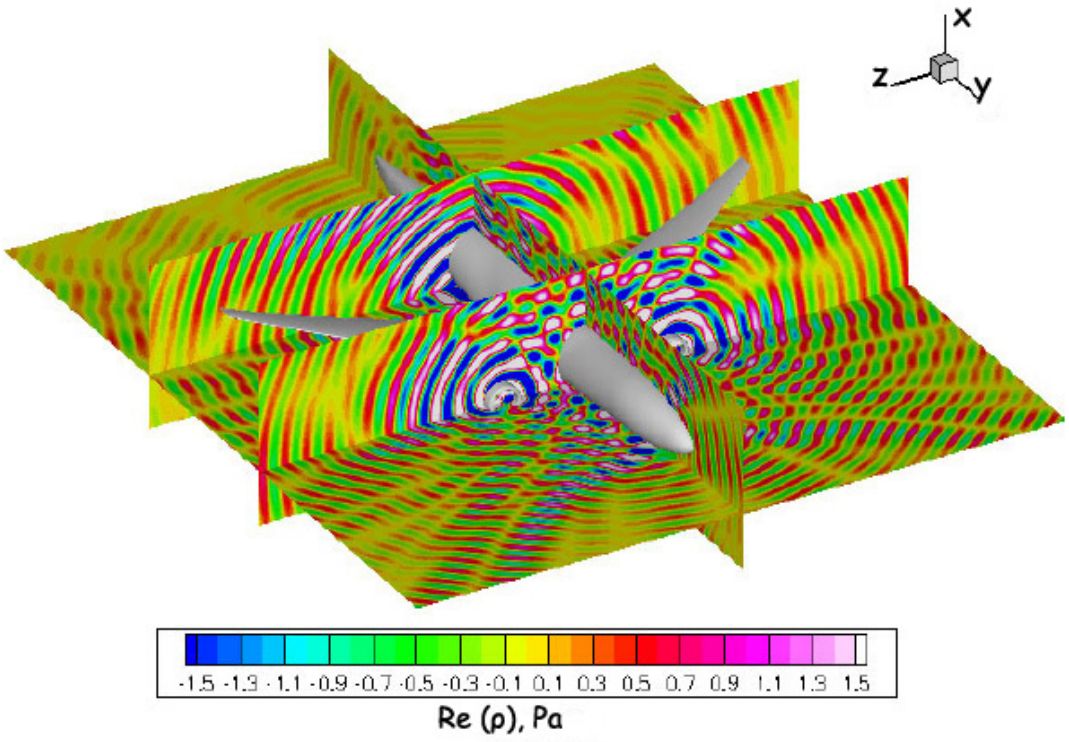

Figure 8: Aeroacoustic contours calculated by FSC in the vicinity of a 2.68% scale model of a commercial transport in flight at 5 kHz [34].

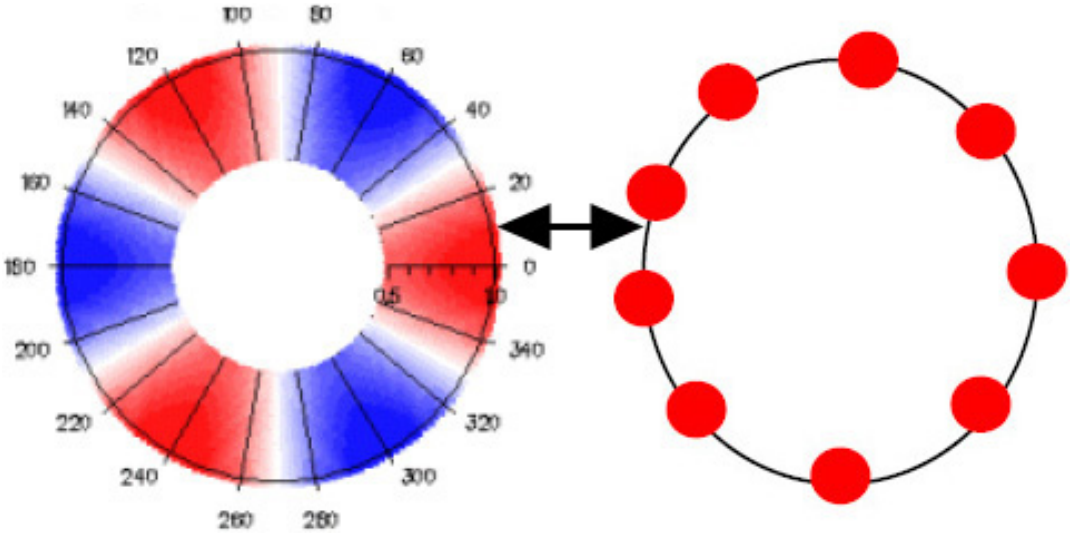

Figure 9: Array of monopole sources (right) used to model the pressure field (left) in a section of the exhaust duct [38].

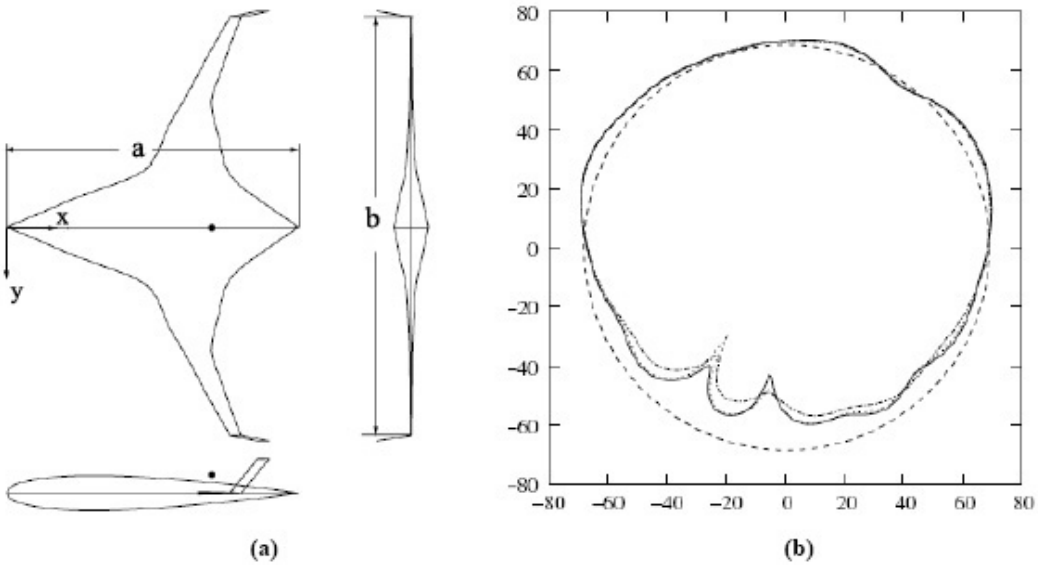

Figure 10: (a) test configuration, (b) sound directivity pattern, $kr = 500$, solid line : $y = 0$, dotted line : $y = b/2$, and dash-dot line : $y = b$ [39].

geometries and 3D aircraft airframe. In order to provide more realistic interpretation of aeroacoustic sources, they also accounted for mean flow refraction effects due to forward flight motion. Authors used point monopole source placed above the geometries. Sound directivity pattern in the farfield at $kr = 500$ for the model configuration illustrated in Figure 10(a), is given in Figure 10(b). Dashed line represents the incident field, solid line, dotted line and dash-dot line represents three spanwise locations: $y = 0, y = b/2$ and $y = b$, respectively, where b is the wingspan. Abscissa of the plot is the x-axis seen on the sketch and z-axis that is out of the paper is the ordinate. Less shielding was obtained directly below the aircraft with respect to the sides. According to the authors this was because of the constructive adding of contributions from various wedges since the source was placed symmetrically above the wing.

To quantify the case of shielding at high frequencies, Agarwal et al [40], used ray tracing technique which is a method applicable to high frequencies but not good at low frequencies. The methodology used to calculate the total amount of acoustic shielding at an observer located in the shadow region involved adding the contributions from all the diffracted rays (edge refracted and creeping rays) and then subtracting the result from the incident field

without the airframe. Numerical solutions with the ray tracing technique in 3D were compared with analytical high-frequency asymptotic solutions for canonical shapes (e.g., ellipse) and were also compared with experiments on model-scale geometry in an anechoic chamber. Authors observed that the shielding near the winglets was less because observers at these locations receive multiple diffracted rays from the winglet. To solve the problem, use of acoustic liners on the winglet was suggested. The authors indicated that the advantage of the ray tracing method was that the direction of the received sound could be discovered. The reason for this is that all rays to particular observers can be tracked graphically which provided valuable physical insight. On the other hand the authors stated that the method had several disadvantages such as being an approximate method restricted to high frequencies. In addition, this method was not efficient for high speed flows since the rays were no longer straight lines and they had to be traced by solving an ordinary differential equation.

Nark et al [41] summarized the acoustic prediction codes, The Aircraft Noise Prediction Program (ANOPP), Fast Scattering Code (FSC), and the Rotorcraft Noise Model (RNM), developed at NASA. They discussed the capabilities and addressed issues related with the coupling of these programs to predict scattering effects on engine fan noise sources from a non-conventional aircraft with a hybrid wing.

Tinetti et al [42] extended FSC for the simulation of engine installation effects involving high frequency sources and large-scale configurations of an arbitrary geometry. The simulations were compared with the data from a 3% scale model blended wing body configuration at NASA Langley Research Center Anechoic Research Facility. The measurements showed good agreement with the predictions for the nacelle-body combination however, for the nacelle alone case agreement was limited. Simulations of other hybrid wing body designs were also conducted at high frequency.

Papamoschou [43] modeled jet noise as the superposition of a wavepacket and a monopole to predict of jet noise shielding by the aircraft airframe. Considering diffraction occurs in the near field, the author showed that jet noise could not be approximated by an omnidirectional point source since it was a distributed and directional type of noise source. The diffraction from the proposed jet noise model was predicted using boundary element method. Based on

the experimental results the author concluded that the wavepacket field contained significant features to jet noise diffraction and monopole source had little contribution.

In summary, the point source assumption is widely used for prediction of SPL of rotor systems. It is believed that the information concerning the limits of a rotor system to be treated as a point source will provide valuable guidance to the researchers. Likewise, determination of validity of using a point source for acoustic shielding experiments of rotor noise will make a considerable contribution to the area in terms of planning proper laboratory measurements.

CHAPTER III

THEORETICAL BACKGROUND

3.1 Inverse Square Law Prediction

3.1.1 Inverse Square Law

For a plane wave, the area of the wavefront is constant as the sound travels, so the intensity, i.e., power per unit area, remains constant regardless of the measurement distance. However it is not the case for a spherical wave where the area of the wavefront increases as the wave travels farther away from the source. Let surface S be specified as a sphere of radius r about the source. Sound power is given by

$$\mathbf{W} = \int \int_S I_r dS \tag{1}$$

where I_r is the magnitude of resultant sound intensity at a distance r from the source over an area ΔS. At the sufficiently large distance from the source where sound pressure (p_{rms}) and particle velocity (u_{rms}) are in phase, the particle velocity can be expressed as

$$u_{rms} = \frac{p_{rms}}{\rho c} \tag{2}$$

where ρc is the characteristic impedance of the medium. Assume that the source is omni-directional and particle velocity and sound pressure are in phase at the observer distance r. Since the sound wave will cover the surfaces of an imaginary sphere in the full space, the sound power is given by

$$\mathbf{W} = I_r S = 4\pi r^2 I_r = \frac{4\pi r^2 p_{rms}^2}{\rho c} \tag{3}$$

Thus, mean squared sound pressure can be expressed as

$$p_{rms}^2 = \frac{\mathbf{W}\rho c}{4\pi r^2} \tag{4}$$

Then the intensity can be expressed as

$$I = \frac{\mathbf{W}}{4\pi r^2} \tag{5}$$

Since the surface area of a sphere is equal to 4π times the square of its radius, the area increases with the square of the distance from the source. Therefore with a source of constant rate of energy production (i.e., constant power) the outward directed intensity decreases as the square of the distance from the source increases, because the product of the intensity and the area through which it passes is equal to the power transmitted by the wave. This is the origin of the inverse square law for intensity for a point monopole source. Any point source, which spreads its influence equally in all directions without a limit to its range, will obey the inverse square law, if there are no reflections or reverberation. By using equation (5) the power at two radial locations, r_1 and r_2, may be expressed as

$$\mathbf{W}_1 = I_1 4\pi r_1^2 \tag{6}$$

$$\mathbf{W}_2 = I_2 4\pi r_2^2 \tag{7}$$

Since there is no power loss in the medium

$$\mathbf{W}_1 = \mathbf{W}_2 \tag{8}$$

Finally, inverse square law is obtained as below

$$(\frac{I_2}{I_1}) = (\frac{r_1}{r_2})^2 \tag{9}$$

As a consequence of inverse square law, the sound is reduced by 6 dB when the distance is doubled. Let $r_2 = 2r_1$. Applying inverse square law and taking the logarithm of both sides on the previous equation

$$10log_{10}(\frac{I_2}{I_1}) = 20log_{10}(\frac{r_1}{r_2}) \tag{10}$$

$$SPL_2 - SPL_1 = 20log_{10}(\frac{r_1}{r_2}) = 20log_{10}(1/2) = -6dB \tag{11}$$

So doubling the distance reduces the sound pressure level by 6 dB. At smaller distances, where typically sound pressure and particle velocity are not in phase, inverse square law will not work because equation (2) will not be satisfied. These quantities being in-phase or not is closely related to the wavelength of propagating spherical wave. The sound pressure of a spherical wave, can be expressed as

$$p(r,t) = P(r)e^{i\omega t} \tag{12}$$

and the corresponding particle velocity

$$u(r,t) = U(r)e^{i\omega t} \tag{13}$$

where ω is the frequency of the signal in rad/sec. The location dependent part of sound pressure is

$$P(r) = \frac{Ae^{-ikr}}{r} \tag{14}$$

where A is the amplitude and k is the wave number of the signal. By using Eulers equation, particle velocity dependence on the location is obtained as

$$U(r) = \frac{1}{\rho c}\frac{A}{r}(1 + \frac{i}{kr})e^{-ikr} \tag{15}$$

If kr is large enough the $\frac{i}{kr}$ term in this expression can be neglected, which makes sound pressure and particle velocity in-phase. In other words, as

$$kr = 2\pi r/\lambda \tag{16}$$

where λ is the wavelength, for large r/λ values sound pressure and particle velocity are in phase. In conclusion, for the distances large enough compared to the wavelength of the sound, sound pressure and particle velocity are in phase and so inverse square law is satisfied [2].

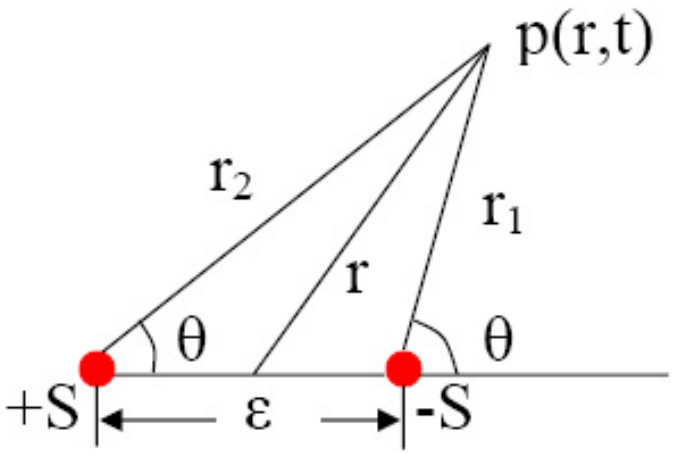

Figure 11: Acoustic dipole source model.

It should be noted that inverse square law is obeyed at large distances even for point dipoles and quadrupoles although their directivity changes. A dipole source is described as the superposition of two monopoles of opposite strength, S and -S, and distance ε apart from each other as shown in Figure 11. From equation (14), it is known that for a spherically symmetric wave the sound pressure is proportional to inverse of the radius, $1/r$. A dipole source is composed of two monopole, i.e., two sources emanating spherically symmetric waves. So, the nominal radius of these waves should be less than ε in order for the two monopoles to be dominated by the $1/r$ term. In the limit where ε is small enough so that $k\varepsilon << 1$ and this source is a point dipole [7].

The sound pressure of a dipole source is given as

$$p = F_0 cos\theta \frac{1 + \imath kr}{4\pi r^2} e^{\imath(\omega t - kr)} \tag{17}$$

where F_0 is the magnitude of the time harmonic wave. This expression shows that at the limit $kr << 1$, i.e., in the near field of the dipole, the sound pressure is dominated by $1/r^2$ term which means the SPL drops by 12 dB doubling the distance. So, unlike monopole source that is dominated only by $1/r$ term, for a dipole source, kr should be large enough so that it is a point source [8].

$$p = Acos\theta(\frac{1}{4\pi r^2} + \frac{\imath k}{4\pi r})e^{\imath(\omega t - kr)} \tag{18}$$

3.2 Noise Shielding Prediction

When the source is blocked by a structure and thus noise shielding is produced, the mechanisms processing the sound waves get more complicated. The basic acoustical phenomena that take place when a noise source is shielded by a barrier are refraction, scattering, and diffraction. In this study, the refracting effect of the local flow field is neglected and it is assumed that no sound is transmitted through the barrier. So the focus will be only on scattering and diffraction. Diffraction and scattering occur when a sound wave encounters a discontinuity, such as an obstacle or an inhomogeneity in the medium, on its path. This generates another group of sound waves spreading out from the discontinuity in a variety of directions [5]. Diffraction may be considered as a subset of scattering. Some mechanisms might be explained by scattering but do not involve diffraction such as in the case of a sound beam reflecting from a rough surface. Diffraction is the reason one can hear another person who is out of sight around the corner or behind a tree. The sound strikes on the corner and scatters around all directions. The waves propagating direct from the source interferes with the scattered waves producing maxima and minima, even nulls at the receiver [6].

3.2.1 Acoustic Field from a Monopole Source in the Presence of a Semi-infinite Plane.

In this section, an approximate closed form solution for the acoustic field produced by the shielding of monopole sound waves by a semi-infinite plane is presented. The theory was developed by MacDonald [15] and Bowman's [18] presentation of the solution is used in this work. The semi-infinite plane is defined as $y = 0, x \geq 0$ in terms of Cartesian coordinates (x, y, z); and as $\varphi = 0$ (upper surface), $\varphi = 2\pi$ (lower surface) in terms of cylindrical coordinates (ρ, φ, z). The geometry is shown in Figure 12. The primary source is a point source located at (ρ_0, φ_0, z_0). The following assumptions are made to specify the problem:

- There is no refraction and transmission.
- There is no flow.

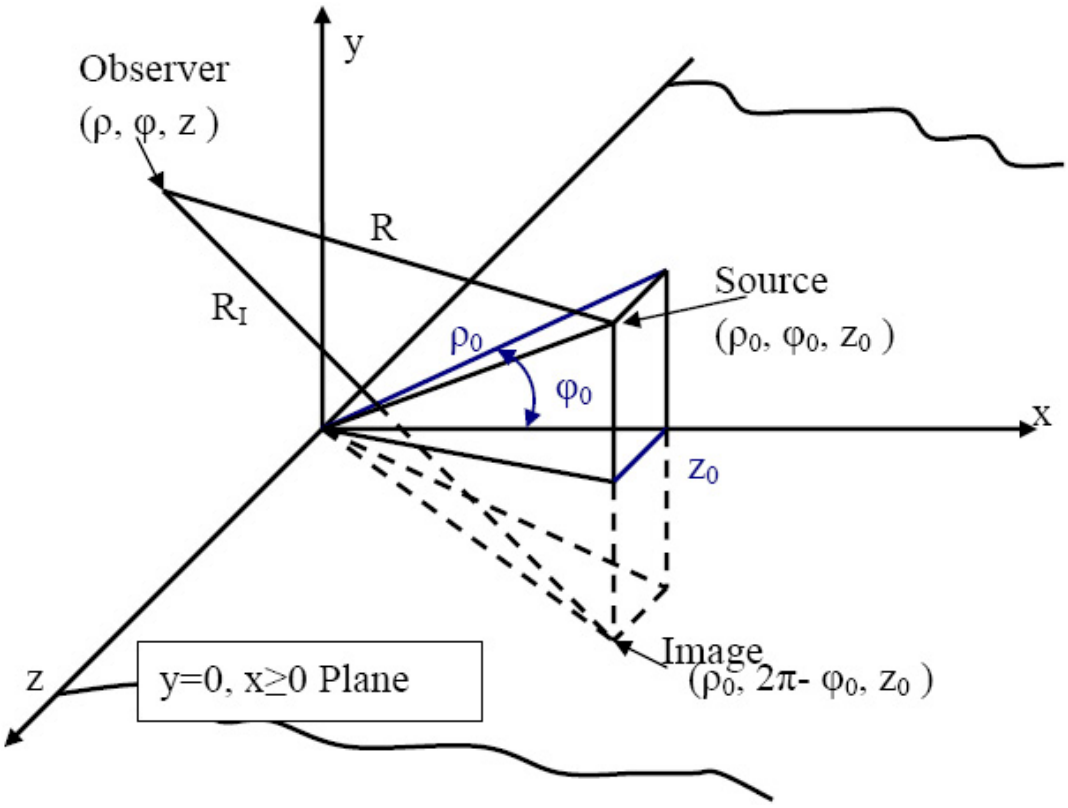

Figure 12: Geometry for a point source shielded by a semi-infinite plane.

- Sommerfeld Radiation Conditions hold [1].
- Semi-infinite plane is a hard boundary.
- Non-dimensional wave number is large. $kr >> 1$, where r is any distance measured from source to the receiver.

From Figure 12 the distance from the point of observation to the source in plane $y = 0$ is

$$R = \sqrt{\rho^2 + \rho_0^2 - 2\rho\rho_0 cos(\varphi - \varphi_0) + (z - z_0)^2} \tag{19}$$

$$= \sqrt{(x - x_0)^2 + (y - y_0)^2 + (z - z_0)^2} \tag{20}$$

The distance from the point of observation to the image of the source in plane $y = 0$ is

$$R_I = \sqrt{\rho^2 + \rho_0^2 - 2\rho\rho_0 cos(\varphi + \varphi_0) + (z - z_0)^2} \tag{21}$$

$$= \sqrt{(x - x_0)^2 + (y + y_0)^2 + (z - z_0)^2} \tag{22}$$

The distance from the source to a point of diffracting edge is

$$R_1 = \sqrt{(\rho + \rho_0)^2 + (z - z_0)^2} \tag{23}$$

The configurations studied in this work require that $k(R_1 - R) >> 1$, $k(R_1 - R_I) >> 1$, and the polar angle of the source, $0 \leq \varphi_0 \leq \pi$. Under the given conditions, the shielded velocity potential is expressed as the sum of geometrical optics field, V_g, and diffracted field, V_d [13].

$$V_s = V_g + V_d \tag{24}$$

$$V_g = \eta(\pi + \varphi_0 - \varphi)\frac{e^{ikR}}{kR} + \eta(\pi - \varphi_0 - \varphi)\frac{e^{ikR_I}}{kR_I} \tag{25}$$

[1]The sources must be sources, not sinks of energy. The energy which is radiated from the sources must scatter to infinity; no energy may be radiated from infinity into the field, from source to the receiver.

$$V_d = - \sqrt{\frac{2}{\pi k R_1}} e^{-i\pi/4} sgn(\pi + \varphi_0 - \varphi) \frac{e^{ikR}}{\sqrt{k(R_1 + R)}} F[\sqrt{k(R_1 - R)}] \quad (26)$$

$$+ sgn(\pi - \varphi_0 - \varphi) \frac{e^{ikR_I}}{\sqrt{k(R_1 + R_I)}} F[\sqrt{k(R_1 - R_I)}] \quad (27)$$

where Fresnel integral, F, is

$$F(\tau) = \int_{\tau}^{\inf} e^{i\mu^2} d\mu \quad (28)$$

and Heaviside step function η is

$$\eta(\psi) = \begin{cases} 1, & \psi > 0 \\ 0, & \psi < 0 \end{cases} \quad (29)$$

and Signum function sgn is

$$sgn(x) = \begin{cases} 1, & x > 0 \\ -1, & x < 0 \end{cases} \quad (30)$$

Both fields V_g and V_d are discontinuous at $\varphi = \pi \pm \varphi_0$.

3.2.2 Prediction of Noise Shielding by a Quadrilateral

In this section, the exact solution given in the previous section is applied for the shielding of monopole sound waves emanating from a point source by a rectangular plate, in an extended form used by Ahtye and McCulley [20]. The procedure was used to predict the shielding of monopole sound (where can be extended to broadband noise) by simple geometrical shapes (rectangular plate and circular cylinder) in the current work.

The basis of the procedure to predict the noise shielding by a quadrilateral was superposition of semi-infinite barrier solutions. Each edge of the barrier (barrier can be a rectangular aluminum sheet or an aircraft wing, same procedure is valid) was extended to plus/minus infinity and the solution explained above was applied to all edges as if they were the edge of a semi-infinite plane barrier. The total shielding at a given field point was found

from the superposition of semi-infinite barrier solutions of all four edges. The shielding is expressed as the sound pressure level between the shielded and unshielded cases:

$$\Delta SPL = SPL_s - SPL_u = 20log_{10}\frac{|p_s|}{|p_u|} \tag{31}$$

In the farfield the acoustic pressure, p, is related to the velocity potential, V, by the expression

$$p = i\omega\rho V \tag{32}$$

So the shielding from one edge can be expressed as follows

$$\Delta SPL = 20log_{10}\frac{|V_s|}{|V_u|} \tag{33}$$

where subscripts, s and u refer to to shielded and unshielded cases, respectively. Since velocity potential is a complex number, the absolute value of the solutions needed to be considered to find the shielding value. However taking the absolute value of the shielding from each edge and then superposing the results means neglecting the phase relationship between the diffracted waves from the edges. So to take this phase relationship into account, first the superposition of the edges was performed and then absolute value was taken. The resultant sound pressure level of shielding for a quadrilateral is, finally, obtained by the following addition of four edges:

$$\Delta SPL = 20log_{10}(\frac{|\sum_{i=1}^{4} V_{s_i}|}{|V_u|}) \tag{34}$$

where unshielded velocity potential is expressed as

$$V_u = \frac{e^{ikR}}{kR} \tag{35}$$

3.2.3 Application of the Shielding Theory

The parameters necessary to predict the shielding of a monopole point source by a quadrilateral are given in Figure 13. Once the dimension of the shield and positions of the source and receiver are provided, the geometric parameters defined in Figure 13 can be calculated. Then the velocity potential for each edge is obtained using equations (25) to (26) for a given frequency. Finally the sound pressure level of shielding is obtained from equation (34). Figure 14 to Figure 16 show the applications of this procedure as a function of source location

parallel to the shield. Each figure is for a different source frequency. Source, labeled as S_1, is assumed to be placed $12''$ away from the shield (on z-axis) and at the mid point of the shield on y-axis as shown in the sketches on the figures. Then keeping the $12''$ distance, the source was shifted $3''$ in the direction of the y-axis parallel to the shield. This second case was labeled as S_2. The following cases labeled as S_3, S_4 show the $6''$ and $9''$ shifts of the source on y-axis, respectively. Figure 14 shows the calculations for the frequency of 1200 Hz. When the source is at the mid point of the shield significant dips are seen due to the interference of the diffracted waves. As the source moves away from the mid point, dips get smoother. Figures 15 and 16 are the corresponding results for 800 Hz and 400 Hz, respectively. It is seen that as the frequency decreases, the effect of the destructive and constructive interferences are reduced, the curves get smoother and the shielding levels reduce. The azimuthal angle, ϕ, given for each source location will be widely used during the presentation of experimental findings in Chapter 6. Next, the source was shifted up and down on z-axis which was perpendicular to the shield. Figure 17, Figure 18, and Figure 19 show the results for 1200Hz, 800 Hz, and 400 Hz, respectively. Again it is observed that as the source moves away from the shield the dips diminish or disappear and as the frequency decreases less shielding is obtained.

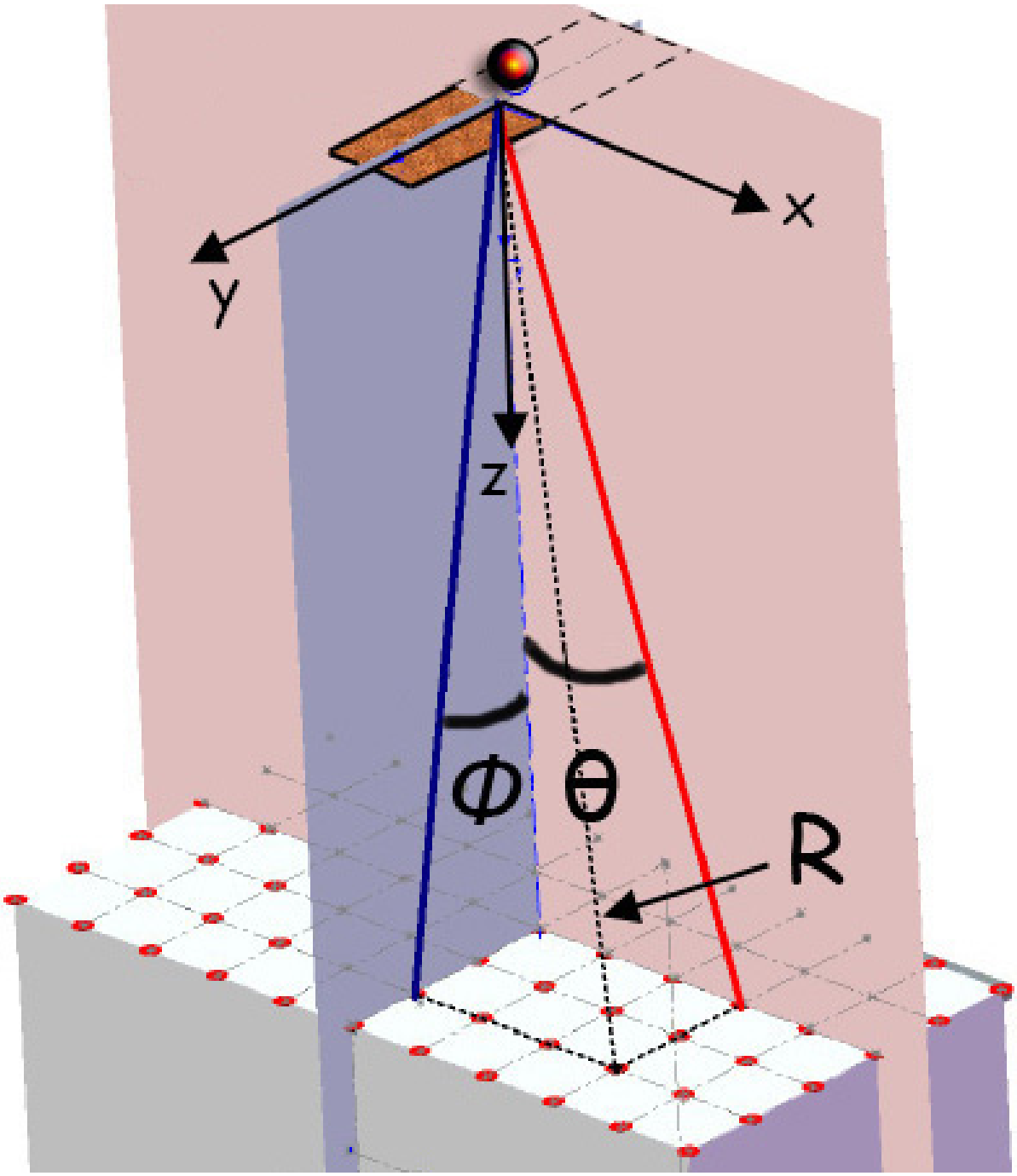

Figure 13: Parameters to predict the shielding of a monopole point source by a quadrilateral.

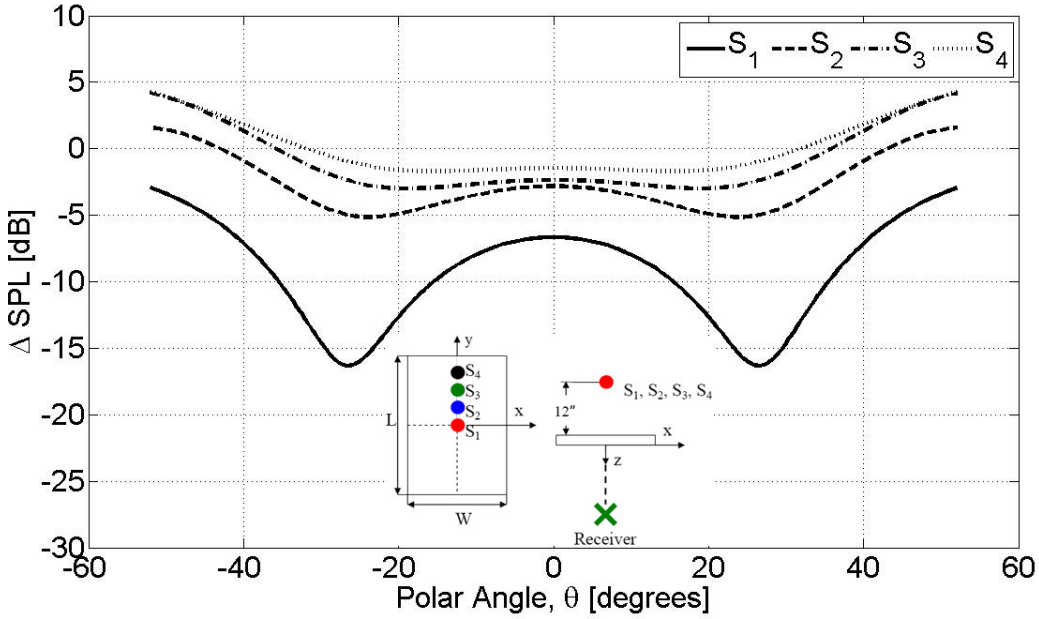

Figure 14: Predicted effect of different source locations along the y-axis. $f = 1200$ Hz, $kW = 7.15$, $kz = 42.9$, $L/W = 1.8$, $\phi_1 = 8.7^o$, $\phi_2 = 10.8^o$, $\phi_3 = 13^o$, $\phi_4 = 15^o$.

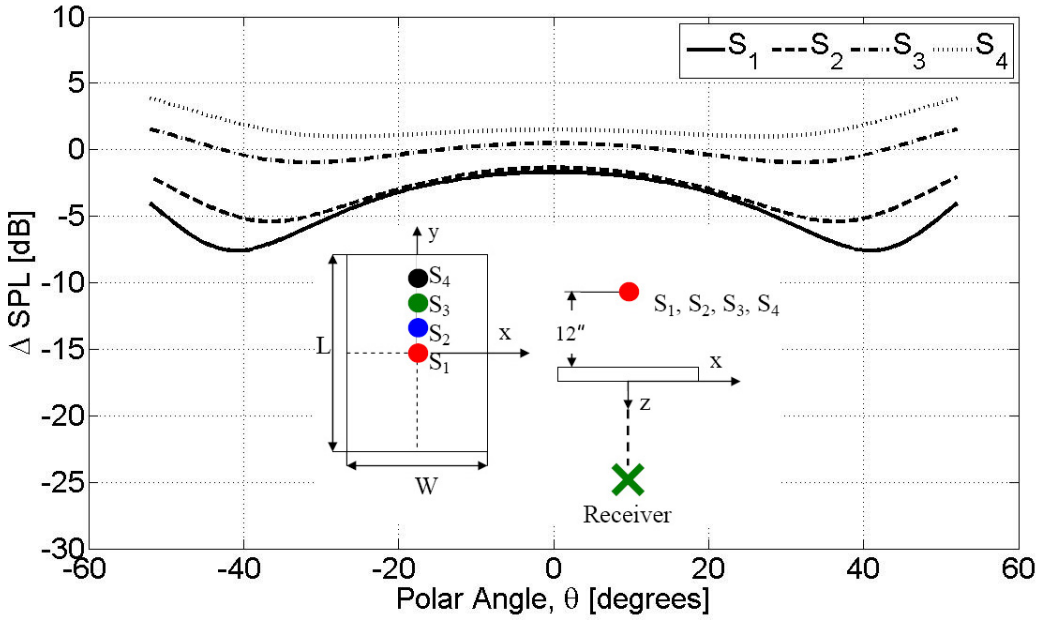

Figure 15: Predicted effect of different source locations along the y-axis. $f = 800$ Hz, $kW = 4.81$, $kz = 28.9$, $L/W = 1.8$, $\phi_1 = 8.7^o$, $\phi_2 = 10.8^o$, $\phi_3 = 13^o$, $\phi_4 = 15^o$.

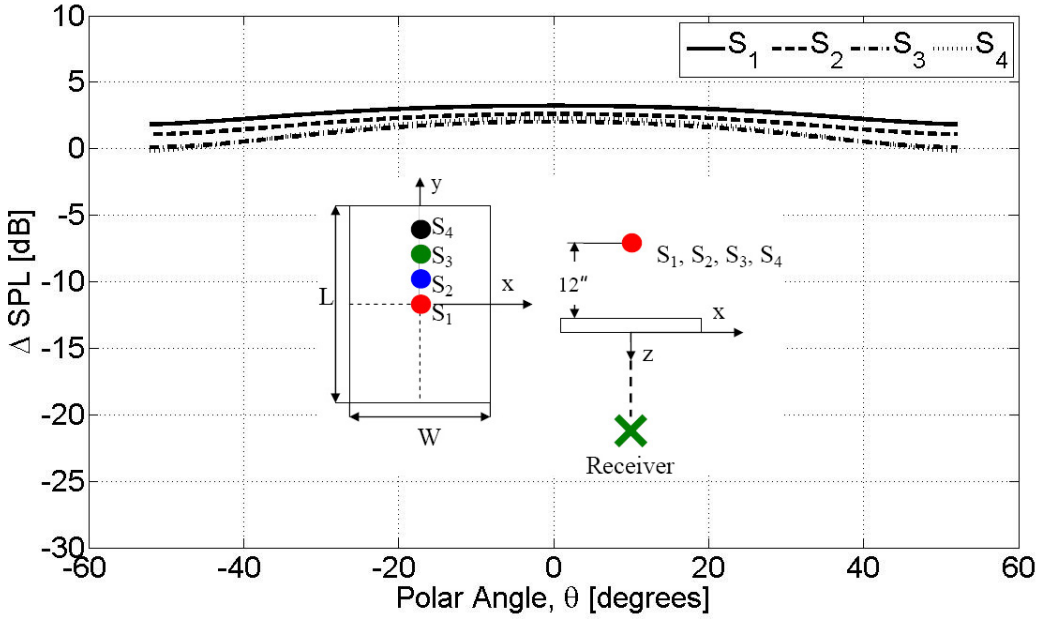

Figure 16: Predicted effect of different source locations along the y-axis. $f = 400$ Hz, $kW = 2.47$, $kz = 14.8$, $L/W = 1.8$, $\phi_1 = 8.7^o$, $\phi_2 = 10.8^o$, $\phi_3 = 13^o$, $\phi_4 = 15^o$.

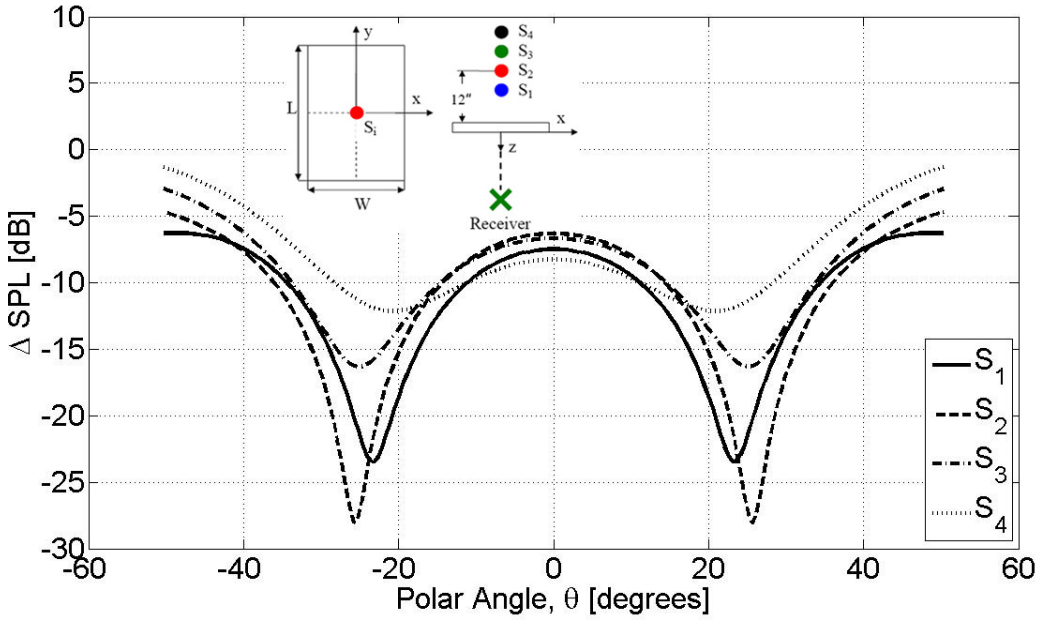

Figure 17: Predicted effect of different source locations along the z-axis. $f = 1200$ Hz, $kW = 7.15$, $kz = 42.9$, $L/W = 1.8$, $\phi_1 = 8.2^o$, $\phi_2 = 8.5^o$, $\phi_3 = 8.7^o$, $\phi_4 = 9^o$.

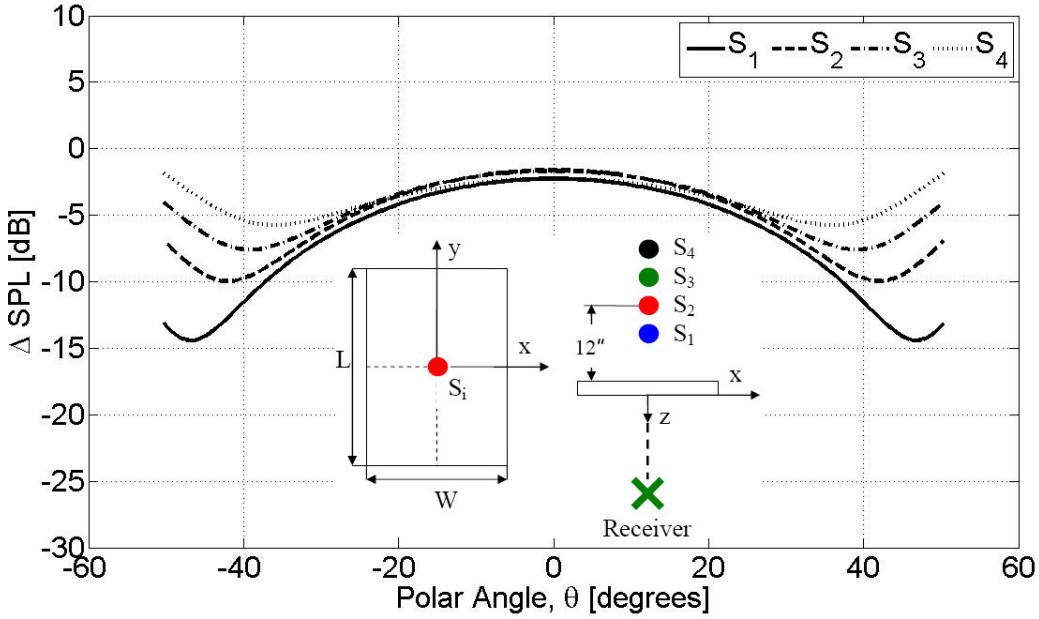

Figure 18: Predicted effect of different source locations along the z-axis. $f = 800$ Hz, $kW = 4.81$, $kz = 28.9$, $L/W = 1.8$, $\phi_1 = 8.2^o$, $\phi_2 = 8.5^o$, $\phi_3 = 8.7^o$, $\phi_4 = 9^o$.

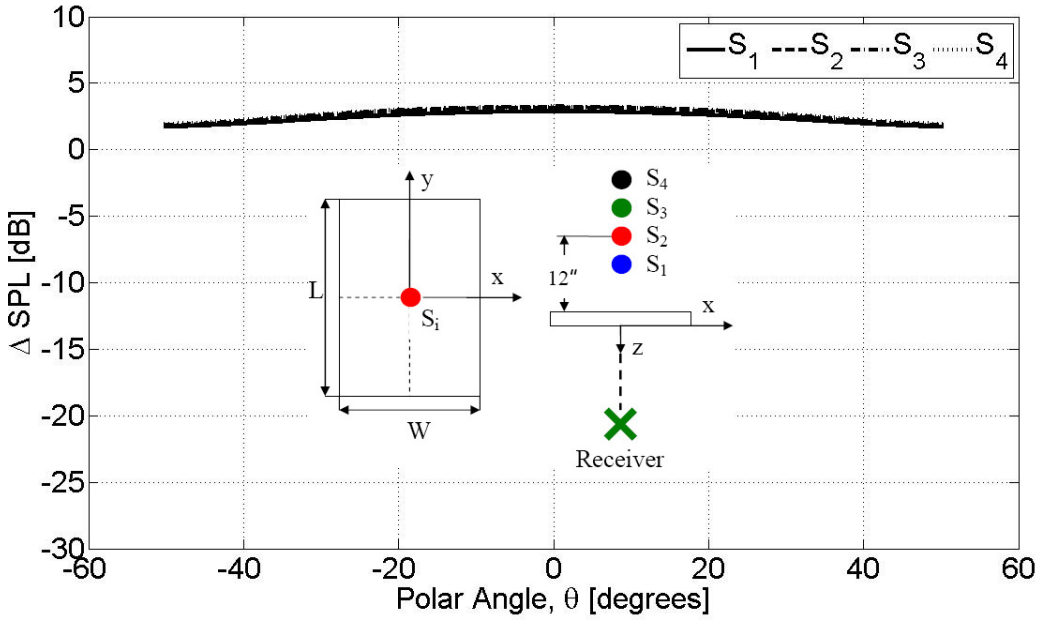

Figure 19: Predicted effect of different source locations along the z-axis. $f = 400$ Hz, $kW = 2.47$, $kz = 14.8$, $L/W = 1.8$, $\phi_1 = 8.2^o$, $\phi_2 = 8.5^o$, $\phi_3 = 8.7^o$, $\phi_4 = 9^o$.

CHAPTER IV

FACILITIES AND EXPERIMENTAL PROCEDURE

The experimental procedure employed in this thesis was based on acquiring, analyzing and comparing noise data from several source configurations. These configurations include a point sound source using an electro-acoustic driver, several sizes of unducted, and ducted rotors, several sizes of rectangular barriers for shielding these noise generators. Since the prediction methods under consideration use inverse square law and shielding of a point source by a semi-infinite barrier, the experiments were formalized around these concepts.

The experiments were carried out under two main parts. The purpose of the first part was to determine proper acoustic geometric farfield conditions for a rotor noise source. In order to achieve this goal the effect of rotor radius, duct length and measurement angle parameters on the measurement distance were explored. Second part aimed at determining validity of using point source to represent rotor noise source for acoustic shielding experiments. The shielding of a monopole source and the shielding of a rotor noise sources were compared by test configurations consisting of rectangular plates and ducts of various dimensions. In addition, the experimental findings from the shielding of rotor noise sources by finite length plates and ducts were compared with the available analytical predictions for shielding and scattering of a point source by a semi infinite planar barrier. The experimental data helped to understand the importance of noise source characteristics on several geometrical parameters of the shield and source positioning, on the shielding of noise, in the farfield.

All of these experiments were conducted in the anechoic test chamber of Georgia Tech Research Institute (GTRI)/Cobb County Research Facility (CCRF). The facilities, instrumentation and the experimental setups are discussed under the following sections.

4.1 Experimental Facility and Instrumentation

The static jet anechoic facility at the Georgia Tech Research Institute (GTRI)/Cobb County Research Facility (CCRF) was employed for the experiments that need to be implemented in an anechoic chamber. A picture of the test facility with the current test setup is shown in Figure 20. The chamber measures 22 ft long by 20 ft wide and is 28 ft high between structural walls. All interior surfaces are lined with polyurethane foam wedges 15″ long, rendering the facility 99% echo free at frequencies above 200 Hz. A cherry-picker crane is used to gain access to instrumentation and test installations for calibration, test set up modifications, and maintenance, thus eliminating the access platforms and their attendant reflection problems. The crane is stowed by remote control under an anechoic cover during all acoustic test operations. Microphones may be placed anywhere in the room up to a distance of 15″ from the wedge tips so as to be beyond any wedge near field effects [45]. The chamber is calibrated by a point source [1], seen in Figure 21(a), composed of an inverse conical horn mounted to a loudspeaker that is capable of providing proper sound at frequencies over 200 Hz. The calibration results in Figure 21(b) show that the experiments confirm ISL for the frequencies above 200 Hz, up to 20 kHz. So the chamber is proven to be anechoic in this frequency range.

Acoustic pressure levels were acquired with B & K 4939 quarter-inch condenser microphones, which were used in conjunction with half-inch BK 2669 pre-amplifier and adapter. B & K 4231 sound calibrator was used for the calibration of the microphones. A Nexus conditioner amplifier was used, which was connected to Agilent E1421B mainframe computer, which in turn operated the frequency analyzer Signal Calc 620. All the experiments included a reference microphone at a fixed location of chosen angle and distance to the source to account for any noise level changes from one run to another while the microphones were traversed to various locations.

The power to run the rotors was provided, by a Kollmorgen AKM43K Brushless Servomotor with 10 hp power and 6000 rpm maximum angular speed driven by a Xenus Servo Amplifier controlled with Copley Motion Explorer 2 software. The motor itself was placed quite far from the rotor so that it was neither in the duct nor close to the duct entrance.

Figure 20: GTRI/CCRF Static Jet Anechoic Facility.

This was accomplished by employing a 4-ft long shaft coupled to the electric motor shaft. SKF Needle Roller/Thrust Bearings were used to stabilize the shaft.

4.2 Unducted and Ducted Rotor Geometric Farfield Experiments

The purpose of these experiments was to ensure that the microphone was located in the geometric farfield. To determine the limits of geometric farfield of model-scale ducted and unducted rotors, acoustic data was acquired in the anechoic facility. SPL spectra was obtained at various rotor rpms, microphone distances and polar directions. In the SPL versus distance plots when the variation started conforming to the ISL, which provides a 6 dB decrease in sound per doubling of the distance, the microphone was typically considered to be in the geometric farfield.

4.2.1 Unducted Rotor Experiments

To perform the unducted rotor experiments, a 1 HP Dayton Universal AC/DC Open Motor with a maximum speed of 7500 rpm was used to drive four bladed rotors with 6 degree built-in pitch. A schematic of the setup is shown in Figure 22(a) and a photograph is shown in

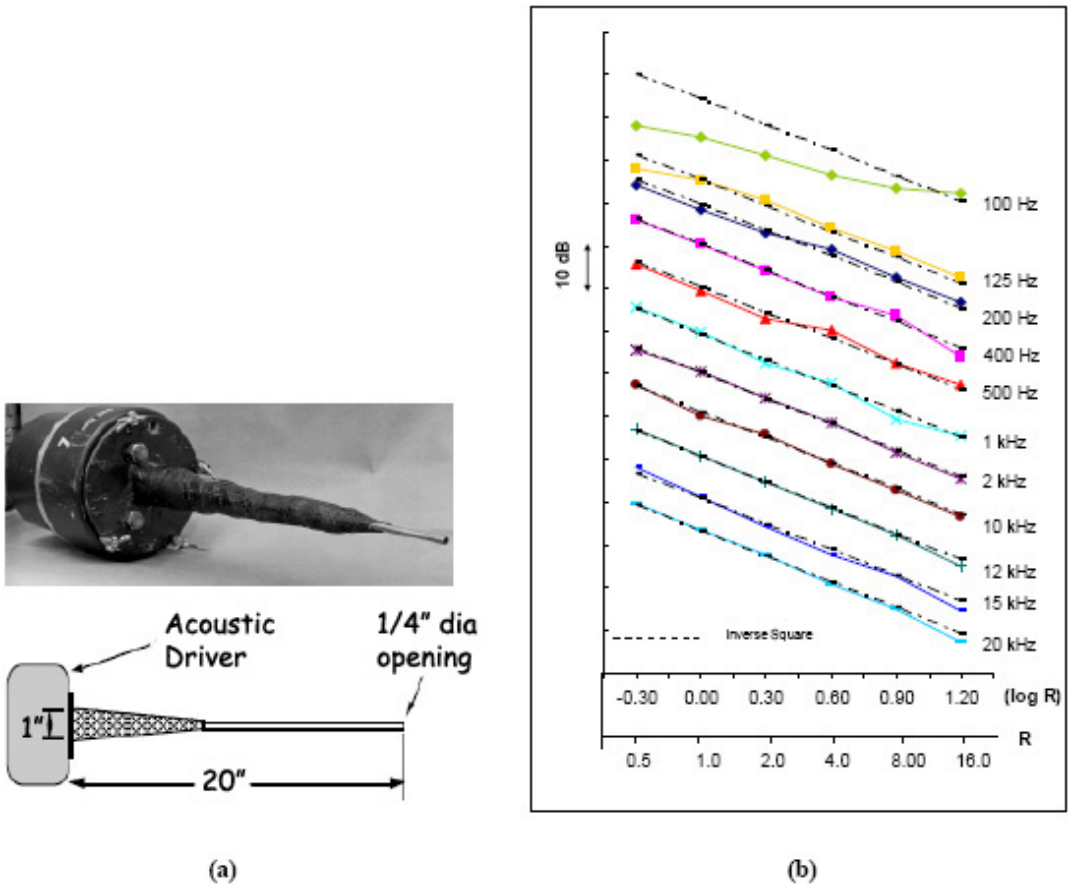

Figure 21: (a) Inverse conical horn mounted to an acoustic driver providing monopole sound emission, (b) GTRI/CCRF Static Jet Anechoic Facility calibration results cite Turkdogru.

Figure 22(b). The microphone angles used for these tests were $\alpha = 0^o, \alpha = 45^o, \alpha = 90^o$ with respect to the rotor shaft as shown in 22(c). Rotor was run under static conditions. The unducted rotor acoustic measurements were made at 6 points starting with the first measurement at 1/2 ft and the last at 16 ft from the rotor center, each time doubling the distance. The reference microphone, always kept at the same spot, was used to account for any source output variation during the measurements.

4.2.2 Ducted Rotor Experiments

Data for SPL variation with distance was obtained as a function of rotor radius, motor rpm, duct length, and angle. Experimental setup mainly consisted of three different sized ducts with outer diameters equal to $7.5''$, $14''$, and $24''$ that were used for $6.5''$, $13''$, and $23''$ diameter rotors, respectively, with a $0.25''$ tip clearance. Three $7.5''$ outer diameter ducts with lengths of $12''$, $24''$, and $36''$, shown in Figure 23, were also tested for the purpose of obtaining geometric farfield data as a function of duct length. To keep the structure that was built to hold the ducts away from the rotor flow, the duct and the holding structure was linked to each other by a semi-circular support mounted to the duct. The diagrams showing all these test variables are given in Figure 24[1] for the unducted case and in Figure 25 for the ducted case. In Figure 24 the experiments are classified in terms of test angles, rotor diameters and motor angular speed. Data for the unducted rotor was acquired for three measurement angles, namely $\alpha = 0^o$, $\alpha = 45^o$, and $\alpha = 90^o$. $\alpha = 0^o$ refers to the direction perpendicular to the propeller disc plane. For all angles, data for two diameters ($D = 6.5'', 13''$) was obtained. The angular speeds for each rotor are listed in the figure under the rotor diameter.

The tests were first run by traversing the microphone along $\alpha = 0^o$ angle. The noise spectra were acquired at 17 consequent locations as the microphone was traversed radially away from the duct exit. The farthest distance was $32D$ ($D = 6.5''$). The reference microphone was located at $\alpha = 90^o$ angle with the traversing microphone. The traversing

[1]Tip speeds for the $D = 6.5''$ rotor are at 6000 rpm and at 7500 rpm are 10205 ft/min and 12756 ft/min, respectively. Likewise, tip speeds for the $D = 13''$ rotor are at 3750 rpm and at 3575 rpm are 10205 ft/min and 12756 ft/min, respectively.

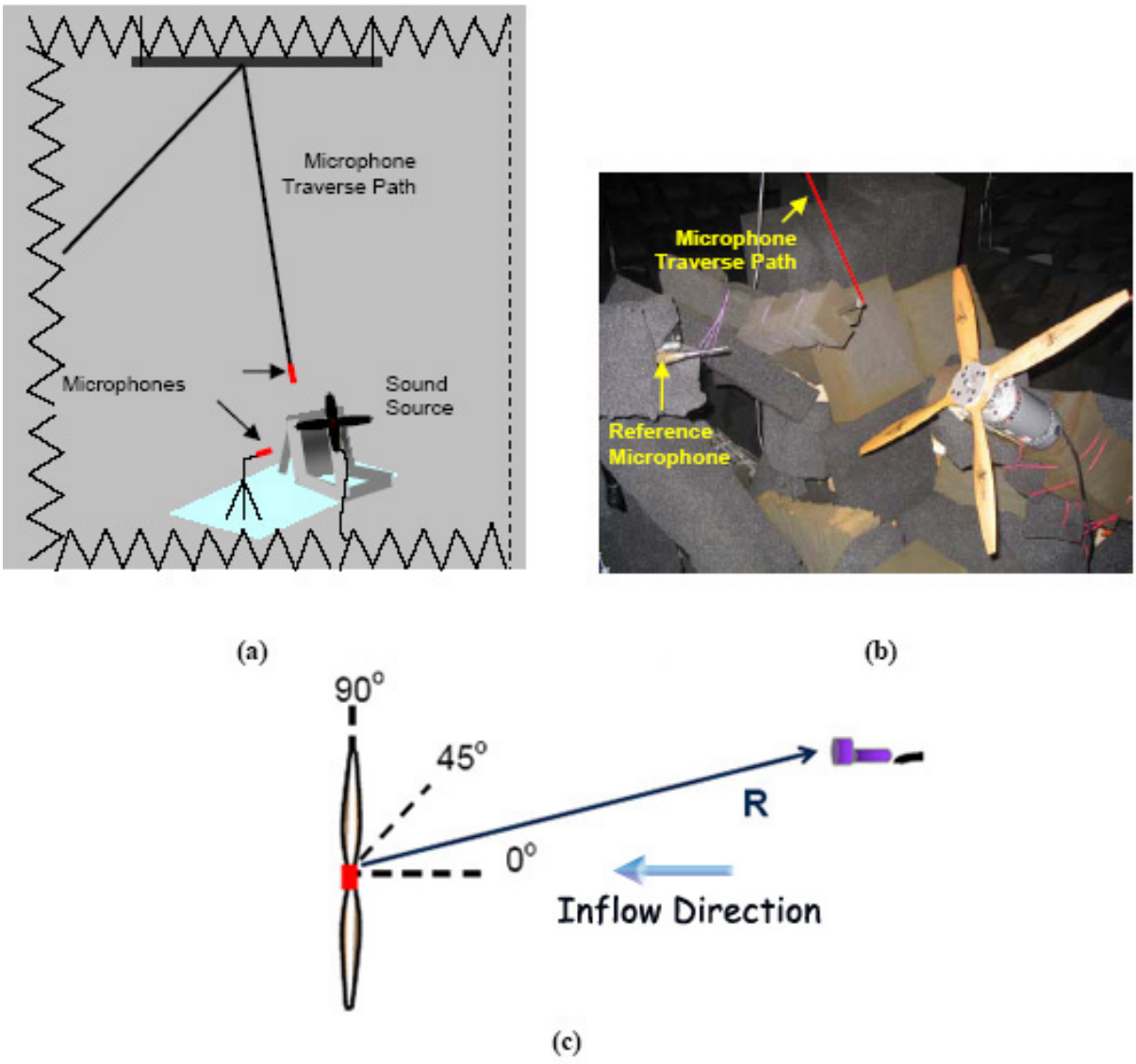

Figure 22: (a) Schematic description , (b) photographic view of unducted rotor test setup, (c)position of the Test Angles

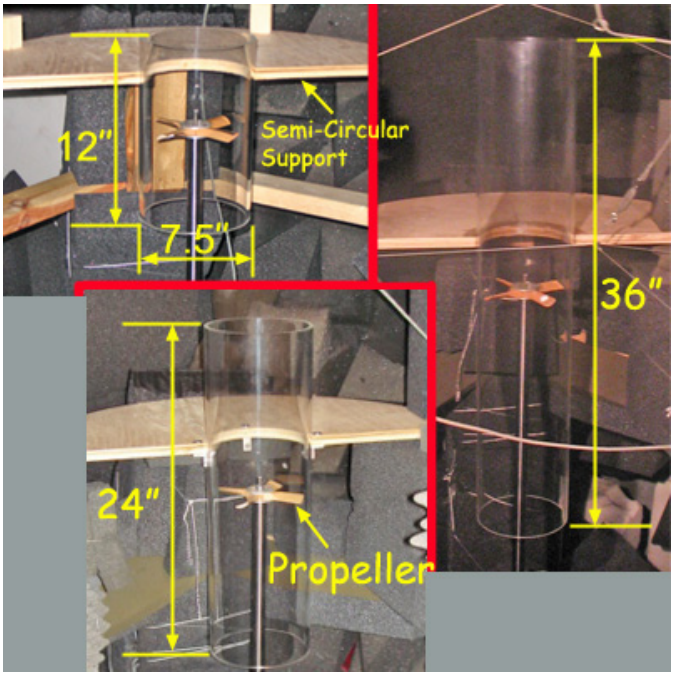

Figure 23: 7.5″ outer diameter ducts with the lengths of 12″, 24″, and 36″.

microphone was then moved to $\alpha = 90^o$ configuration and reference microphone to $\alpha = 0^o$ and another set of tests was performed. The same procedure was again applied for a third set of tests for which the microphone was traversed along $\alpha = 30^o$ and reference microphone was positioned at $\alpha = 0^o$.

Ducted test data was acquired for three angles, $\alpha = 0^o$, $\alpha = 30^o$, $\alpha = 90^o$. In Figure 25[2] duct lengths added to the measurement parameters and in this case, duct outer diameters are used instead of the rotor diameters. Duct outer diameter of $D_D = 7.5''$ was tested for all angles and, additionally, $D_D = 14''$ duct with $L = 24''$ was tested at $\alpha = 0^o$. Three duct lengths were chosen for the $D_D = 7.5''$ diameter which are: $L = 12'$, '$L = 24''$, and $L = 36''$. The test angular speeds are listed under each category.

The electric motor and the bearings for stable rotation were placed inside a sound and vibration isolation box, shown in Figure 26, to maximize the signal-to-noise ratio. Additionally, a structure was built around the box to hold the duct without creating an additional interference of the structure with the rotor flow. Before moving to the anechoic

[2]Tip speeds for the rotor inside $D_D = 7.5''$ duct are 9695 ft/min at 5700 rpm and 10205 ft/min at 6000 rpm.

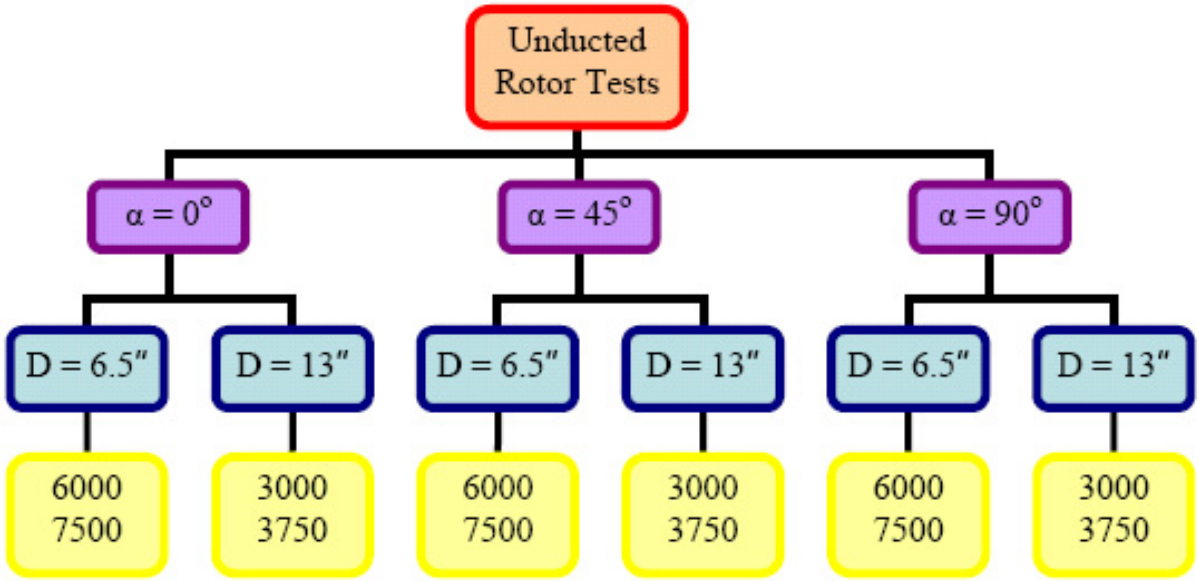

Figure 24: Measurement variable diagram for the unducted rotor experiments.

chamber, experiments were performed outside the anechoic chamber to obtain the most efficient design. When the motor was running with no duct or blades attached to the hub, low frequency tones up to 500 Hz, as shown in Figure 26, were obtained. The noise measurements were made by a $1/4''$ microphone located 2 ft from the rotor center and at an angle perpendicular to the shaft axis. Although there are no propeller blades, peaks as much as 14 dB higher than the ambient noise are observed. The circled peaks, at $f = 333Hz$ in Figure 27(a) and at $f = 380Hz$ in Figure 27(b) are the blade passing frequencies that would be observed if a four-bladed propeller was inserted and ran at the given rpms. So, when the propeller was inserted if the structure would be used the way it was, the blade passing frequency could be contaminated by other sources of noise. Because the structure holding the duct was coupled with the box of the motor and bearings, this structure was suspected to have produced some additional noise due to the structural vibrations. To mitigate this issue and to ensure that the structural noise was not masking the rotor noise, an uncoupled structure was designed and built. The sound and vibration isolation box, labelled as '1', was placed inside a heavy and sturdy box, labelled as '2' in Figure 28. In 'Box 1' rubber vibration dampers are seen to be placed around long screws. 'Box 1' holds the electric motor and the bearings with the long screws mounted to both. These screws are purposely

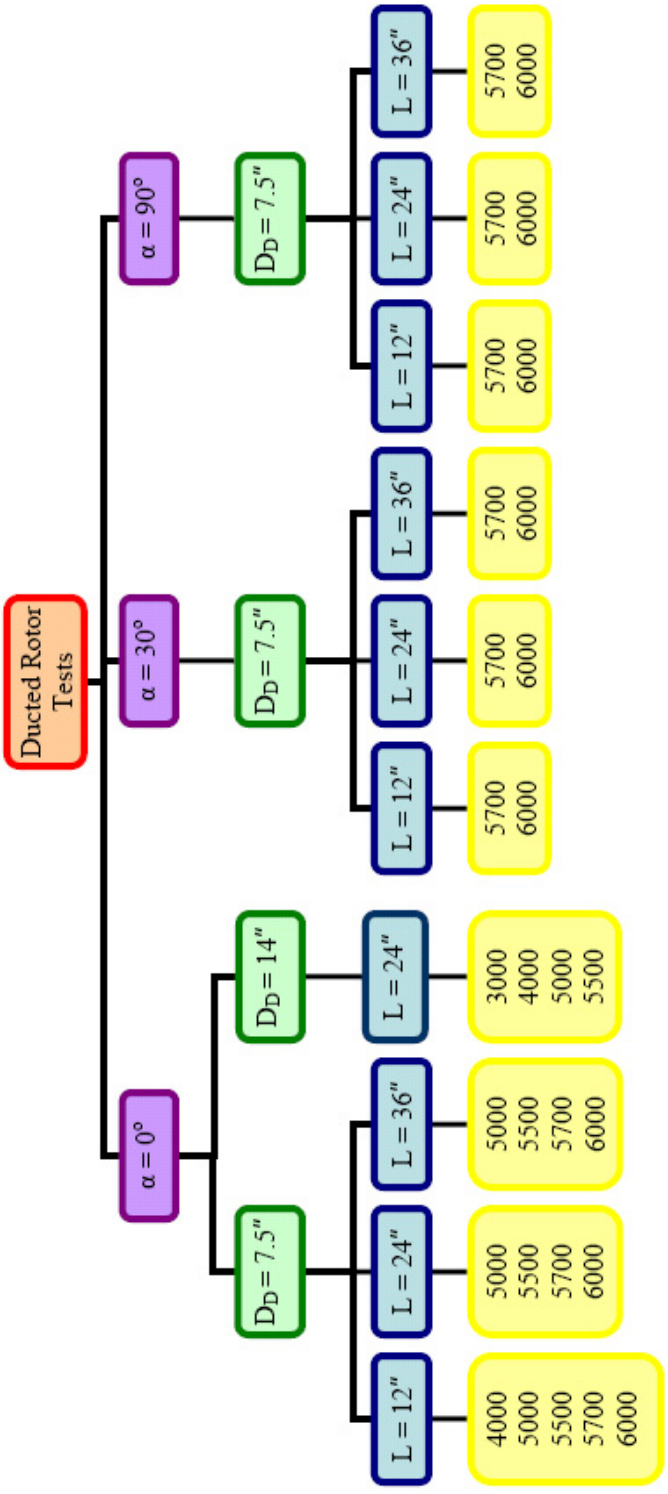

Figure 25: Measurement variable diagram for the ducted rotor experiments.

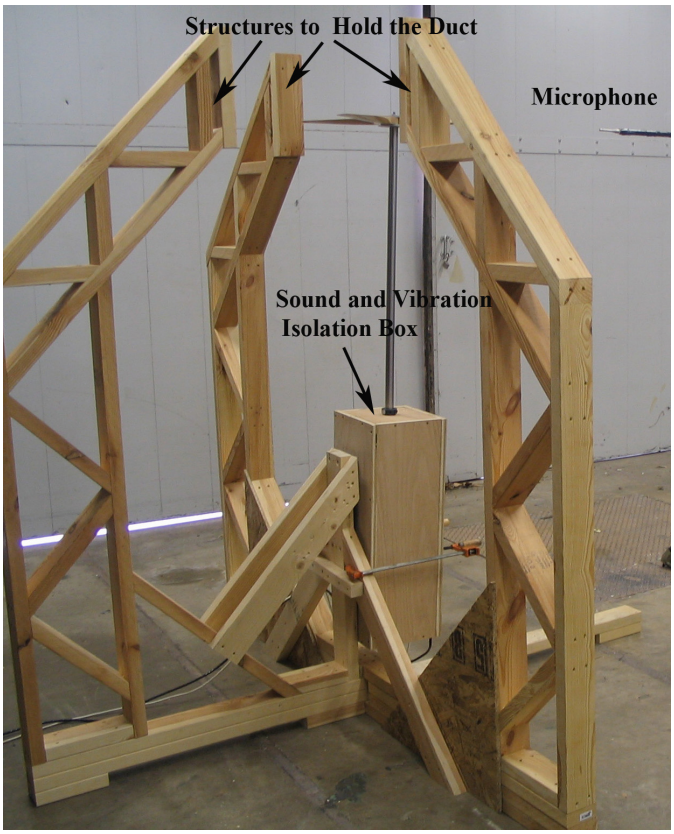

Figure 26: The coupled setup structure.

made to facilitate the placement of rubber vibration dampers to avoid the transmission of vibration from the motor and bearings to the box shell. Another rubber vibration damper was placed between the 'Box 1' and 'Box 2' for preventing the transmission of vibrations between two boxes. The new spectra, with no propeller blades, obtained are shown for the uncoupled case are shown in Figure 28. It is seen that the presumed blade passing frequency peaks that were observed for the coupled case have now dissappared and many of the tones associated with the motor and shaft noise have also reduced considerably.

In Figure 30(a) and 30(b) the coupled and uncoupled cases are presented comparatively for 4000 rpm and 5700 rpm, respectively. The excess noise, observed when the structure was coupled, was interpreted as a consequence of structural vibrations. To avoid structural noise effect the experiments were performed with the uncoupled duct holding structure.

The setup was moved to the anechoic chamber. Figure 31 shows the structures that holds the duct inside the anechoic chamber. The motor, the bearing box, the duct, and

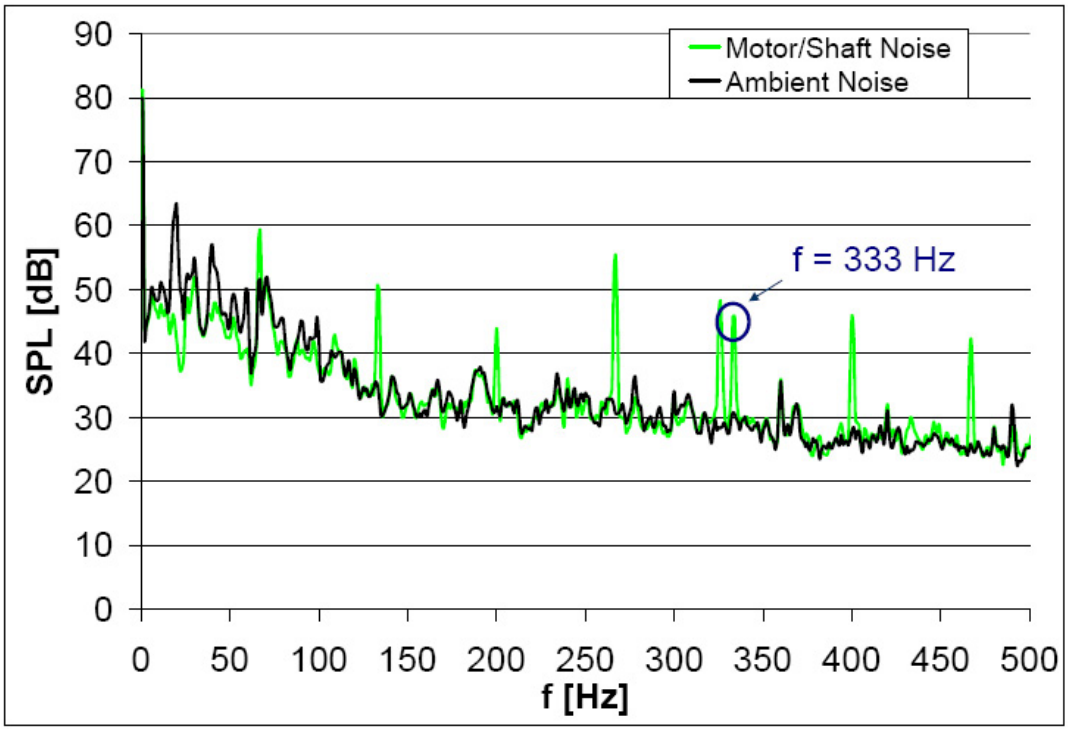

(a)

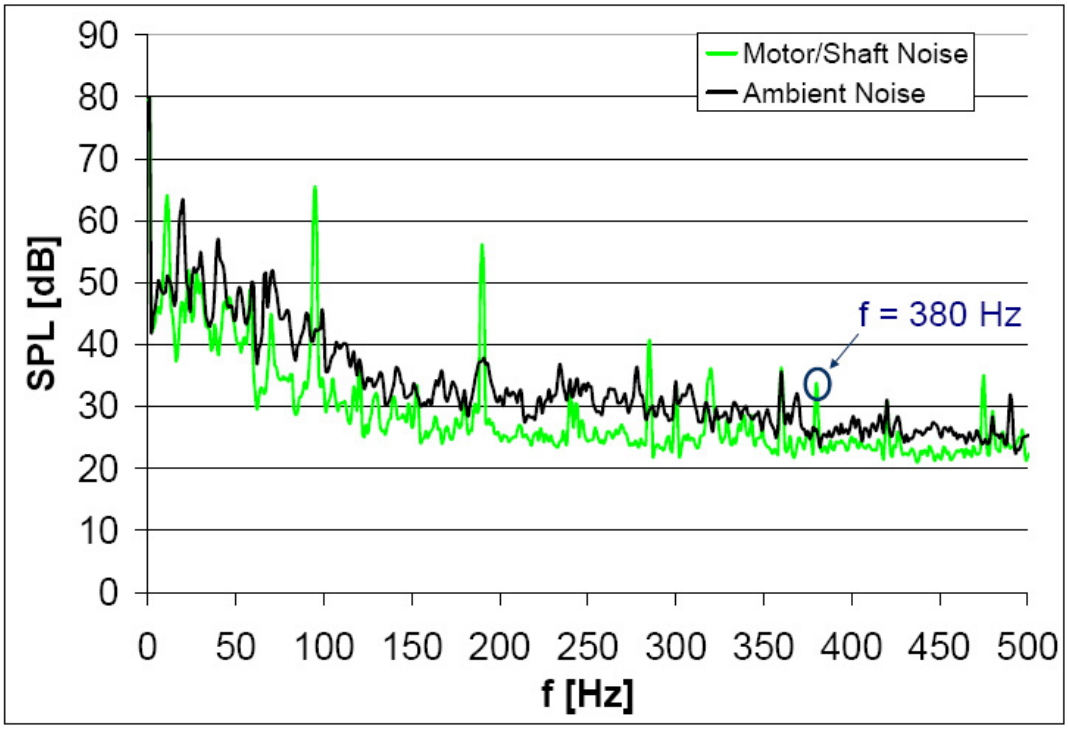

(b)

Figure 27: Noise spectrum of coupled setup structure obtained in an non-anechoic environment no blades attached to the hub, (a) shaft run at 4000 rpm, BPF = 266.6 Hz; (b) shaft run at 5700 rpm, BPF = 380 Hz.

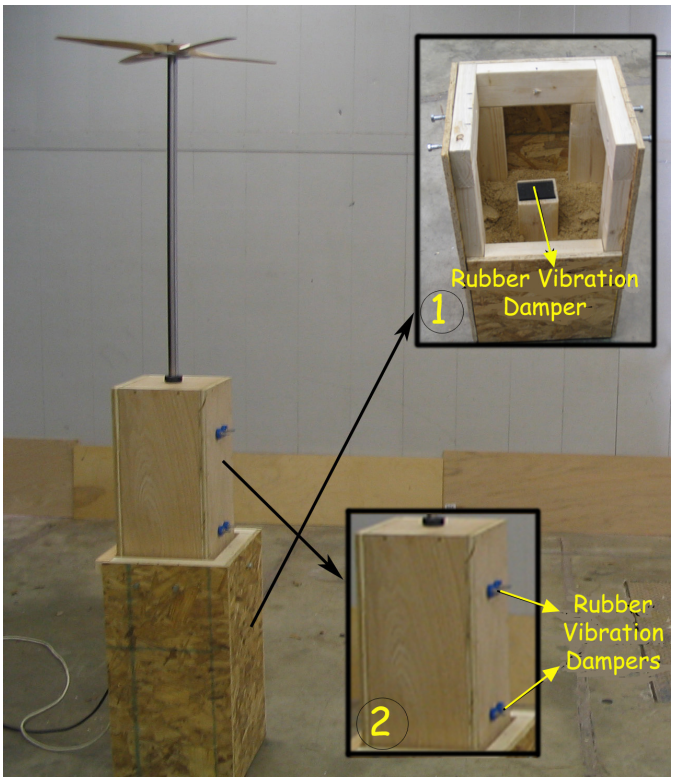

Figure 28: The uncoupled setup structure, box 2 fits inside box 1.

the rotor as placed in the chamber can be seen in Figure 32. To eliminate contamination of the measured acoustic data by reflections from the duct support facility, the structures that hold the duct and drives the rotor were all covered with sound absorbing polyurethane foam $4''$ thick as seen in Figure 33.

A schematic of the entire microphone traverse paths inside the anechoic chamber is given in Figure 34. The out flow direction α, is referred to as the 0^o and the rotor in-plane direction as the 90^o. Ducted rotor noise presented here was acquired in three traverse directions ($\alpha = 90^o, \alpha = 30^o$ and $\alpha = 0^o$). The microphones could be traversed to any desired location using a system driven by a stepper motor that is controlled by a Labview program, specially written for traversing the microphone away from the duct outlet or the rotor itself in a range from $24''$ from the mid point of rotor plane to $16''$ from the anechoic wedges. The microphones were protected with windscreens from the direct effect of the rotor induced flow. A photograph of the setup showing the microphone traverse directions is given in Figure 35.

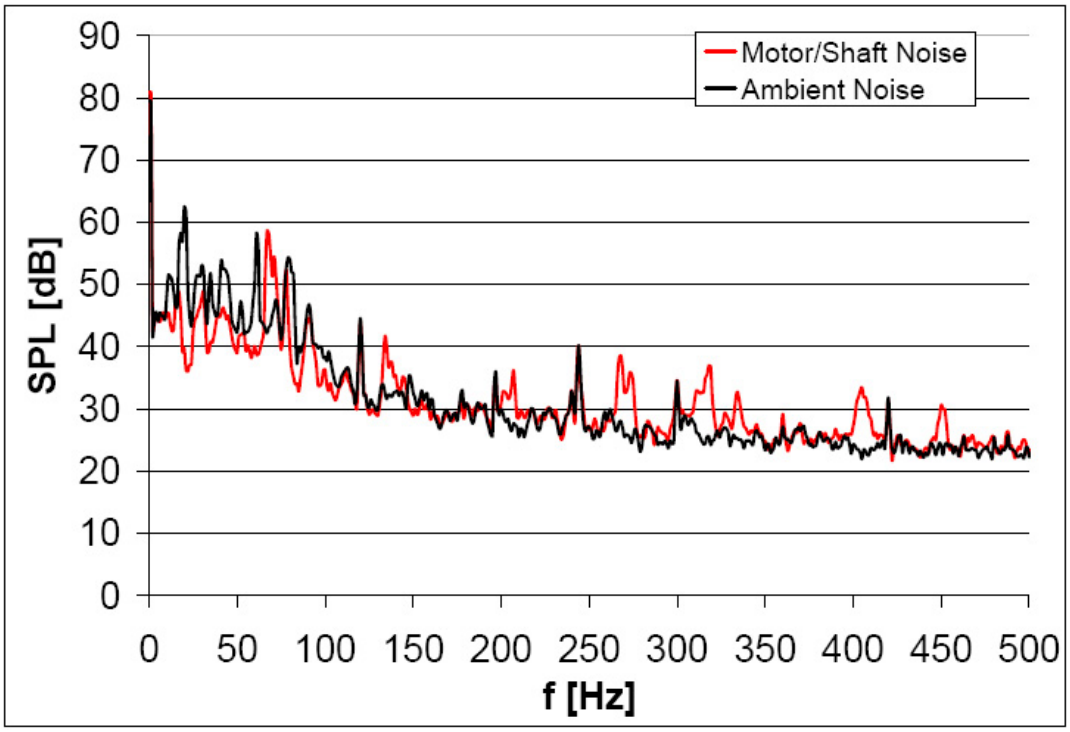

(a)

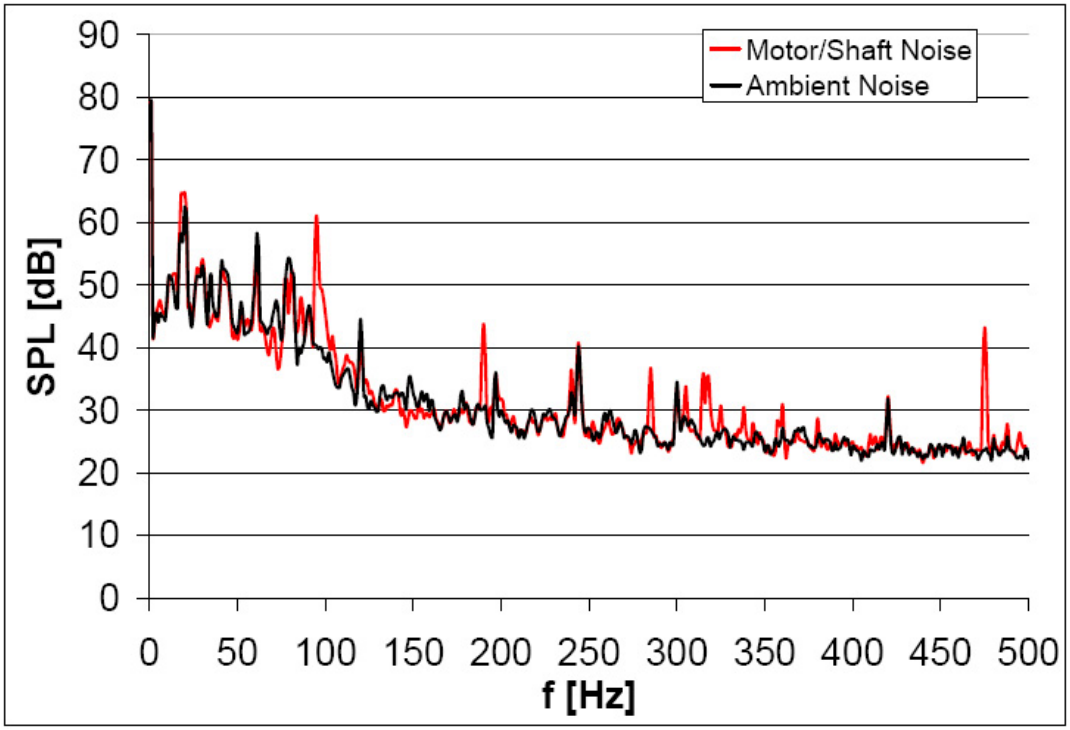

(b)

Figure 29: Noise spectrum of uncoupled setup structure obtained in a non-anechoic environment no blades attached to the hub,(a) shaft run at 4000 rpm, BPF = 266.6 Hz; (b) shaft run at 5700 rpm, BPF = 380 Hz.

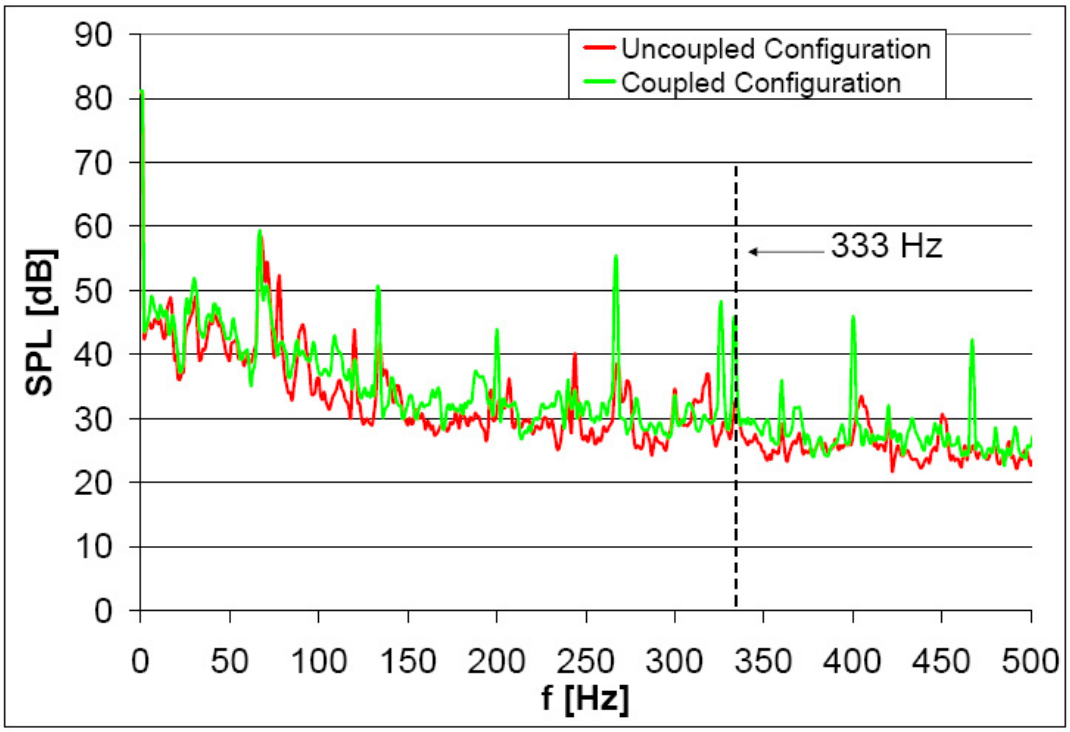

(a)

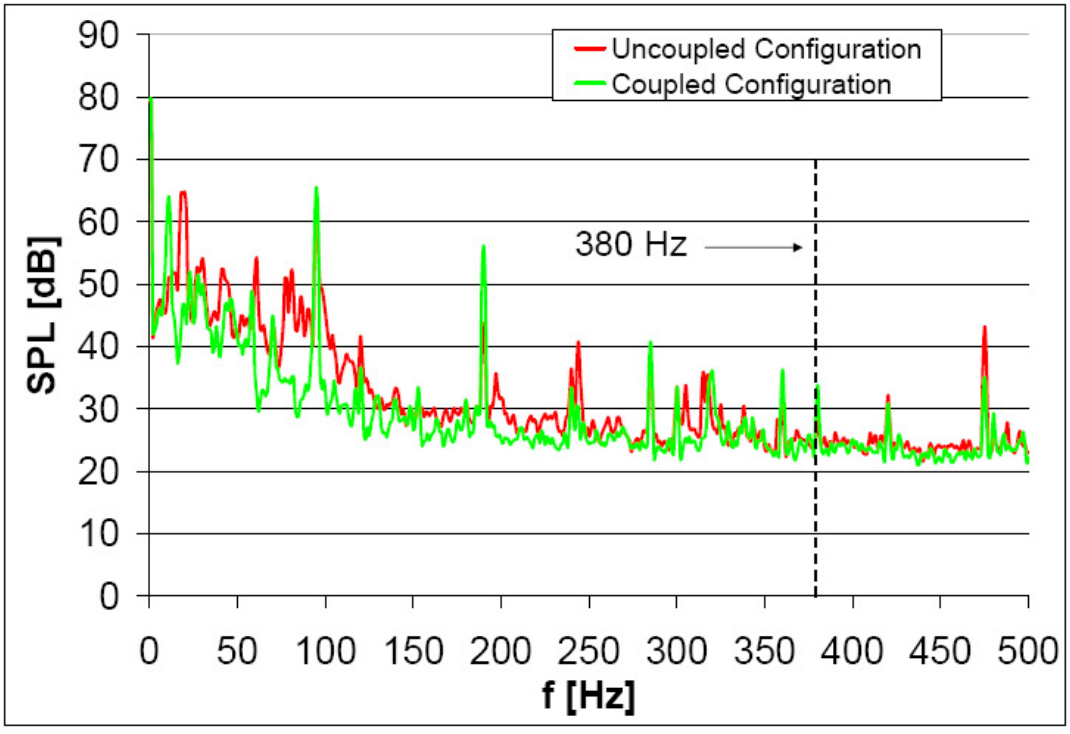

(b)

Figure 30: Operating noise spectra obtained at a non-anechoic environment for coupled and uncoupled configurations at rotational speeds of (a) 4000 rpm, (b) 5700 rpm.

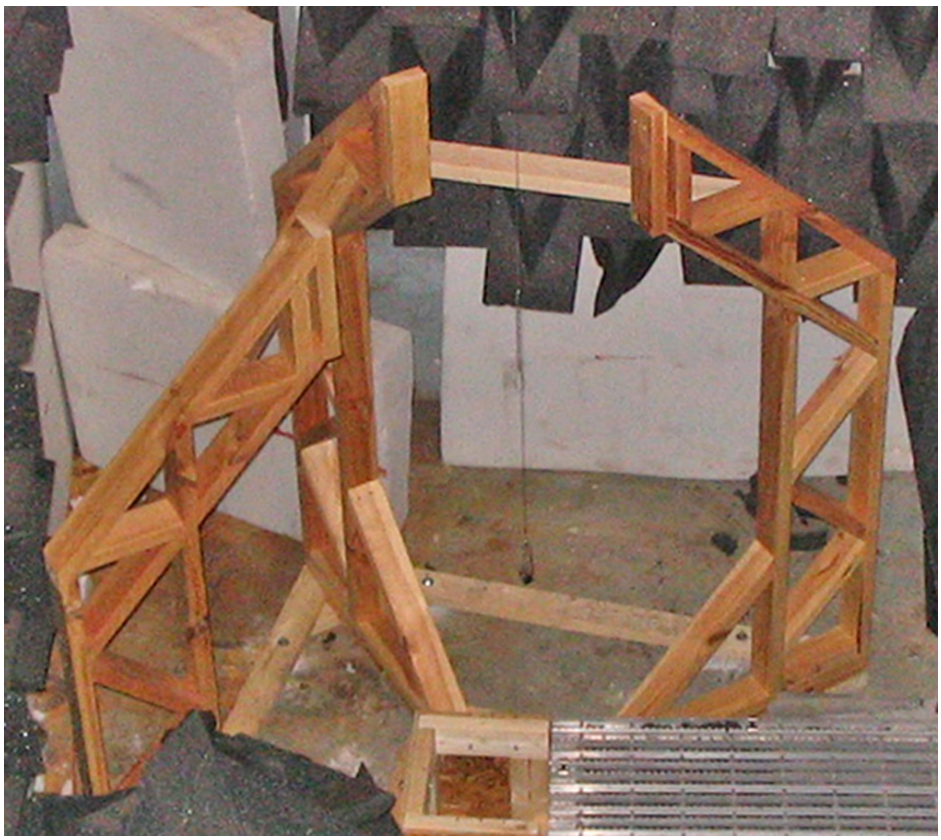

Figure 31: The structures that support the duct, placed inside the anechoic chamber.

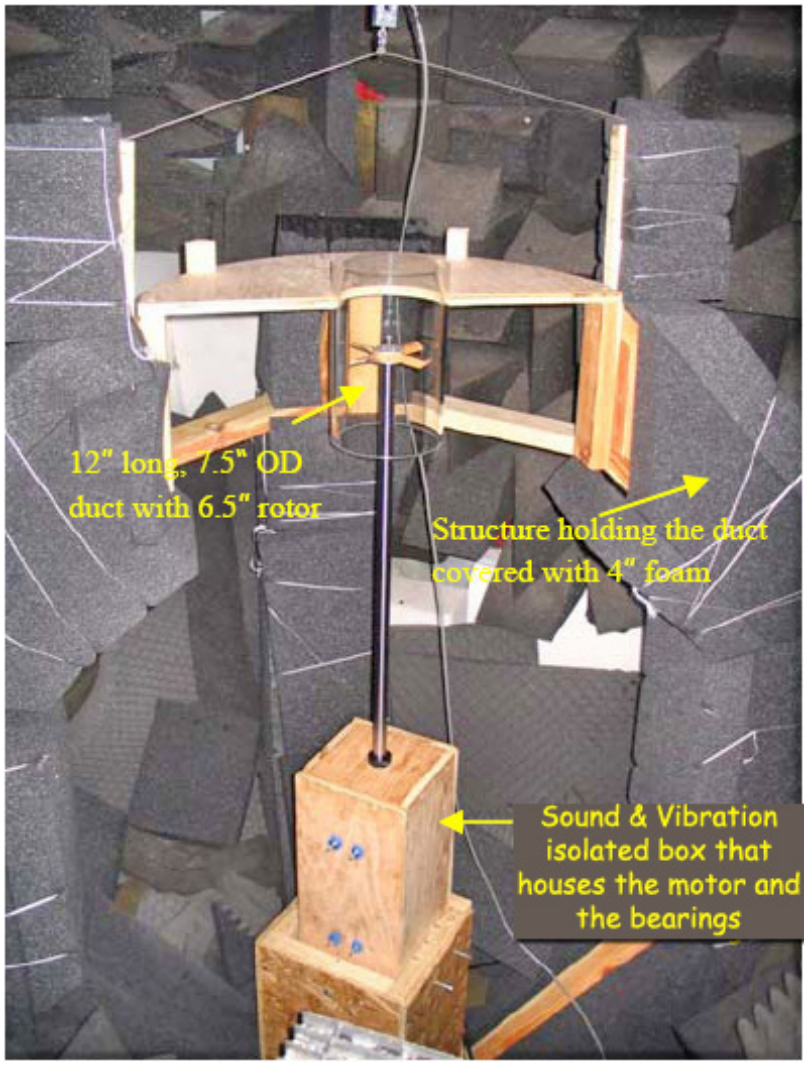

Figure 32: Test structure parts.

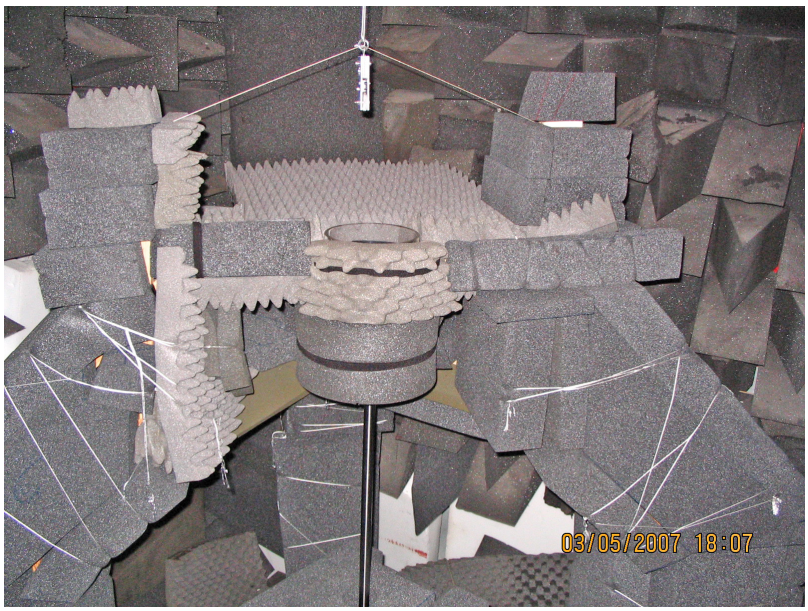

Figure 33: Test structure covered entirely by polyurethane foam.

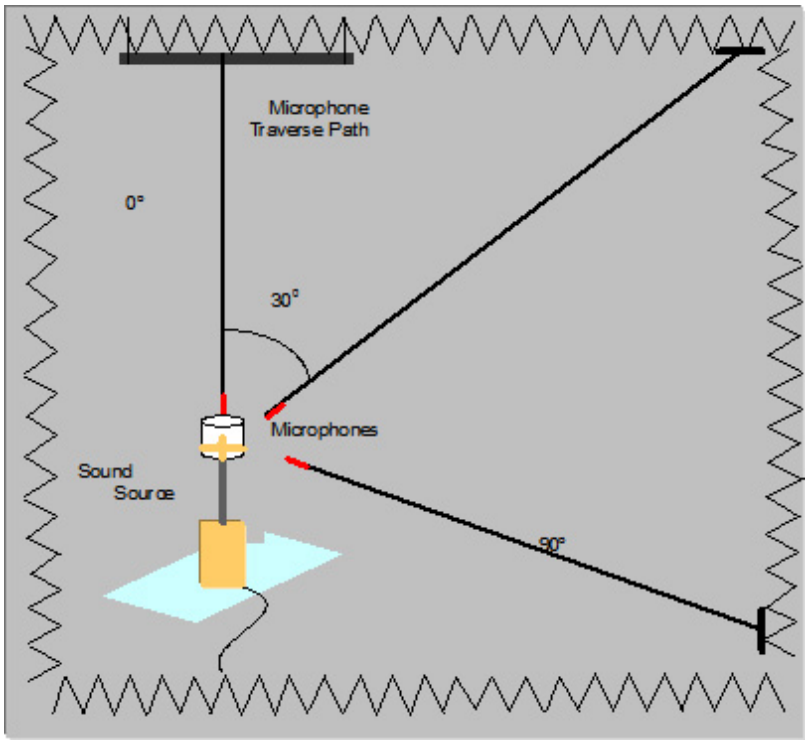

Figure 34: Measurement setup in GTRI Anechoic Static Jet Flow Facility.

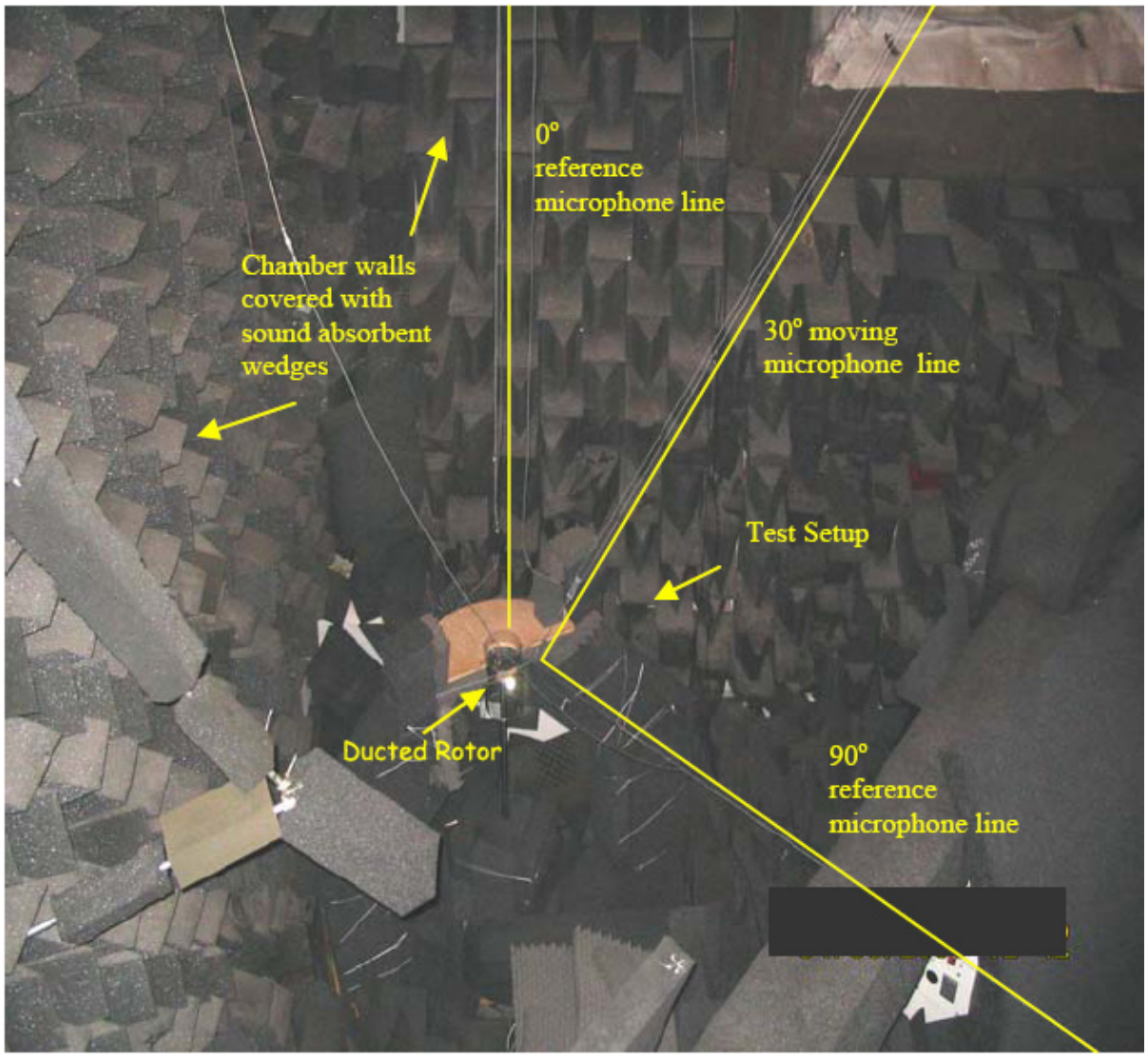

Figure 35: Geometric farfield measuremet setup inside the anechoic chamber.

4.3 Test Setup for Examining Point Source Assumption for Shielding of Rotating Noise Sources

The purpose of this portion of the experimental program was to determine the validity of using a point source in place of an actual rotor as the source in predicting shielding of rotor noise. Effect of many, not all, of the parameters discussed in the last section was measured for a rotor shielded by a rectangular plate. The experimental variables were: the locations of the source and the microphone relative to the shielding structure, which include the measurement distance and angle with respect to the shield, the source distance to the shield, and position of the source and the shield with respect to each other. Furthermore, dependence of these parameters on different shielding configurations, i.e., shield geometry and dimensions were studied. Two shields were tested: (1) a planar, and (2) a cylindrical surface. The rotor noise shielded by a planar structure will be compared with the case when rotor is replaced by a point source.

The test configurations are shown in Figure 36. Figure 36(a) shows a rectangular shield. Both a point sound source and a propeller were used to produce sound. The rotor noise shielded by a planar structure will be compared with the case when rotor is replaced by a point source. Figure 36(b) shows the configuration tested with a full cylindrical duct. This work is focused on the shielding of tonal noise generated by the rotor so the noise due to the resonance of the duct and the production of higher order modes are not investigated.

4.3.1 Point Source Experiments

4.3.1.1 Sound Recording Setup and Controls

The measurement setup inside the chamber is shown in Figure 37. A reference microphone is placed 80″ from the source. Six microphones were placed 6″ apart from each other on the vertical axis of a 3D traverse mechanism. One of the microphone was positioned pointing exactly towards the source. The 3D traverse could move microphone array, 90″ to 150″ away from the source, back and forth; and ±30″ away from the origin of the traverse, from left to right. So, using this system it was possible to measure noise any point inside a 60 x 30 x 60 in^3 cube.

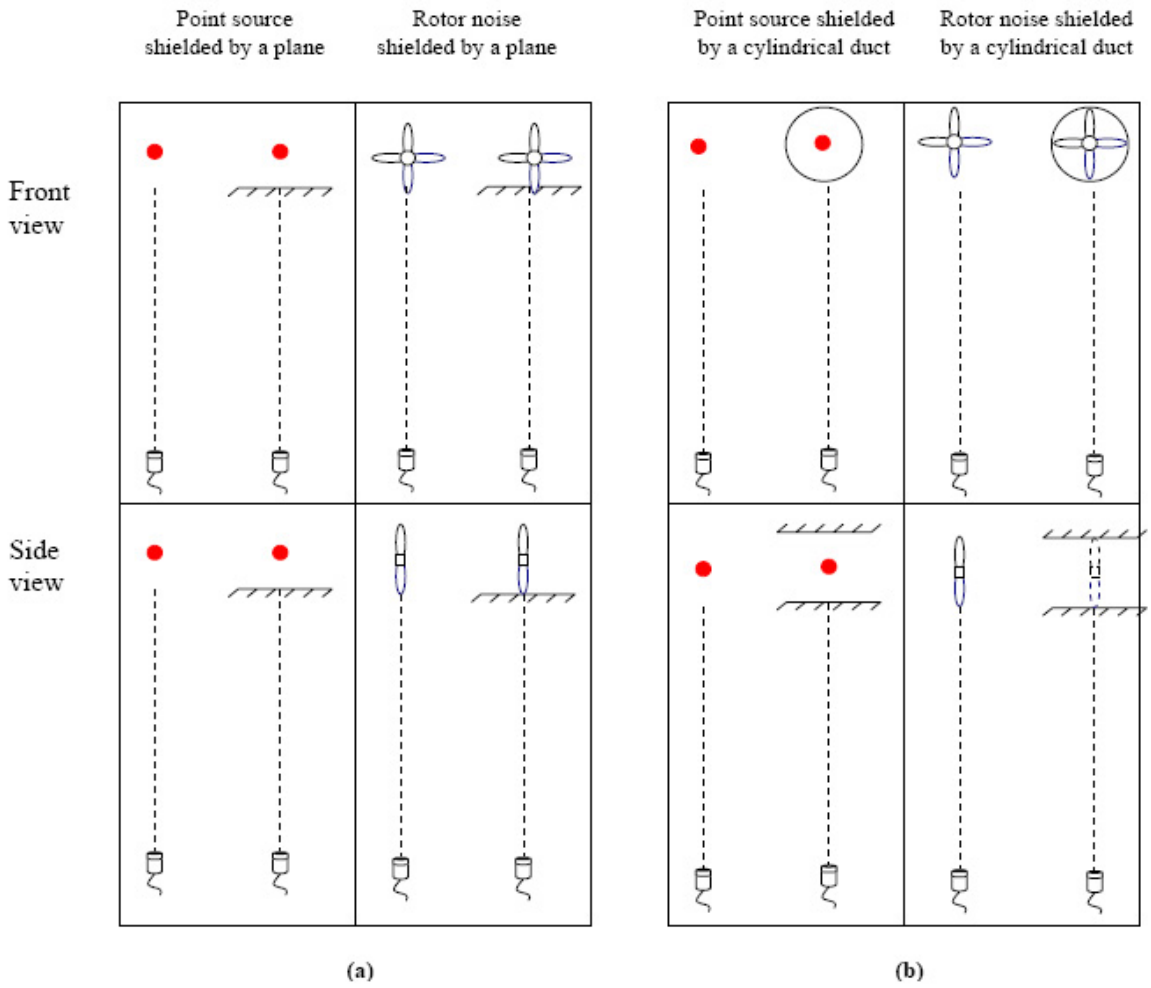

Figure 36: Shielding tests configurations.

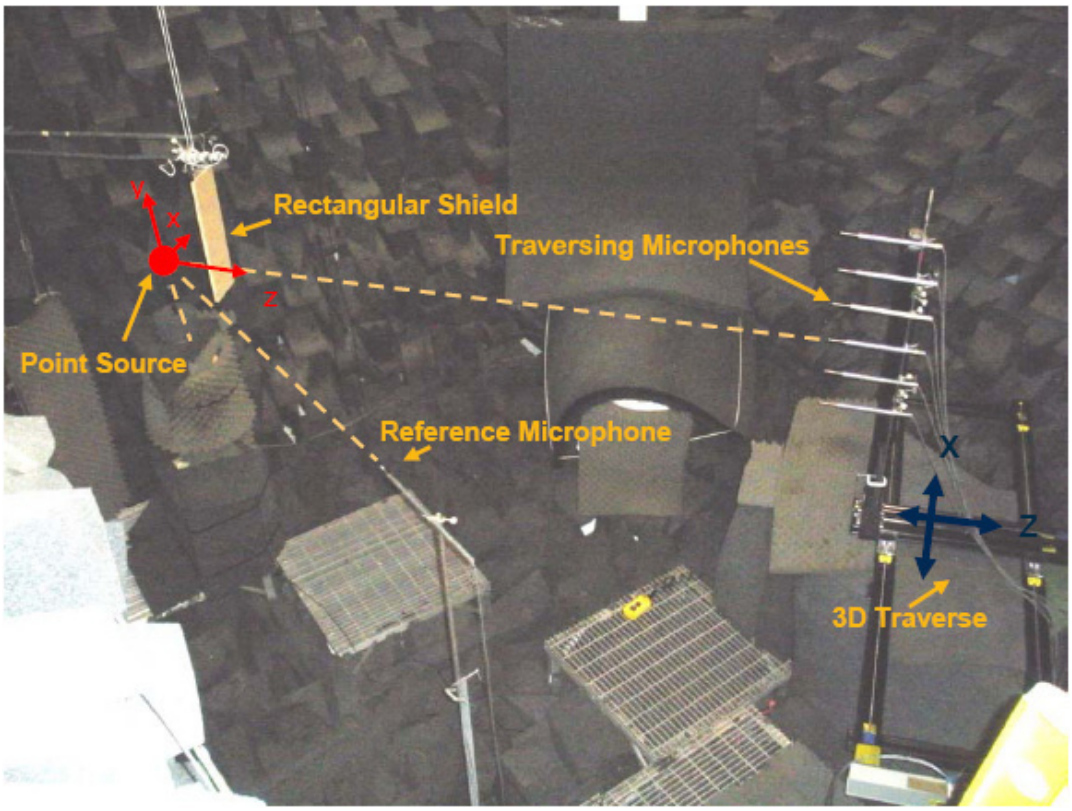

Figure 37: Noise shielding measurement setup inside the anechoic chamber.

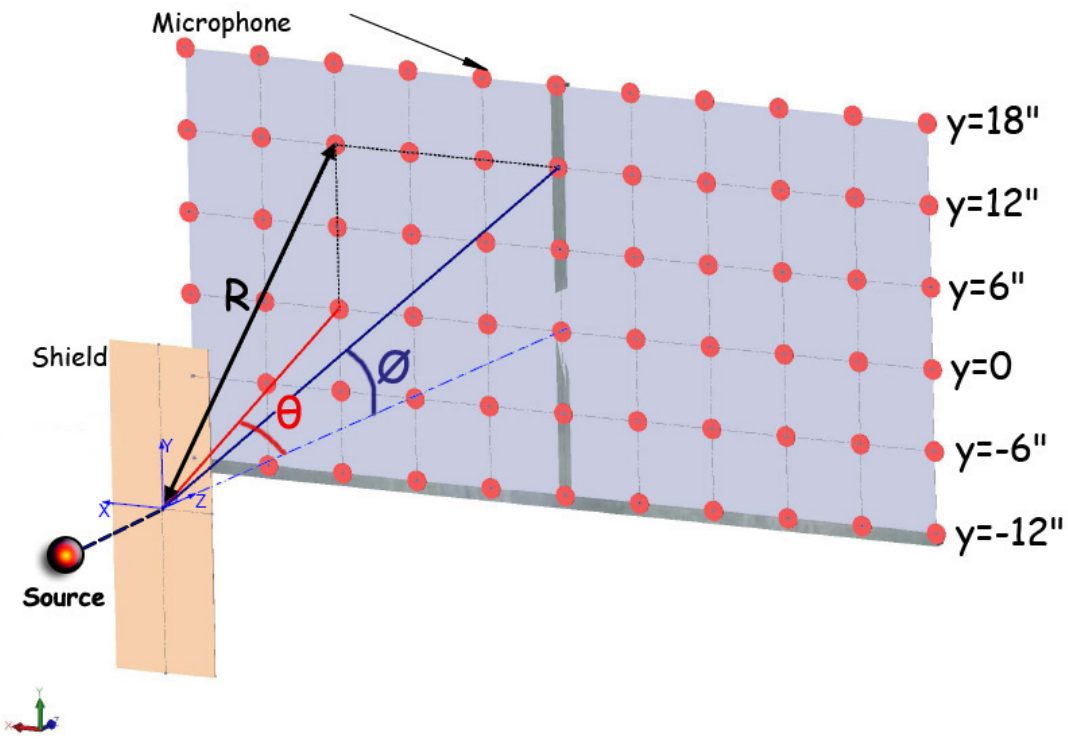

Figure 38: 3D view of the measurement mesh.

A 3D view of the measurement mesh used for the experiments is shown in Figure 38. The six microphones placed on y-axis were traversed along the x-axis in 6″ steps. Sound at 11 x 6 points were measured on an area of 60 x 30 in^2. The measurement plane was parallel to the shield plane and perpendicular to z-axis. The traverse could also move in the third dimension, z-axis. The data was acquired in three planes in the z direction labeled as z_1, z_2, and z_3 planes in Figure 39.

The experiments were controlled from outside the chamber by the computer configuration shown schematically in Figure 40. The electronic signal produced by a signal generator was fed both to the speaker inside the chamber and recorded by the main control computer. The signal voltage was also recorded. The output of a microphone inside the chamber were recorded by the same control computer. The data from eight channels, seven of them noise data acquired by the microphones and one the input signal of the speaker, was gathered for the analysis.

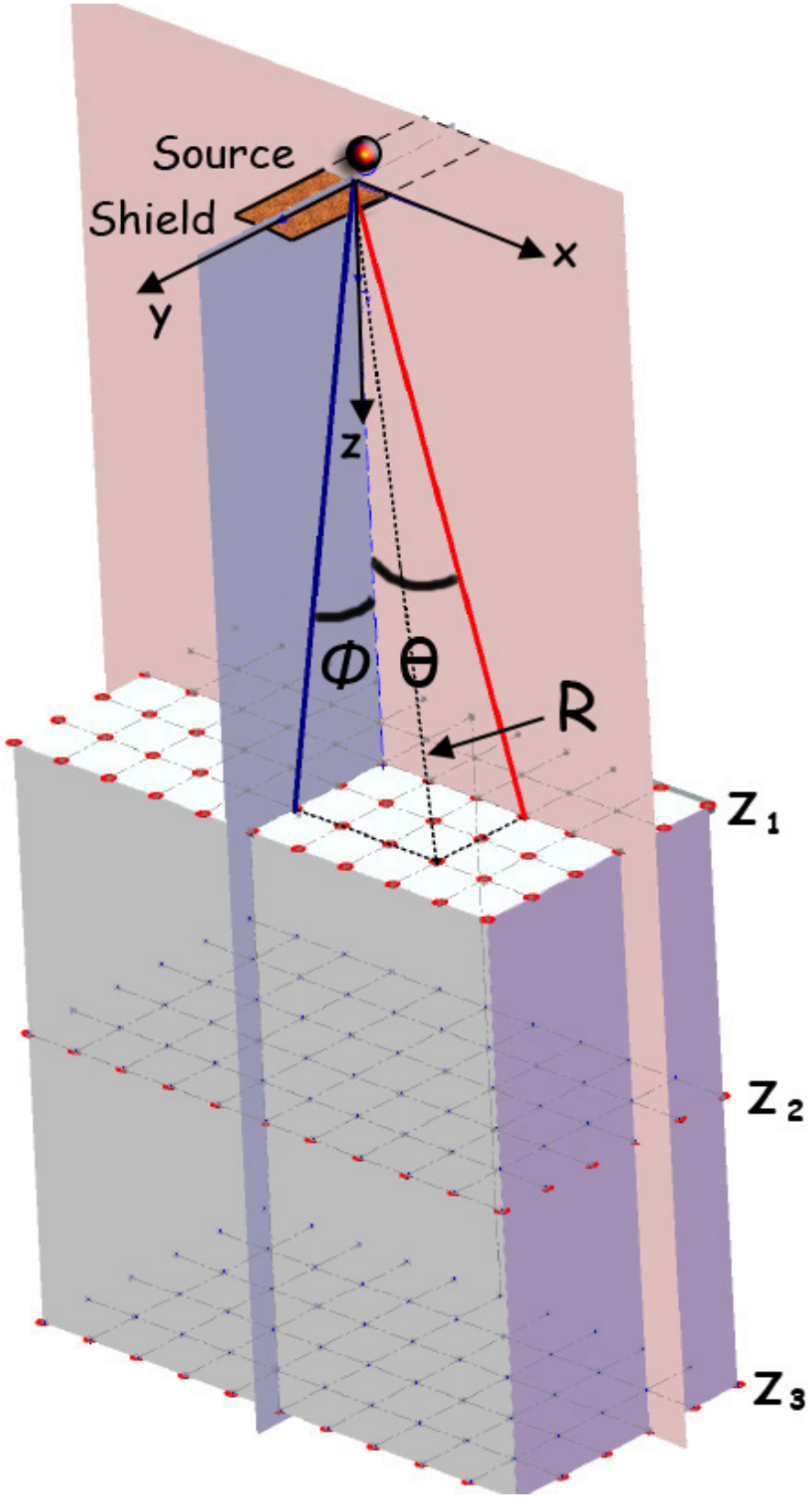

Figure 39: 3D view of shielding experimentation parameters.

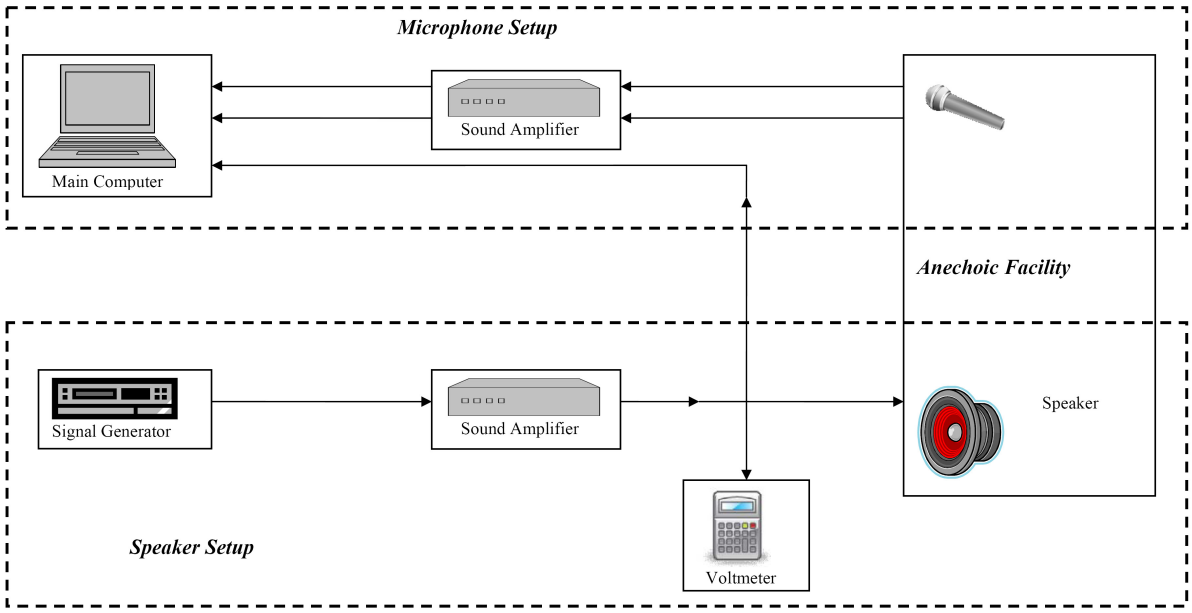

Figure 40: Computer configuration controlling the experiment.

4.3.1.2 Noise Source Setup

The monopole source, which is composed of an inverse conical horn mounted to a low-frequency electro-acoustic driver, is shown in Figure 41. Data was first acquired with the monopole source. the propeller hub center was then placed at the semi locations where the monopole sund source was located for the point source experiments. The point source locations that were tested with respect to the shield are schematically shown in Figure 42. The main experimental parameters used for point source experiments and later for the rotor source experiments are shown in Figure 39 and are measurement distance, R, polar angle, θ, and azimuthal angle, ϕ. During the presentation of the experimental results in Chapter 6, instead of measurement distance, R, one or more of the cartesian coordinate components, i.e. x, y, or z, of it, that is the most representation for the given case will be specified to provide a clearer understanding of the configuration. The positions of the microphone traverse and the noise source with respect to each other are given from front and side views in Figure 43.

A picture of the measurement set up with the point source and shield installed is given

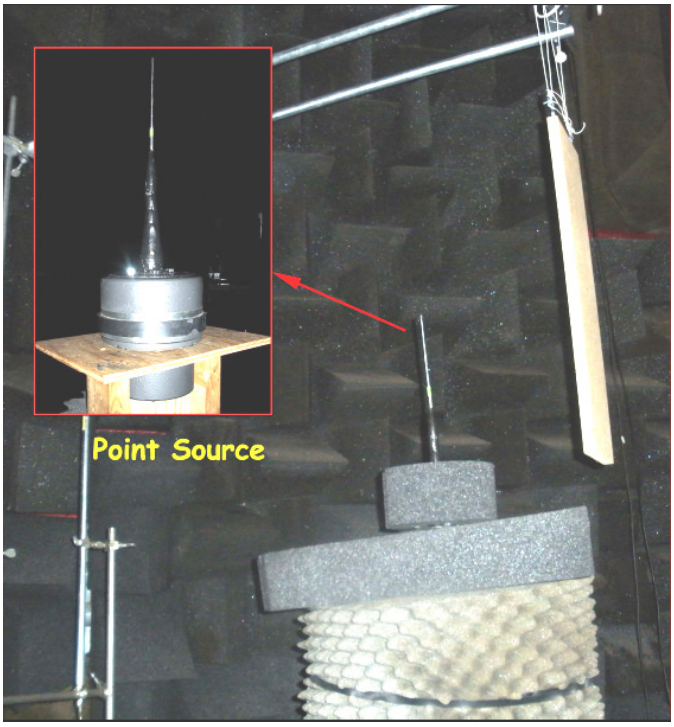

Figure 41: Point source setup.

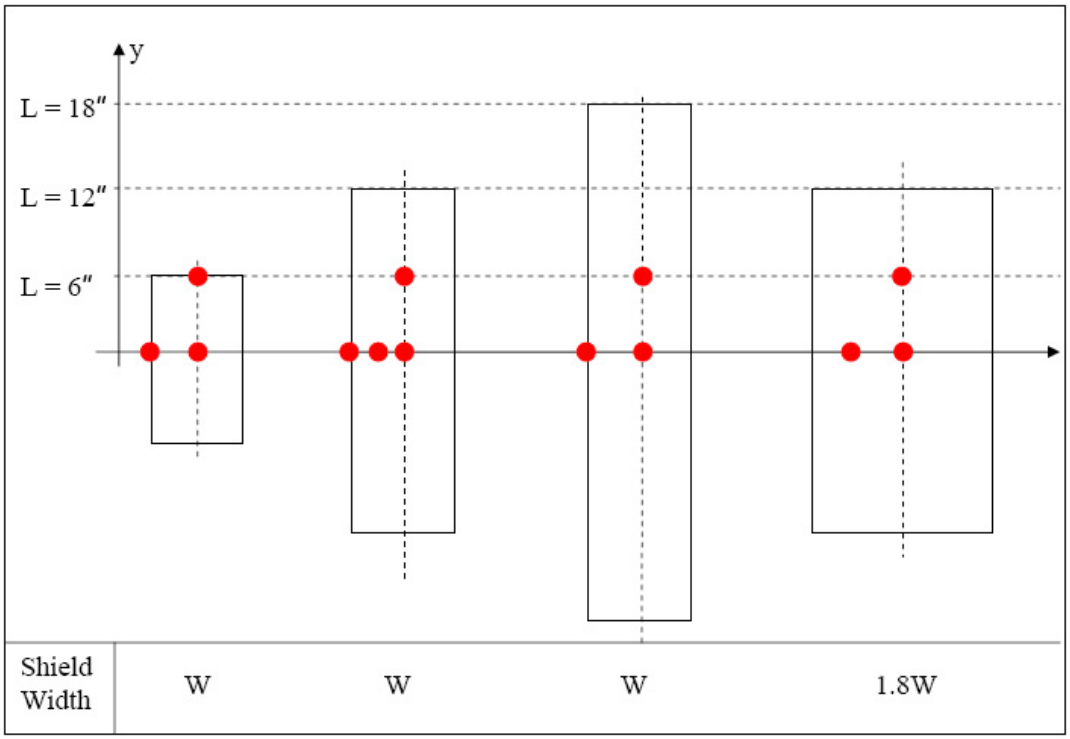

Figure 42: Point source positions with respect to the shielding plane. $W = 7.25''$.

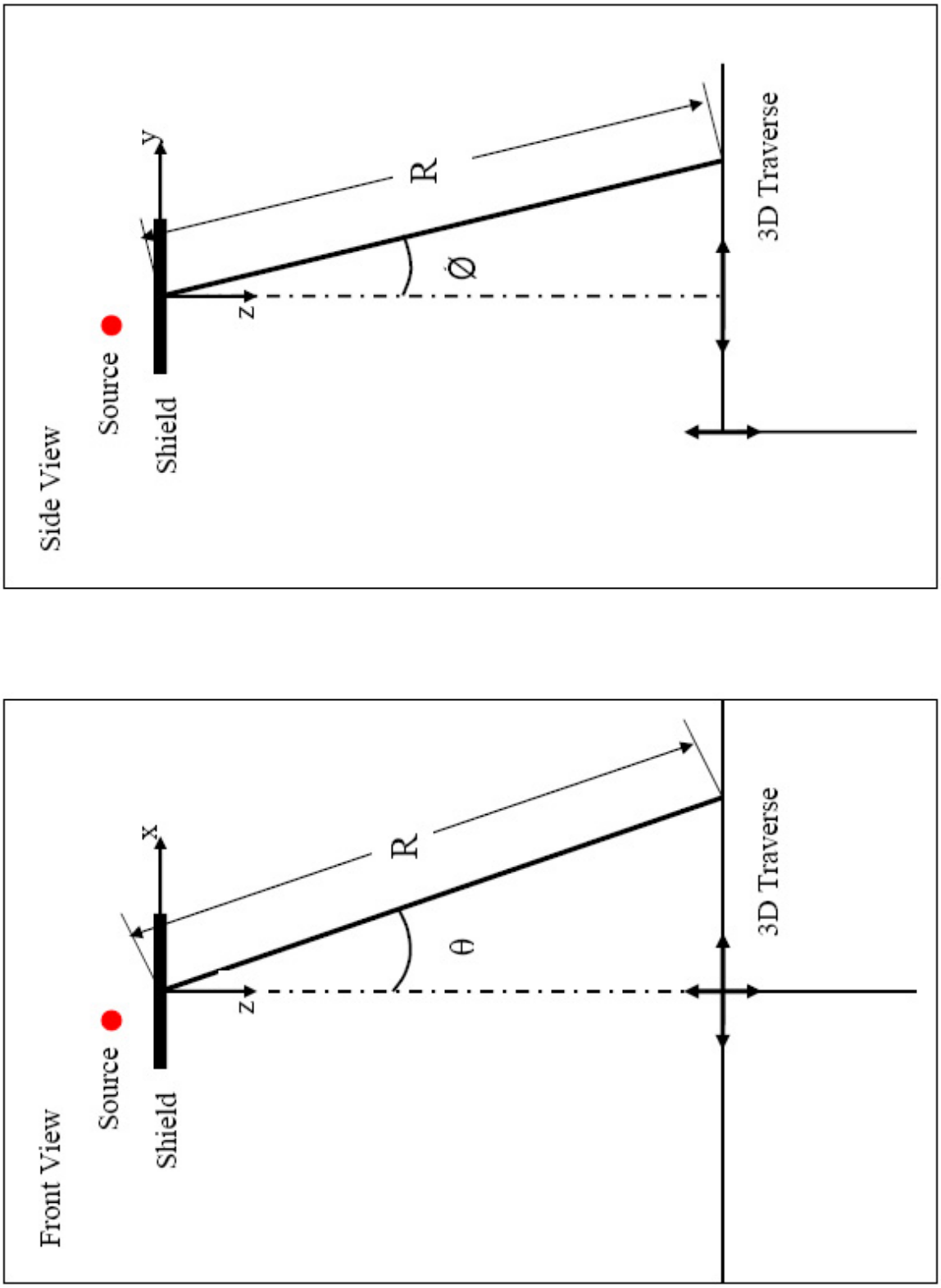

Figure 43: Front and side views of shielding experimentation parameters.

in Figure 44. Since the source was placed on a heavy structure, it was kept at a fixed point and the shield was moved with respect to the source. The microphones were also moved with respect to the source. However, the calculations were made as if the shield mid point was always at the same fixed point and the source and the microphones were moving with respect to it. The reason for changing the main coordinate system from the source to the shield was to have a better understanding of the real applications.

4.3.1.3 Rectangular Shield Setup

After a few iterations the best configuration to suspend the rectangular shields was found to be the structure shown in Figure 44. This structure is composed of $1/2''$ diameter pipes built to suspend the shield at the desired points on the 3D space between the source and microphones. It was made sure that the only barrier blocking the sound waves was the shield itself.

The choice of the rectangular shield dimensions were based on the dimensions of the ducts tested. The width and length of the rectangular shields were chosen to be the compatible with the diameter and length of the ducts, respectively. The rectangular shields were made up of $3/4''$ thick, high density wood. The dimensions of the shields were: $7.25''$ x $12''$, $7.25''$ x $24''$, $7.25''$ x $36''$, and $13''$ x $24''$. The shields are shown in Figure 45.

A picture of the measurement setup with the point source was given in Figure 37. In Figure 46, the same general view of the setup is given where microphones were attached to longer pipes used to reach closer distances from the source.

4.3.1.4 Circular Shield (Duct) Setup

All the ducts tested had the inner diameter of $7''$. Ducts of three lengths, $12''$, $24''$ and $36''$, were tested. A structure holding the ducts was added to the setup and the structure holding the rectangular shield was removed. An additional piece was attached to the inverse conical horn to make sure that there was enough clearance between the duct outlet and the speaker. The point source together with the $12''$ length duct, $24''$ length duct, and alone are shown in Figures 47(a),47(b), and 47(c), respectively. The point source exit was placed to the center of the duct.

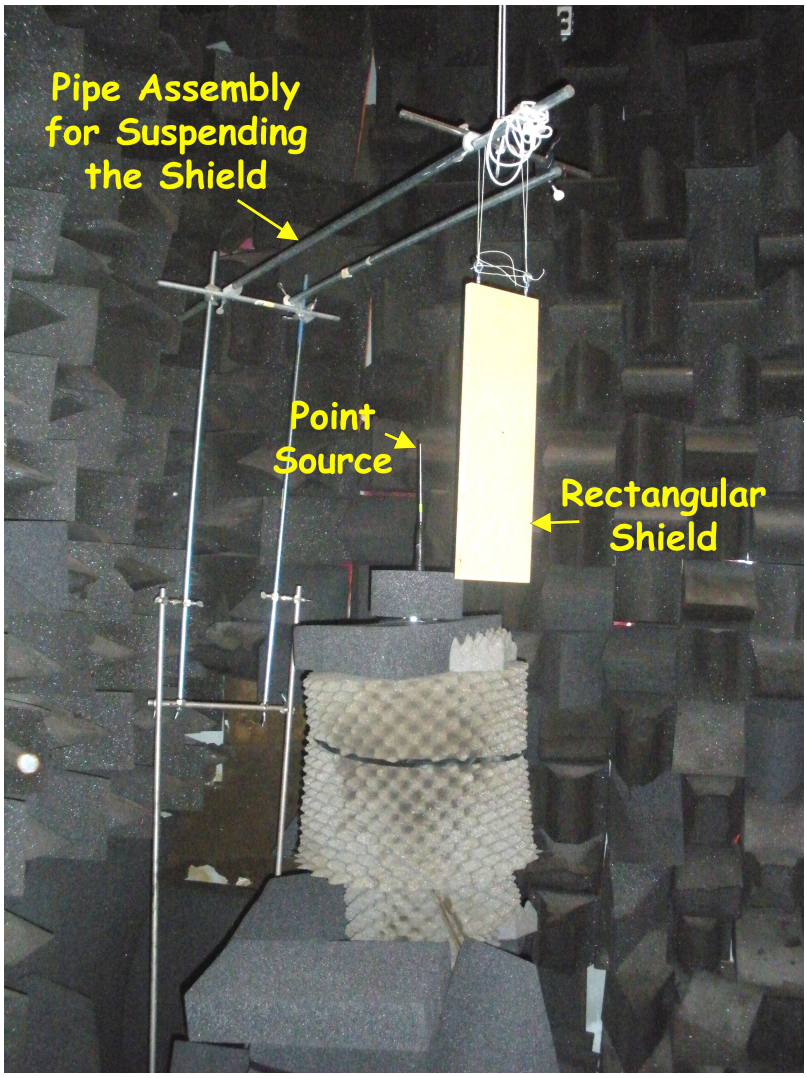

Figure 44: Measurement setup for rectangular shielded point source experiments.

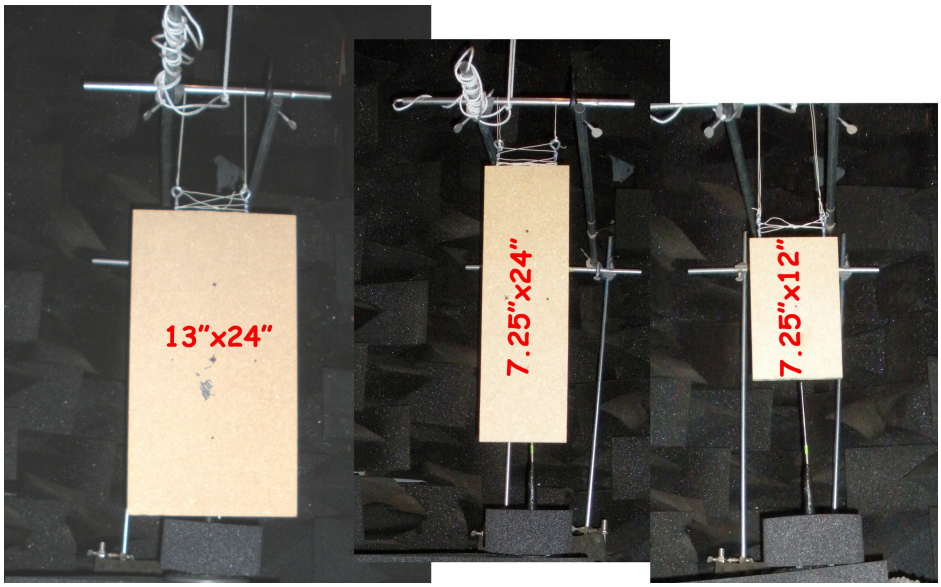

Figure 45: The rectangular shields used for tests.

Figure 46: Measurement setup inside the chamber with longer pipes installed to hold the microphones.

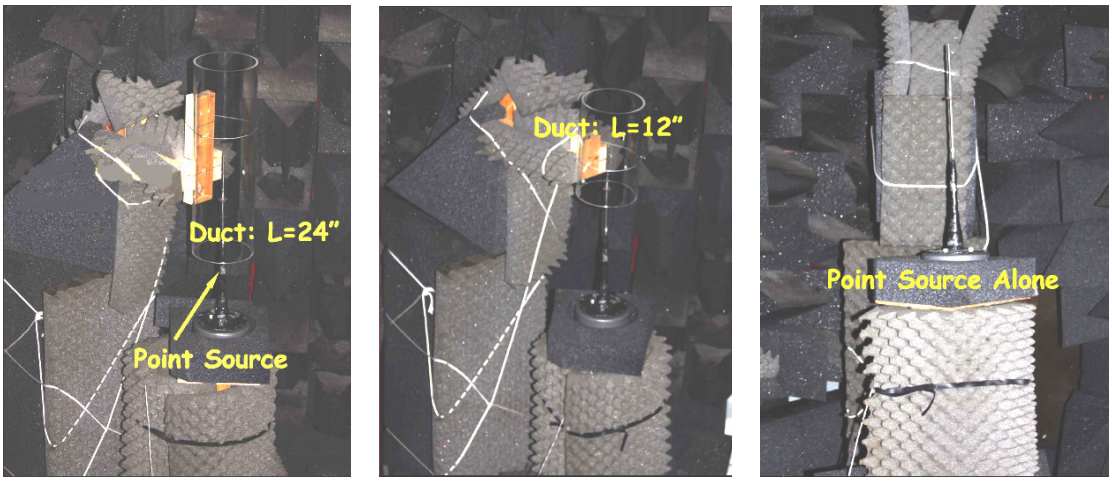

(a) (b) (c)

Figure 47: Point source and cylindrical ducts used for the ducted point source tests.

4.3.2 Rotor Experiments

This part of the experiments was performed by replacing the point source with a rotor. The mid point of the rotor was placed exactly where the point source was. The diameters of the rotors used for testing were 6.5″ and 13″. The setup that was shown in Figure 28 was installed first. However overheating problems occurred for the motor and the bearings due to the longer working periods compared to previous runs. The box around the motor and bearings was removed to provide air for cooling. The structure was left as seen in Figure 48.

The rectangular shields described in the previous section were used to test the shielding for 6.5″ rotor. 13″ rotor was tested only with 13″ x 24″ shield. The rotor hub center locations that were tested are schematically shown with respect to the shield in Figure 49. A picture of the measurement setup with the rotor and shield installed is provided in Figure 50 and a wide angle view of the entire test setup is given in Figure 51.

For the ducted rotor case, the 6.5″ diameter rotor was used with a tip clearance of 0.25″. The the center of the rotor was again placed at the exit of the point source, which was the center of the duct. The structure used to hold the duct is shown in Figure 52(a) and 52(b) is a front view of the setup before it was covered with foam. In Figure 52(c) the setup is shown as it was during the experiments where entire setup was covered with foam.

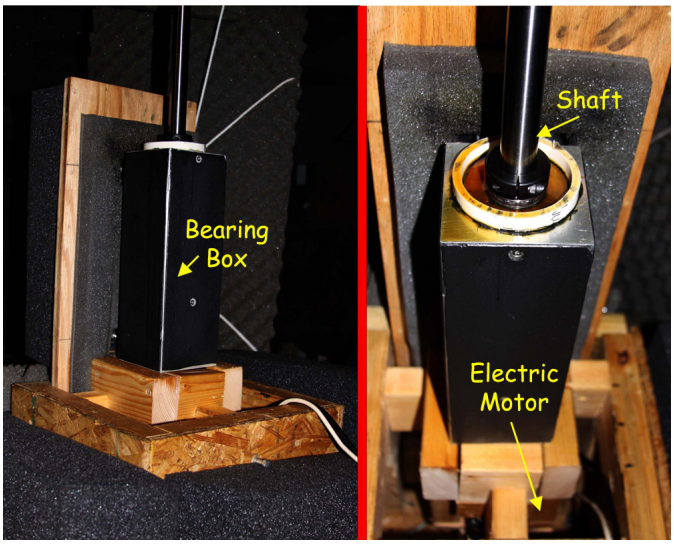

Figure 48: Bearing and motor combination used to run the rotor for shielding experiments.

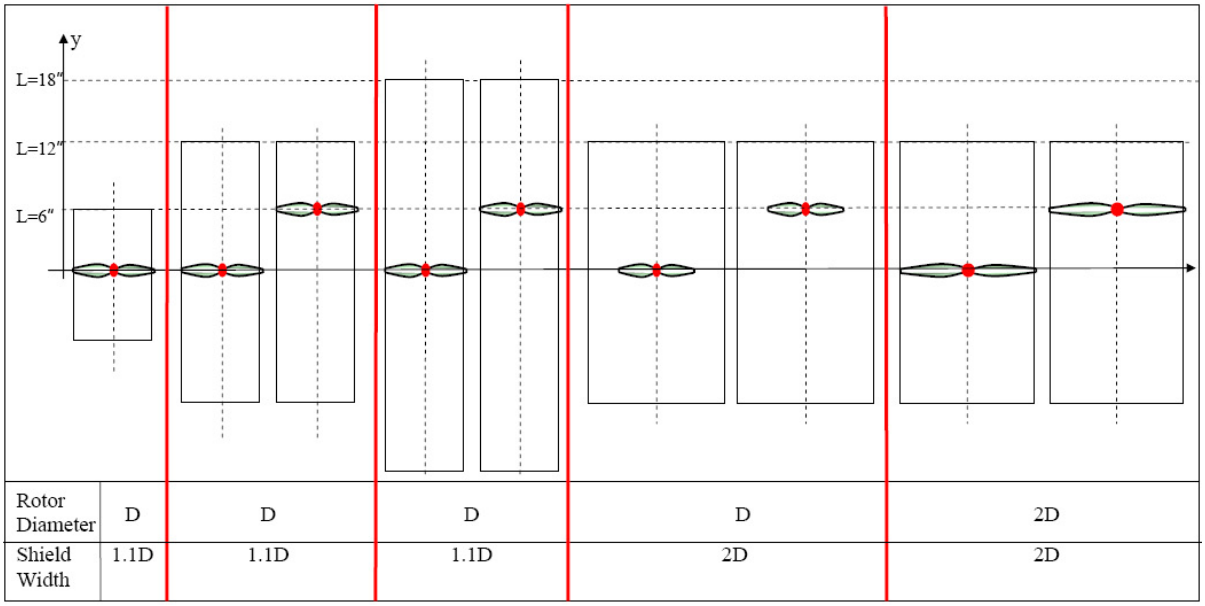

Figure 49: Rotor source positions with respect to the shielding plane. $D = 6.5''$.

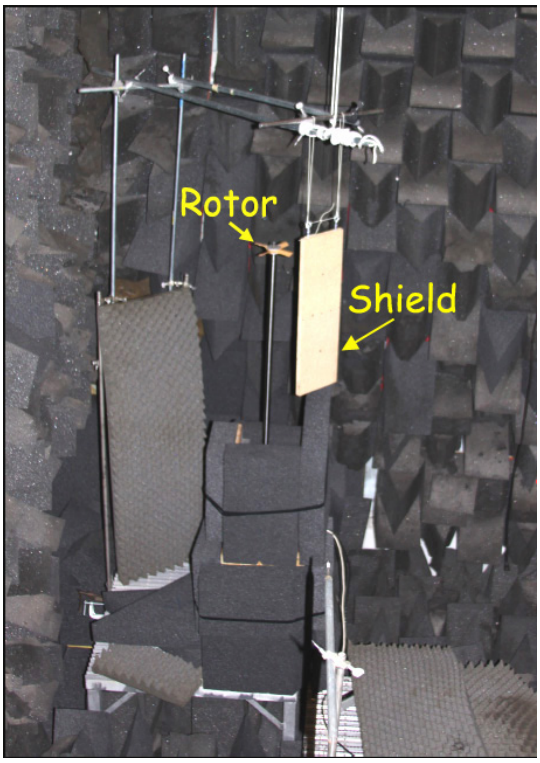

Figure 50: Measurement setup inside the chamber with the rotor installed.

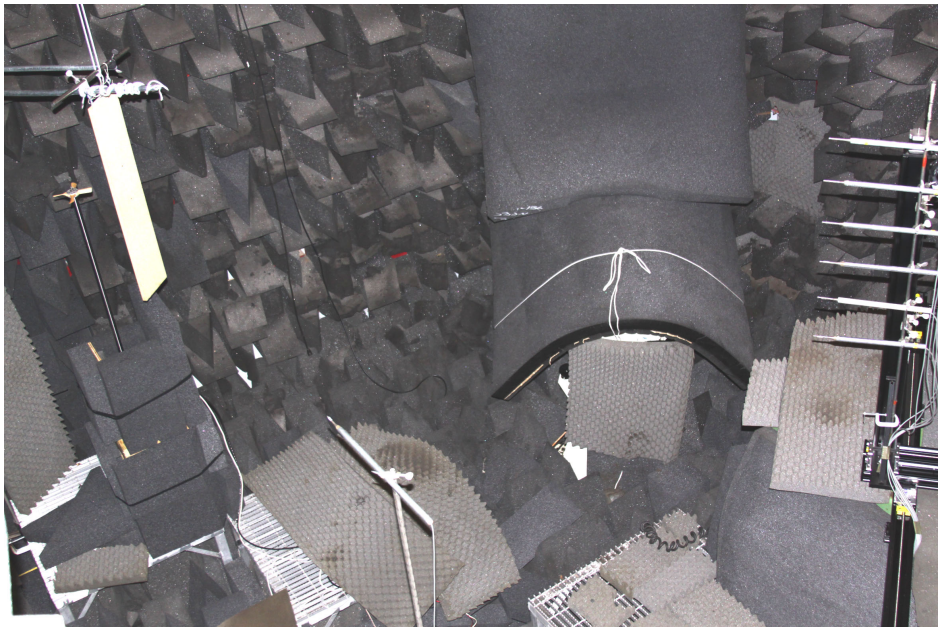

Figure 51: Wide angle view of the measurement setup inside the chamber with the rotor installed.

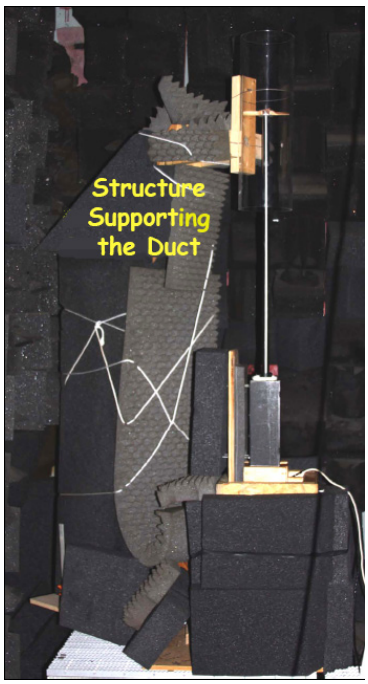

(a)

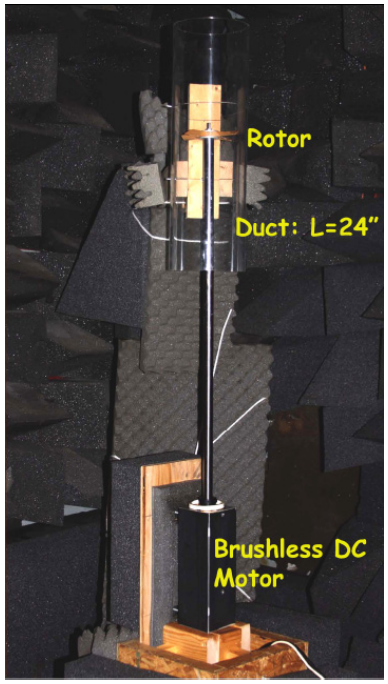

(b)

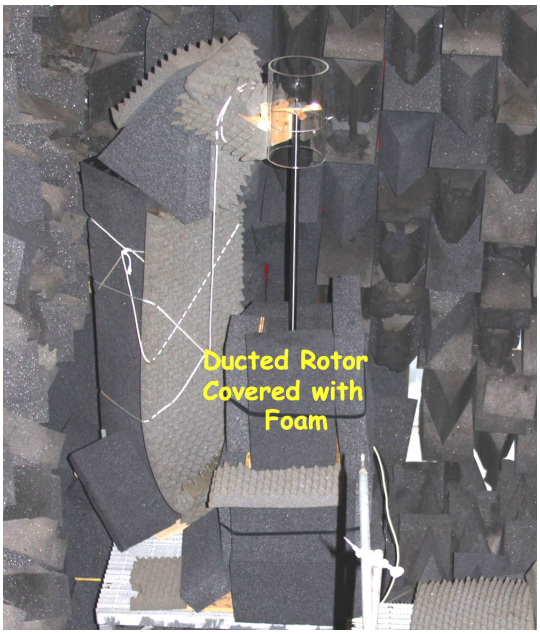

(c)

Figure 52: Ducted rotor test setup, (a) side view; (b) front view; (c) all covered with foam.

CHAPTER V

DETERMINATION OF GEOMETRIC FARFIELD FOR DUCTED AND UNDUCTED ROTORS

5.1 Unducted Rotor Experiments

All acoustic data is analyzed in narrowband with a frequency resolution(Δf) of 1.5 Hz in the frequency range from 0 to 12800 Hz. The results are presented as the measured SPL variation with the ratio of the measurement distance, R, to rotor diameter, D. All data has been normalized with respect to a reference microphone to account for any source output variation from run to run. These results are compared with the theoretical variation using the ISL. The ISL curve is given in a band of 2 dB corresponding to an expected ± 1 dB measurement error. The measured sound pressure level differences are plotted at blade passing frequencies, their second harmonics, and at selected broadband noise peaks [46].

Typical acoustic spectra of the open rotor at 90^o, 45^o, and 0^o appear in Figures 53, 54, and 55, respectively. The rotor was run at 7500 RPM so the BPF was 500 Hz. In all cases, the first and second harmonics of the BPF are significant in the spectra and the rest are buried in broadband noise. As the angle gets smaller, the second harmonic looses its intensity. When the receiver is in the plane of the rotor disk ($\alpha = 90^o$), broadband noise levels show an increase around 1500 Hz and drop down uniformly as the frequency increases. At 45^o broadband noise keeps mostly the same level showing a decrease after 3000 Hz. And at 0^o broadband noise levels start lowering after 1500 Hz.

In Figure 56, the ISL match for the acoustic data for smaller size rotor (D=6.5) in the rotor disk plane is shown. The rotor was run at 7500 rpm and first and second harmonics of BPF are presented. The trend tends to improve at low frequencies and gets closer to the theoretical range at smaller microphone distances. The results for 45^o and 0^o measurement angles are given in Figure 57 and Figure 58, respectively. The analysis of the smaller size showed that the R/D ratio for the geometric farfield is between 8 and 10.

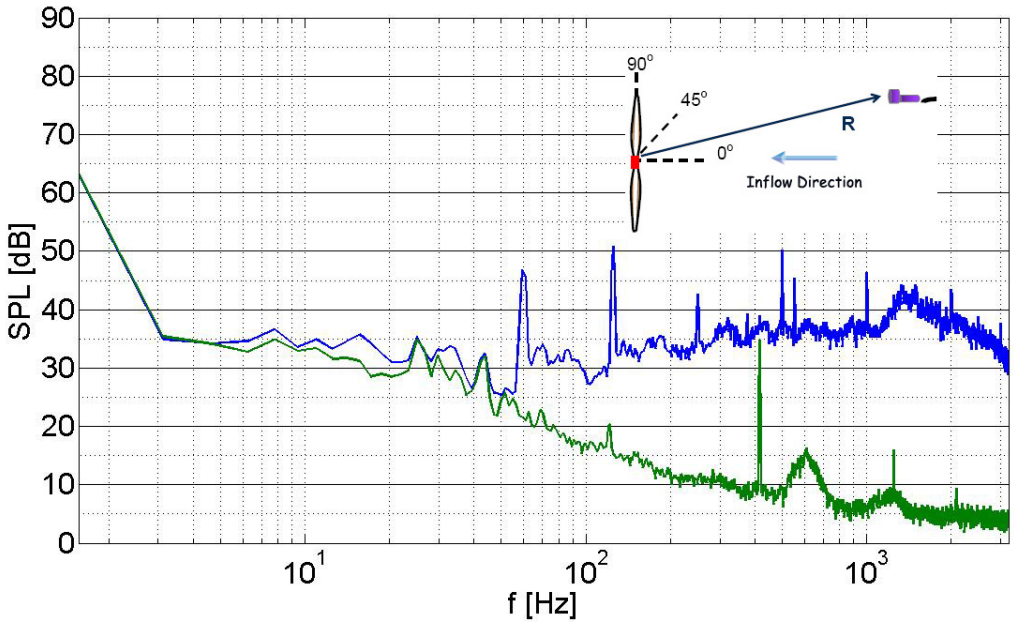

Figure 53: Acoustic spectrum of a 6.5″ diameter unducted rotor at $\alpha = 90^o$. $rpm = 7500$, $R/D = 15$, $n_B = 4$, $\Delta f = 1.5$ Hz.

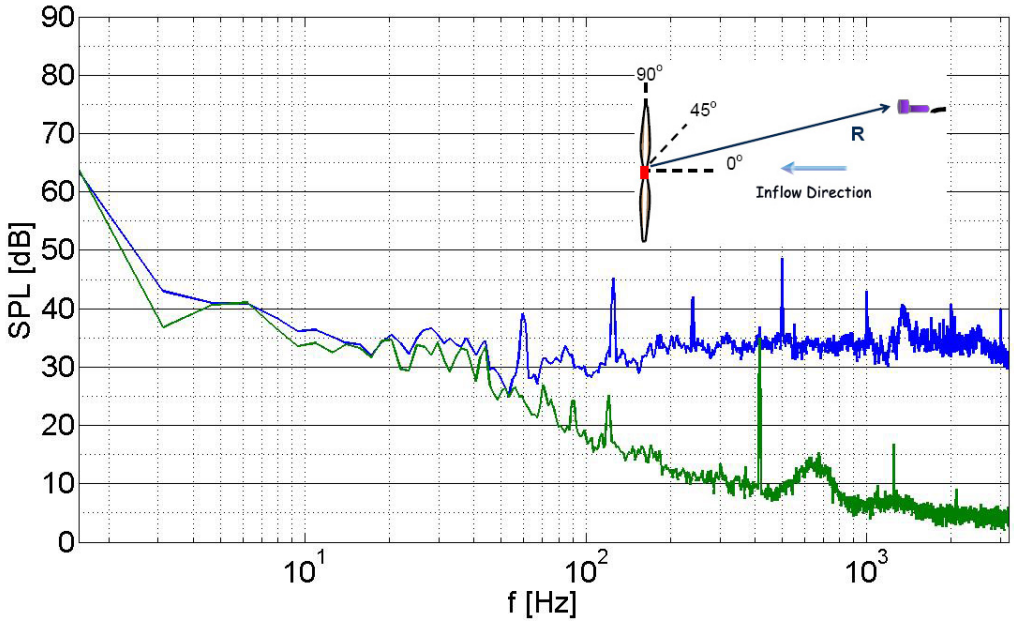

Figure 54: Acoustic spectrum of a 6.5″ diameter unducted rotor at $\alpha = 45^o$. $rpm = 7500$, $R/D = 15$, $n_B = 4$, $\Delta f = 1.5$ Hz.

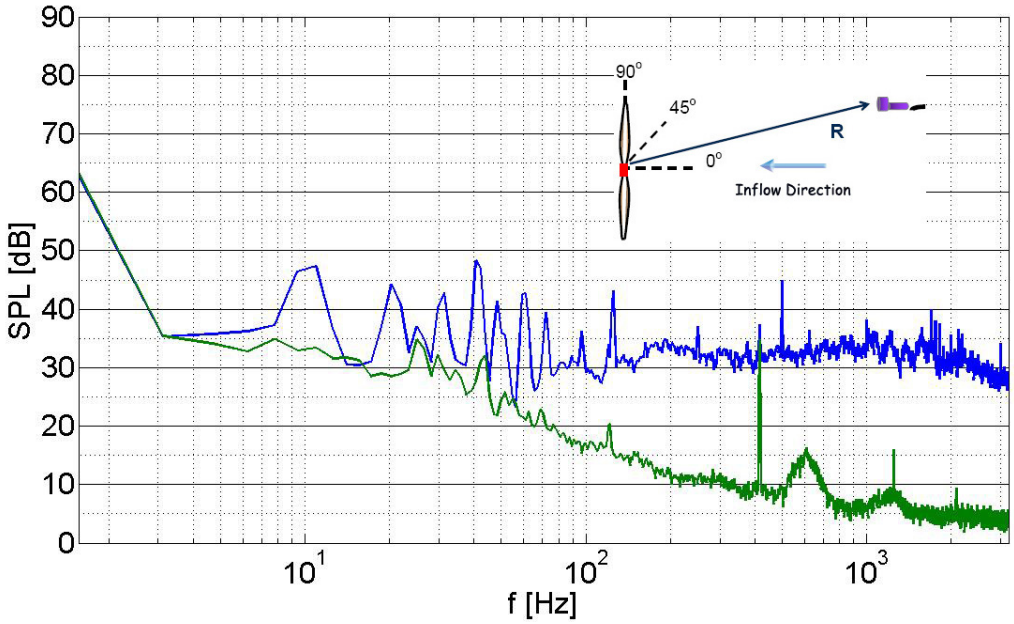

Figure 55: Acoustic spectrum of a 6.5″ diameter unducted rotor at $\alpha = 0^o$. $rpm = 7500$, $R/D = 15$, $n_B = 4$, $\Delta f = 1.5$ Hz.

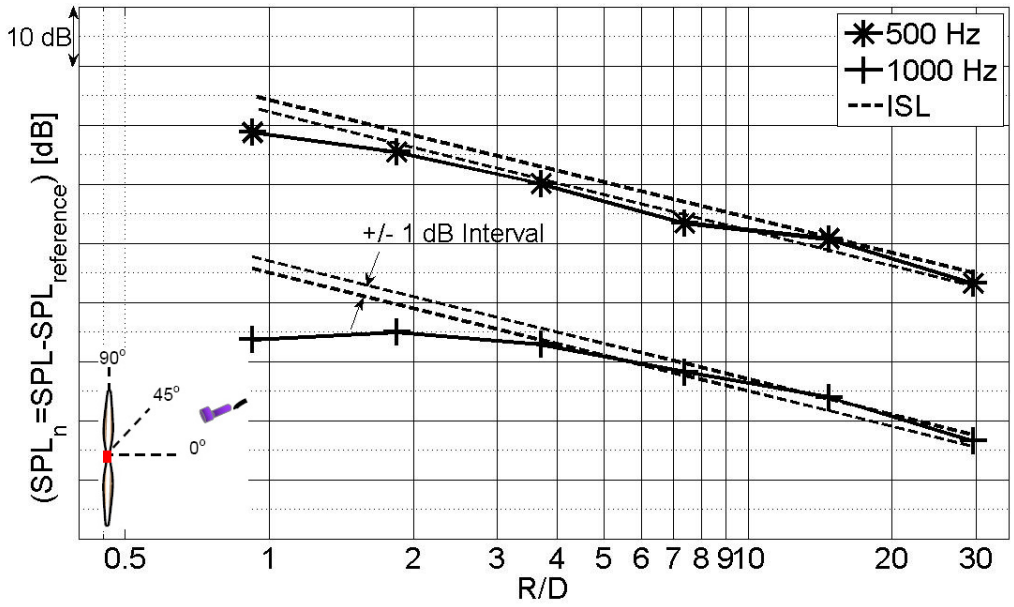

Figure 56: Comparison of measurement data with ISL for open rotor. $D = 6.5''$, $\alpha = 90^o$

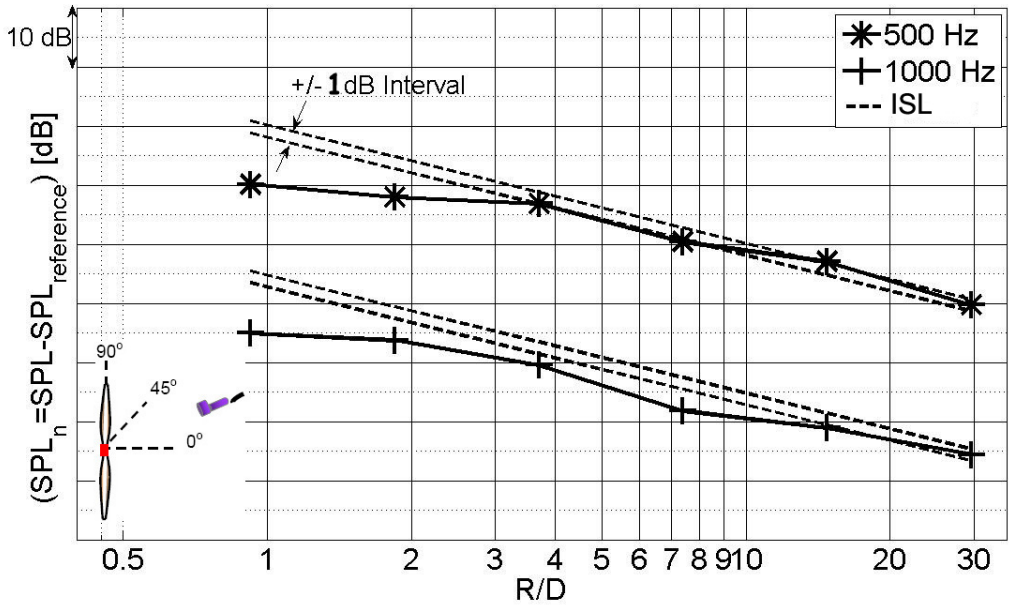

Figure 57: Comparison of measurement data with ISL for open rotor. $D = 6.5''$, $\alpha = 45^o$

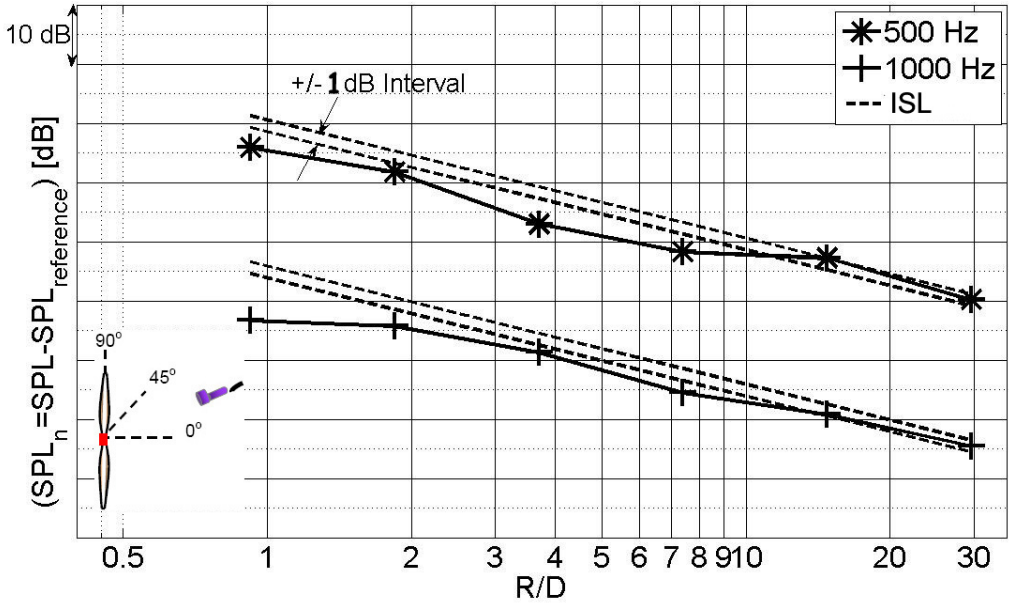

Figure 58: Comparison of measurement data with ISL for open rotor. $D = 6.5''$, $\alpha = 0^o$

Because the peaks over 1000 Hz were not enough higher than the broadband noise, it was not possible to analyze high frequencies with the 6.5″ diameter rotor. To analyze higher fequencies, the 13″ diameter rotor was ran at 3750 rpm angular speed and the data was taken in the rotor disk plane. Figure 59(a) shows the data for low frequency, i.e. frequencies below 1000 Hz, results and Figure 59(b) shows the data for high frequency results. Similar analysis is performed in Figures 59(a) and 59(b) at 45^o, and in Figure 61 at 0^o. The peaks that were not at least 10 dB higher than the broadband level in the spectra were not included in the result. For this reason data at some frequencies don't appear at every angle. It is observed that, at frequencies higher that 1000 Hz the experiments get somewhat closer to the ISL interval. However, in general, it is concluded that the R/D ratio for the geometric farfield is between 8 and 10.

Note that in this case, data was acquired only at $\alpha = 0^o$, 45^o, and 90^o in the forward quadrant. Since no data was acquired in the aft quadrants, further work is needed to draw firm conclusions as to the farthest microphone distance at which the propeller can be treated as a point source at microphone locations in the aft quadrants both for the ducted and unducted configurations.

5.2 Ducted Rotor Experiments

The unducted setup was not appropriate for adding a duct around the rotor. In addition, because the rotor was so close to the rest of the structure, it was suspected that the noise due to the interaction of rotor inflow with the structure would interfere with the rotor noise itself. For these reasons, a new setup, described in Section 4.1.1, was built to run the ducted rotor tests. The rotor was run at 5700 rpm and 6000 rpm angular speeds for each case. Like the unducted case, rotor was run under static conditions and the inflow direction was away from the microphone. Also, a set of data was acquired by changing the direction of the flow induced by the rotor with the rotor angular speed of 6000 rpm. This was done by changing the direction of rotation of the propeller.

The analysis parameters and the error intervals are kept the same as for the unducted case except, that instead of 1.5 Hz used for the unducted propeller the acoustic data is

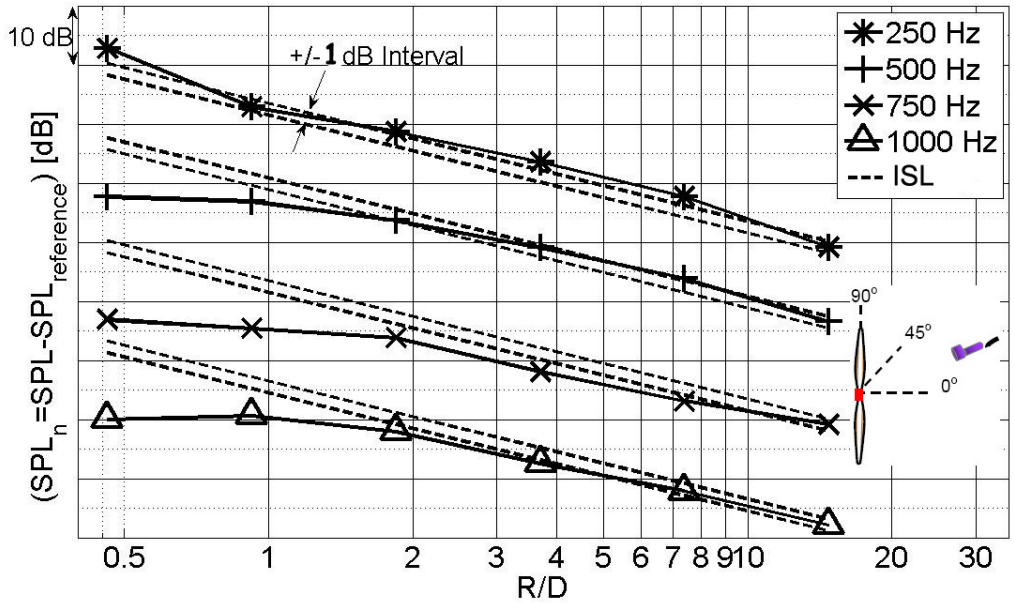

(a)

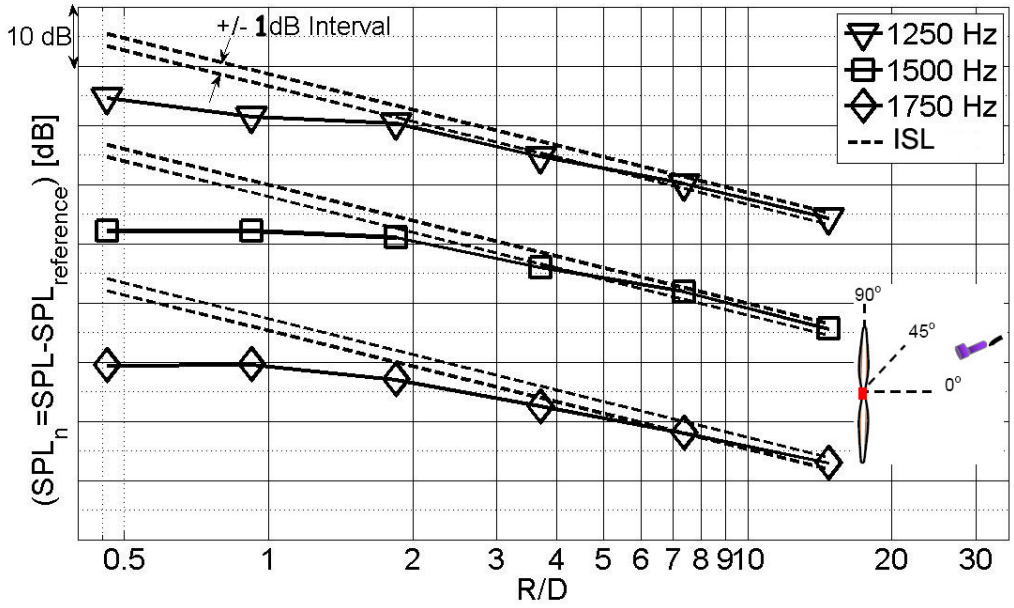

(b)

Figure 59: Comparison of measurement data with ISL for open rotor at (a) low frequencies, (b) high frequencies. $D = 13''$, $\alpha = 90^o$.

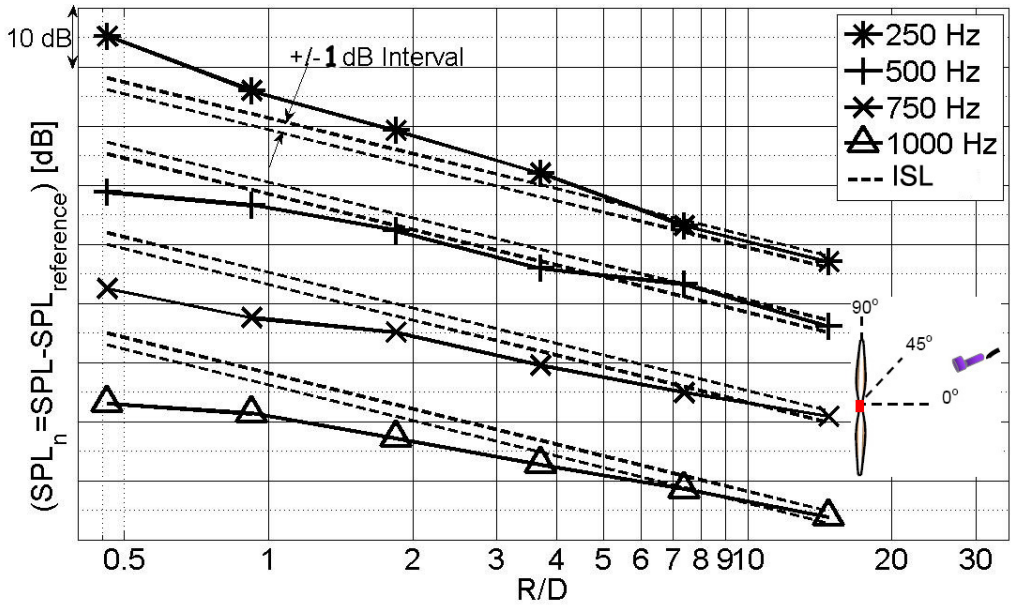

(a)

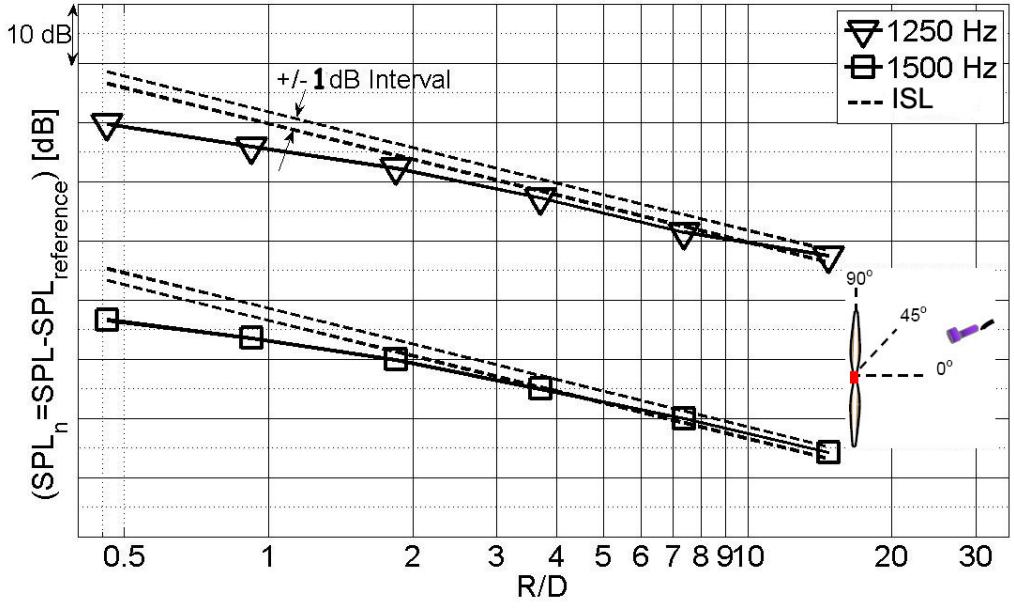

(b)

Figure 60: Comparison of measurement data with ISL for open rotor at (a) low frequencies, (b) high frequencies. $D = 13''$, $\alpha = 45^o$.

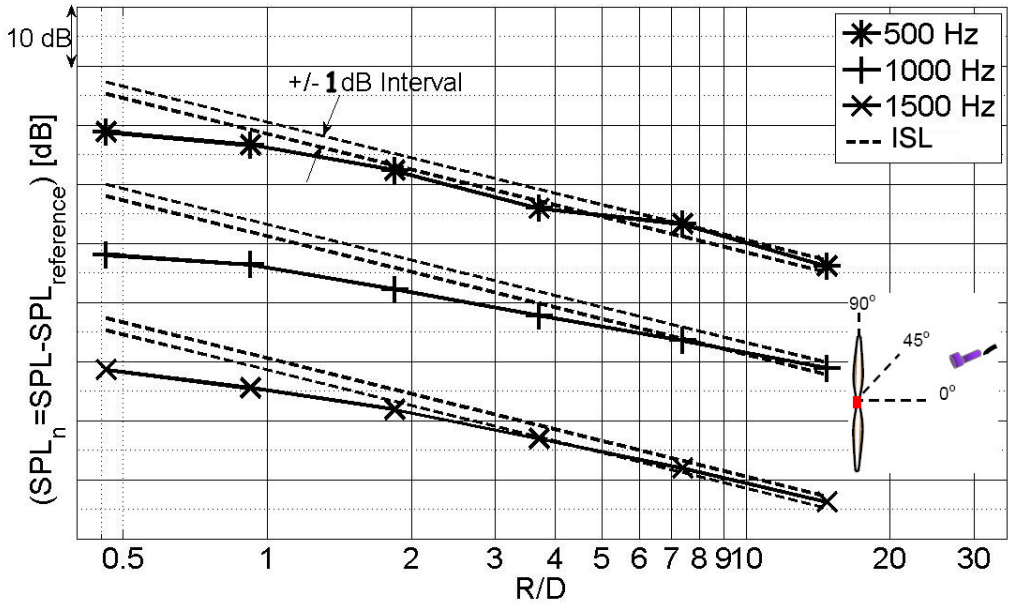

Figure 61: Comparison of measurement data with ISL for open rotor. $D = 13''$, $\alpha = 0^o$

analyzed with a frequency resolution (Δf) of 1 Hz. Typical acoustic spectra of a ducted rotor at 0^o, 30^o, and 90^o are shown in Figures 62, 63, and 64, respectively.

In the frequency spectra, some leakage was observed around the peaks. This was related to the small rpm variations during the experiments due to small voltage variations. So integrated SPL in a ± 5 Hz frequency interval was computed around each peak to examine the data. For instance when 400 Hz is quoted in the following figures it actually refers to the 395 Hz - 405 Hz interval.

Figure 65 shows the geometric farfield results for the first harmonics 333 Hz, 380 Hz and 400 Hz of the $6.5''$ diameter rotor running at 5000, 5700 and 6000 rpm, respectively. The measurement angle is $\alpha = 0^o$ with respect to the fan inlet axis. Based upon these results, it appears that the microphones need to 25 or more duct diameters or farther away from the ducted rotor exit in order for the ISL is obeyed. At $R/D_D = 10$ the deviation from ISL can be as much as 3 dB. Likewise, if the same SPL data is plotted with respect to duct length instead of duct diameter as shown in Figure 66, the results show that R/L should be between 13 and 15 in order for the ISL to be satisfied for a ducted rotor. The difference between Figure 65 and Figure 66 is that in the first case SPL is plotted with respect to

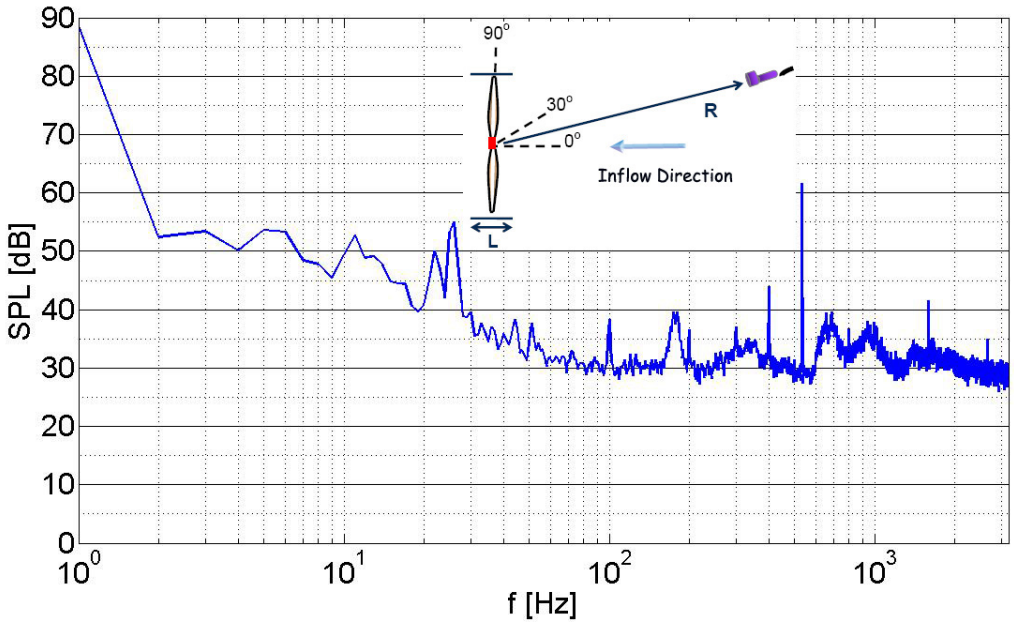

Figure 62: Acoustic spectrum of a ducted rotor at $\alpha = 0^o$. $rpm = 6000$, $D_D = 7''$, $L_D = 12''$, $R/D = 25$.

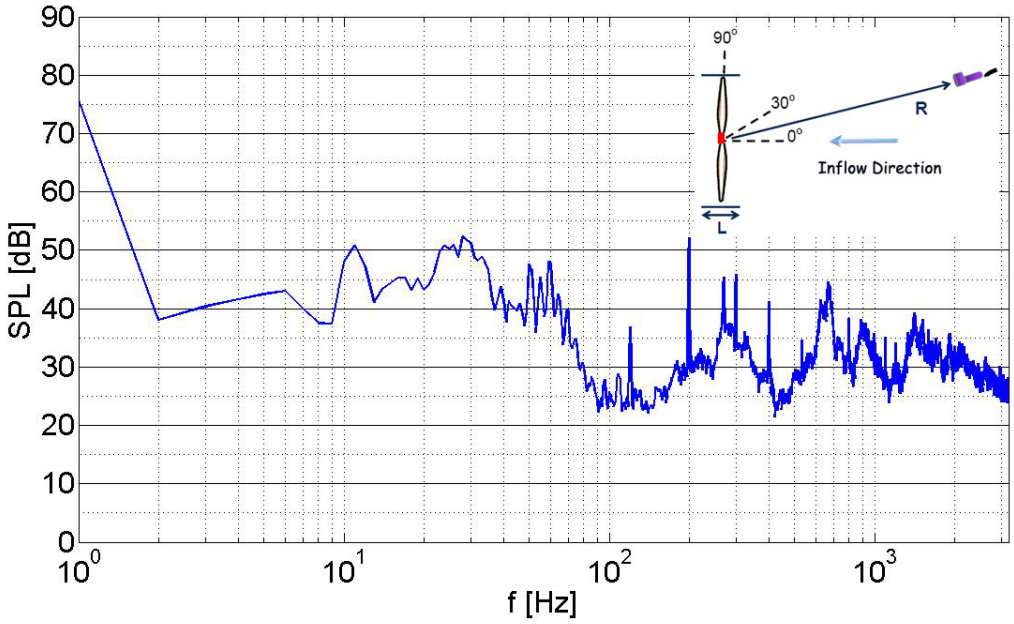

Figure 63: Acoustic spectrum of a ducted rotor at $\alpha = 30^o$. $rpm = 6000$, $D_D = 7''$, $L_D = 12''$, $R/D = 25$.

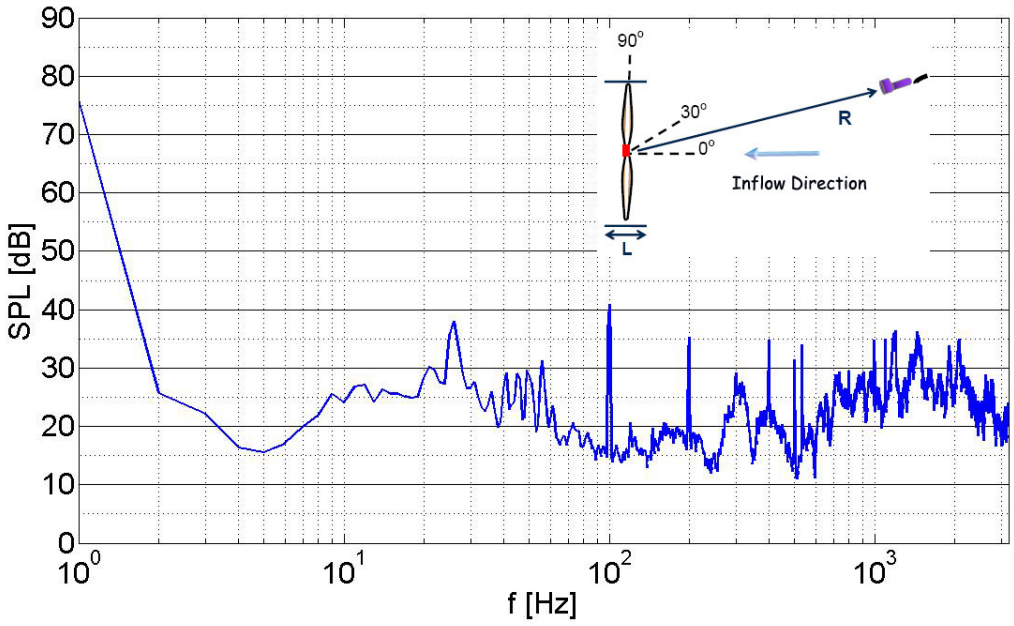

Figure 64: Acoustic spectrum of a ducted rotor at $\alpha = 90^o$. $rpm = 6000$, $D_D = 7''$, $L_D = 12''$, $R/D = 25$.

R/D_D and in the second case it is plotted with respect to R/L.

In Figure 67 the tests performed with duct flow induced by the rotor upwards towards the microphone and downwards away from the microphone are compared for the same test configuration at 6000 rpm angular speed. The results obtained from these two cases are found to be very close to each other. The fact that the distance that the trend starts to deviate from the ISL, which is $R/D_D = 23$, is the same for both cases implies that the rotor noise source appears to be located at from both the inlet and outlet of the duct, as indeed it should.

The tests were performed by covering every item of the setup with foam, including the circular piece used to support the duct and the outer surface of the duct, by default. This default configuration is labeled as 'Configuration 1' in the diagram. Two more cases were investigated for the duct of $L = 12''$ length. In 'Configuration 2', the duct support was not covered with foam and in 'Configuration 3' both duct support and duct outer surface was not covered with foam. The effect of the reflecting surfaces are clearly seen in Figure 68. As the reflecting surface area is increased the experimental results confirm the ISL at farther

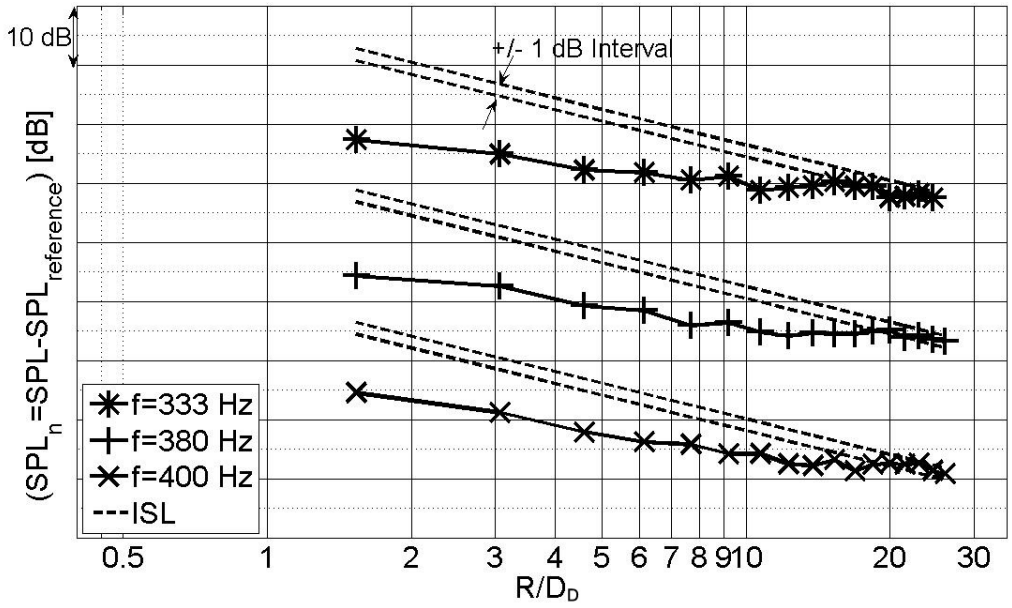

Figure 65: Comparison of measurement data with ISL for ducted rotor. $\alpha = 0^o$, $D = 6.5''$, $D_D = 7.5''$, $L_D = 12''$.

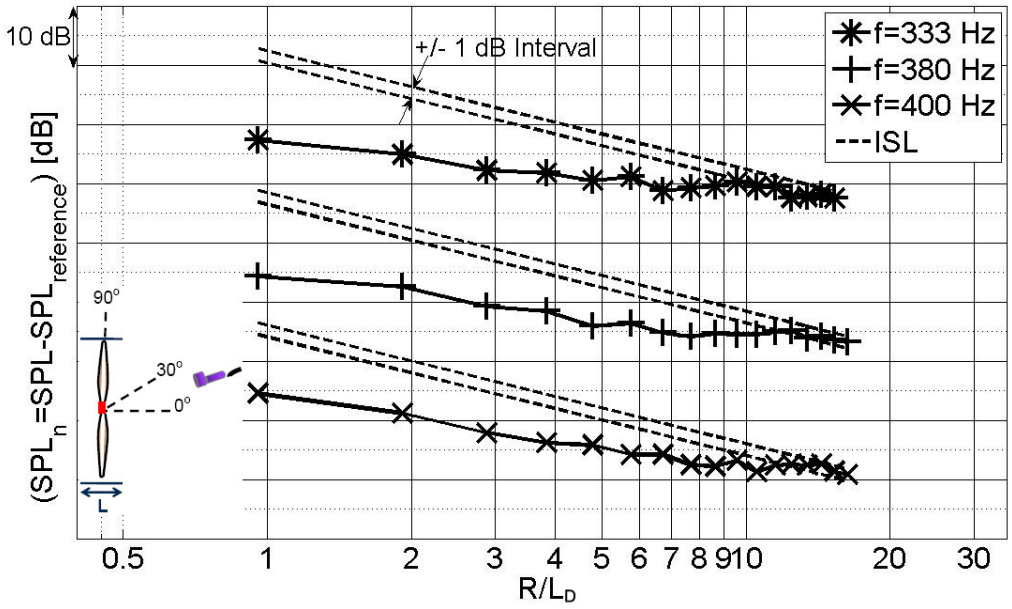

Figure 66: Comparison of measurement data with ISL for ducted rotor. $\alpha = 0^o$, $D = 6.5''$, $D_D = 7.5''$, $L_D = 12''$.

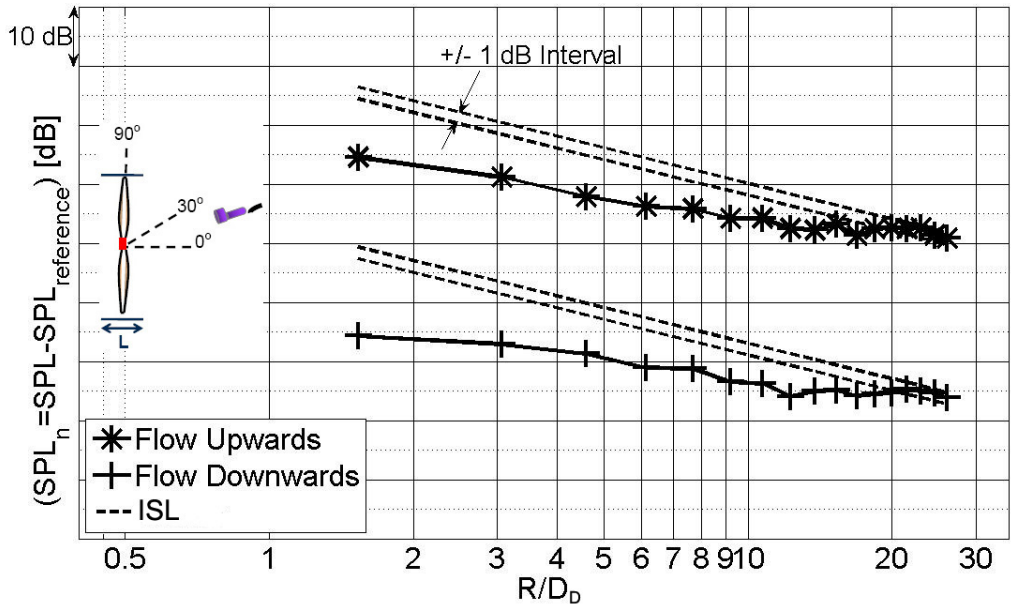

Figure 67: Comparison of measurement data with ISL for ducted rotor. $f = 400$ Hz, $\alpha = 0^o$, $D = 6.5''$, $D_D = 7.5''$, $L_D = 12''$.

distances.

In Figure 69 gives the measurement angle dependence for the BPF of the rotor run at 6000 rpm. The experimental data moves farther away from the ideal range as the measurement angle comes closer to $\alpha = 0^o$. The distance that the ISL is satisfied is R/D=23 for $\alpha = 0^o$ while it drops to $R = 17$ for $\alpha = 30^o$ and for $\alpha = 90^o$ the data almost satisfies the ideal case at all points. If the two endings of the duct are assumed to be two separate noise sources, the distance where these two sources act as one is the farfield of a ducted configuration. When the receiver is at 90^o the two endings, thus the two sources, are at the same distance from the receiver. However, when the receiver is at 0^o one of the sources is a duct length farther away from the receiver than the second. For this reason, the ISL is satisfied at a closer distance as the receiver point moves from 0^o to 90^o.

The results of a set of measurements performed to determine the distance that the rotating machinery systems should satisfy in order to be in the geometric farfield is presented. This, first ever, investigation on geometric farfield of ducted and unducted rotors showed that the unducted rotors meet the geometric farfield condition for R/D greater than about

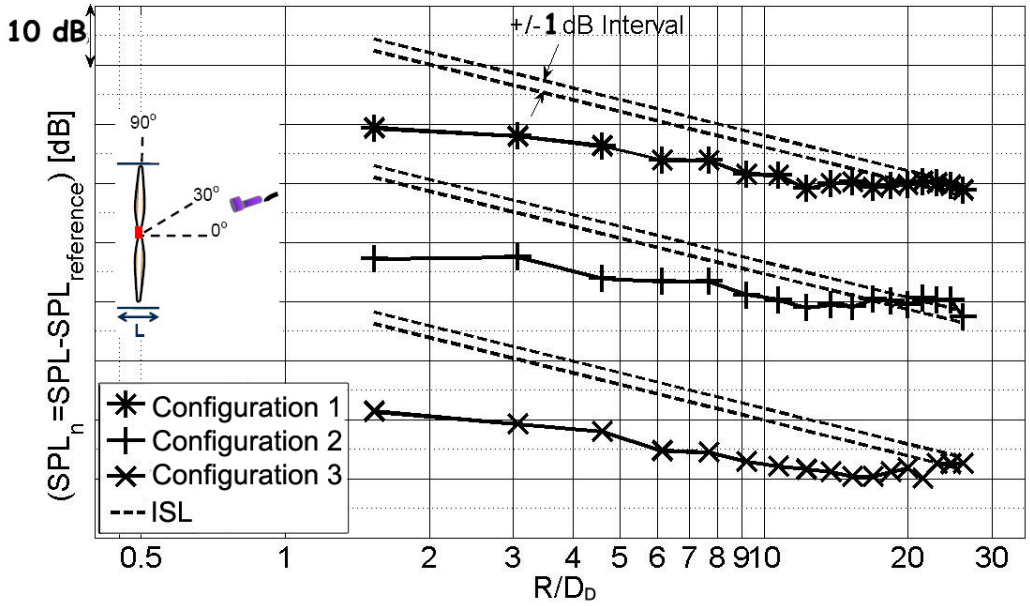

Figure 68: Comparison of measurement data with ISL for ducted rotor. $f = 400$ Hz, $\alpha = 0^o$, $D = 6.5''$, $D_D = 7.5''$, $L_D = 12''$.

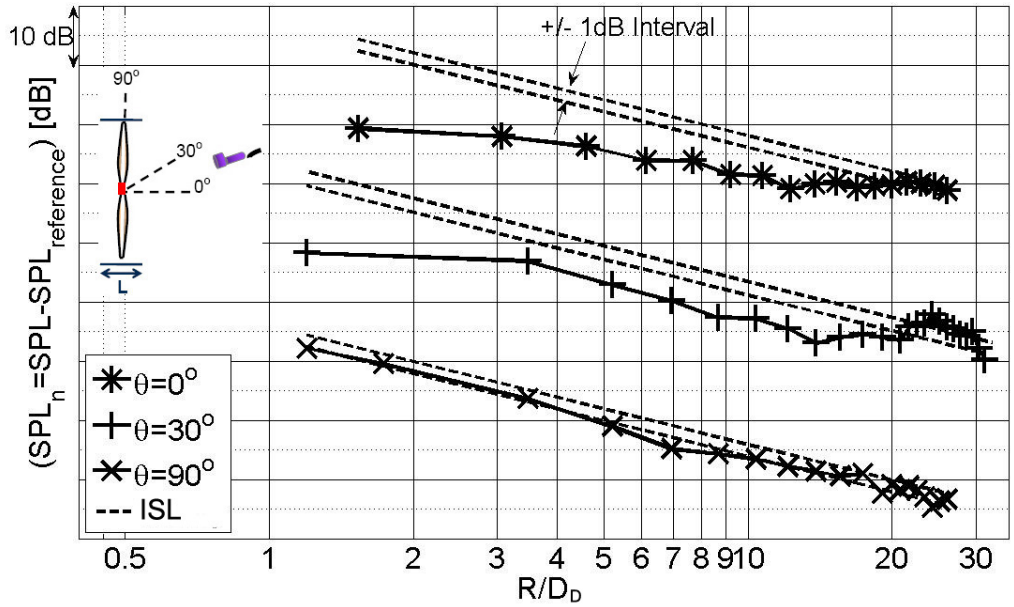

Figure 69: Comparison of measurement data with ISL for ducted rotor. $f = 400$ Hz, $D = 6.5''$, $D_D = 7.5''$, $L_D = 12''$.

10. However, the corresponding R/D for a ducted rotor was found 25 or more. These different findings for the ducted and unducted configurations were attributed to the fact that the largest dimension of the ducted rotor was not the radius but the duct length. Interpreting the results according to the duct length parameter showed that R/L should be 15 or more to satisfy the geometric farfield conditions.

It is concluded that as the frequency increases the geometric farfield is satisfied at closer locations. It is seen that as the measurement angle changes from $\alpha = 0^o$ to $\alpha = 90^o$ the experimental data tends to fit the ISL at smaller distances. This appears to be related to the fact that the noise emanates from both openings of the duct. For both openings to appear as a single point source to a microphone the distance would be expected to be larger when the microphone is located along the flow direction or duct axis compared to when the microphone is located at right angles to this direction. Thus both the duct or rotor diameter and the duct length play an important role in determining the distance where the microphones can be said to be in the geometric farfield [23].

Note that in this case, data was acquired only at $\alpha = 0^o$, 45^o, and 90^o in the forward quadrant and as $\alpha = 180^o$ behind the propeller. No data was acquired between 90^o and 180^o. Further work is needed to draw firm conclusions as to the farthest microphone distance at which the propeller can be treated as a point source at microphone locations in the aft quadrants both for the ducted and unducted configurations.

5.3 Simulation of the Rotor Source by Multiple Point Sources

5.3.1 Theoretical Analysis

The rotor was simulated such that it was made up of point sources collectively emanating sound power whose sum is equal to the sound power emanating from one point source located at the center of the rotor. Let a monopole point sound source of power W shown in Figure 70(a), produce a sound pressure level of SPL_0 at a distance R, associated with the source at the rotor center, corresponding to sound intensity of I_0. The sound intensity at a distance R can be expressed as

$$I_0 = \frac{W_0}{4\pi R^2} \tag{36}$$

It is assumed that the source at the rotor center is equivalent to n sources, each of power W_p as shown in Figure 70(b), on the periphery of the rotor tip. Sijtsma et al of Netherland carried out extensive testing to locate the sources of dominant sound in rotors, in particular helicopters and wind turbines [47]. A phased array located directly under the rotor blades was used. They showed that the dominant noise to be distributed along the tip of the blades. This placement of sources on the tip was based on the observation of dominant rotor sources being at the periphery in this work of Sijtsma. Thus the intensity, from each point on the periphery, at the microphone located at a distance R_p [1] is obtained as follows

$$I_p = \frac{W_p}{4\pi R_p^2} \backsimeq \frac{W_0}{4\pi n R_p^2} \tag{37}$$

The SPL, from a single source at point P, measured at the microphone can be calculated by the following equation

$$\begin{aligned} SPL_p &= 10log_{10}(\frac{I_p}{I_{Ref}}) & (38)\\ &= 10log_{10}(\frac{W_0/4\pi n R_p^2}{I_{Ref}}) & (39) \end{aligned}$$

Thus, n point sources, with equal sound power, were placed on the periphery of the rotor disk at equi-spaced angles to simulate the rotor. So, the sound pressure level for the rotor is the sum of the SPLs obtained from each of the n point sources as follows

$$SPL = \sum_{p=1}^{n} 10log_{10}(\frac{W_0/4\pi n R_p^2}{I_{Ref}}) \tag{40}$$

The derivation above clearly doesn't take the phase shifts between the sources into account. Continuing with the initial idea that the rotor was simulated such that it was made up of point sources collectively emanating sound power whose sum is equal to the sound power emanating from one point source located at the center of the rotor, the SPL

[1] Note that $R_p = R'$ for Figure 70(b).

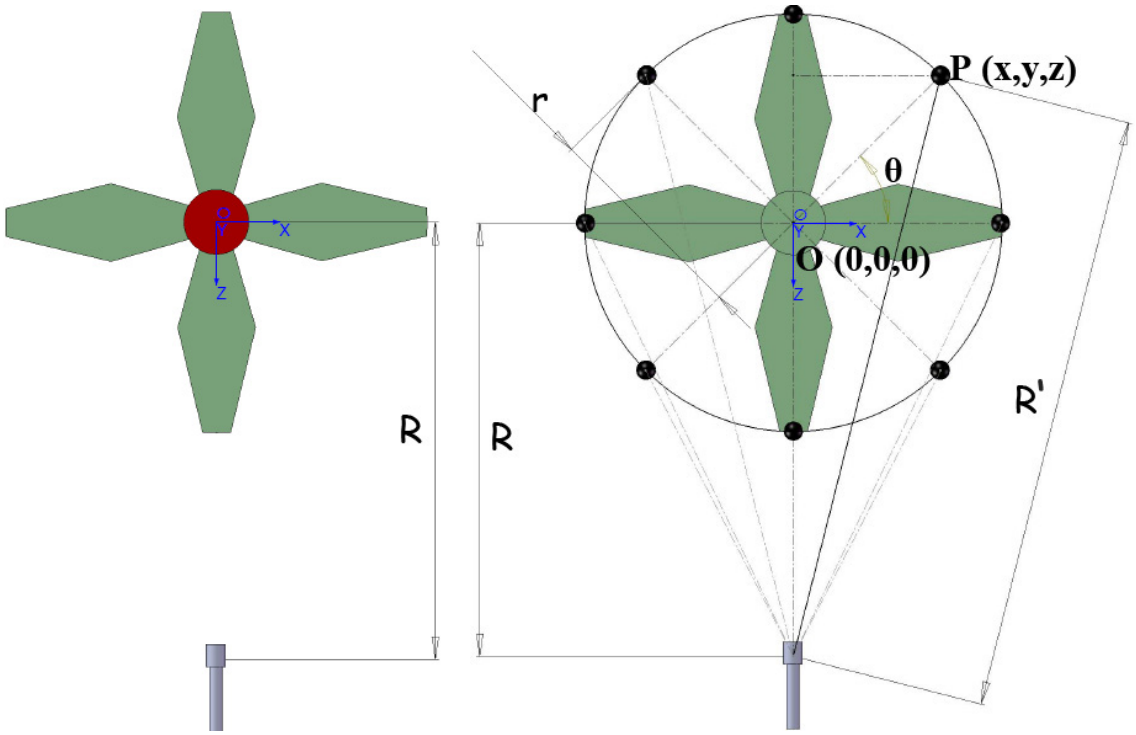

Figure 70: Construction of multi point source approach, (a) single point source at the center, (b) multiple point sources on the periphery.

is reformulated in terms of acoustic pressure to include the phase difference between the sources. In mathematical terms, the acoustic pressure for a spherical wave is expressed as follows

$$p(r,t) = \frac{A}{r} e^{\imath(\omega t - kr)} = P(r) e^{\imath\omega t} \tag{41}$$

The acoustic pressure of the single source that was placed at the center point O, is measured at a distance R as

$$p_0(R,t) = \frac{A_0}{R} e^{\imath(\omega t - kR)} = P(R) e^{\imath\omega t} \tag{42}$$

The acoustic pressure at the microphone, at R' due to sound emanating from of one of the sources on the multi point source circle, is measured at a distance R' as

$$p_p(R',t) = \frac{A_p}{R'} e^{\imath(\omega t - kR')} = P(R') e^{\imath\omega t} \tag{43}$$

From Figure 71, the measurement distance from the j-th point source on the periphery to the i-th microphone is

$$R'_{ji} = \sqrt{(R_i + r sin\alpha_j)^2 + (r cos\alpha_j)^2} \tag{44}$$

Then the acoustic pressure of the j-th source measured at the i-th microphone is

$$p_{ji}(R'_i,t) = \frac{A_{ji}}{R'_{ji}} e^{\imath(\omega t - kR'_{ji} - \phi)} \tag{45}$$

where ϕ is the phase shift between two consecutive sources on the periphery.

So the total pressure at i-th microphone due to n sources placed on the periphery

$$p_i(R',t) = \sum_{j=1}^{n} \frac{A_{ji}}{R'_{ji}} e^{\imath(\omega t - kR'_{ji} - \phi)} \tag{46}$$

$$= e^{\imath\omega t} \sum_{j=1}^{n} \frac{A_{ji}}{R'_{ji}} e^{-\imath(kR'_{ji} + \phi)} \tag{47}$$

Keeping in mind that the time dependent term, $e^{i\omega t}$, is common at all points, the total SPL at the i-th microphone due to n sources placed on the periphery is

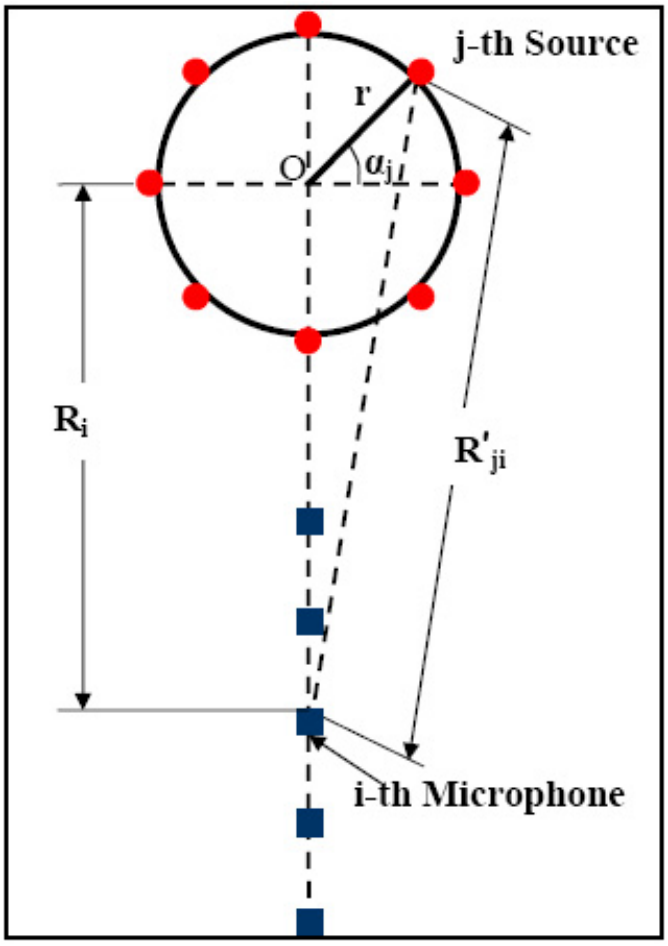

Figure 71: Multi point source construction in detail.

$$SPL_i = 10log_{10}(\frac{p_{i_{rms}}}{p_{Ref}})^2 \quad (48)$$

$$= 10log_{10}(\frac{|\sum_{j=1}^{n} \frac{A_{ji}}{R'_{ji}} e^{-\imath(kR'_{ji}+\phi)}|\sqrt{2}}{P_{Ref}})^2 \quad (49)$$

$$SPL_i = 10log_{10}(\frac{p_{i_{rms}}}{p_{Ref}})^2 = 10log_{10}(\frac{|\sum_{j=1}^{n} \frac{A_{ji}}{R'_{ji}} e^{-\imath(kR'_{ji}+\phi)}|\sqrt{2}}{P_{Ref}})^2 \quad (50)$$

The MATLAB code that was developed to compute the described procedure is given in Appendix B.

5.3.2 Application of Multiple Point Source Simulation

The approach was first applied neglecting the phase relationship using equation (40). The main rotor simulation parameters varied to test the approach were rotor diameter, D, number of sources on the periphery, n, frequency of the harmonic, f. The results for $D = 6.5''$ and $D = 13''$ rotors simulated by $n = 50$ sources at $f = 1000$ Hz are shown in Figure 72. Many such trials showed that the perfect fit to $1/R^2$ line seen in these cases is independent of the rotor simulation parameters, it is always a perfect fit.

Then the approach was recomputed including a phase lag, ϕ, between each source. The results for variable values in Figure 72 were recalculated using equation (50) under the assumption that all the sources are in phase, i.e., $\phi = 0$. The results shown in Figure 73 were similar to those of the case where phase relationship was neglected.

When the phase lag, $\phi = pi/4$, was assumed for $D = 13''$ diameter rotor at $f = 1000$ Hz where number of sources is $n = 50$ the results shown in Figure 74 are obtained. As it is seen the sound pressure levels for the experimental findings and the multiple point source approach match very well. This shows that the deviations from the ISL are closely related to the phase relationship between the sources of rotor noise. Although this was the right combination of rotor parameters (phase shift, number of point sources, and frequency) for the $D = 13''$ diameter rotor, when the rotor size is reduced to half, $D = 6.5''$, no deviations from the $1/R^2$ line are observed as shown in Figure 75(a). Then, again for $D = 6.5''$ rotor the frequency is changed to $f = 500$ Hz as shown in Figure 75(b), calculations show a small

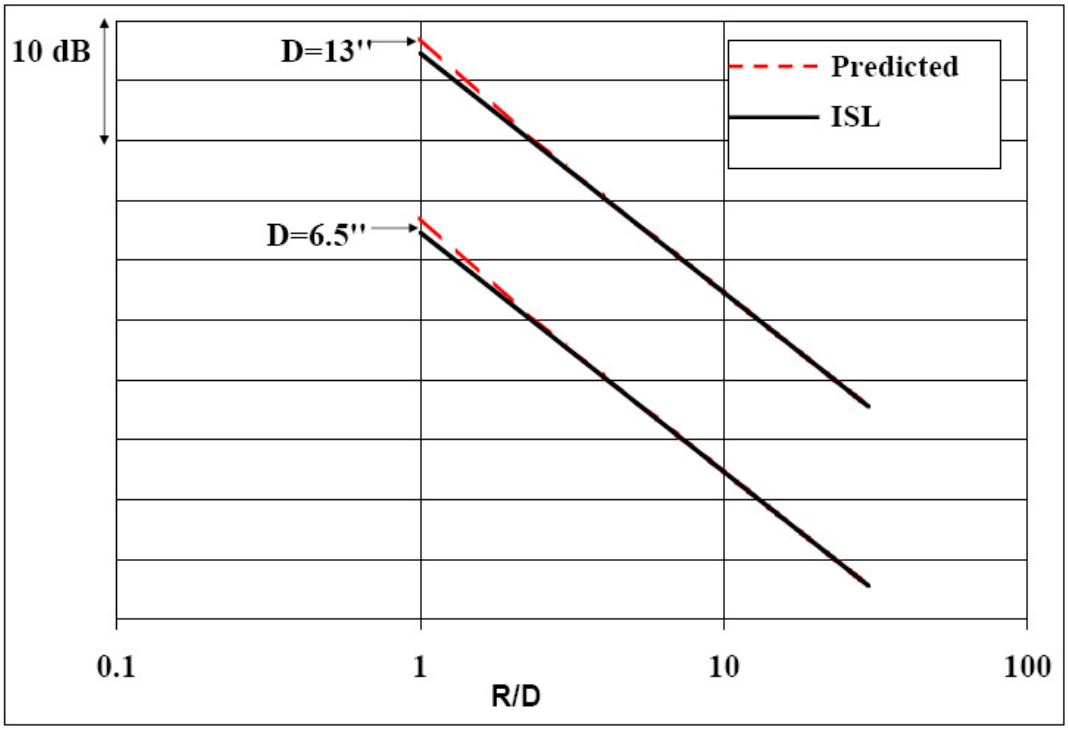

Figure 72: Multi point source simulation neglecting the phase relationship. $n = 50$, $f = 1000$ Hz.

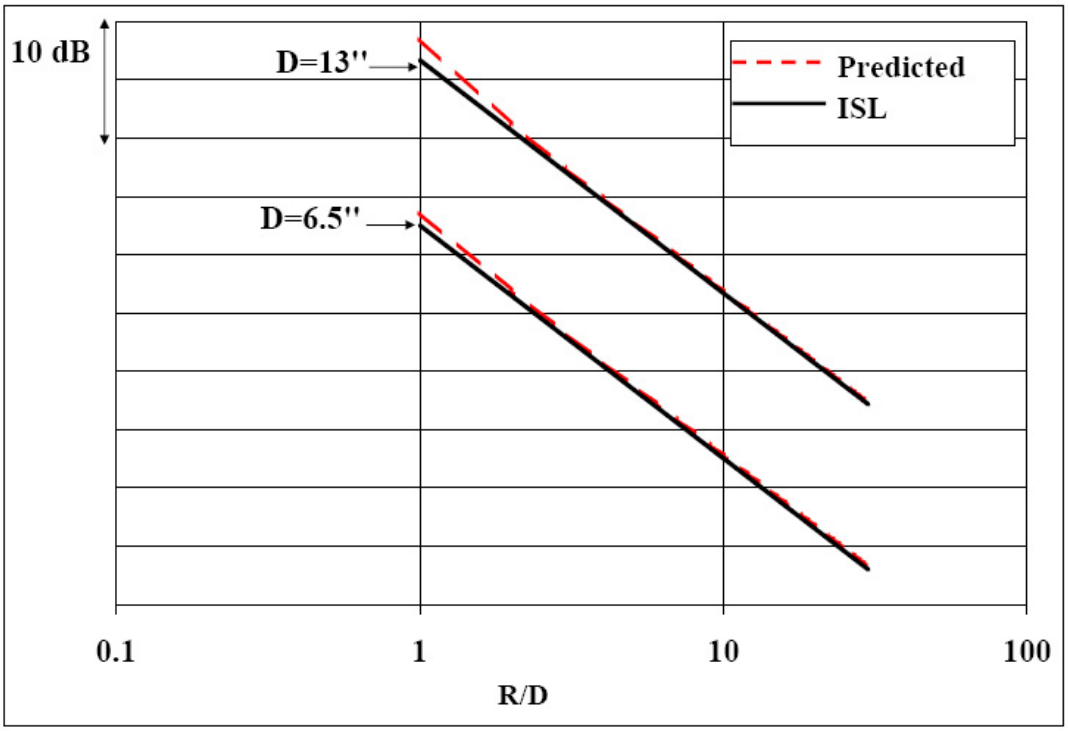

Figure 73: Multi point source simulation assuming all the sources are in phase, $\phi = 0$. $n = 50$, $f = 1000$ Hz.

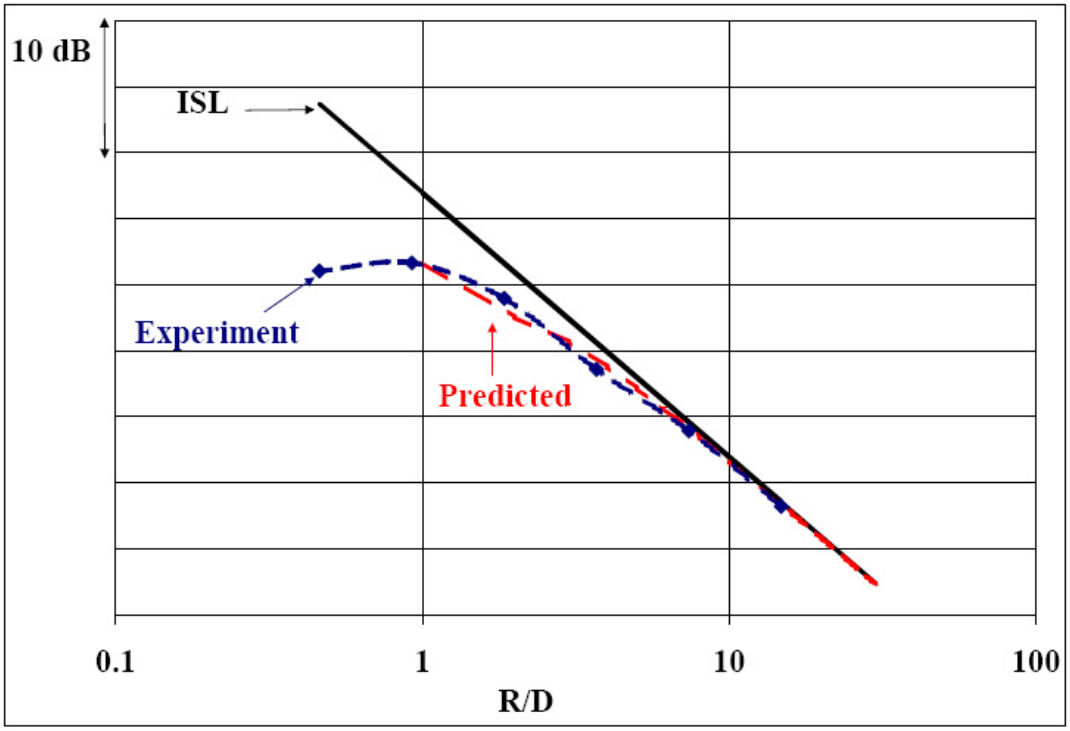

Figure 74: Multi point source simulation compared with experiment. $D = 13''$, $n = 50$, $\phi = \pi/4$, $f = 1000$ Hz.

deviation at about three rotor diameters. But the calculations still does not match the experimental findings. To be able to come to a general conclusion for the right combination of rotor parameters, further investigation is needed on the phase relationship for rotor noise sources which is beyond the scope of this thesis.

The calculations were performed for several other combinations of the rotor simulation parameters. Through the experimental findings it was concluded, in Section 5.1 that for a rotor, ISL was satisfied at distances 8-10 diameters. By trial-error an appropriate combination that gives the same results for $D = 6.5''$ diameter rotor as in experiments is obtained. The findings for $\phi = \pi/8$ phase shift, $n = 50$ sources are given in Figure 76(a) and 76(b), at frequencies, 1000 Hz and 500 Hz, respectively. Although the necessary distance match in order for the ISL to be applicable is found for these frequencies, the near field sound pressure levels does not match. While the calculations show an increase of SPL in the near field, the experiments show a decrease. This inconsistency was also observed during the experiments. The SPL does not always get lower then the ISL prediction in the near field

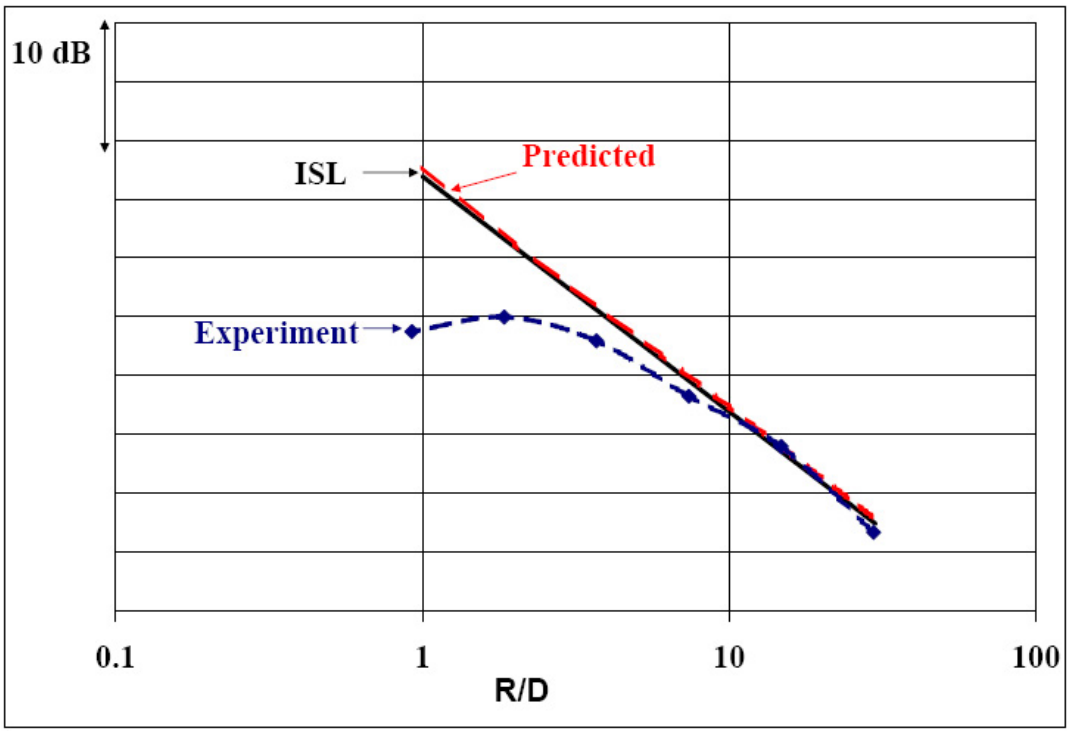

(a)

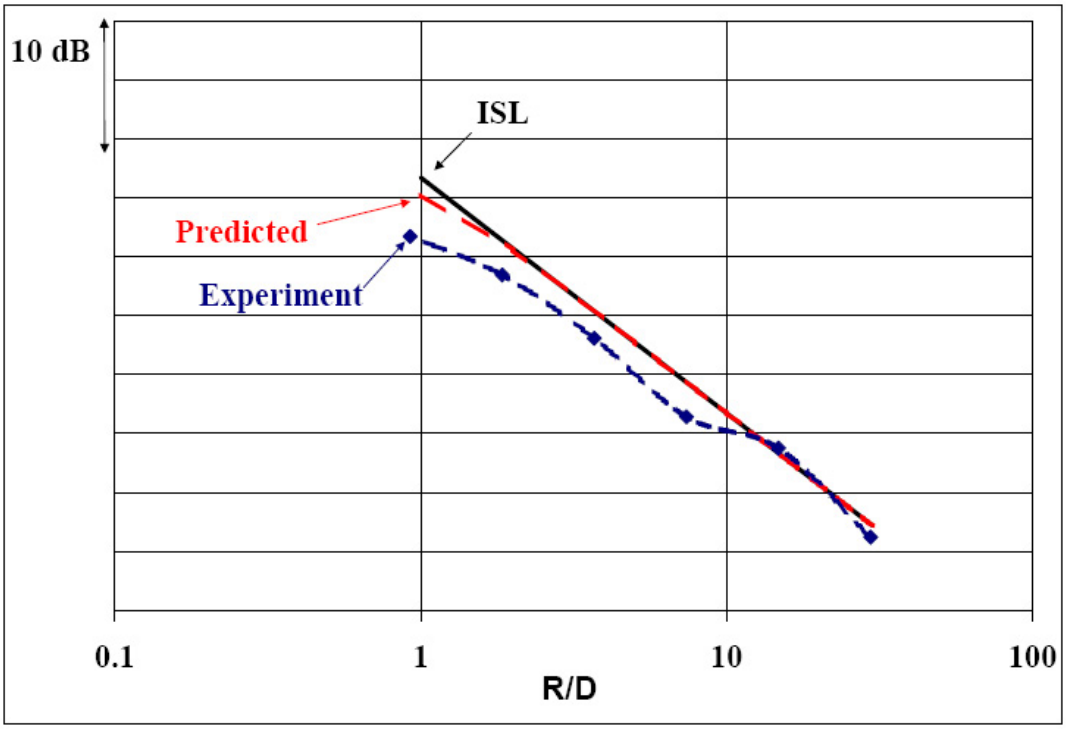

(b)

Figure 75: Multi point source simulation compared with experiment. $D = 6.5''$, $n = 50$, $\phi = \pi/4$, (a) $f = 1000$ Hz; (b) $f = 500$ Hz.

but shows an increase in some situations. So, it is concluded that this kind of behavior is due to the phase relationship.

In general, it is concluded that the phase lag between the sources on a rotor is the main reason for the deviations from the ISL in the near field. The phase lag between the sources clearly have a relationship with the rotor diameter and the frequency, and also the number of sources when the rotor is simulated by point sources. Since the harmonic noise and BPF and its harmonics are the focus of this work, the frequencies investigated depend on the rotor rpm and number of blades. So these parameters must also be effective on the phase lag.

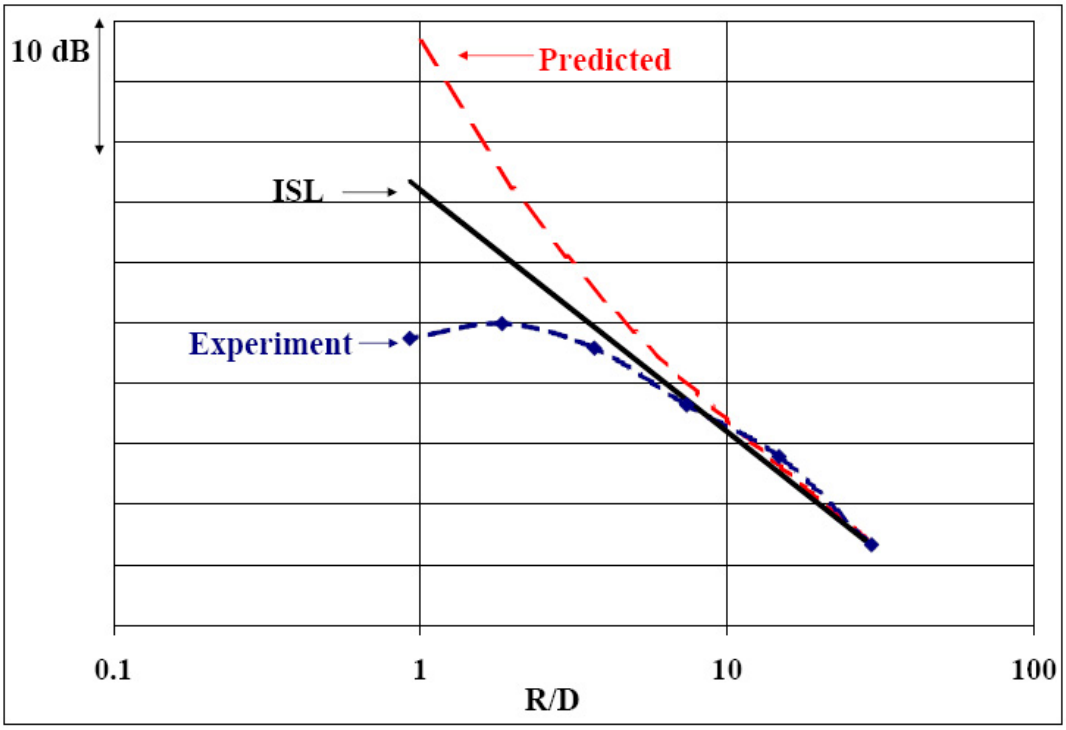

(a)

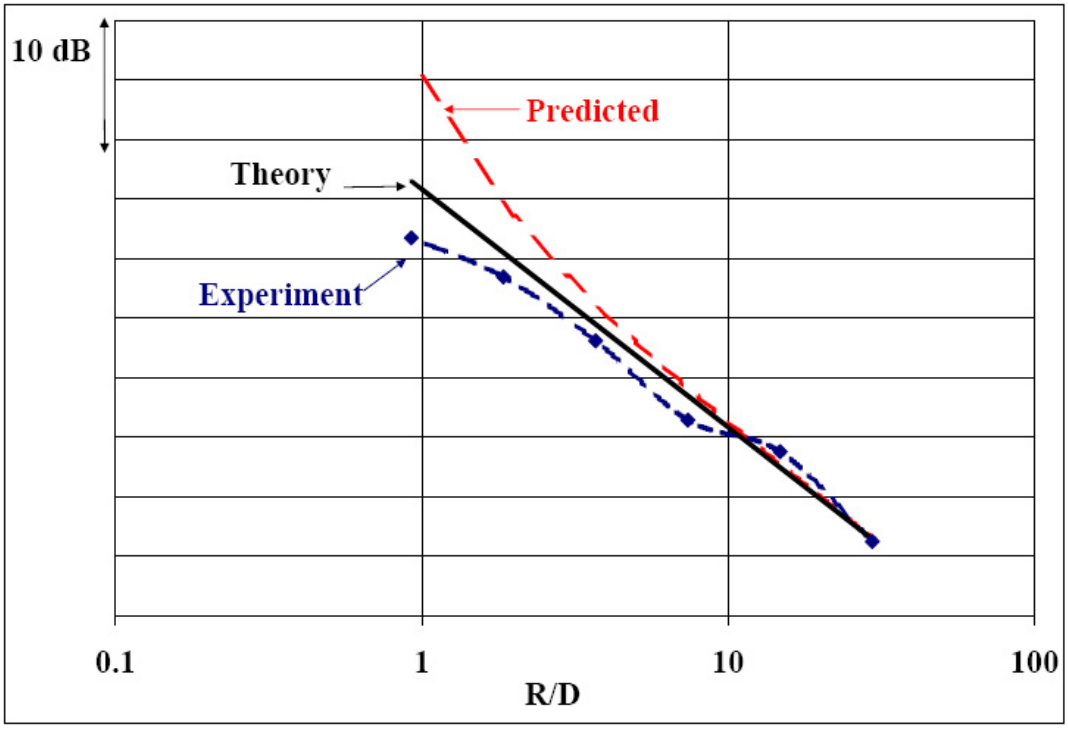

(b)

Figure 76: Multi point source simulation compared with experiment. $D = 6.5''$, $n = 50$, $\phi = \pi/8$, (a) $f = 1000$ Hz; (b) $f = 500$ Hz.

CHAPTER VI

VALIDITY OF POINT SOURCE ASSUMPTION FOR ROTOR NOISE WITH SHIELDING

6.1 Point Source Experiments

The experimental findings presented in this section were obtained from the tests performed on the configuration illustrated earlier in Figure 39, Figure 43. Detailed data from six microphones is presented here. The microphone array traversed parallel to the x-axis (see Figure 38). The data was examined as a function of θ for various ϕ at different frequencies [48].

For all results presented in this work, whenever the data was acquired on different days or for different configurations (e.g. with and without shield), the reference microphone data allowed the authors to correct for any variation in the source power from one test to another. If the SPL of the reference microphone remained the same from one test to another, no correction was needed. It is for this reason the shielded levels show a subscript 'n' as in 'SPL_n' to indicate that the data is normalized. Normalized data at a microphone is thus presented as

$$SPL_n = [SPL - SPL_{ReferenceMicrophone}] \tag{51}$$

6.1.1 Unshielded Experiments

First, the point source experiments were performed without shielding, on the same configuration at two separate times separated by almost one month. Although the same coordinate system that was used for shielded configurations still applies, the origin of the coordinate system is the point source in this case. The data from the two separate tests were compared with each other to check the repeatability of the experiments. Selected results for 1200 Hz and 400 Hz are shown for $z = 90''$ in Figure 77 and Figure 78, respectively. Good matches produced between two sets of data proves that the point source tests were repeatable.

This point source configuration was also checked if the ISL applies. The test chamber was

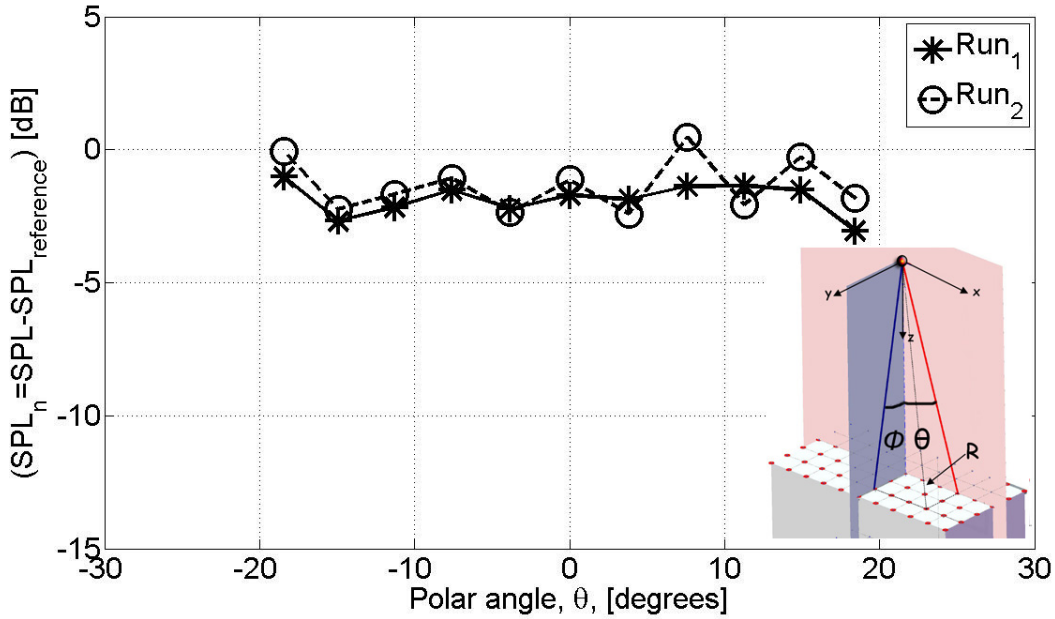

Figure 77: Comparison of two test runs of unshielded point source experiments as a function of polar angle, θ. $f = 1200$ Hz, $\phi = 11.3$, $kz = 49.5$.

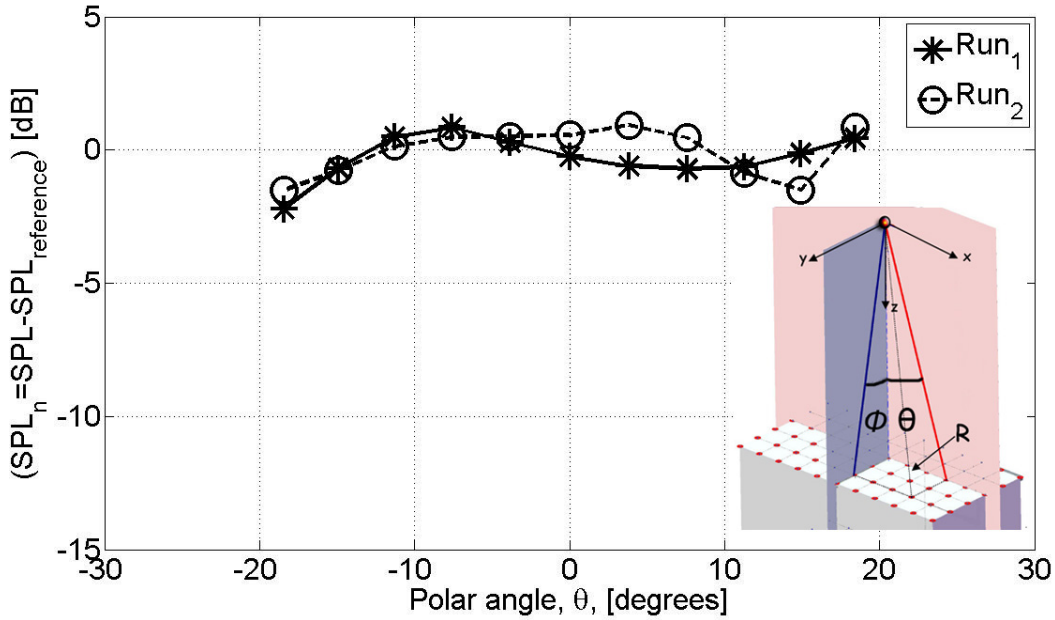

Figure 78: Comparison of two test runs of unshielded point source experiments as a function of polar angle, θ. $f = 400$ Hz, $\phi = 11.3$, $kz = 17.1$.

found to be anechoic for frequencies above 200 Hz by chamber calibration tests. The results of these tests were given in Figure 21(b) in Chapter 4. The calibration tests were performed while the chamber was completely empty and only one microphone was used. However, the present tests were performed by an array of six microphones placed $6''$ apart from one other, which could have caused errors due to the interferences between the microphones. In addition to this, some structures that could cause extra reflections, like the microphone and source supports, had to be placed inside the chamber. Due to these additional effects it was not possible to obtain the same results as the calibration tests. It is believed that for these reasons, the data may deviate by as much as ± 2 dB as the microphone array is traversed. This may be the reason for the data to display small peaks and valleys in Figure 77 and in many plots appear in this chapter. Unfortunately this was unavoidable, short of using a single microphone instead of an array. The schedule of the facility dictated the use of the array. With this reservation, ISL was observed within ± 2 dB for the point monopole source without the shield in place but in the presence of the microphone array and its traversing support.

Typical results are shown from Figure 79 to Figure 81. In each figure data for two separate tests, performed on different days is shown. Data for $f = 1200$ Hz is shown for 0^o in Figure 79 and for 10^o in Figure 80. Data shown in Figure 81 were obtained when the microphone traverse line was moved $18''$ above that used for data shown in Figures 79 and 80. The measurement plane and traverse line is shown in the inset in each figure. There were a few outliers (out of ± 2 dB range) in the data, shown by circled symbols in Figures 79 - 81. These data were not considered in driving any conclusions from the present investigation.

6.1.2 Rectangular Shield Experiments

The findings for a point source shielded by several sizes of rectangular shields are presented in this section. The tonal noise is investigated. It was mentioned in Chapter 4 that the measurements were performed while the source was fixed and the shield was moved with respect to it. During the experiments it was more convenient to move the shield rather

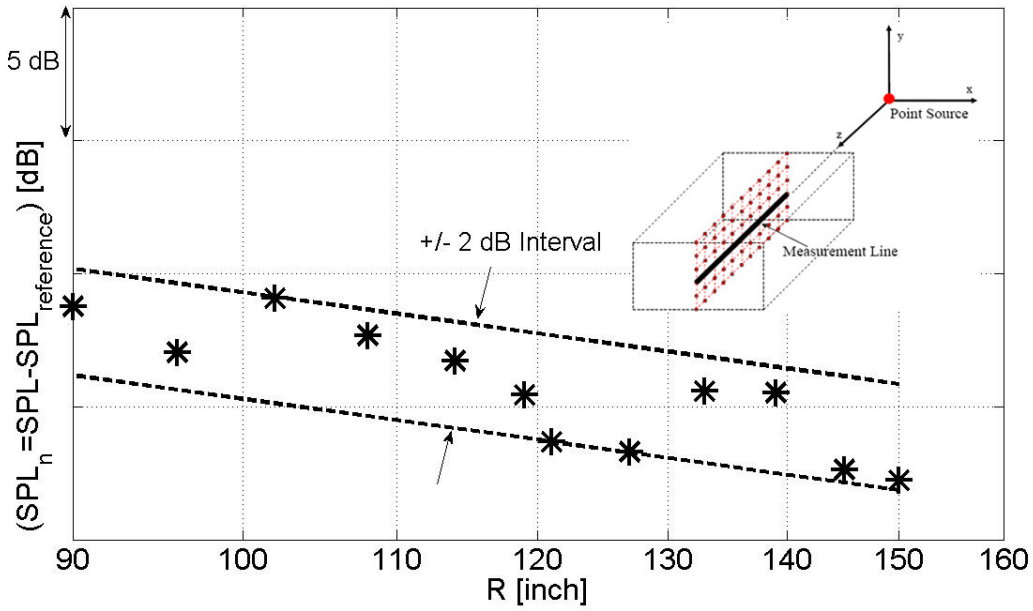

(a)

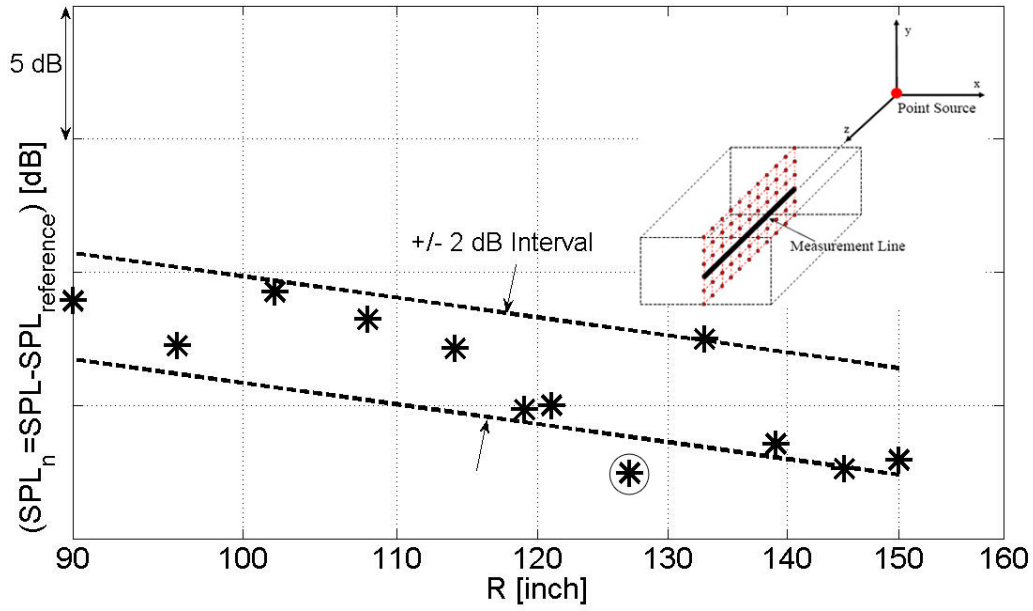

(b)

Figure 79: ISL match for point source in ±2 dB error interval. $f = 1200$ Hz, $\theta = 0^o$, $\phi = 0^o$, (a) first run, (b) second run.

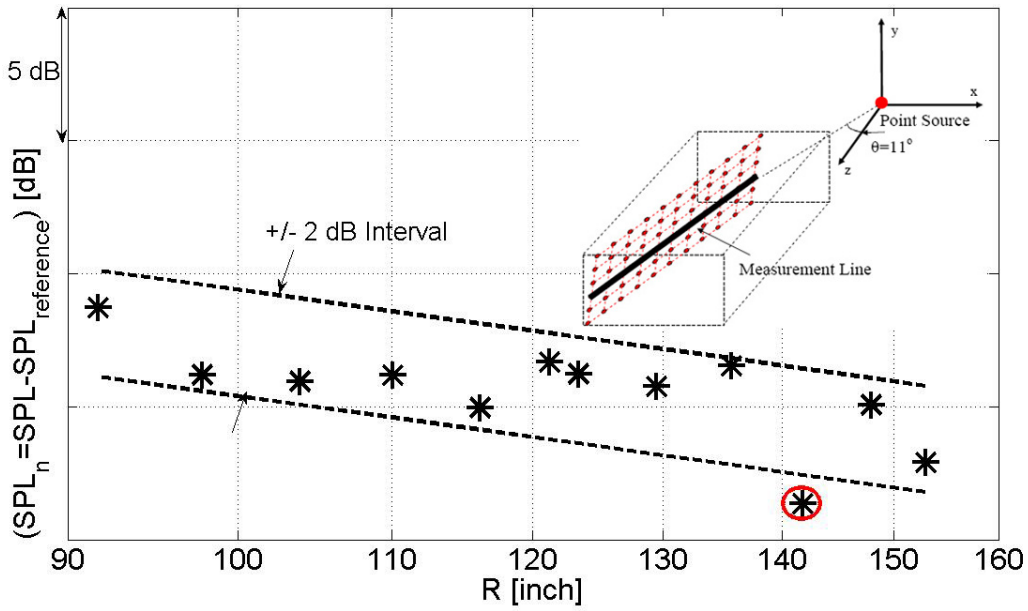

(a)

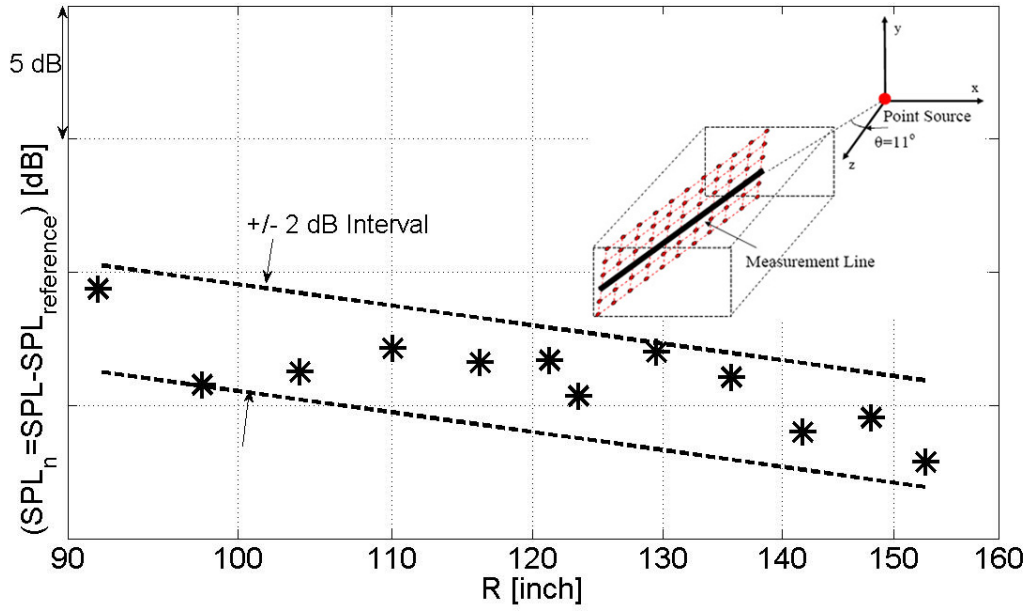

(b)

Figure 80: ISL match for point source in ±2 dB error interval. $f = 1200$ Hz, $\theta = 10^o$, $\phi = 0^o$, (a) first run, (b) second run.

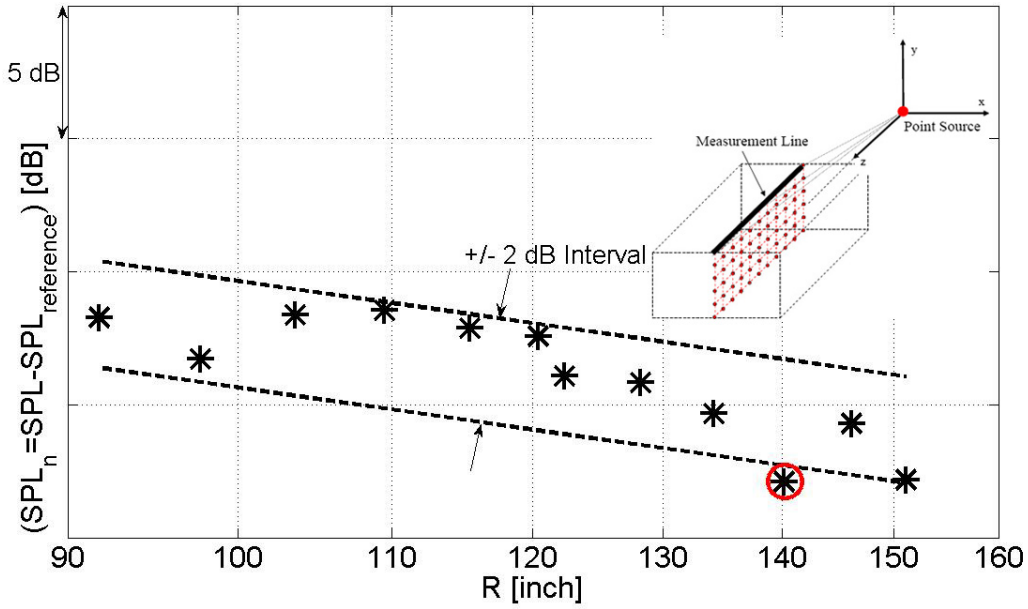

(a)

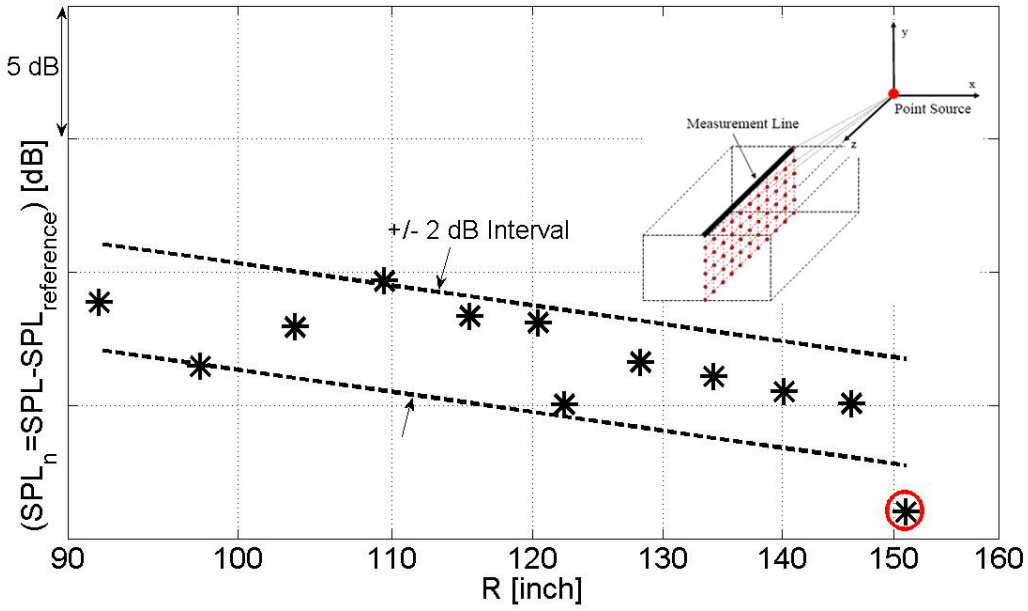

(b)

Figure 81: ISL match for point source in ±2 dB error interval. $f = 1200$ Hz, $\theta = 0^o$, ϕ changes as z changes while y is fixed, (a) first run, (b) second run.

than the source since the source was attached to a heavy structure that was difficult to relocate. On the other hand, the mid point of the shield was chosen as the center of the general coordinate system used in this work, i.e., the analysis of the experimental data was made as if the shield was fixed and the source was moved with respect to it. This different choice of coordinate systems between the experiments and the data analysis is the reason for ϕ to change when the source location is changed even if the data is acquired at the same receiver point. The experimental findings are compared with the predictions described in Chapter 3. The labels 'Experiment' and 'Theory' refer to measured and calculated data corresponding to cases explained by the illustrations and descriptions.

It was mentioned in Chapter 3 that shielding is presented as the difference between shielded data and unshielded data as follows

$$\Delta SPL_n = [SPL_{n(withShield)} - SPL_{n(withoutShield)}] \tag{52}$$

So, as ΔSPL_n becomes more negative more shielding is obtained.

6.1.2.1 Effect of Source Location

The effect of point source location is investigated by comparing the experimental results with the predictions. Subscripts S_1 and S_2 in labels 'Experiment' and 'Theory' refer to measured and calculated data corresponding to sources S_1 and S_2 shown above the shield on the illustrations in each figure. The theory is compared with experimental data for source S_1 in sub-figure (a) and S_2 in sub-figure (b). The information for both S_1 and S_2 is plotted together in sub-figure (c).

The source location was, first, changed on z-axis, i.e., source was moved up and down. When the source (S_1) was placed at $z = -W/2$, the shielding pattern as a function of polar angle, θ, was obtained as in Figure 82(a) for $f = 1200$ Hz. When the source(S_2) was moved farther from the shield, to $z = -0.9W$, a different shielding pattern was obtained as shown in Figure 82(b). By moving the source higher, the azimuth angle corresponding to the fixed microphone array changed from $\phi = 12.2^o$ to $\phi = 13^o$. In Figure 82(c), the two cases are compared. The results presented in Figure 82 are for a value of $\phi(\approx 13^o)$. Similar

results were obtained for a smaller $\phi(\approx 8.5^o)$ as shown in Figure 83. It seems that within the measurement error of ± 2 dB, the measured data agrees well with the shielding levels predicted by using the theory described in Chapter 3. It is seen that moving the source towards the center increases the shielding somewhat.

Effect of source distance from the shield along z-axis was also investigated at 400 Hz as shown in Figures 84 and 85 for the large and small values of ϕ ($\phi \approx 13^o$ in Figures 84, and $\phi \approx 8.5^o$ in Figure 85). It is found that the shielding amount are not as large at lower frequencies although the predictions and measurements match well directly under the shield ($\theta = 0^o$). It was seen that at 400 Hz, moving the source far from the shield, from S_1 to S_2, makes some difference but not as much as that at the higher frequency of 1200 Hz as it was seen in Figures 82 and 83.

Figures 86 and 87 show the effect of lateral movement of the point source, i.e. source was moved parallel to the shield, at 1200 Hz. It was seen that moving the source laterally parallel to the major axis y reduces the shielding in the range of interest. So, more shielding is obtained if the source is placed closer to the center point . This comparison was repeated at 400 Hz as shown in Figures 88 and 89. It was, again, seen that at 400 Hz little shielding was obtained irrespective of the lateral position of the source. Thus, both measurements and predictions indicate that one can maximize shielding by due positioning of the source above the shield at higher frequencies.

In Figures 90 and 91 the source location was moved sideways parallel to the minor axis of the rectangular shield (source was moved to the left, parallel to the shield). It was seen that moving the source to the sideways shifts the shielding pattern sideways as indicated by the shift of the peaks and valleys in the direction of shifting the source to the left in Figures 90 and 91.

It was also noticed that the accuracy of the match of the experimental data with the theory was not excellent. Most of the experimental data appear to have serious dips or indications thereof on the two ends, indicating destructive interference. Subsequent analysis indicates that the location and magnitude of these dips is quite sensitive to the precision with which the sources are placed with respect to the shield surface. Small rotations of the

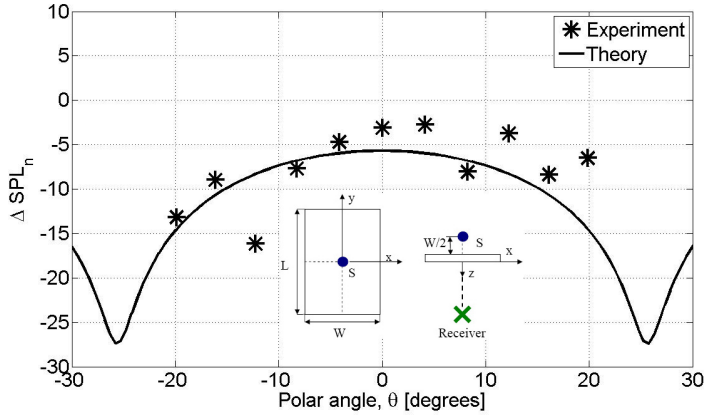

(a)

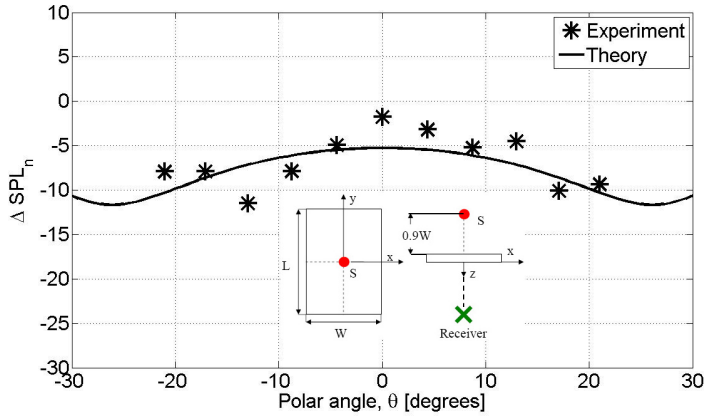

(b)

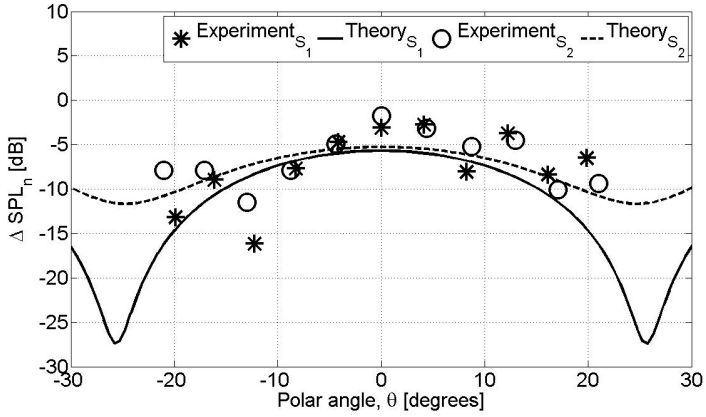

(c)

Figure 82: Effect of source location for a point source along z direction, as a function of polar angle, θ. $f = 1200$ Hz, $kW = 7.15$, $L/W = 1.8$, (a) S_1 with $\phi_1 = 12.2^o$ and $kz = 45.7$, (b) S_2 with $\phi_2 = 13^o$ and $kz = 42.9$, (c) comparison of S_1 and S_2.

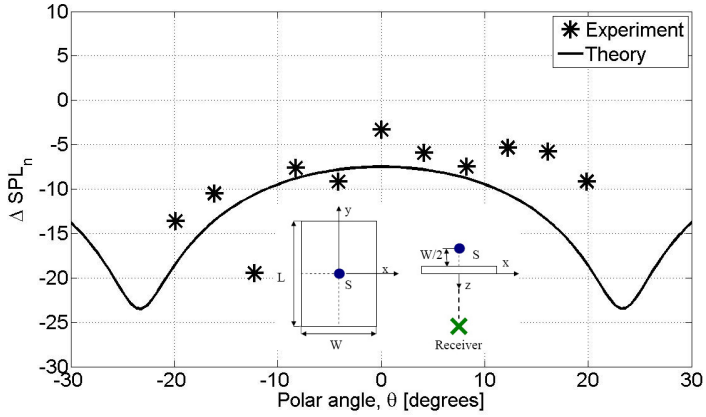

(a)

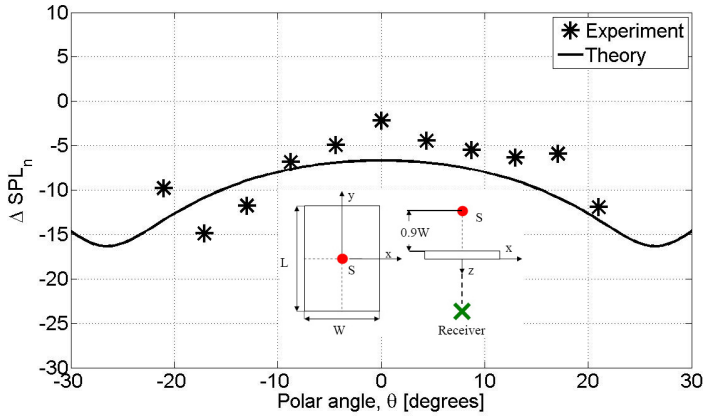

(b)

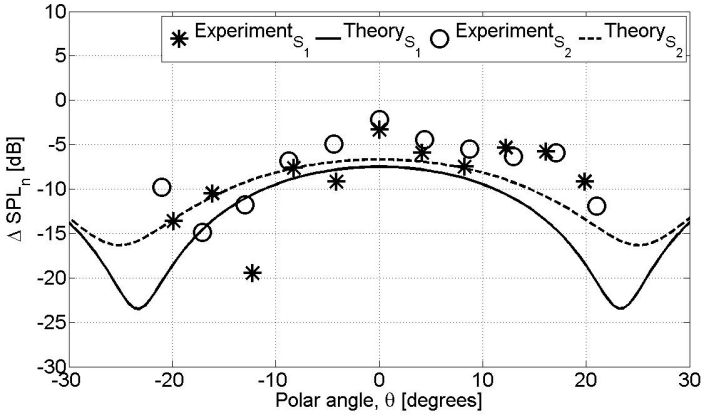

(c)

Figure 83: Effect of source location for a point source along z direction, as a function of polar angle, θ. $f = 1200$ Hz, $kW = 7.15$, $L/W = 1.8$, (a) S_1 with $\phi_1 = 8.2^o$ and $kz = 45.7$, (b) S_2 with $\phi_2 = 8.7^o$ and $kz = 42.9$, (c) comparison of S_1 and S_2.

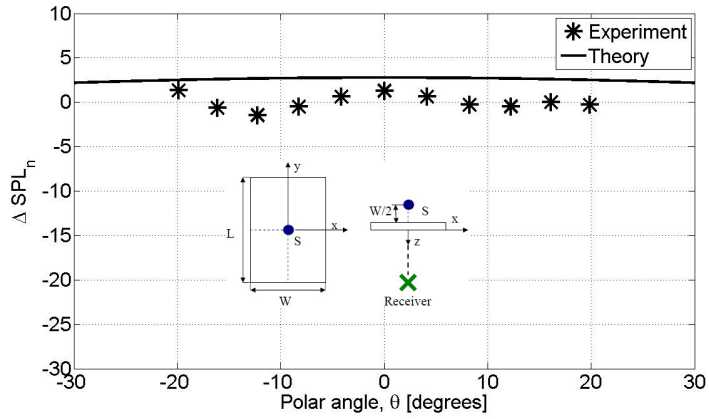

(a)

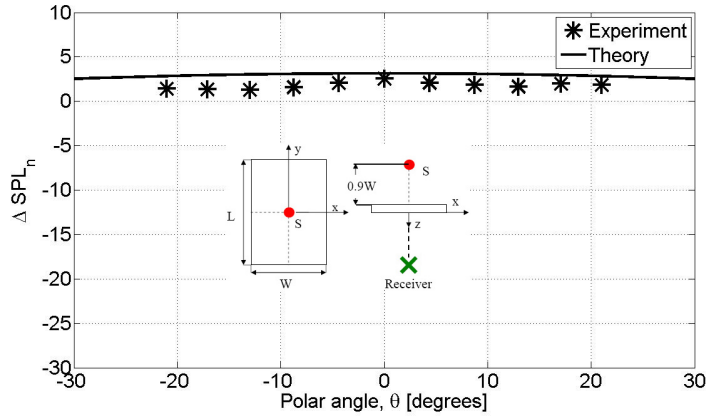

(b)

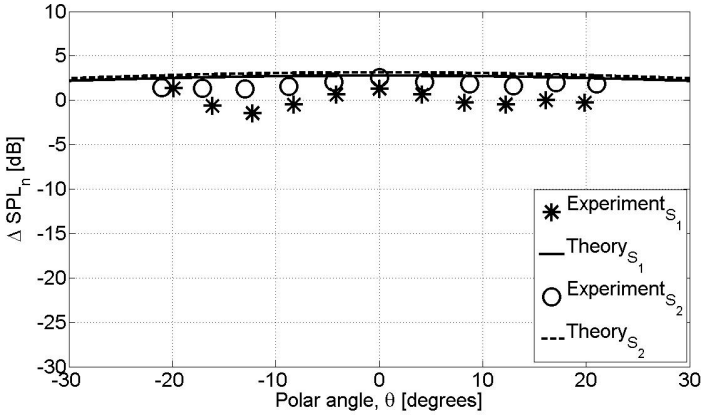

(c)

Figure 84: Effect of source location for a point source along z direction, as a function of polar angle, θ. $f = 400$ Hz, $kW = 2.47$, $L/W = 1.8$, (a) S_1 with $\phi_1 = 12.2^o$ and $kz = 15.8$, (b) S_2 with $\phi_2 = 13^o$ and $kz = 14.8$, (c) comparison of S_1 and S_2.

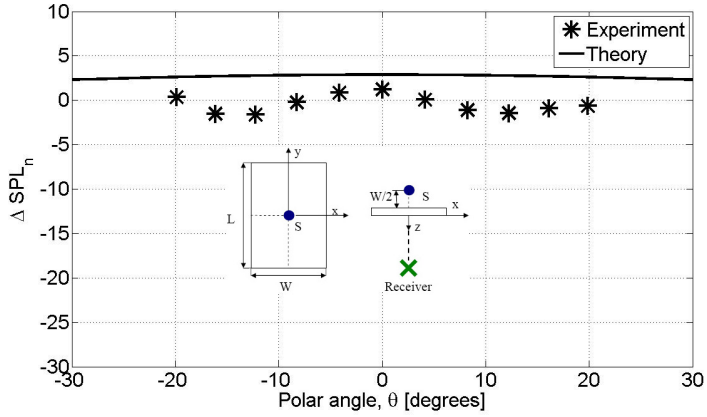

(a)

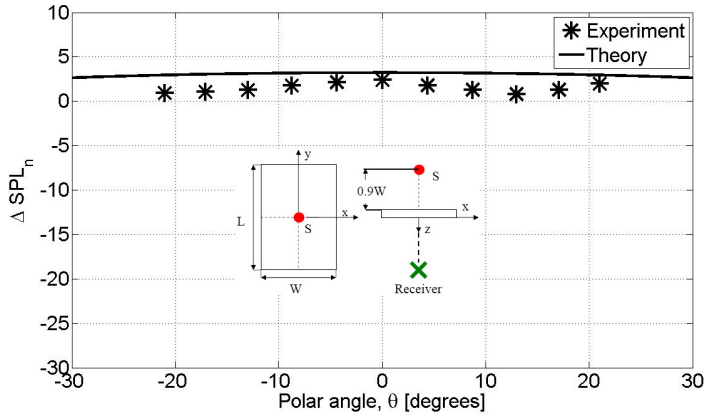

(b)

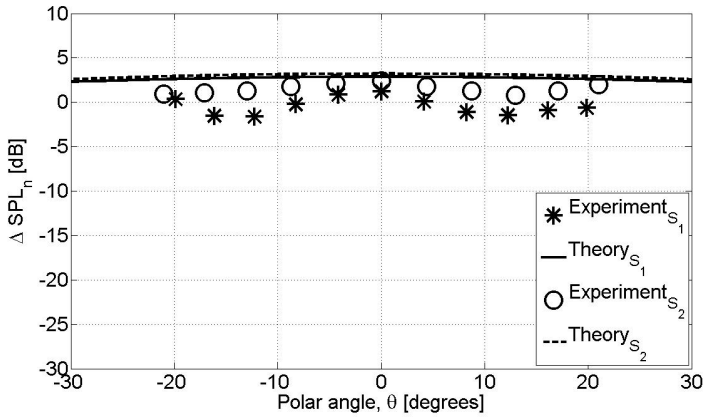

(c)

Figure 85: Effect of source location for a point source along z direction, as a function of polar angle, θ. $f = 400$ Hz, $kW = 2.47$, $L/W = 1.8$, (a) S_1 with $\phi_1 = 8.2^o$ and $kz = 15.8$, (b) S_2 with $\phi_2 = 8.7^o$ and $kz = 14.8$, (c) comparison of S_1 and S_2.

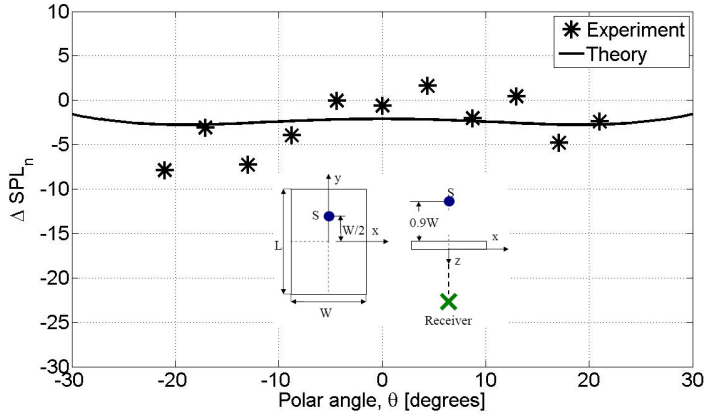

(a)

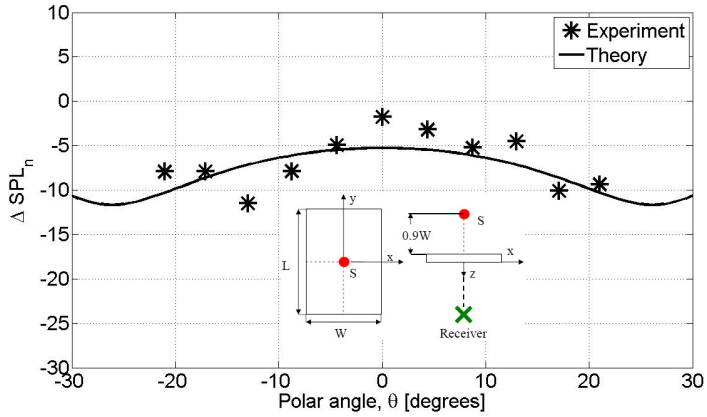

(b)

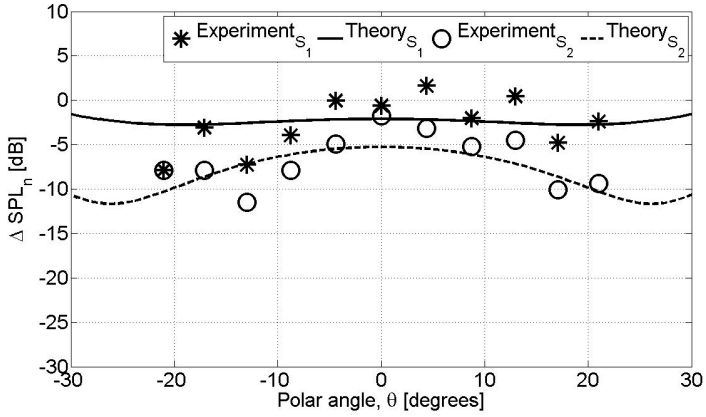

(c)

Figure 86: Effect of source location for a point source along y direction, as a function of polar angle, θ. $f = 1200$ Hz, $kz = 42.9$, $kW = 7.15$, $L/W = 1.8$, (a) S_1 with $\phi_1 = 17.1^o$, (b) S_2 with $\phi_2 = 13^o$, (c) comparison of S_1 and S_2.

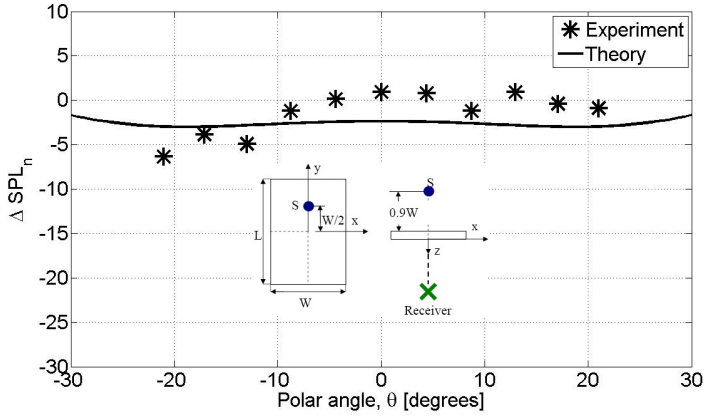

(a)

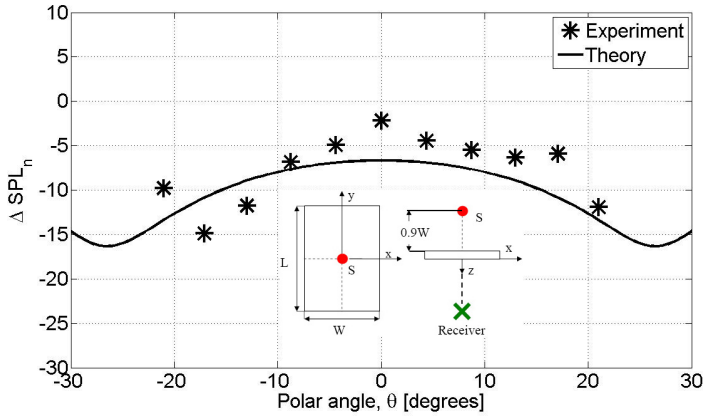

(b)

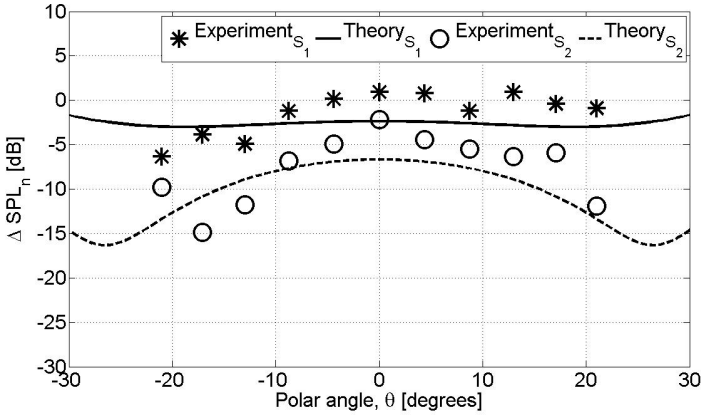

(c)

Figure 87: Effect of source location for a point source along y direction, as a function of polar angle, θ. $f = 1200$ Hz, $kz = 42.9$, $kW = 7.15$, $L/W = 1.8$, (a) S_1 with $\phi_1 = 13^o$, (b) S_2 with $\phi_2 = 8.7^o$, (c) comparison of S_1 and S_2.

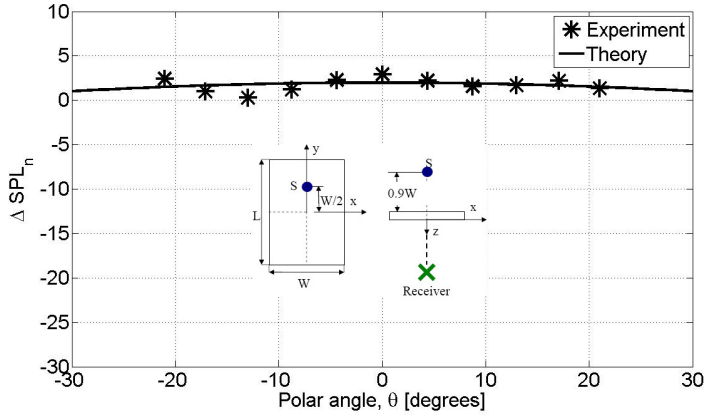

(a)

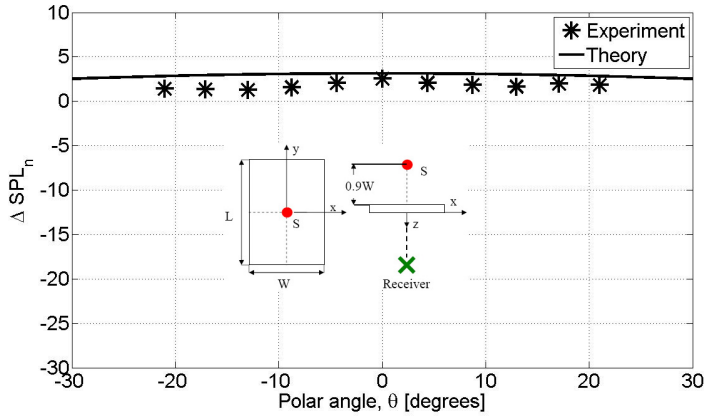

(b)

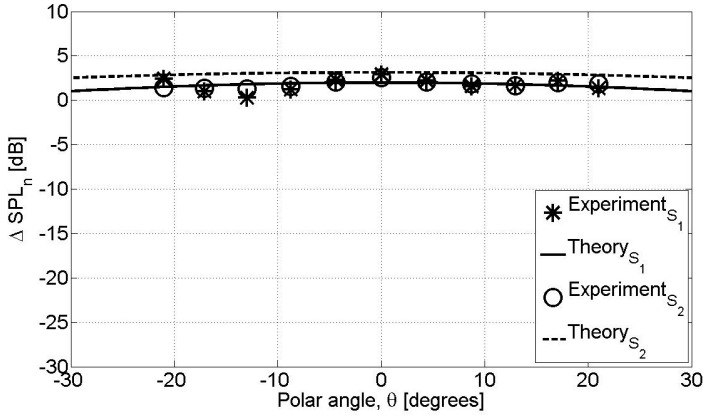

(c)

Figure 88: Effect of source location for a point source along y direction, as a function of polar angle, θ. $f = 400$ Hz, $kz = 14.8$, $kW = 2.47$, $L/W = 1.8$, (a) S_1 with $\phi_1 = 17.1^o$, (b) S_2 with $\phi_2 = 13^o$, (c) comparison of S_1 and S_2.

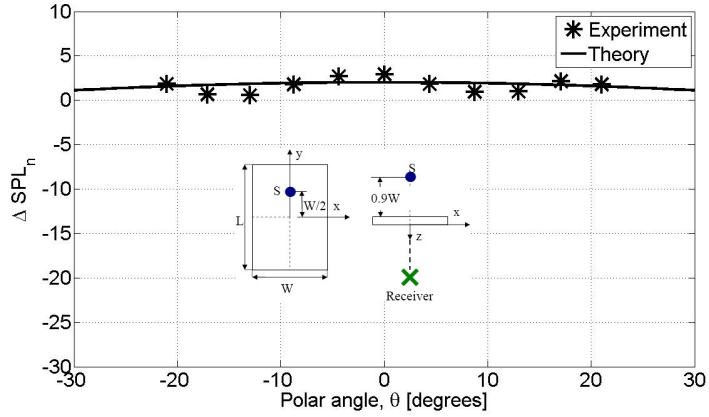

(a)

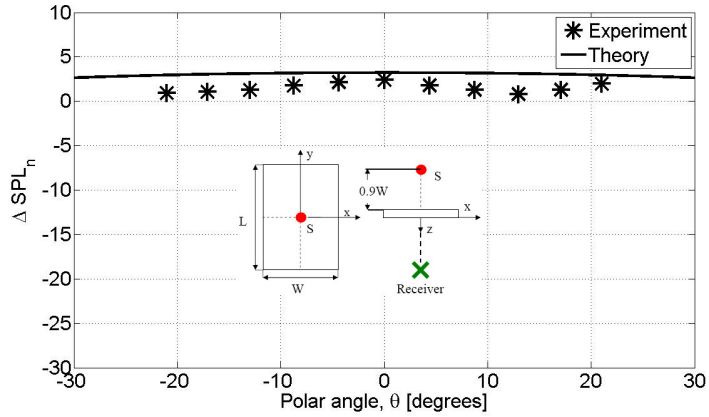

(b)

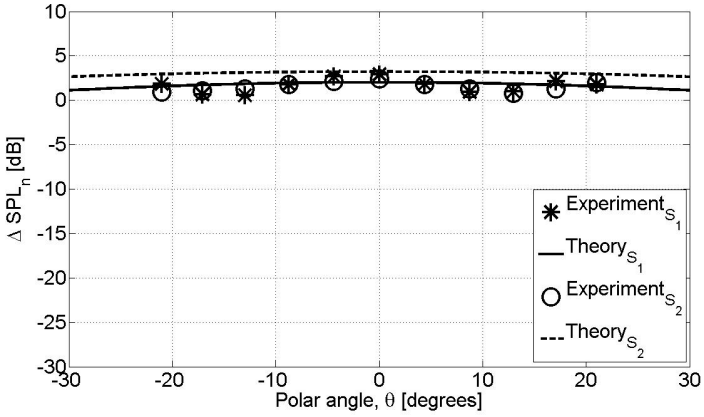

(c)

Figure 89: Effect of source location for a point source along y direction, as a function of polar angle, θ. $f = 400$ Hz, $kz = 14.8$, $kW = 2.47$, $L/W = 1.8$, (a) S_1 with $\phi_1 = 13^o$, (b) S_2 with $\phi_2 = 8.7^o$, (c) comparison of S_1 and S_2.

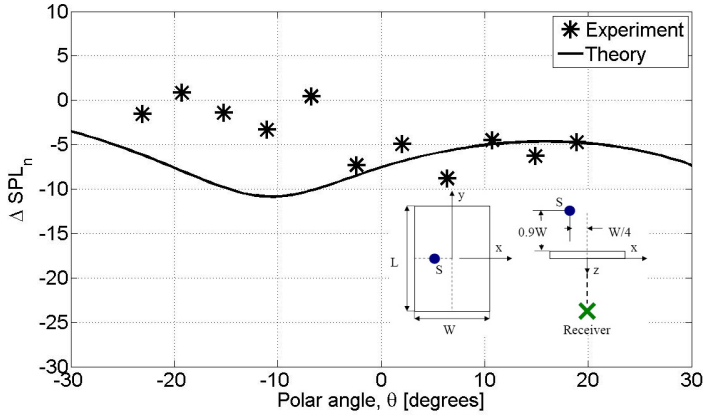

(a)

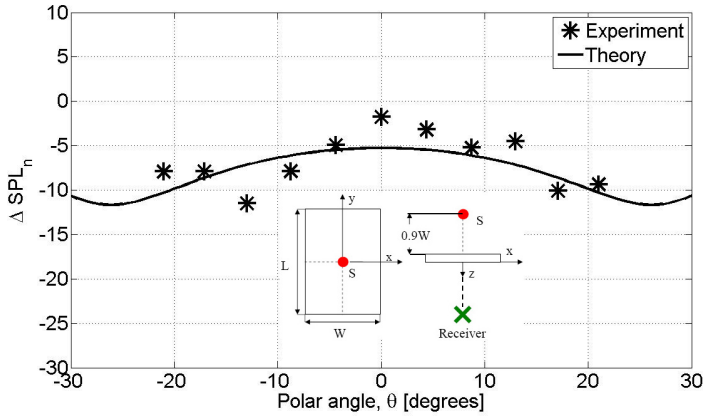

(b)

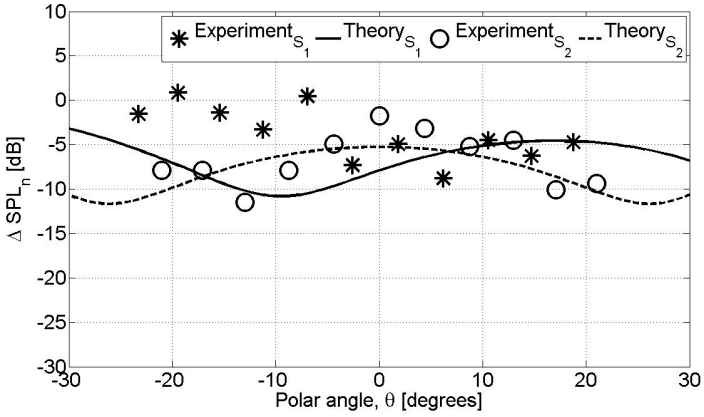

(c)

Figure 90: Effect of source location for a point source along x direction, as a function of polar angle, θ. $f = 1200$ Hz, $kz = 42.9$, $kW = 7.15$, $L/W = 1.8$, (a) S_1 with $\phi_1 = 12.2^o$, (b) S_2 with $\phi_2 = 13^o$, (c) comparison of S_1 and S_2.

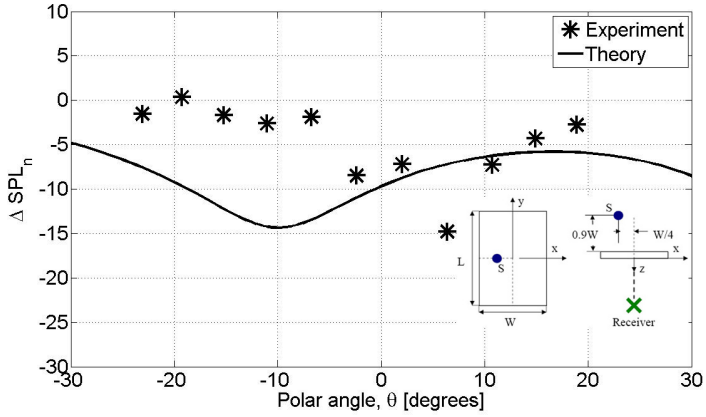

(a)

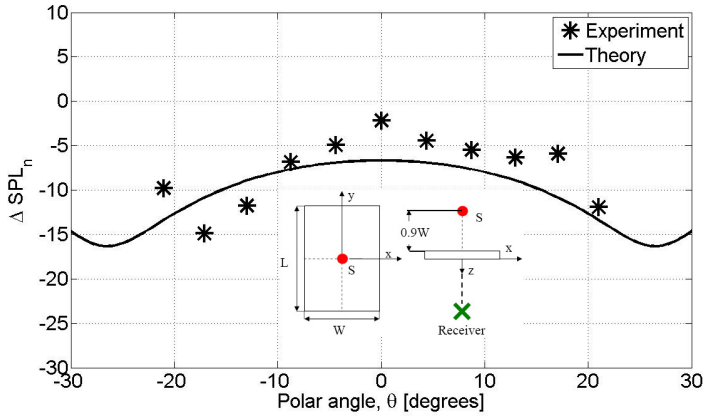

(b)

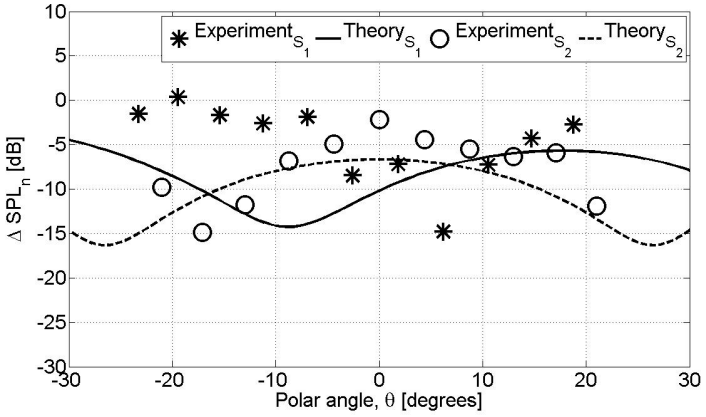

(c)

Figure 91: Effect of source location for a point source along x direction, as a function of polar angle, θ. $f = 1200$ Hz, $kz = 42.9$, $kW = 7.15$, $L/W = 1.8$, (a) S_1 with $\phi_1 = 8.2^o$, (b) S_2 with $\phi_2 = 8.7^o$ (c) comparison of S_1 and S_2.

3D traverse, the microphones or the shield, or unwanted small displacements of the source to the sides could cause shifts on the shielding pattern. For example, in a simulation, source 'S_2' in Figure 90(b) and 91(b) was purposely moved $0.1W$ to the right of the shield mid point, to see sensitivity of small misalignment on shielding. The results are presented in Figures 92(a) and 92(b) for $\phi = 13^o$ and $\phi = 8.7^o$, respectively. It was observed that this small shift of placement produced much better fit with the theory, especially the location and the magnitude of the dip.

6.1.2.2 Effect of Distance from the Back of the Shield

The effect of the microphone distance from the back of the shield, on the shielding is investigated in this section. Results for three values of the dimensionless variable, kz, are shown in Figure 93 for 1200 Hz. The same data is shown in Figure 94, for all three values of kz together. Within the measurement errors, the range of kz values tested, kz had little effect on shielding and predicted data matched the measurements well. The analysis is repeated at 400 Hz for the same configuration in Figure 95, and these three cases are plotted together in Figure 96. It was observed once again that the measurements match the predictions and that the effect of measurement distance become less significant as the frequency is decreased.

In Figures 93 to 96 the source was located $0.9W$ from the upper surface of the shield. It was found that larger shielding is obtained as the source is moved closer to the shield, say, to $z = W/4$ point, as shown in the illustrations on Figures 97(a), 97(b), and 97(c) for $kz = 42.9$, $kz = 66.6$, and $kz = 82.5$, respectively. These three cases are plotted together in Figure 98. A quick comparison with Figure 94 shows that the average levels of shielding are larger now.

As the final case, the source is placed back to $z = 0.9W$ position and moved forward to $y = W/2$ location, as shown in the illustrations on Figures 99(a), 99(b), and 99(c) for $kz = 42.9$, $kz = 66.6$, and $kz = 82.5$, respectively. These three cases are plotted together in Figure 100.

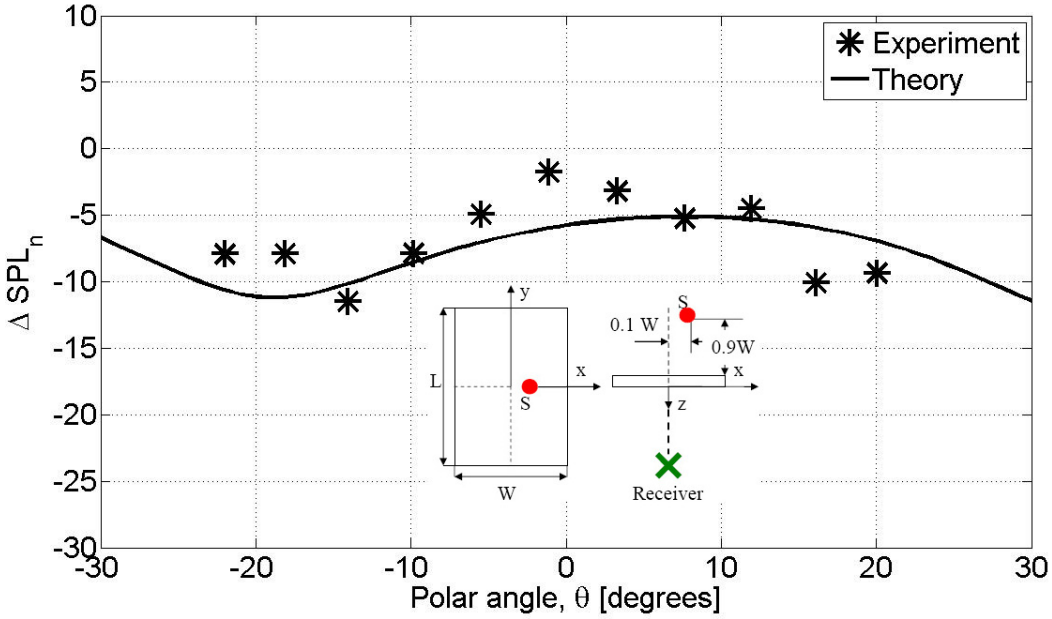

(a)

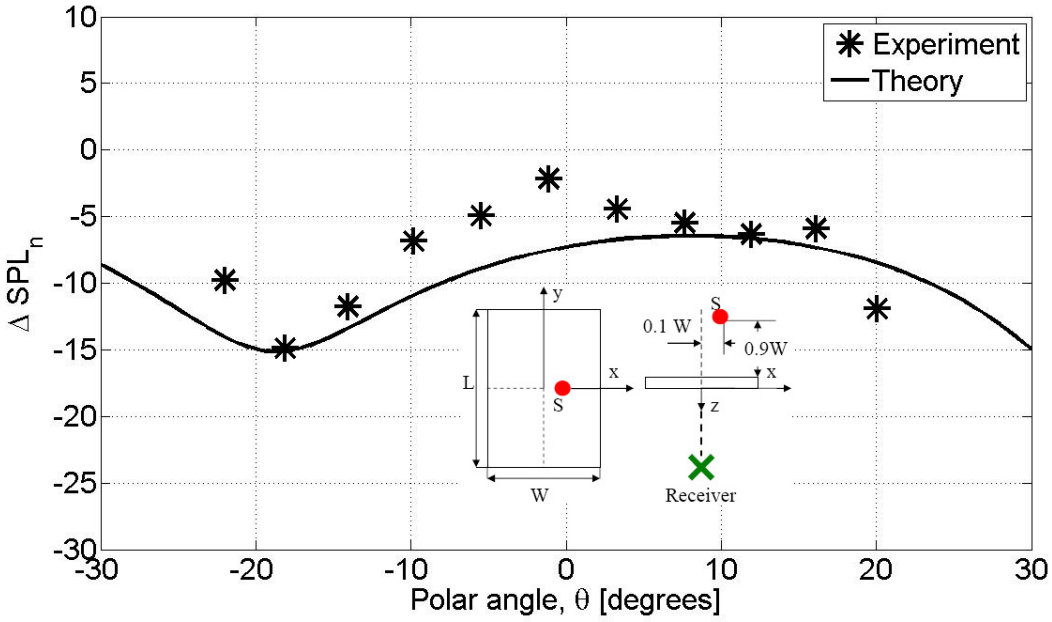

(b)

Figure 92: Source location moved $0.1W$ to the right. $f = 1200Hz$, $kz = 42.9$, $kW = 7.15$, $L/W = 1.8$, (a) $\phi = 13^o$ (b) $\phi = 8.7^o$.

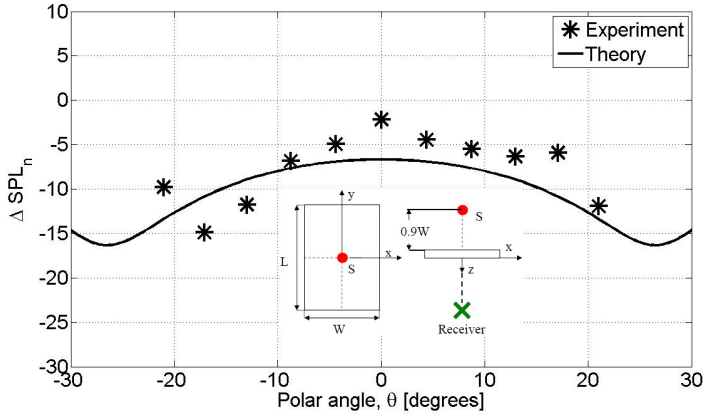

(a)

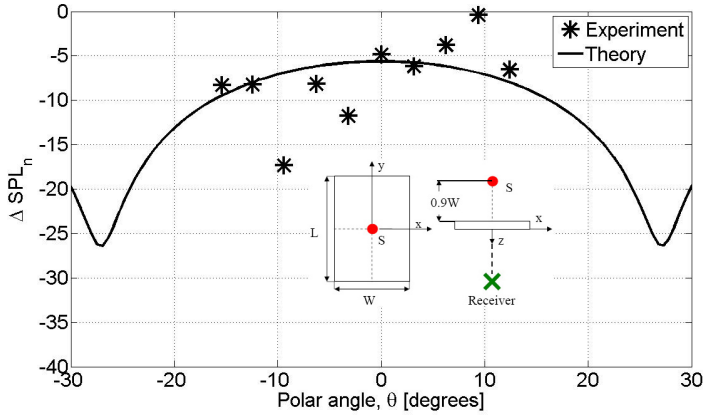

(b)

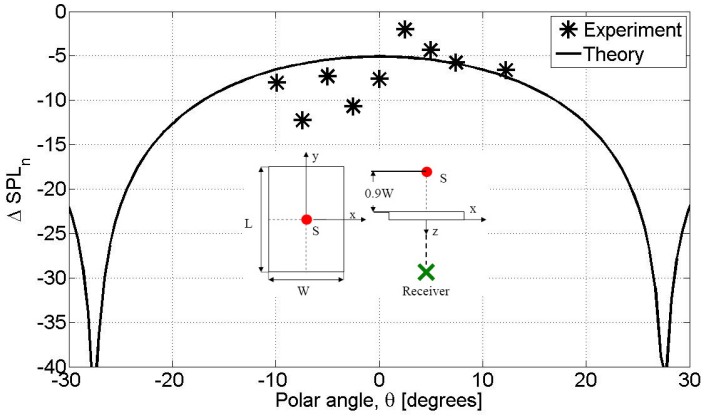

(c)

Figure 93: Effect of measurement distance for a point source, as a function of polar angle, θ. $f = 1200$ Hz, $kW = 7.15$, $L/W = 1.8$, (a) $kz = 42.9$, $\phi_1 = 8.7^o$, (b) $kz = 60$, $\phi_2 = 6.3^o$, (c) $kz = 75.9$, $\phi_2 = 5^o$.

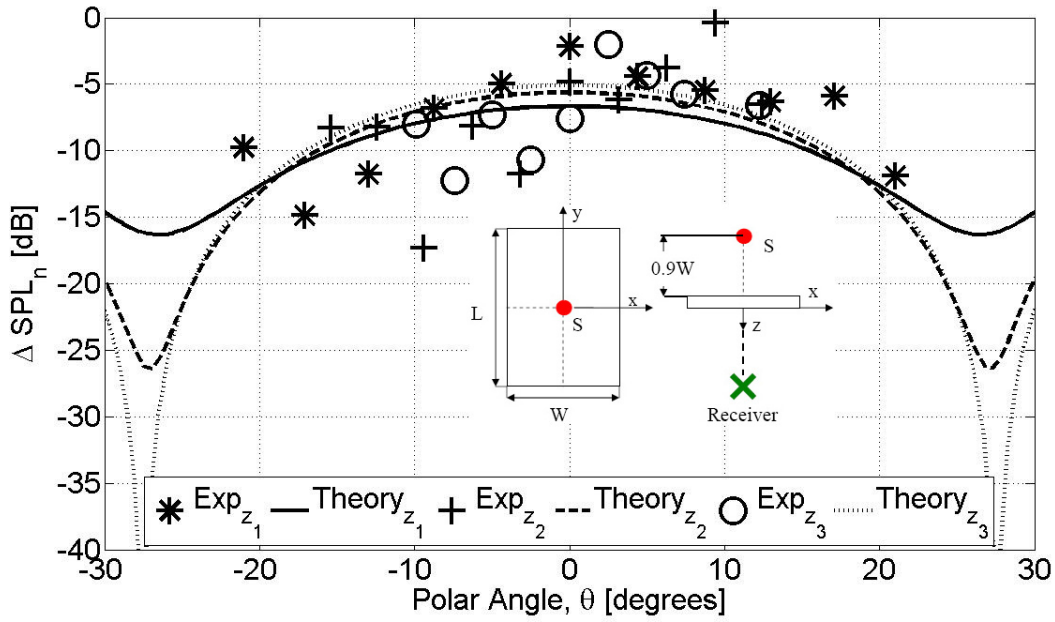

Figure 94: Effect of measurement distance comparatively for a point source, as a function of polar angle, θ. $f = 1200$ Hz, $kW = 7.15$, $L/W = 1.8$, $kz_1 = 42.9$, $\phi_1 = 8.7^o$, $kz_2 = 60$, $\phi_2 = 6.3^o$, $kz_3 = 75.9$, $\phi_2 = 5^o$.

6.1.3 Experiments with a Round Duct as a Shield

The rectangular shield was replaced by a $D_D = 7''$ diameter duct. Ducts of several lengths were tested. The point source was was placed at the center of the duct. The shielding obtained at 1200 Hz for two duct lengths ($L = 1.7D_D$ and $L = 3.4D_D$) is given in Figure 101. The experimental data for shielding of point source by a duct was compared with the calculations for point source shielded by a rectangular shield. To calculate the shielding, it was assumed that the point source was placed above a rectangular shield at a distance of duct radius. The width and length of the rectangular plane corresponds to the duct diameter and length, respectively.

Since this work is focused on the shielding of tonal noise generated by the rotor, the noise due to the resonance of the duct and the production of higher order modes are not investigated. The higher order modes are produced at frequencies higher than about 1200 Hz for a duct of diameter $7''$. So shielding by a hard-walled duct at frequencies equal to less than 1200 Hz will be considered.

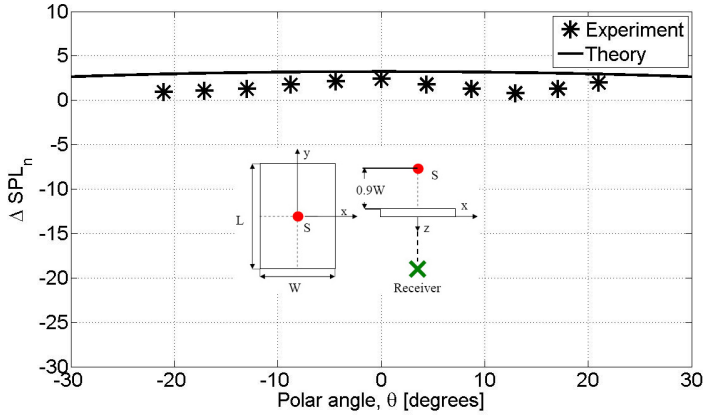

(a)

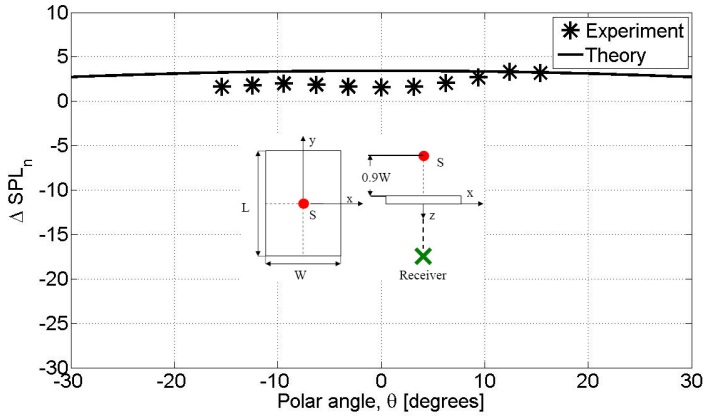

(b)

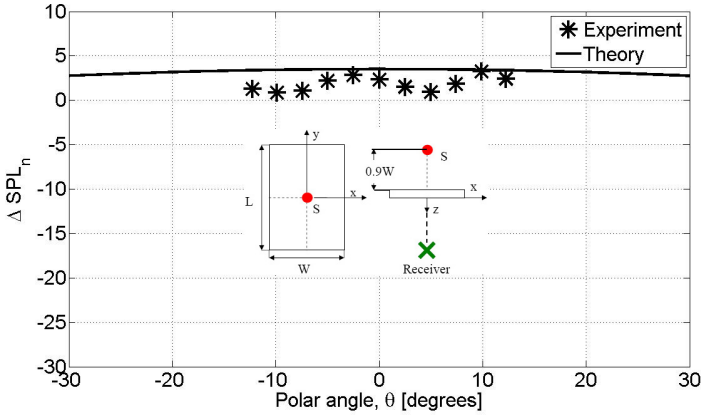

(c)

Figure 95: Effect of measurement distance for a point source, as a function of polar angle, θ. $f = 400$ Hz, $kW = 2.47$, $L/W = 1.8$, (a) $kz = 14.8$, $\phi_1 = 8.7^o$, (b) $kz = 20.7$, $\phi_2 = 6.3^o$, (c) $kz = 26.2$, $\phi_2 = 5^o$.

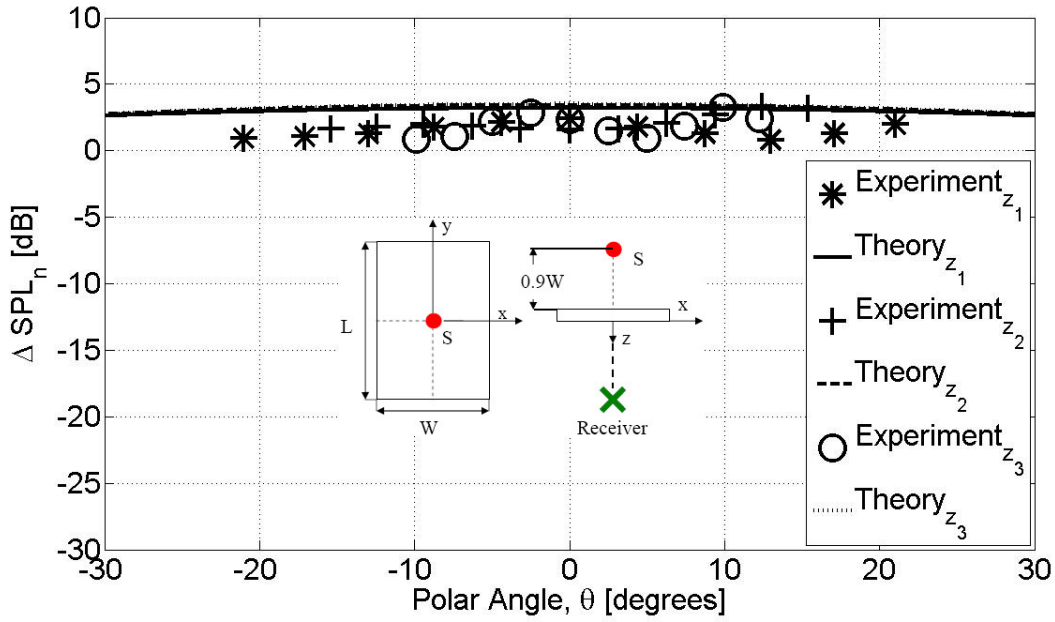

Figure 96: Effect of measurement distance comparatively for a point source, as a function of polar angle, θ. $f = 400$ Hz, $kW = 2.47$, $L/W = 1.8$, $kz_1 = 14.8$, $\phi_1 = 8.7^o$, $kz_2 = 20.7$, $\phi_2 = 6.3^o$, $kz_3 = 26.2$, $\phi_2 = 5^o$.

The results for the measurement angle, $\phi = 11.8^o$, showed that the calculation underestimated the shielding amount for the shorter duct. However, when the duct length was doubled a better fit was obtained. Figure 102 shows the results where the measurement angle was $\phi = 0^o$, i.e., the microphone and the point source were in line. The calculations based upon a rectangular shield still cannot estimate the shielding by the shorter duct as seen in Figure 102(a). At $\theta = 0^o$ the experiments make a dip and the highest shielding is obtained. However, the calculations show the opposite and the lowest shielding was obtained at $\theta = 0^o$. When there is a rectangular shield, due to the symmetry of the configuration, the constructive interference of the diffracted waves from the two edges of the duct increases shielding somewhat. When the duct is inserted, since these edges don't exist, the shielding is increased around $\theta = 0^o$. Doubling the duct length, gives again a better fit as seen in Figure 102(b).

The comparisons performed for 1200 Hz frequency was repeated for 400 Hz in Figure 103 and Figure 104 at $\phi = 11.8^o$ and $\phi = 0^o$ angles, respectively. Poor shielding estimates were obtained at lower frequency in both cases. Increasing the duct length didn't make

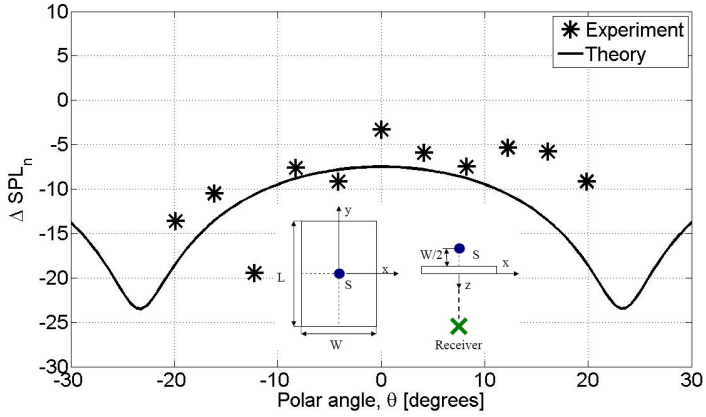

(a)

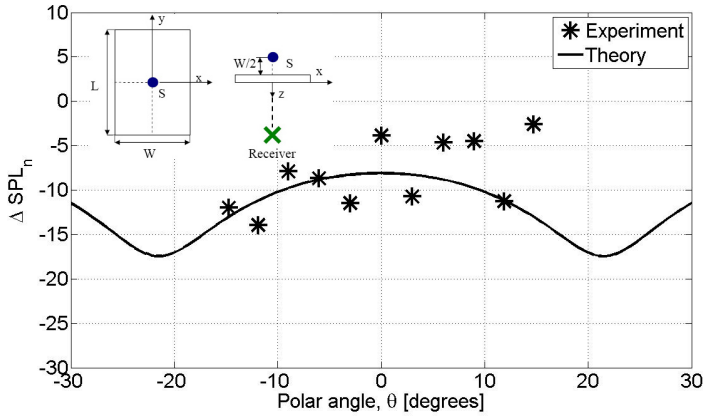

(b)

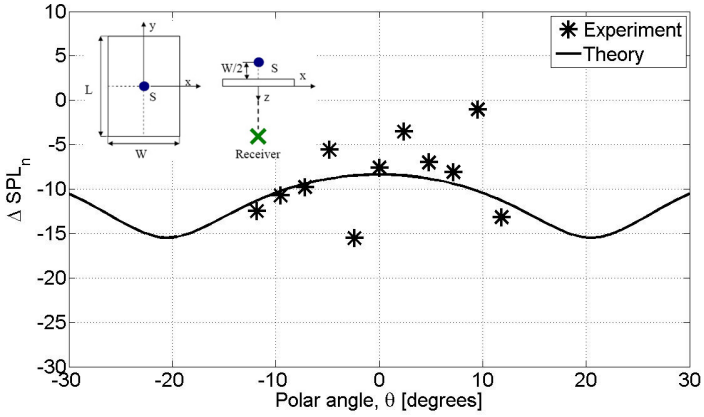

(c)

Figure 97: Effect of measurement distance for a point source, as a function of polar angle, θ. $f = 1200$ Hz, $kW = 7.15$, $L/W = 1.8$, (a) $kz = 45.7$, $\phi_1 = 8.2^o$, (b) $kz = 62.7$, $\phi_2 = 6^o$, (c) $kz = 78.7$, $\phi_2 = 4.8^o$.

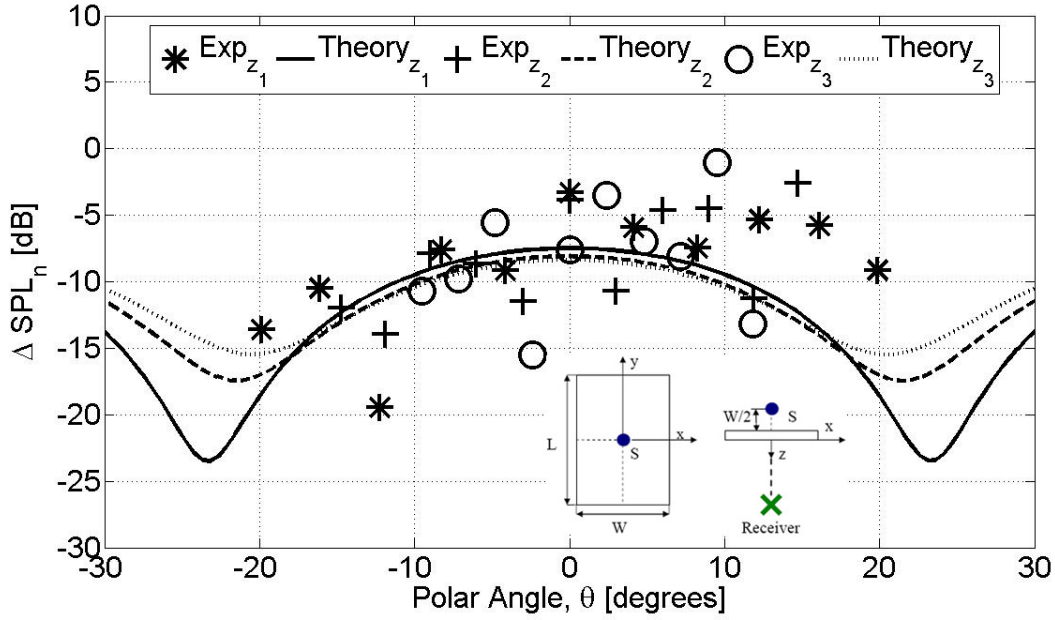

Figure 98: Effect of measurement distance comparatively for a point source, as a function of polar angle, θ. $f = 1200$ Hz, $kW = 7.15$, $L/W = 1.8$, $kz = 45.7$, $\phi_1 = 8.2^o$, $kz = 62.7$, $\phi_2 = 6^o$, $kz_3 = 78.7$, $\phi_2 = 4.8^o$.

difference at this frequency.

No shielding model is available for sources shielded by round ducts. In reality, the problem becomes one of transmission of sound through a duct and then diffracted around the periphery of the duct exit at both ends. A simplistic view to explain why higher shielding is obtained in this case compared to that predicted by a rectangular shield is that the sound reaching the exit is partly reflected back towards the source and the diffraction is experienced only that portion of sound that is transmitted. This is expected to show up as reduced acoustic level outside the duct. Likewise, one would expect less transmission at lower frequencies, thus showing even lower level in the farfield as indeed seen at 400 Hz in this case. Detailed analysis of this data is beyond the scope of this thesis.

6.2 Rotor Experiments

6.2.1 Unshielded Experiments

A typical acoustic spectrum of rotor noise is presented in Figure 105. This particular spectrum was acquired from a $D = 6.5''$ diameter rotor, at $\theta = 0$, $\phi = 0$, and $z/D = 13.8$.

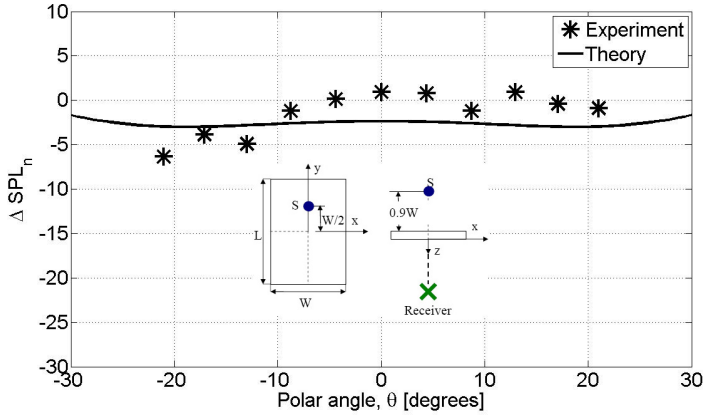

(a)

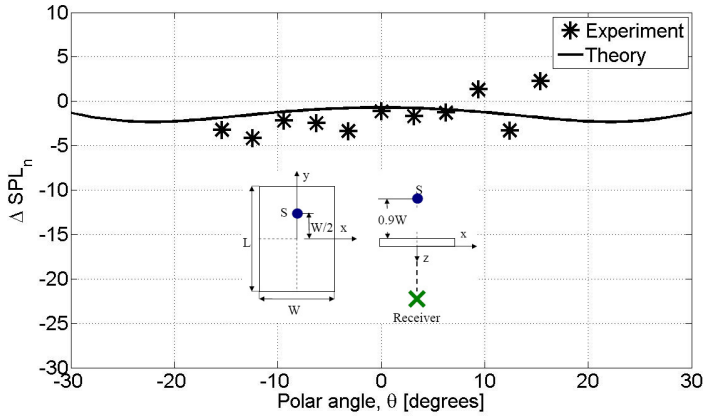

(b)

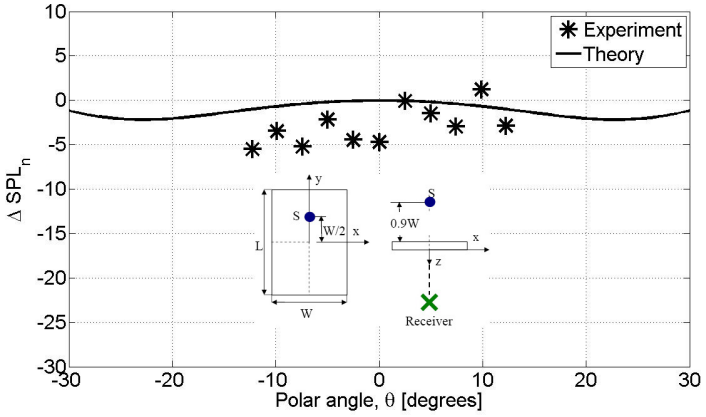

(c)

Figure 99: Effect of measurement distance for a point source, as a function of polar angle, θ. $f = 1200$ Hz, $kW = 7.15$, $L/W = 1.8$, (a) $kz = 42.9$, $\phi_1 = 13^o$, (b) $kz = 60$, $\phi_2 = 9.4^o$, (c) $kz = 75.9$, $\phi_2 = 7.4^o$.

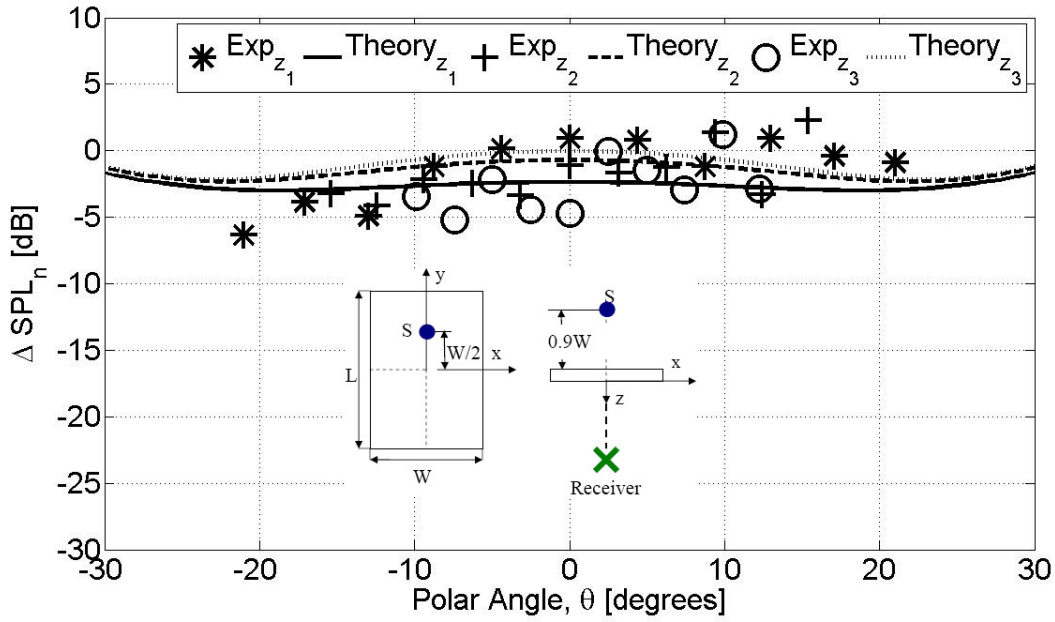

Figure 100: Effect of measurement distance comparatively for a point source, as a function of polar angle, θ. $f = 1200$ Hz, $kW = 7.15$, $L/W = 1.8$, $kz_1 = 42.9$, $\phi_1 = 13^o$, $kz_2 = 60$, $\phi_2 = 9.4^o$, $kz_3 = 75.9$, $\phi_2 = 7.4^o$.

The rotor was 4 bladed and run at 6000 rpm; so BPF was 400 Hz. Significant peaks are at BPF, below BPF, and at its harmonics up to 1300 Hz. The source for the lower frequencies was the imbalance of the rotor. Since the purpose of these tests is to see if the rotor acts like a point source, it was decided that all the harmonics could be used for the analysis. The frequency resolution of the spectrum is 1 Hz. Some leakage was observed around the peaks. This was attributed to the small rpm variations during the experiments due to small voltage variations. So a ± 5 Hz frequency interval was selected around each peak and data integrated over 10 Hz. For instance when 400 Hz is mentioned it is actually the 395 Hz-405 Hz interval. Experimental shielding for the rotor was computed and compared with the theoretical shielding based upon a point sound source at the same frequency.

6.2.2 Rectangular Shield Experiments

The main measurement parameters used in this section are measurement distance, R, polar angle, θ, and azimuthal angle ϕ; just as it was for the point source experiments. The measurement configuration for the shielded rotor experiments is illustrated in Figure 106.

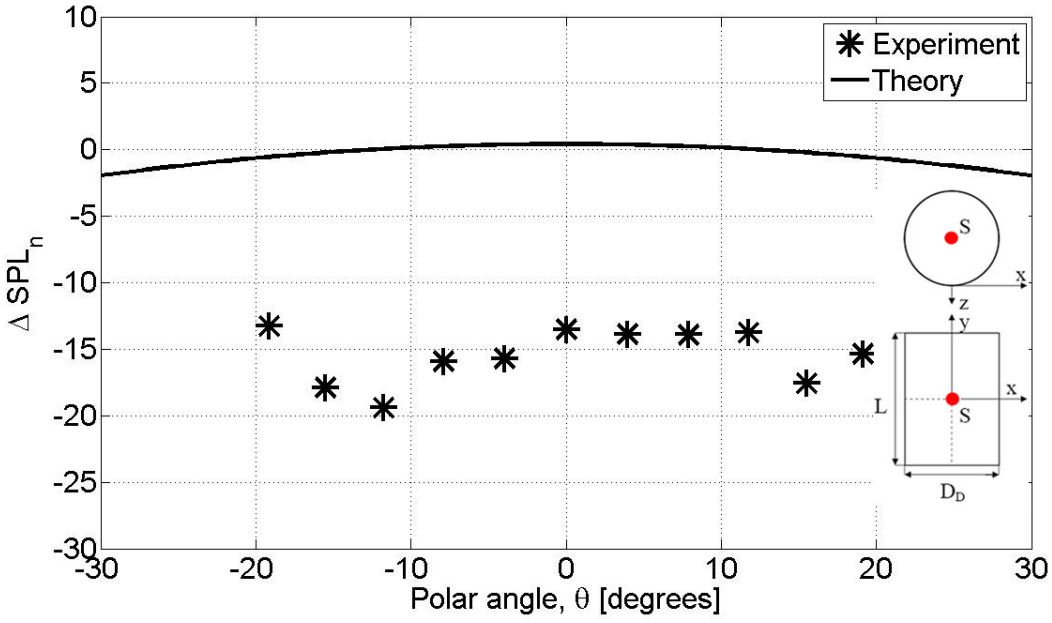

(a)

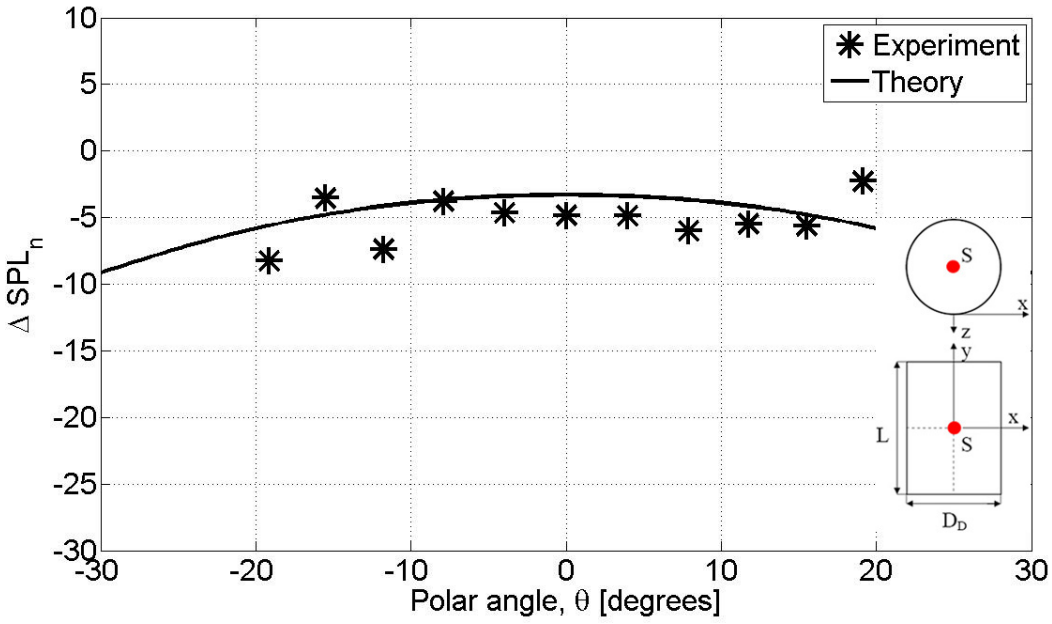

(b)

Figure 101: Noise shielding for a point source placed inside ducts of different lengths, as a function of polar angle, θ. $f = 1200Hz$, $\phi = 11.8^o$, $kz = 47.6$, $kD_D = 3.85$, (a) $L/D_D = 1.7$, (b) $L/D_D = 3.4$.

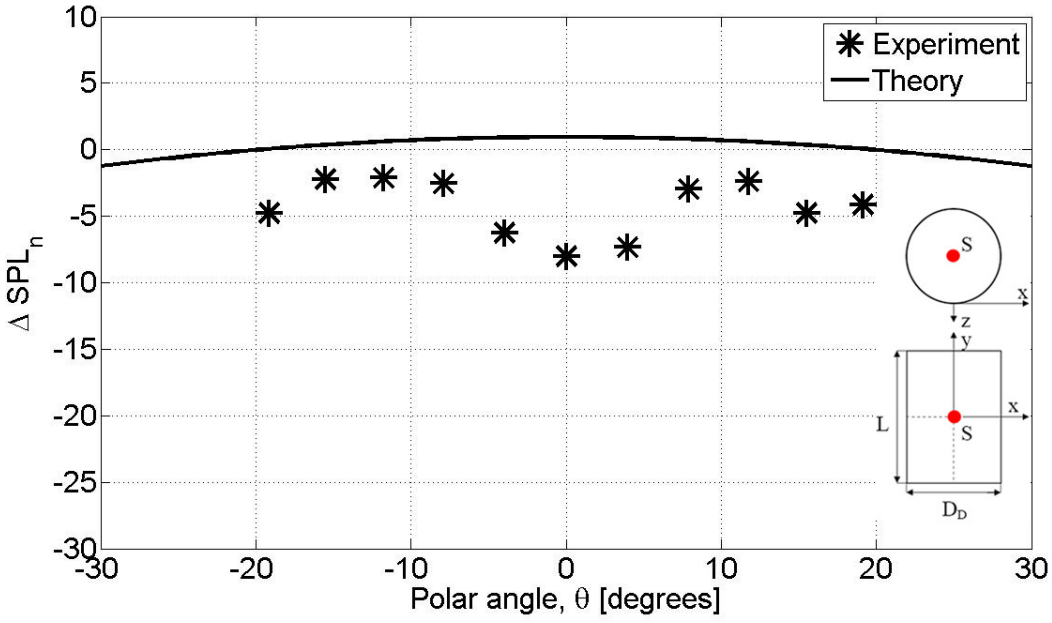

(a)

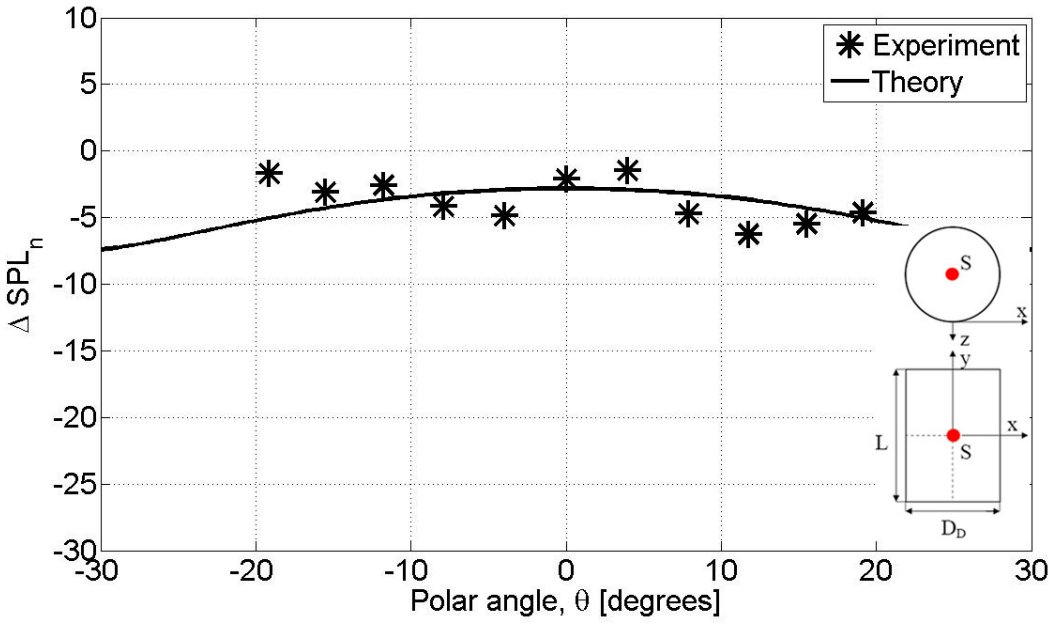

(b)

Figure 102: Noise shielding for a point source placed inside ducts of different lengths, as a function of polar angle, θ. $f = 1200Hz$, $\phi = 0^o$, $kz = 47.6$, $kD_D = 3.85$, (a) $L/D_D = 1.7$, (b) $L/D_D = 3.4$.

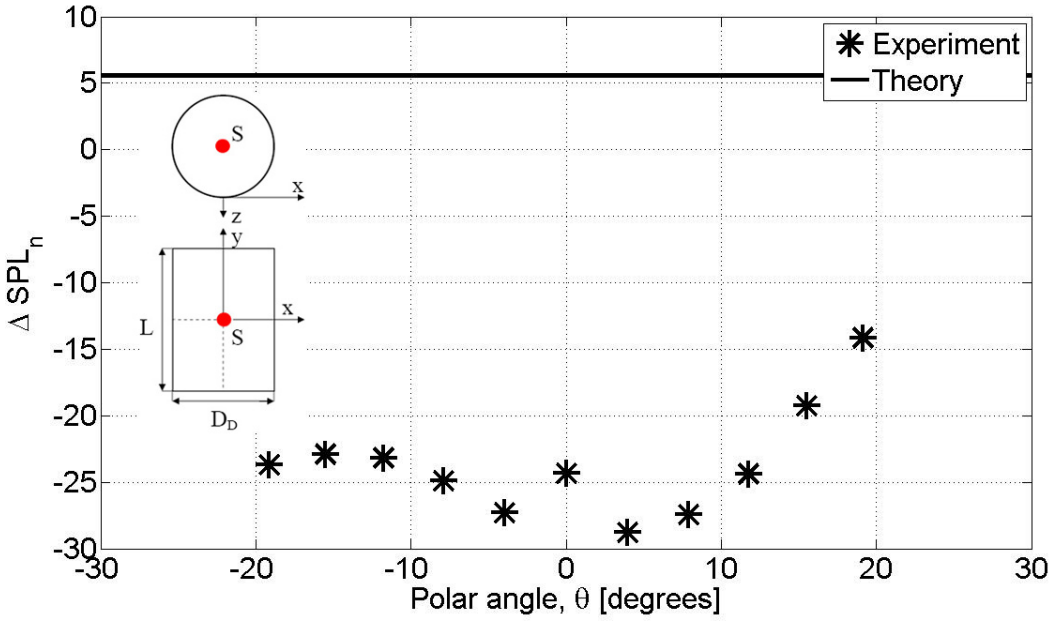

(a)

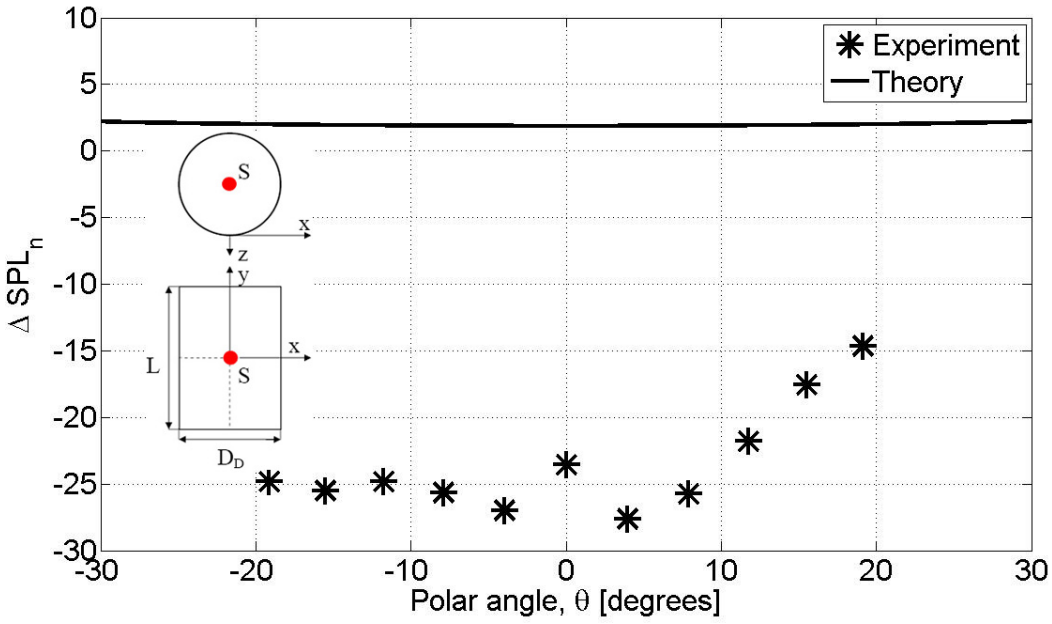

(b)

Figure 103: Noise shielding for a point source placed inside ducts of different lengths, as a function of polar angle, θ. $f = 400Hz$, $\phi = 11.8^o$, $kz = 16.4$, $kD_D = 1.33$, (a) $L/D_D = 1.7$, (b) $L/D_D = 3.4$.

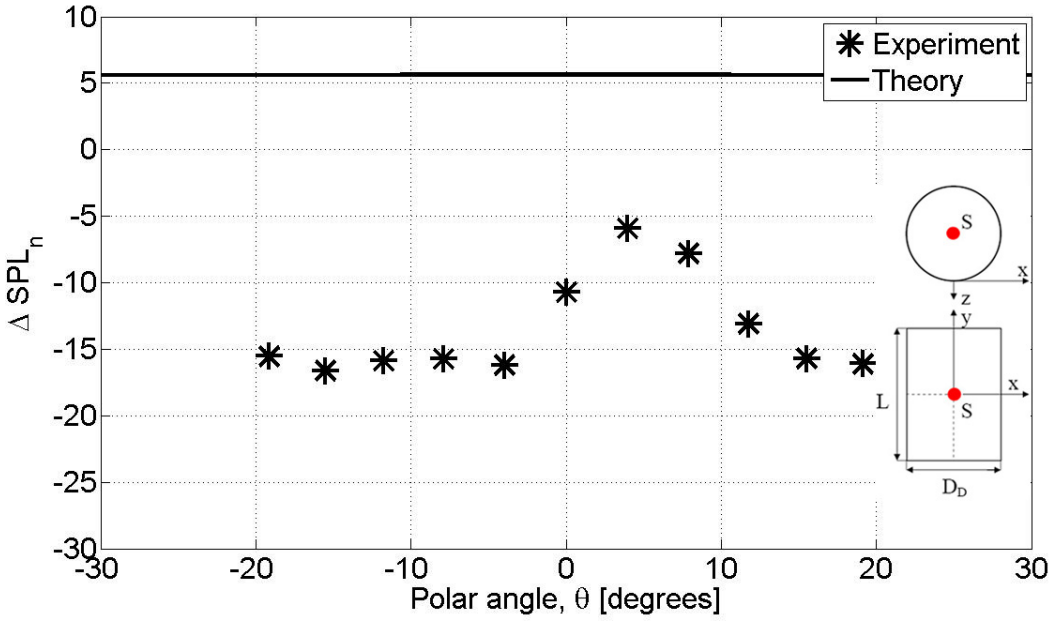

(a)

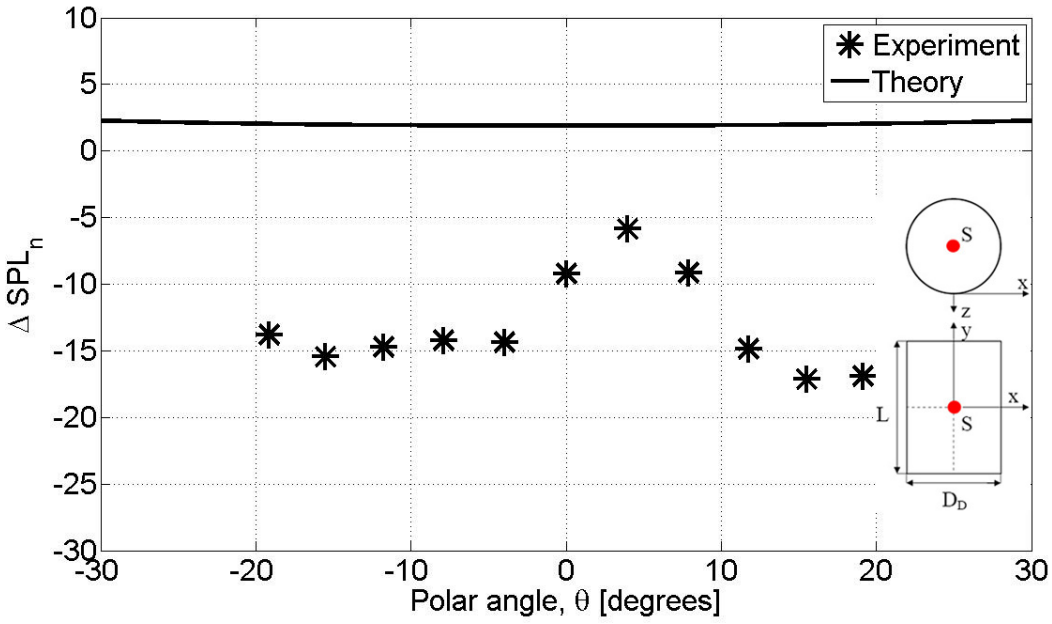

(b)

Figure 104: Noise shielding for a point source placed inside ducts of different lengths, as a function of polar angle, θ. $f = 400Hz$, $\phi = 0^o$,, $kz = 16.4$, (a) $L/D_D = 1.7$, $kD_D = 1.33$, (b) $L/D_D = 3.4$.

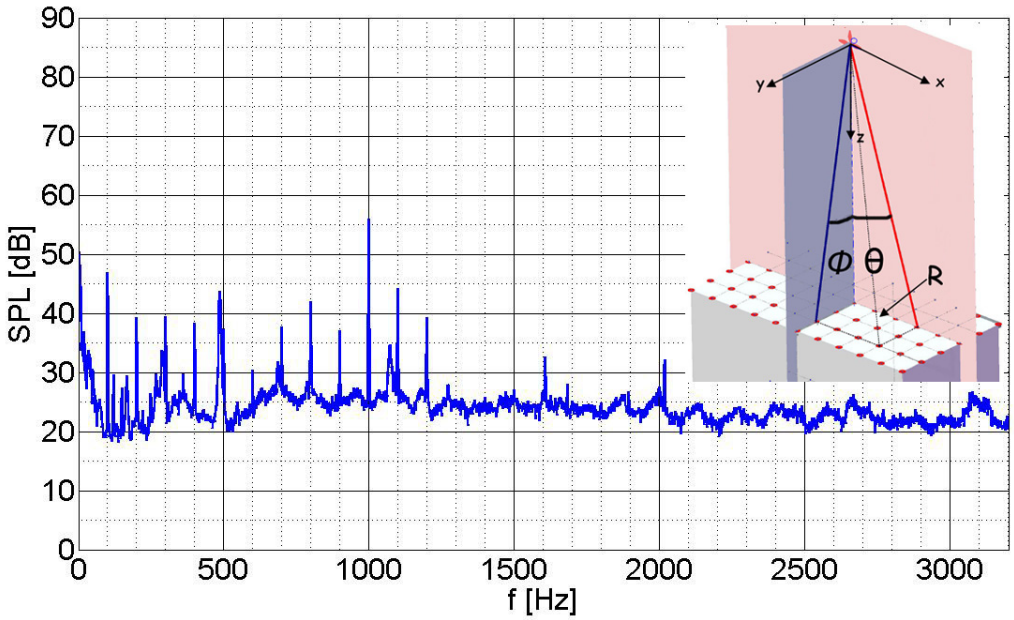

Figure 105: Spectrum of rotor noise. $D = 6.5''$, $z/D = 13.8''$, $\theta = 0^o$, $\phi = 0^o$, 6000 rpm, BPF = 400 Hz, $n_B = 4$, $\Delta f = 1$ Hz.

In Chapter 5 author showed that a rotor can be treated as a point source at the center of the rotor only when the observer to source distance was at least 10 rotor diameters or farther. To make sure that the rotor itself, without any shield can be considered as a point source, the distance between the center of the rotor and the receiver is chosen to be large enough so that this condition applies. Unless another value is indicated this distance is $90''$ for the $6.5''$ diameter rotor for the results presented in this work, providing $R/D = 13.8$. Figure 107 shows a typical spectrum of a $6.5''$ diameter open rotor with the shield for an RPM of 6000. The rotor remaining the same place as in Figure 105, the shield is placed 0.9 shield width (1.8 rotor diameters) below the rotor center. The rotor inflow is towards $-y$ direction. The tones for the unshielded case are still seen when the shield is inserted. The levels increased in some cases like 400 Hz and decreased in some cases like 1200 Hz. Broadband noise levels are lower for the high frequencies, especially above 1500 Hz.

The shielding calculations and experimental findings at 1200 Hz are compared in Figure 108(a) and 108(b) for $\phi = 13^o$ and $\phi = 0^o$, respectively. The theory overestimates the experimental findings at least 5 dB for the $\phi = 13^o$ case. When $\phi = 0^o$, i.e., when the source

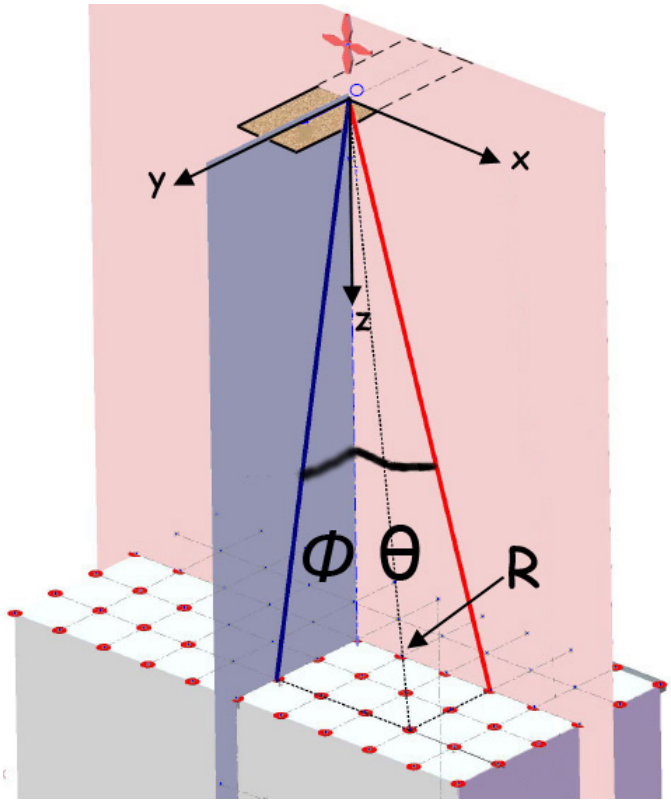

Figure 106: Illustration of rotor configuration shielded by a rectangular barrier.

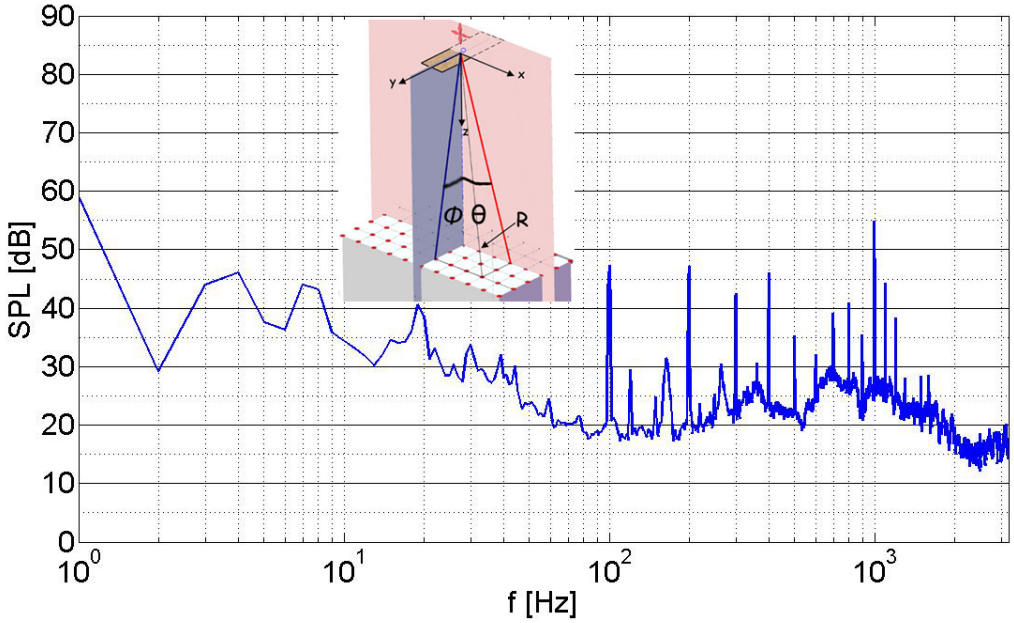

Figure 107: Spectrum of rotor noise shielded by a rectangular barrier. $D = 6.5''$, $z = 78''$, $\theta = 0^o$, $\phi = 0^o$, $L/W = 1.8$, 6000 rpm, BPF = 400 Hz, $n_B = 4$, $\Delta f = 1$ Hz, $d/W = 0.4$.

center is aligned with the microphone, the gap between the experiments and calculations is even larger and the dips seen in calculated results don't exist for experiments. In fact, shielding is almost insignificant for rotor.

The data shown in the last figure was for a frequency of 1200 Hz. This is the third harmonic of the rotor BPF. This frequency was chosen first as at this frequency the point source experiments displayed reasonable shielding. The analysis is repeated for 800 Hz and 400 Hz in Figures 109 and 110, respectively, for the two different ϕ values. It is observed that the shielding is positive at low frequencies which means that the existence of the shield increases the noise over the limited values of θ for which data was acquired.

The rotor was moved $0.5W$ forward parallel to the shield still remaining $0.9W$ above the shield as shown by the illustrations in Figure 111. The experimental findings and calculations are again compared at angles $\phi = 13^o$ and $\phi = 0^o$ in Figure 111(a) and Figure 111(b), respectively, at 1200 Hz. In this case, although the theory still overestimates the shielding, calculations results are closer to the experiments then the previous case where the rotor was placed in the middle. The comparison can be considered to be good, though, if this data is also assumed to be within ± 2 dB as assumed for the point source data earlier.

The analysis is repeated for 1100 Hz, 800 Hz and 400 Hz in Figures 112, 113, 114 respectively. It is observed that at the lowest frequency, no matter where the receiver is positioned, no shielding is obtained.

6.2.2.1 Effect of Rotor Location

The effect of rotor location on shielding is investigated in this section. The two cases: rotor placed at the center and at $0.5W$ forward of the center, as shown by the illustrations on Figure 115 are compared. 'S_1' denotes the rotor position with $0.5W$ offset from the center and 'S_2' denotes the rotor at the center. In Figure 115(a) the receiver is located at the azimuthal angles of $\phi_1 = 13^o$, $\phi_2 = 8.7^o$ for the sources 'S_1' and 'S_2', respectively. In Figure 115(b) the receiver changes location moving closer to the center. In this case the corresponding azimuthal angles are $\phi_1 = 0^o$ and $\phi_2 = 0^o$, respectively.

The results shown in Figure 115 were for a frequency of 1200 Hz. Similar results for 800

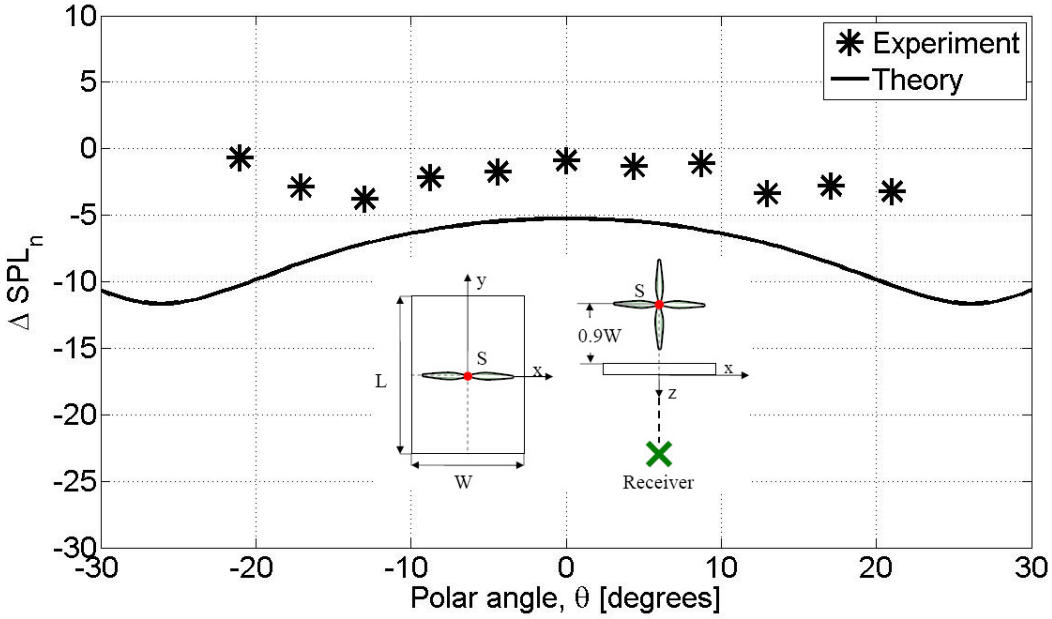

(a)

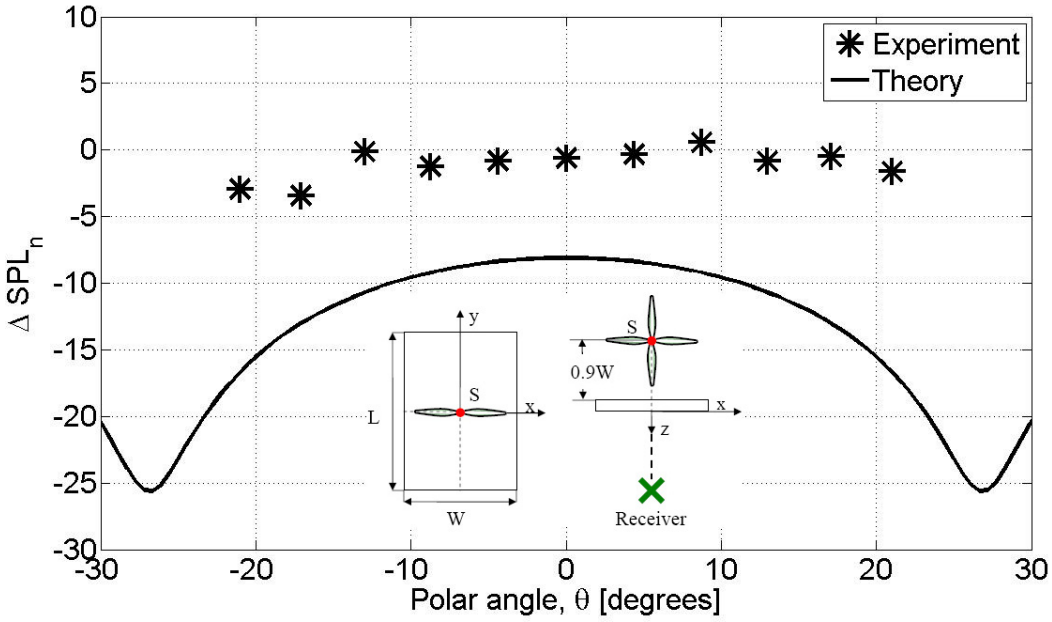

(b)

Figure 108: Noise shielding for a rotor source, as a function of polar angle, θ. $f = 1200Hz$, $kW = 7.15$, $L/W = 1.8$, $D = W/2$, $kz = 42.9$, (a) $\phi = 13^o$, (b) $\phi = 0^o$.

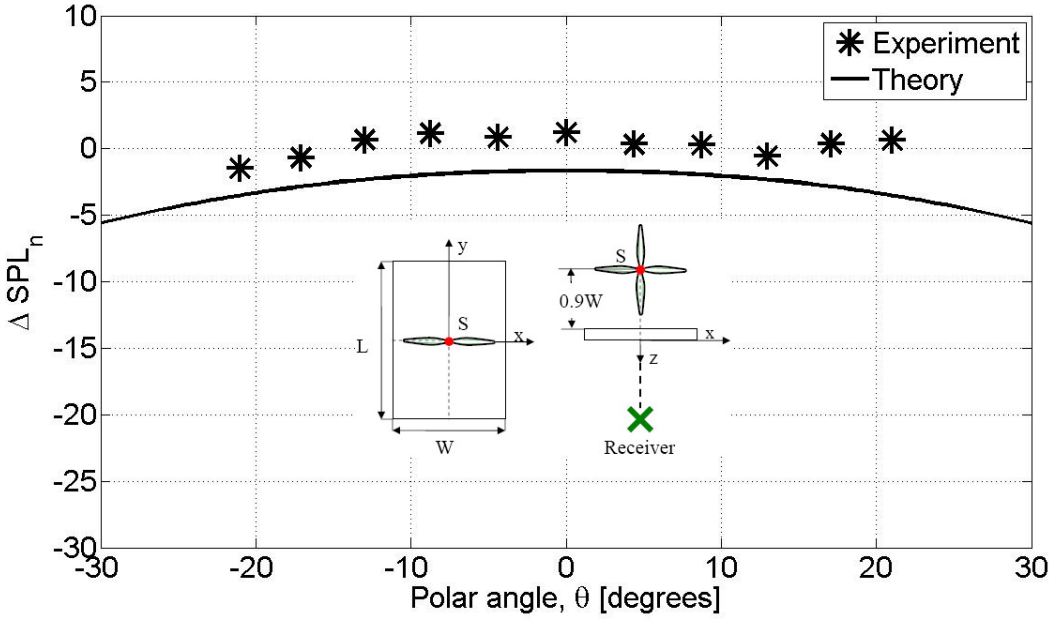

(a)

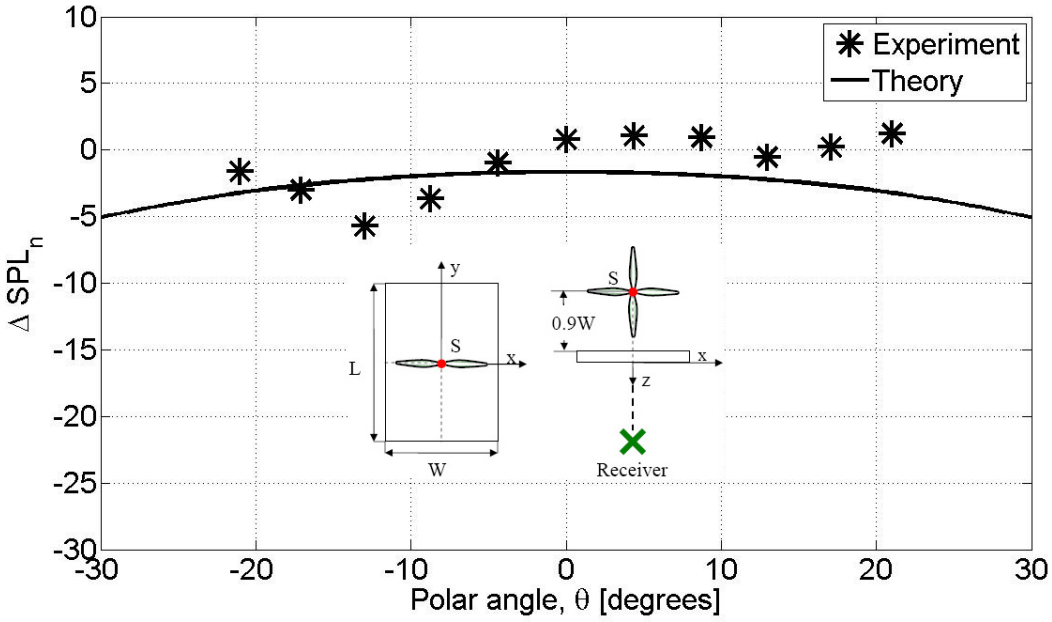

(b)

Figure 109: Noise shielding for a rotor source, as a function of polar angle, θ. $f = 800Hz$, $kW = 4.81$, $L/W = 1.8$, $D = W/2$, $kz = 28.9$, (a) $\phi = 13^o$, (b) $\phi = 0^o$.

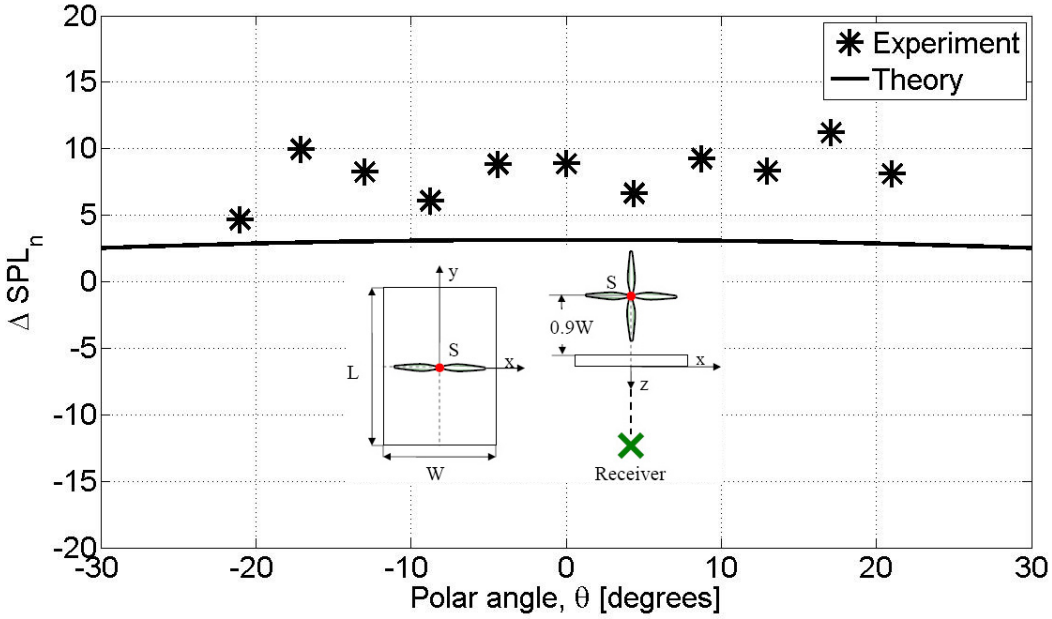

(a)

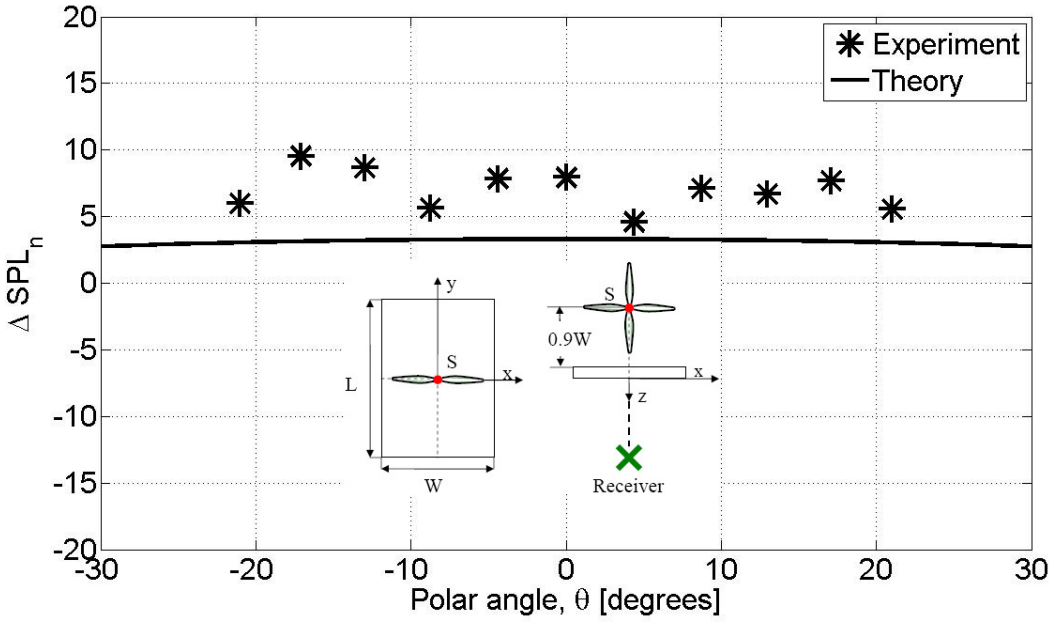

(b)

Figure 110: Noise shielding for a rotor source, as a function of polar angle, θ. $f = 400Hz$, $kW = 2.47$, $L/W = 1.8$, $D = W/2$, $kz = 14.8$, (a) $\phi = 13^o$, (b) $\phi = 0^o$.

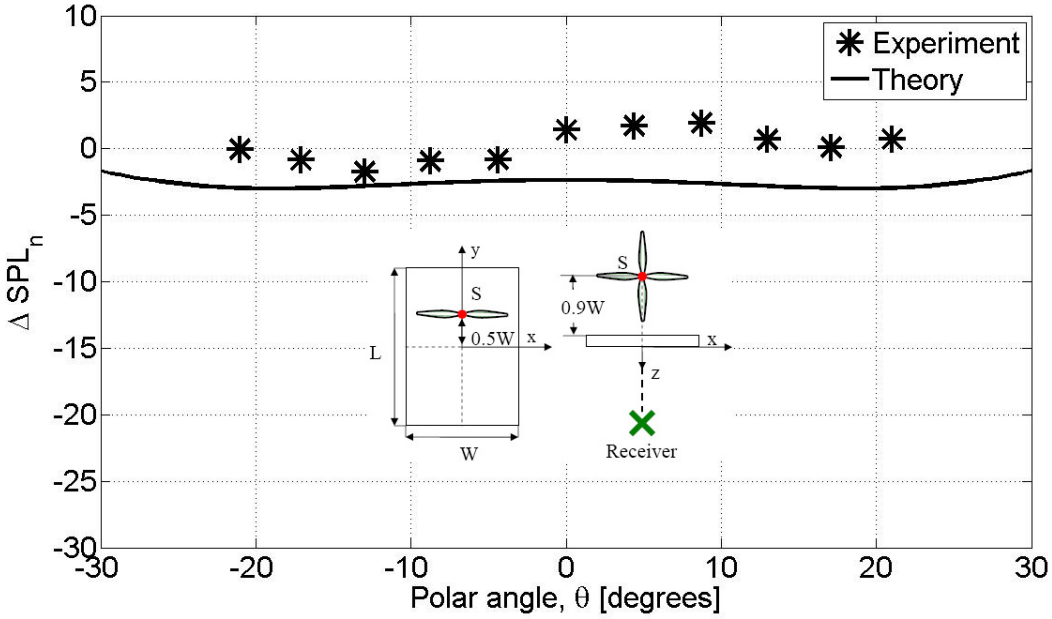

(a)

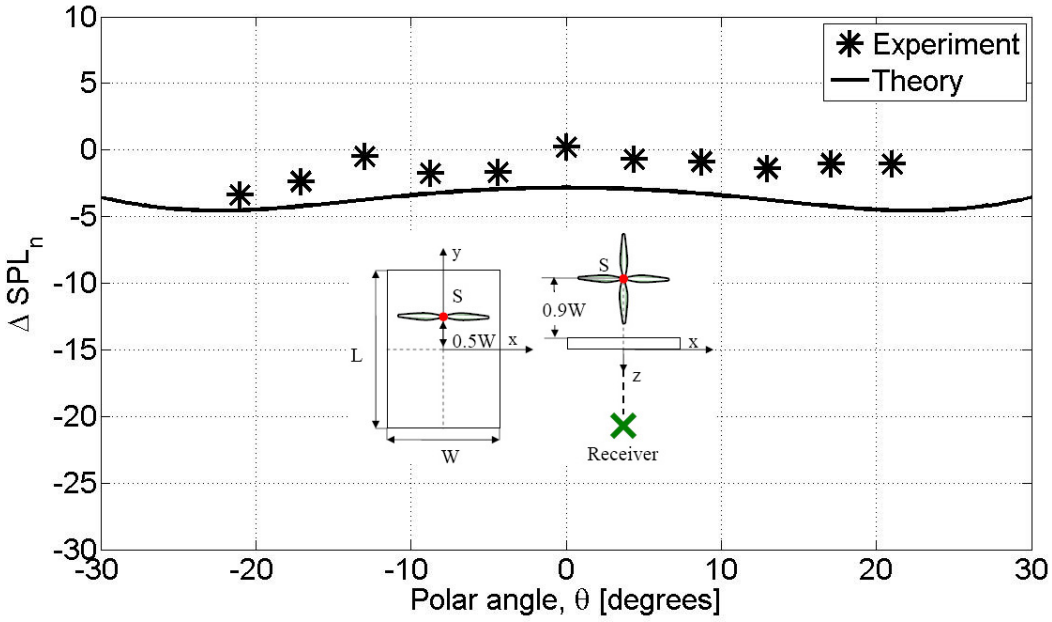

(b)

Figure 111: Noise shielding for a rotor source, as a function of polar angle, θ. $f = 1200Hz$, $kW = 7.15$, $L/W = 1.8$, $D = W/2$, $kz = 42.9$, (a) $\phi = 13^o$, (b) $\phi = 0^o$.

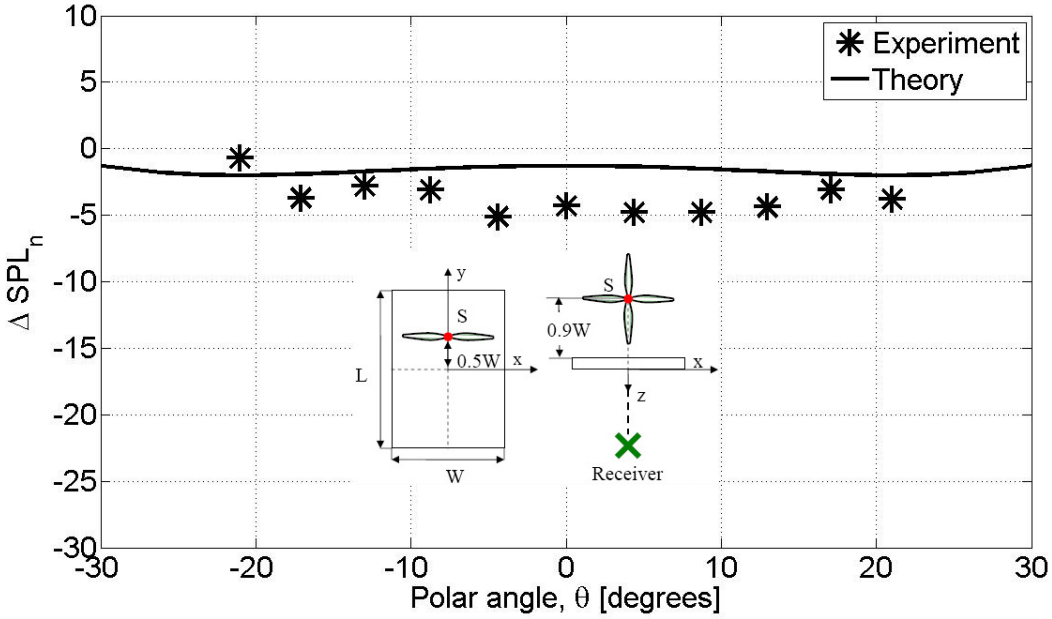

(a)

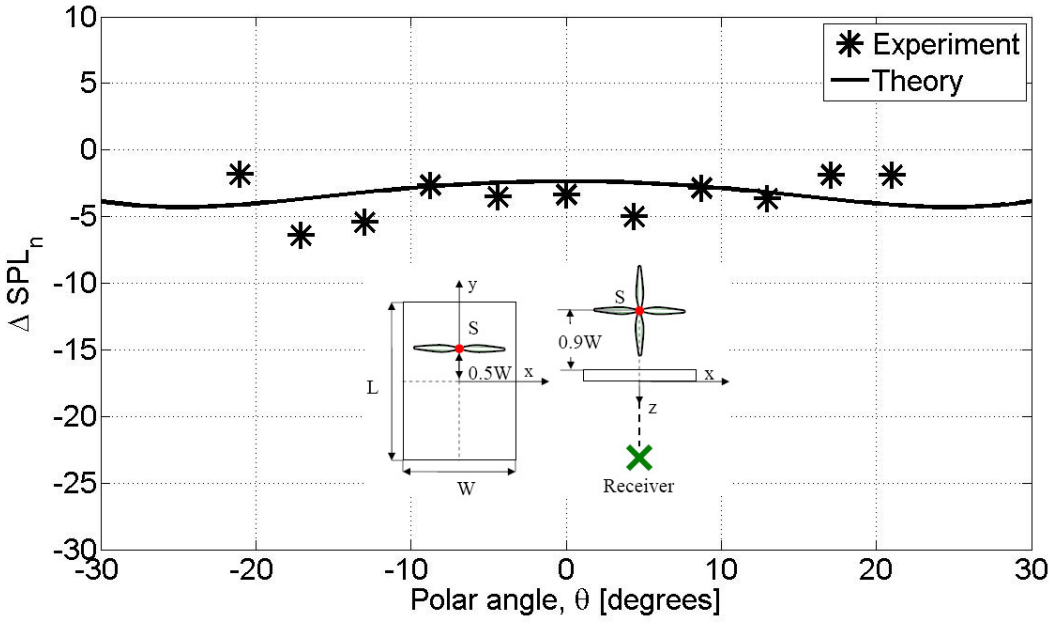

(b)

Figure 112: Noise shielding for a rotor source, as a function of polar angle, θ. $f = 1100Hz$, $kW = 6.5$, $L/W = 1.8$, $D = W/2$, $kz = 39$, (a) $\phi = 13^o$, (b) $\phi = 0^o$.

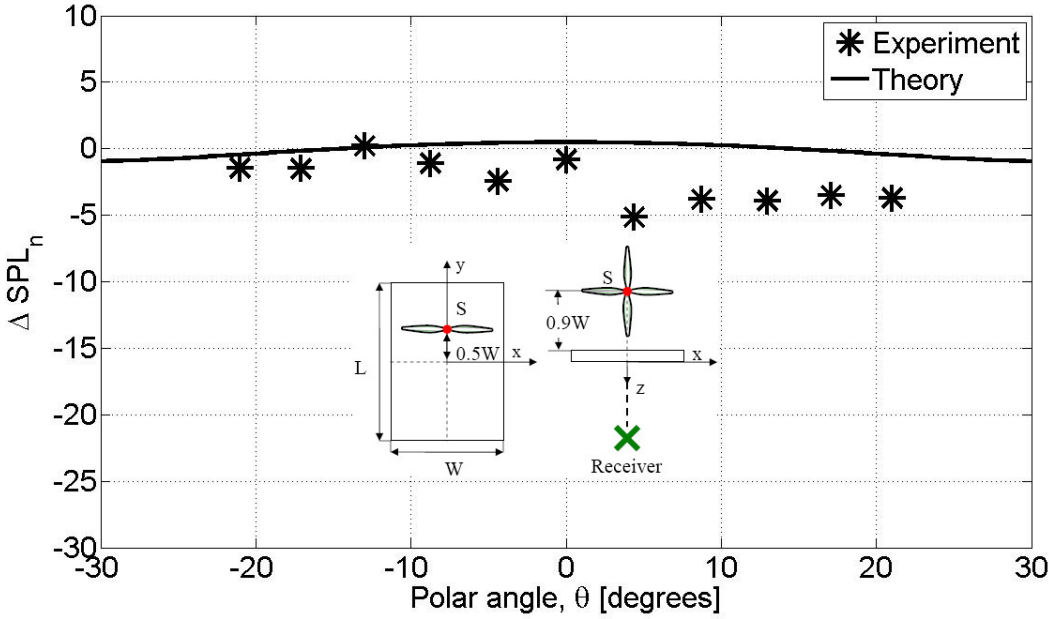

(a)

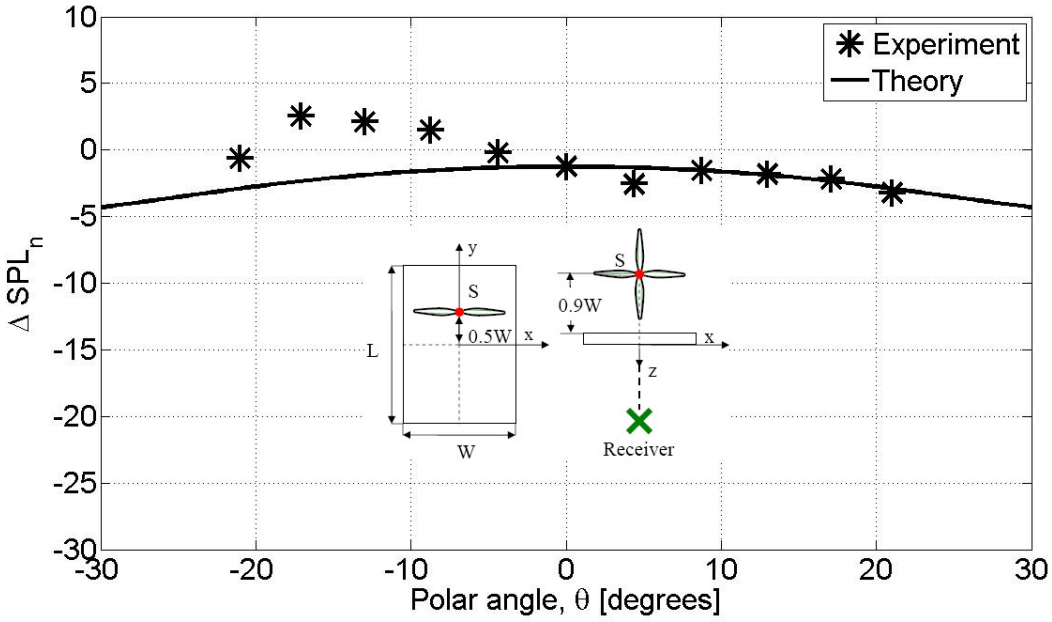

(b)

Figure 113: Noise shielding for a rotor source, as a function of polar angle, θ. $f = 800Hz$, $kW = 4.81$, $L/W = 1.8$, $D = W/2$, $kz = 28.9$, (a) $\phi = 13^o$, (b) $\phi = 0^o$.

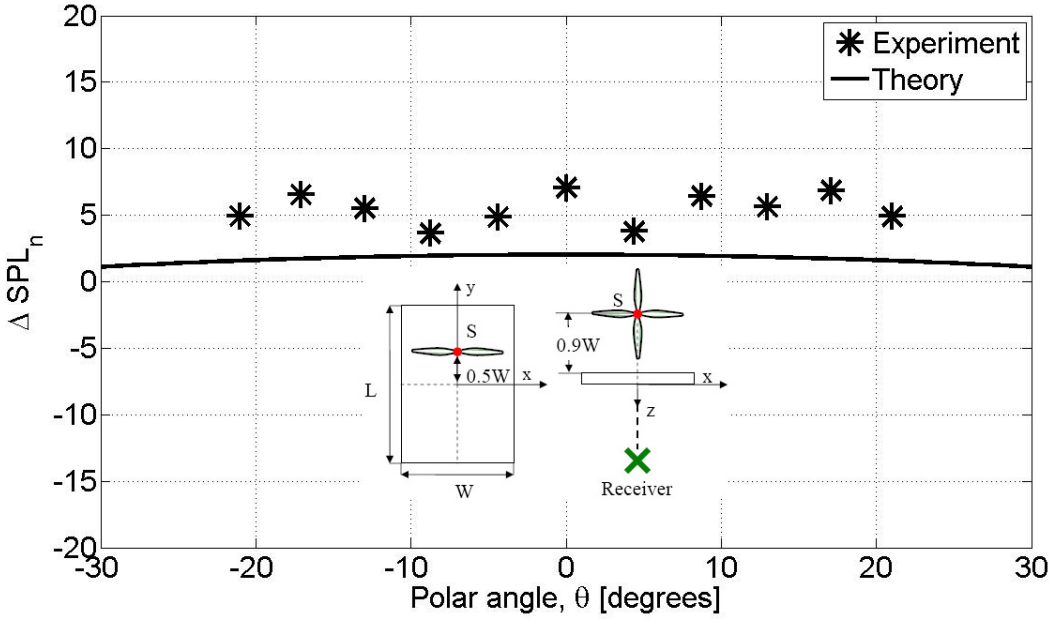

(a)

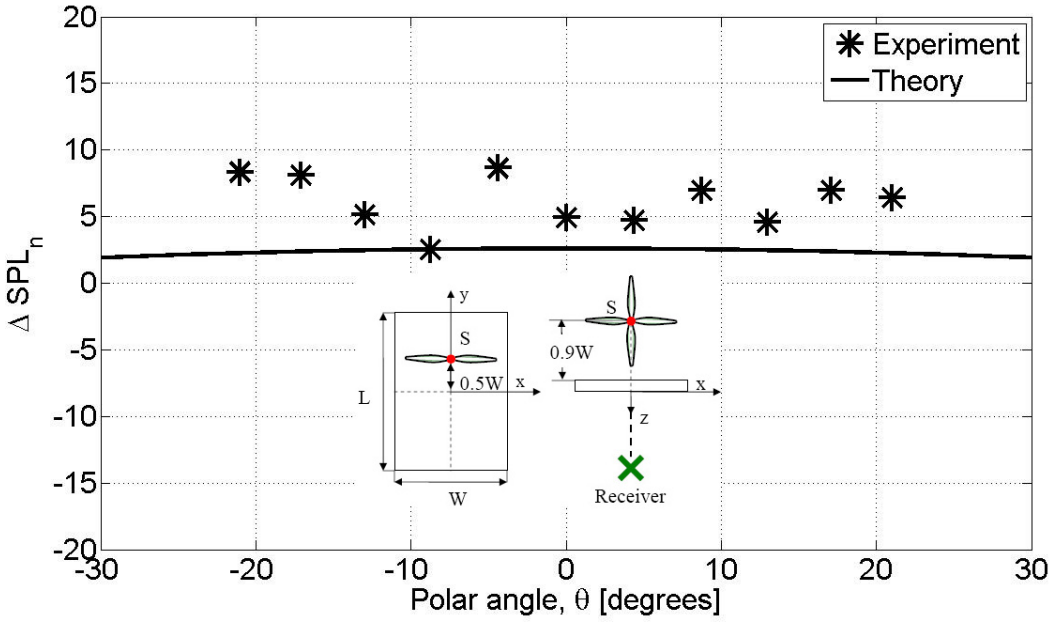

(b)

Figure 114: Noise shielding for a rotor source, as a function of polar angle, θ. $f = 400Hz$, $kW = 2.47$, $L/W = 1.8$, $D = W/2$, $kz = 14.8$, (a) $\phi = 13^o$, (b) $\phi = 0^o$.

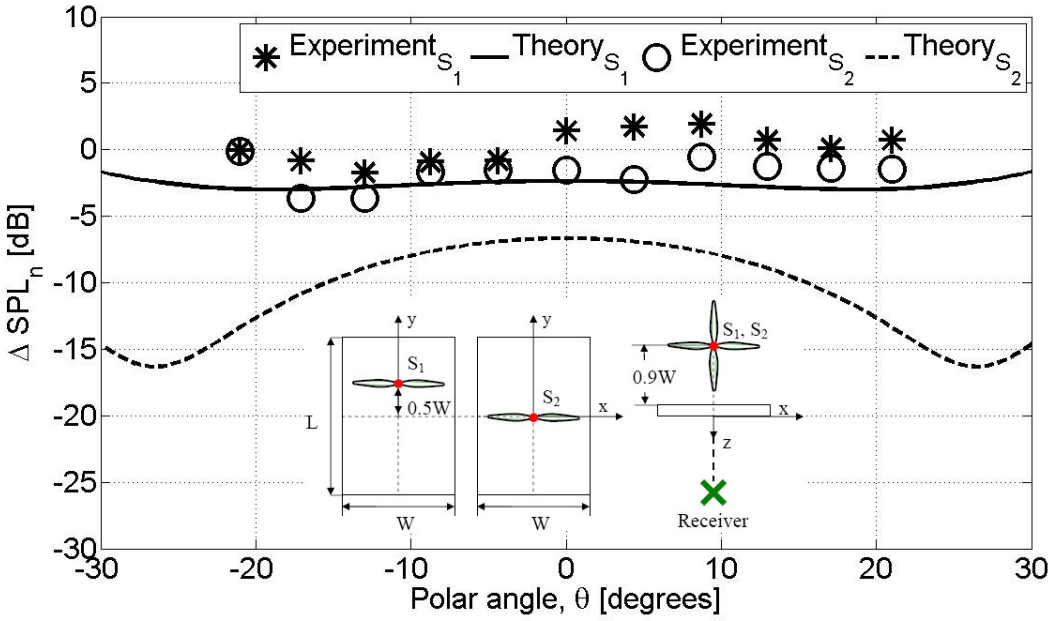

(a)

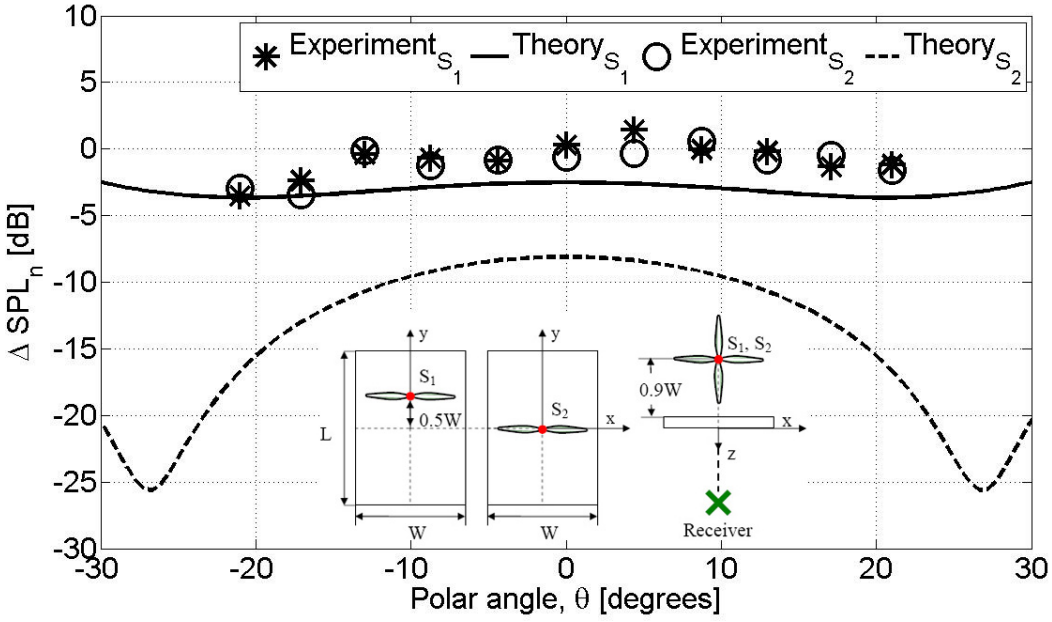

(b)

Figure 115: Effect of source location for a shielded rotor source, as a function of polar angle, θ. $f = 1200Hz$, $kW = 7.15$, $L/W = 1.8$, $D = W/2$, $kz = 42.9$, (a) $\phi_1 = 13^o$, $\phi_2 = 8.7^o$, (b) $\phi_1 = 0^o$, $\phi_2 = 0^o$.

Hz and 400 Hz are shown in Figure 116 and 117, respectively.

In general, it was observed that when the source is shifted forward, the experimental shielding levels did not change as much as the calculated levels (for a point source), at high frequencies. Previous calculations (given in Chapter 3) performed moving the point source forward showed that as the point source moves farther away from the center, the shielding decreases and the rate of decrease becomes slower (see Figure 14 to Figure 16).

6.2.2.2 Effect of Distance from the Back of the Shield

Effect of moving the receiver away from the shield was studied for three z coordinates of the microphone mesh shown in Figure 38. Typical results for a frequency of 1200 Hz are shown in Figure 118 for the three z values (kz = 42.9,60, and 75.9) for reducing ϕ. Note that these results are plotted together for each z in Figure 119. It is seen that propeller noise shielding measurement do not match the predictions by using a point source assumption. The conclusions are very similar for the lower frequencies (see Figure 120 - 123). If anything, in the narrow θ region increase in noise (instead of shielding) is obtained.

6.2.2.3 Effect of Shield Width

In Figure 124(a) and 124(b) the measured shielding is compared with the calculated shielding at 1200 Hz for two shield widths, $W = D$ ($L/W_1 = 3.3$) and $W = 2D$ ($L/W_1 = 1.8$), respectively. In Figure 124(c) these two cases are compared with each other. The measured data is labeled as 'Experiment' with the subscripts 'W_1' and 'W_2' for these two shield widths. The corresponding calculated values are shown as 'Theory' with the same subscripts. The wider shield labeled by 'W_2' provides more shielding.

Figures 125 and 126 show the shielding of the same configuration at 800 Hz and 400 Hz, respectively. At 800 Hz, the shielding from two widths are almost the same at most points. At 400 Hz again increase in noise is observed in both widths more than the calculations suggest and more noise increase is observed for the wider shield.

The rotor moved to $0.5W$ location and the analysis was performed for frequencies of 1200 Hz and 1100 Hz in Figures 127 and 128, respectively. Note that the data is again analyzed at $\phi = 13^o$. In each case shielding measurement match 2-3 dB compared to theoretical

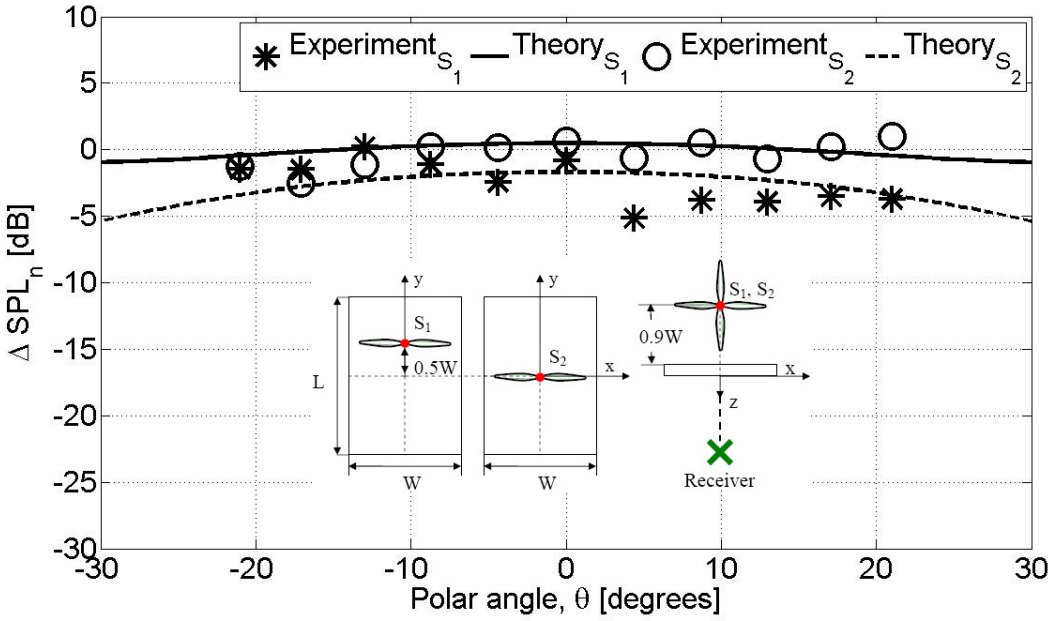

(a)

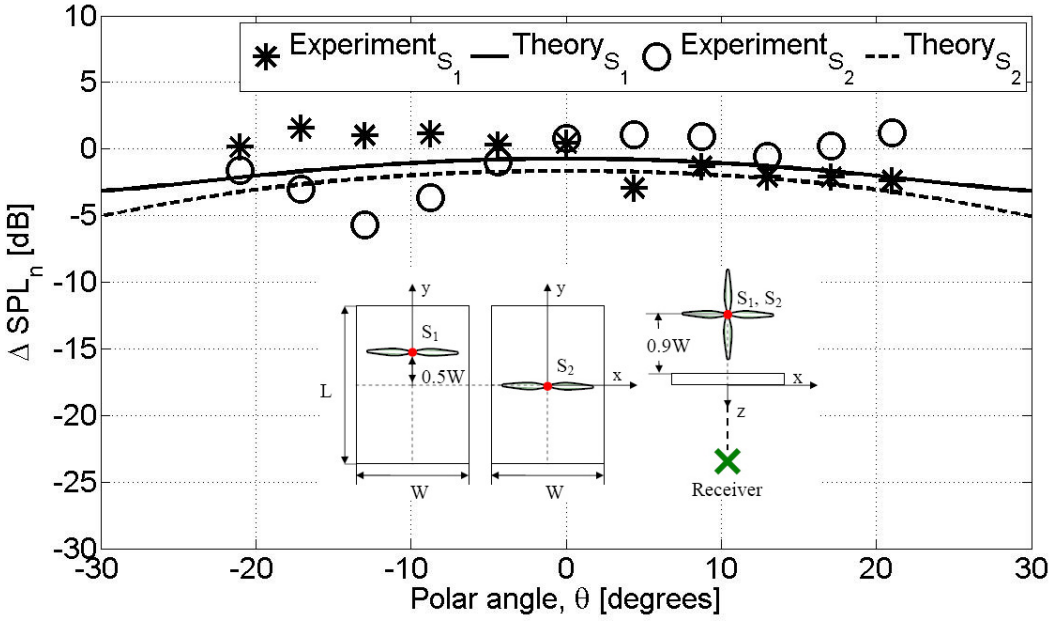

(b)

Figure 116: Effect of source location for a shielded rotor source, as a function of polar angle, θ. $f = 800Hz$, $kW = 4.81$, $L/W = 1.8$, $D = W/2$, $kz = 28.9$, (a) $\phi_1 = 13^o$, $\phi_2 = 8.7^o$, (b) $\phi_1 = 0^o$, $\phi_2 = 0^o$.

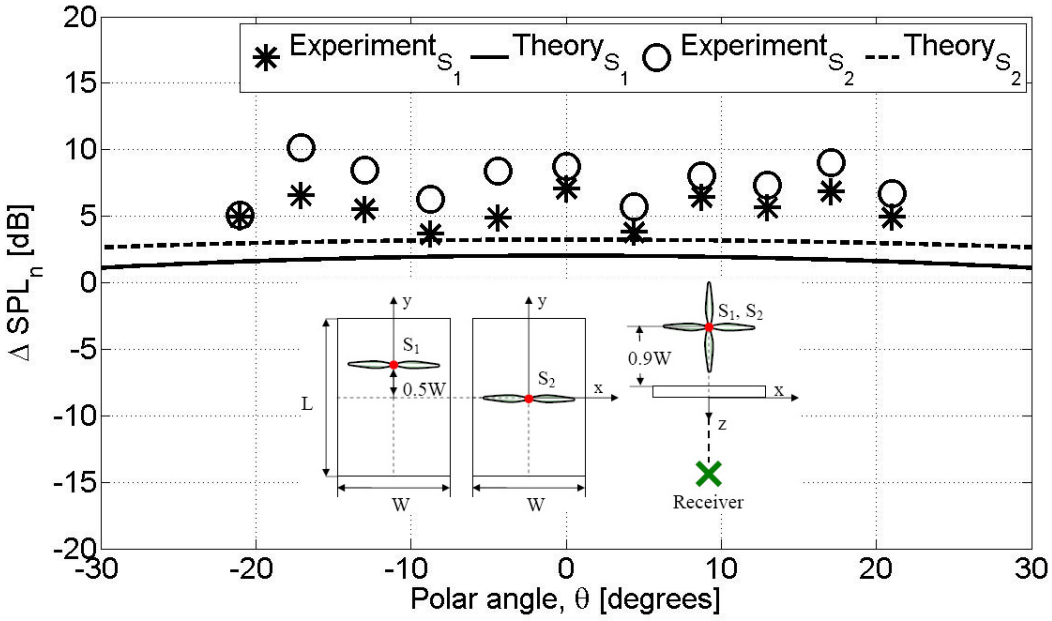

(a)

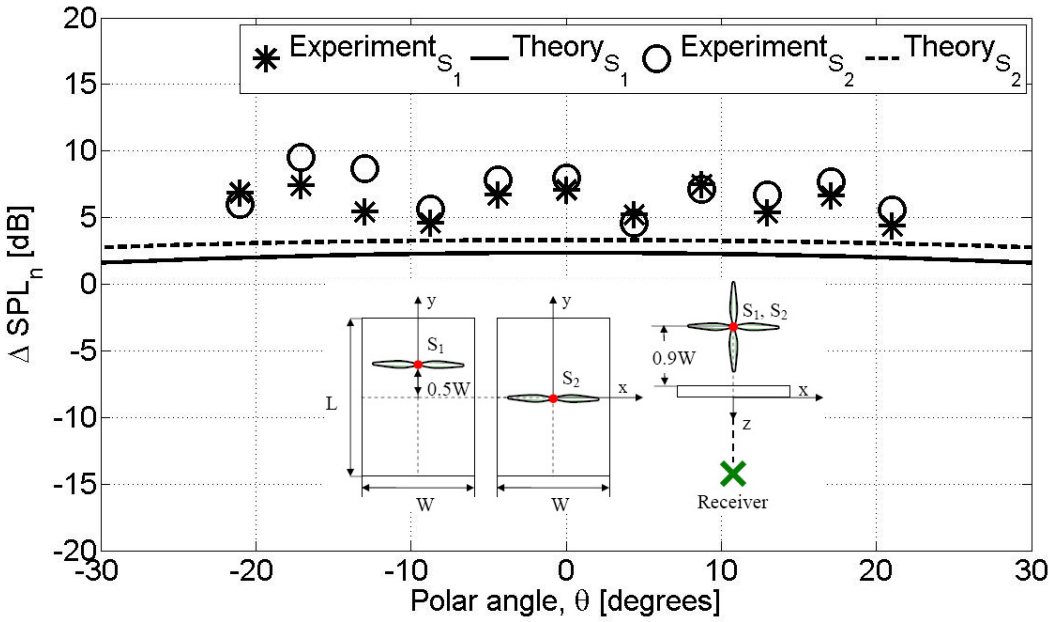

(b)

Figure 117: Effect of source location for a shielded rotor source, as a function of polar angle, θ. $f = 400Hz$, $kW = 2.47$, $L/W = 1.8$, $D = W/2$, $kz = 14.8$, (a) $\phi_1 = 13^o$, $\phi_2 = 8.7^o$, (b) $\phi_1 = 0^o$, $\phi_2 = 0^o$.

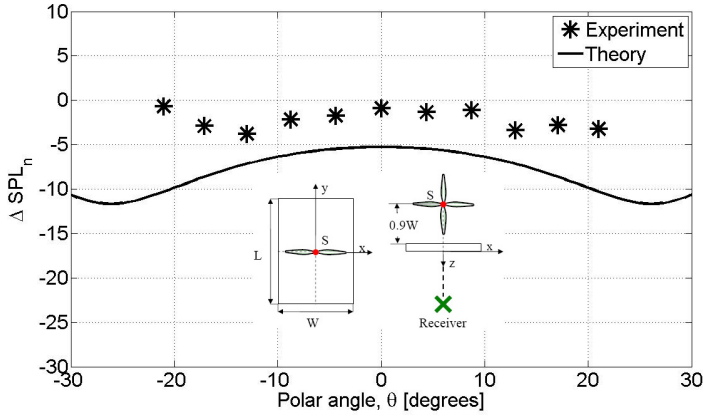

(a)

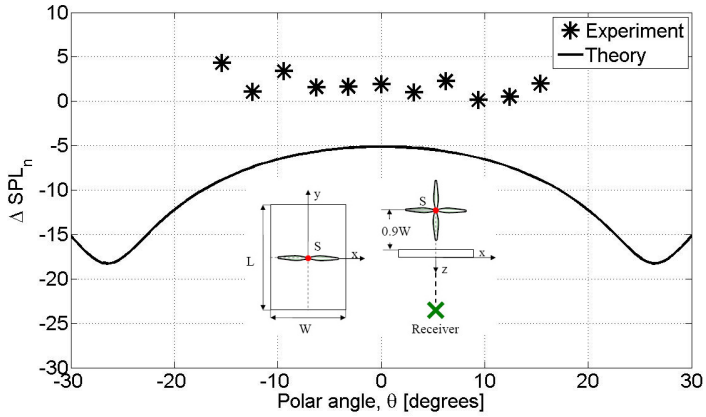

(b)

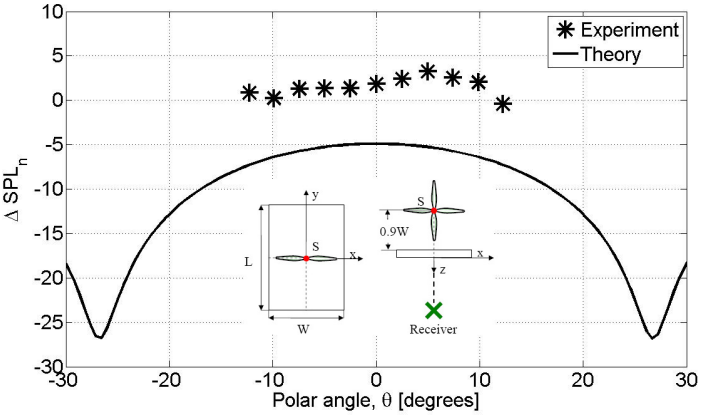

(c)

Figure 118: Effect of measurement distance for a rotor source, as a function of polar angle, θ. $f = 1200$ Hz, $kW = 7.15$, $L/W = 1.8$, (a) $kz = 42.9$, $\phi_1 = 13^o$, (b) $kz = 60$, $\phi_2 = 9.4^o$, (c) $kz = 75.9$, $\phi_2 = 7.4^o$.

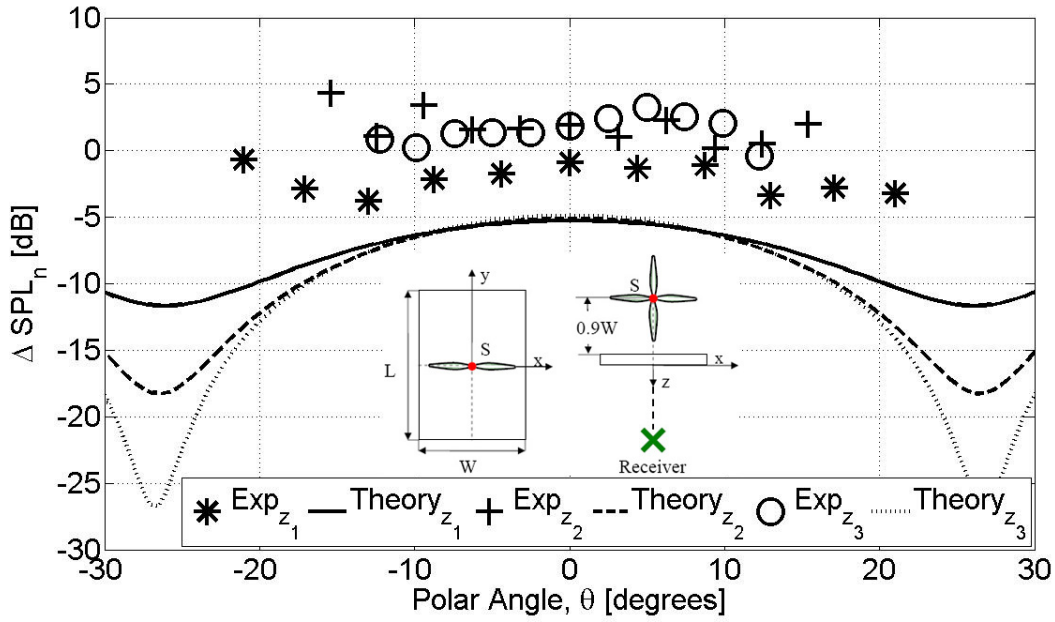

Figure 119: Effect of measurement distance comparatively for a rotor source, as a function of polar angle, θ. $f = 1200Hz$, $kW = 7.15$, $L/W = 1.8$, $kz = 42.9$, $kz_2 = 60$, $kz_3 = 75.9$, $\phi_1 = 13^o$, $\phi_2 = 9.4^o$, $\phi_3 = 7.4^o$.

predictions assuming the source is a point source.

Note that the dips associated with destructive interference show up neither in the theoretical results nor in the measurements. This is because these results are for the configuration where the rotor was not above the center of the shield. It was off-center shifted towards the smaller edge by $0.5W$ as shown schematically on the figures.

The lower frequencies 800 Hz and 400 Hz are presented in Figures 129 and 130, respectively.

6.2.3 Experiments with a Round Duct as a Shield (Ducted Rotor)

Data for the unducted and ducted rotor will be compared in this section. The word 'Shielding' is being used to refer to the difference between the ducted and the unducted SPLs. It is appreciated that a more elegant and proper approach will be explore duct propagation theory and account for the reflections at the two termination of the duct and then study the transmission of sound to the far field. This is beyond the scope of the present thesis. Duct propagation theories often assume an infinitely long duct. In the present study,

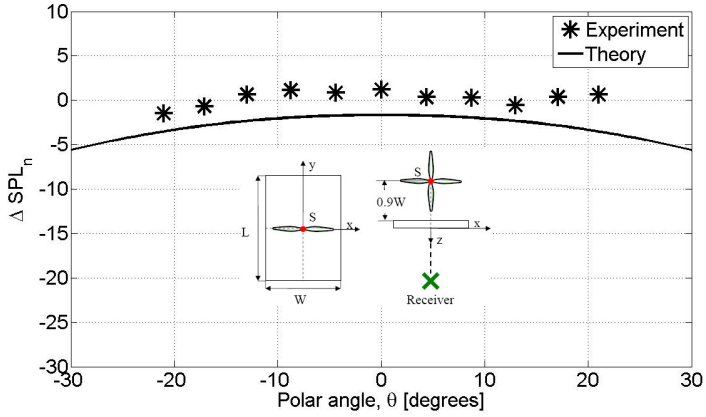

(a)

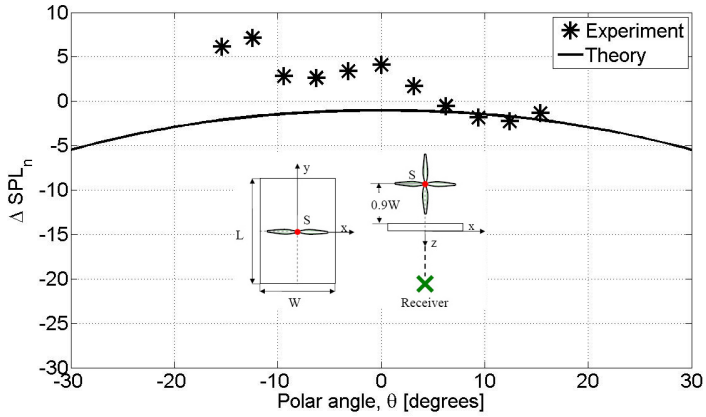

(b)

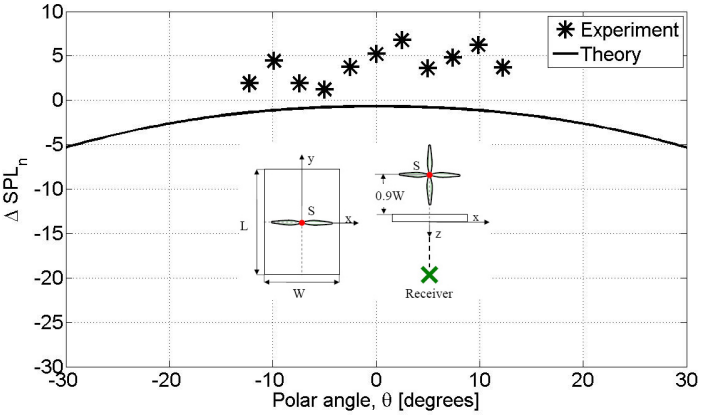

(c)

Figure 120: Effect of measurement distance for a rotor source, as a function of polar angle, θ. $f = 800$ Hz, $kW = 4.81$, $L/W = 1.8$, (a) $kz = 28.9$, $\phi_1 = 13^o$, (b) $kz = 40.3$, $\phi_2 = 9.4^o$, (c) $kz = 51.1$, $\phi_2 = 7.4^o$.

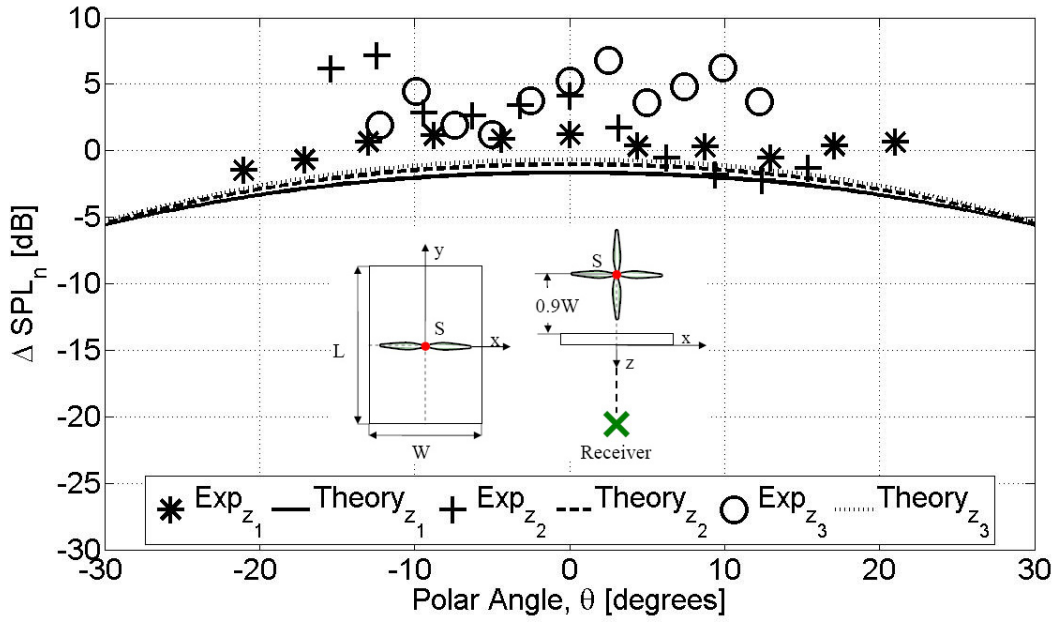

Figure 121: Effect of measurement distance for a rotor source, as a function of polar angle, θ. $f = 800Hz$, $kW = 4.81$, $L/W = 1.8$, $kz_1 = 28.9$, $kz_2 = 40.3$, $kz_3 = 51.1$, $\phi_1 = 13^o$, $\phi_2 = 9.4^o$, $\phi_3 = 7.4^o$.

smaller duct lengths were used and the goal indeed was to see if smaller shrouds for rotors could provide shielding in the sense of shielding as studied for a flat barrier. As such this section will compare the shielding provided by duct with that predicted by flat shield (both predicted and measured). Shielding produced by the ducted configuration for the rotor will be compared with that produced for a point source.

The rotor with diameter $D = 6.5''$ was placed inside a duct of inner diameter $D_D = 7''$ with a clearance of $0.25''$. The configuration is illustrated in Figure 131(a) and 131(b). A typical acoustic spectrum of ducted rotor noise is presented in Figure 132. The main thing to notice here is that the tones that appear in the unshielded case are reduced significantly in the ducted case while at the same time new tones along with the broadband noise are introduced for the ducted case. The reason for this is the resonance of the duct and the production of higher order modes. Since the duct diameter was $7''$ and the higher order modes will be introduced at frequencies higher than about 1200 Hz. So shielding by a hard-walled duct at frequencies equal to less than 1200 Hz will be considered.

Experimental findings for ducted point source and ducted rotor are compared below.

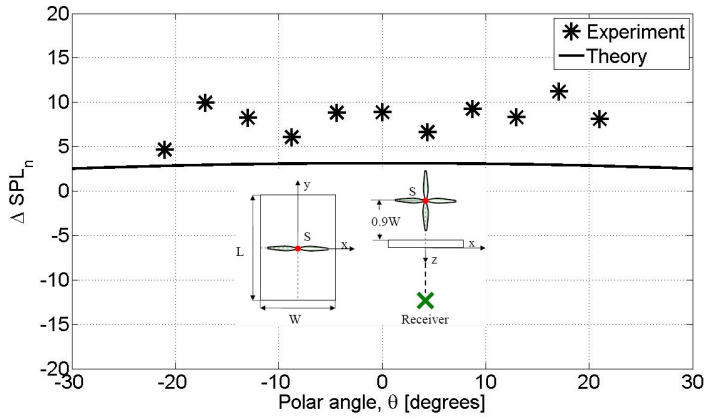

(a)

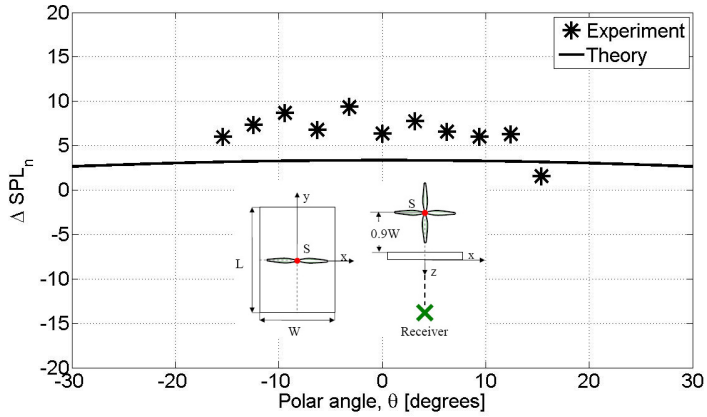

(b)

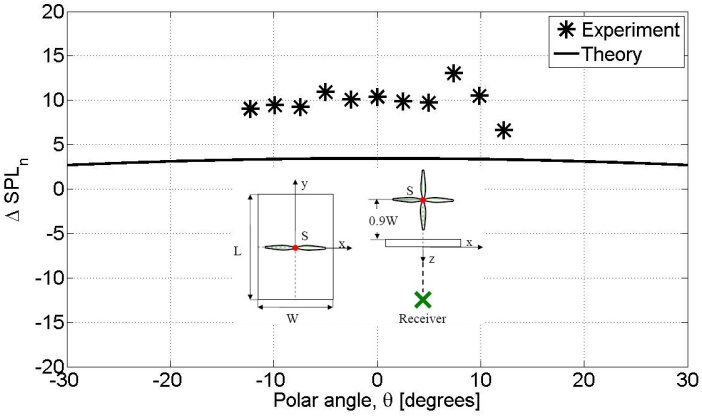

(c)

Figure 122: Effect of measurement distance for a rotor source, as a function of polar angle, θ. $f = 400$ Hz, $kW = 2.47$, $L/W = 1.8$, (a) $kz = 14.8$, $\phi_1 = 13^o$, (b) $kz = 20.7$, $\phi_2 = 9.4^o$, (c) $kz = 26.2$, $\phi_2 = 7.4^o$.

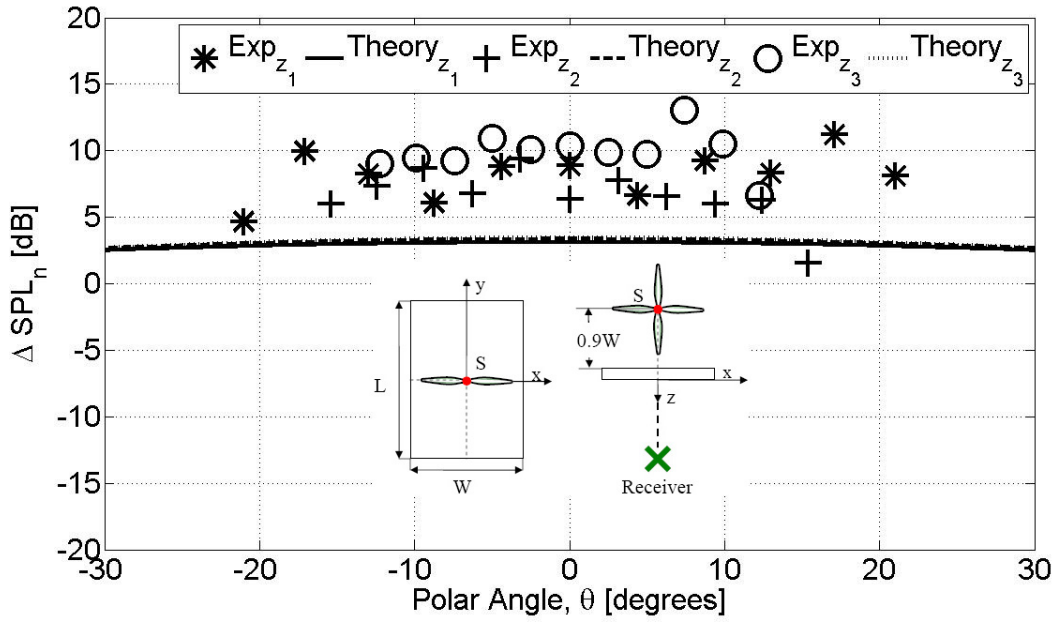

Figure 123: Effect of measurement distance for a rotor source, as a function of polar angle, θ. $f = 400Hz$, $kW = 2.47$, $L/W = 1.8$, $kz_1 = 14.8$, $kz_2 = 20.7$, $kz_3 = 26.2$, $\phi_1 = 13^o$, $\phi_2 = 9.4^o$, $\phi_3 = 7.4^o$.

Before presenting the results it should be brought to the reader's attention that some of the discrete tone data presented in this section have the possibility to being contaminated by the broadband noise. In Figure 132, a spectrum of ducted rotor noise was presented. The spectrum belongs to a 4-bladed rotor ran at 6000 rpm. It is seen that, the difference between 400 Hz and 1200 Hz peaks and the broadband noise is smaller than 10 dB. However these two frequencies have been the concern of this work up to now. So even though the data might be somewhat contaminated by other noise, the results are presented here.

The findings at 1200 Hz are given in Figure 133 when the receiver is at $\phi = 11.8^o$ azimuthal angle. The results for the duct with shorter length, Figure 133(a), shows 5 to 15 dB difference between the rotor source and the point source shielding. When the duct length is increased, Figure 133(b), better match is obtained between the two sources. In $\theta \in [-10^o, 10^o]$ range shielding for two sources perfectly match and at wider angles the difference can go up to 5 dB. When the receiver moves to $\phi = 0^o$ as in Figure 134 the shielding match is even better. In Figure 134(b) the shielding difference between two sources is not more than 3 dB. Although the ducted rotor source shows closer results to

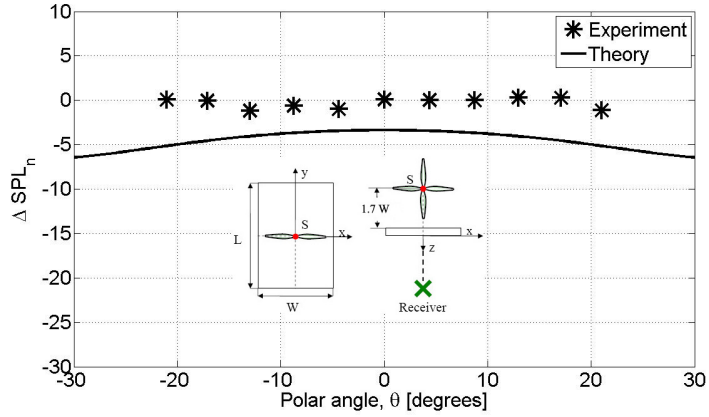

(a)

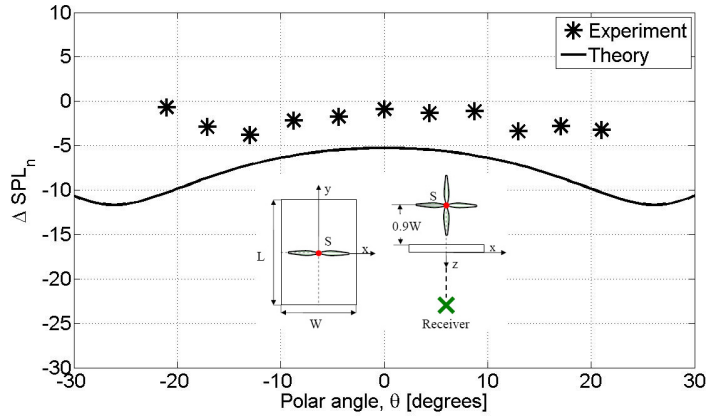

(b)

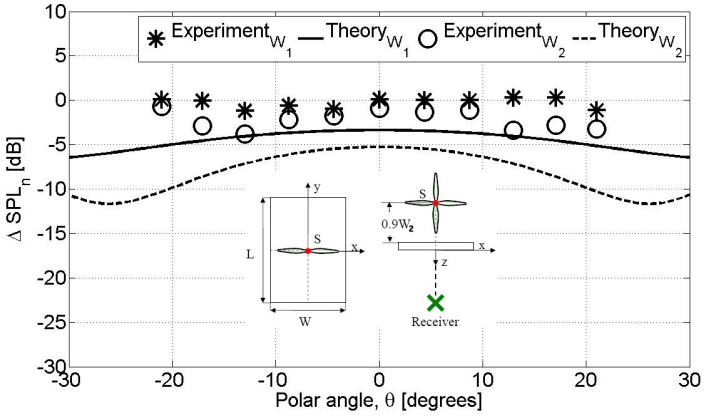

(c)

Figure 124: Effect of shield width for a rotor source, as a function of polar angle, θ. $f = 1200$ Hz, $kz = 42.9$, $\phi = 13^o$ (a) $kW_1 = 3.98$, $L/W_1 = 3.3$, (b) $kW_2 = 7.15$, $L/W_2 = 1.8$, (c) comparison of W_1 and W_2.

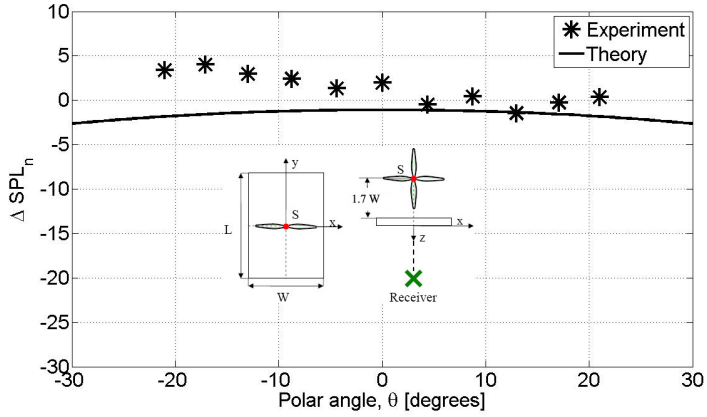

(a)

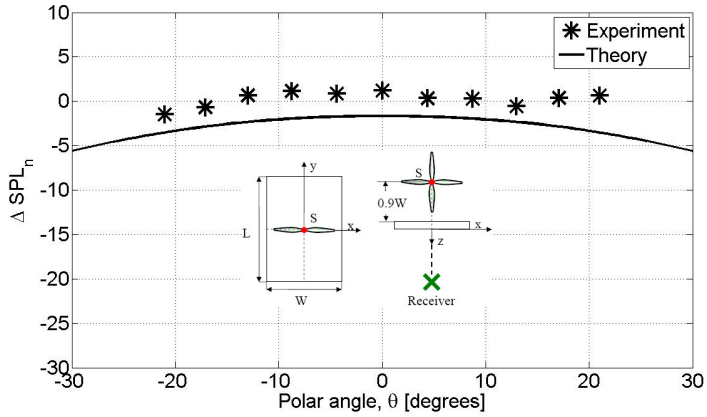

(b)

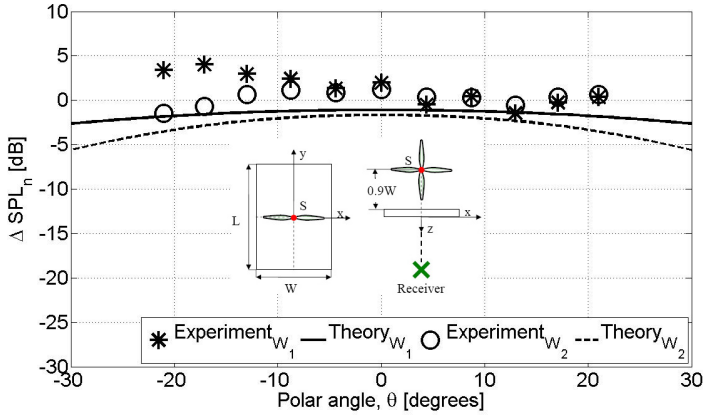

(c)

Figure 125: Effect of shield width for a rotor source, as a function of polar angle, θ. $f = 800$ Hz, $kz = 28.9$, $\phi = 13^o$ (a) $kW_1 = 2.68$, $L/W_1 = 3.3$, (b) $kW_2 = 4.81$, $L/W_2 = 1.8$, (c) comparison of W_1 and W_2.

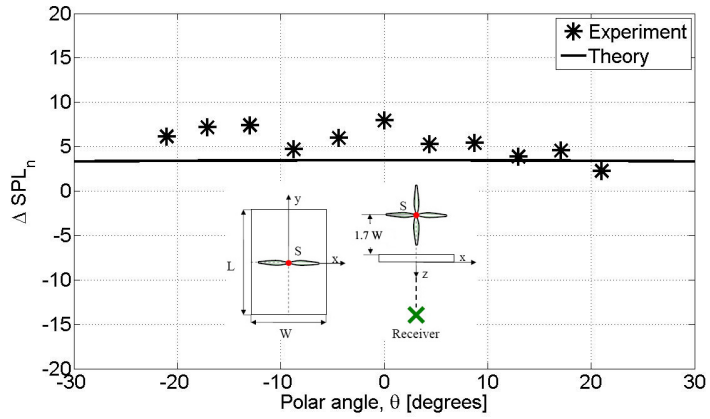

(a)

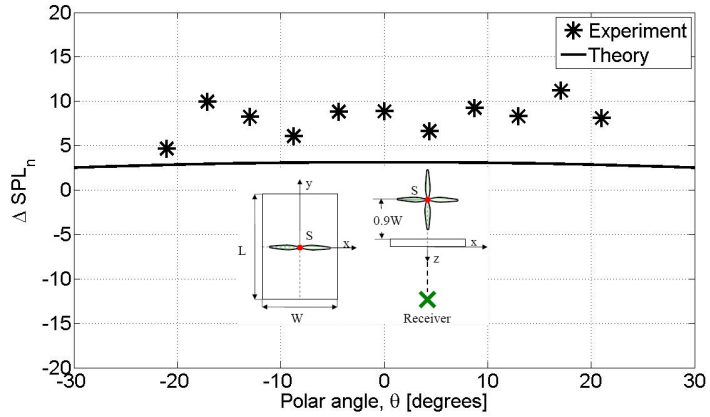

(b)

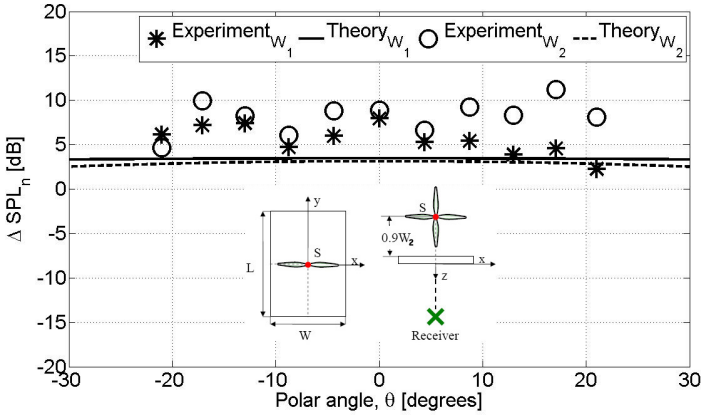

(c)

Figure 126: Effect of shield width for a rotor source, as a function of polar angle, θ. $f = 400$ Hz, $kz = 14.8$, $\phi = 13^o$ (a) $kW_1 = 1.37$, $L/W_1 = 3.3$, (b) $kW_2 = 2.47$, $L/W_2 = 1.8$, (c) comparison of W_1 and W_2.

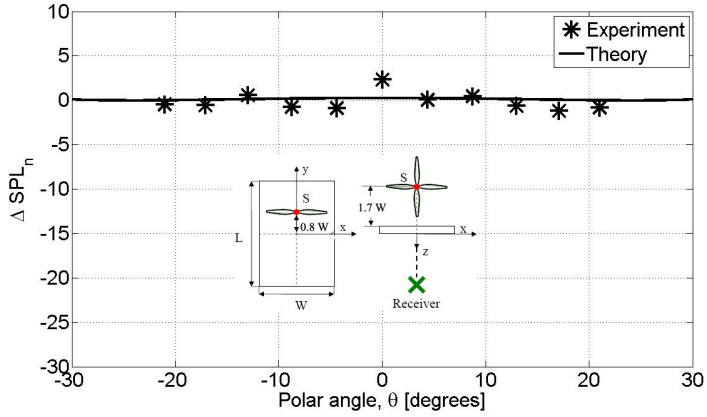

(a)

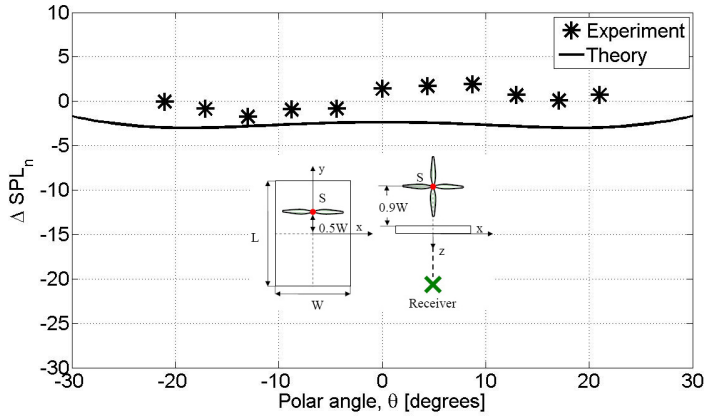

(b)

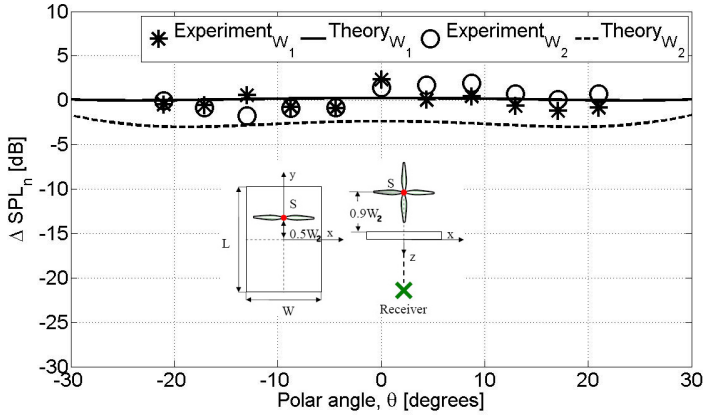

(c)

Figure 127: Effect of shield width for a rotor source, as a function of polar angle, θ. $f = 1200$ Hz, $kz = 42.9$, $\phi = 13^o$ (a) $kW_1 = 3.98$, $L/W_1 = 3.3$, (b) $kW_2 = 7.15$, $L/W_2 = 1.8$, (c) comparison of W_1 and W_2.

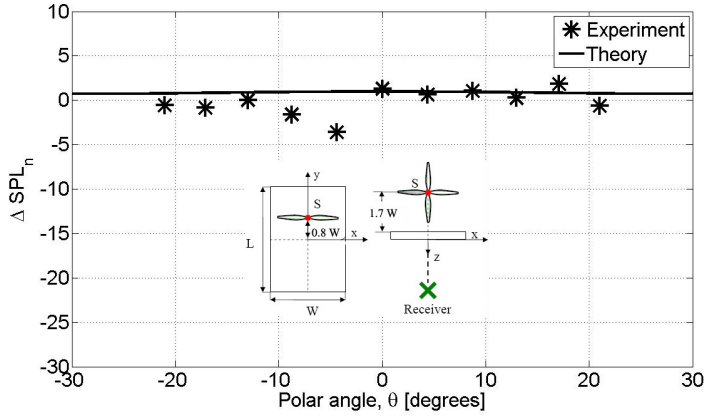

(a)

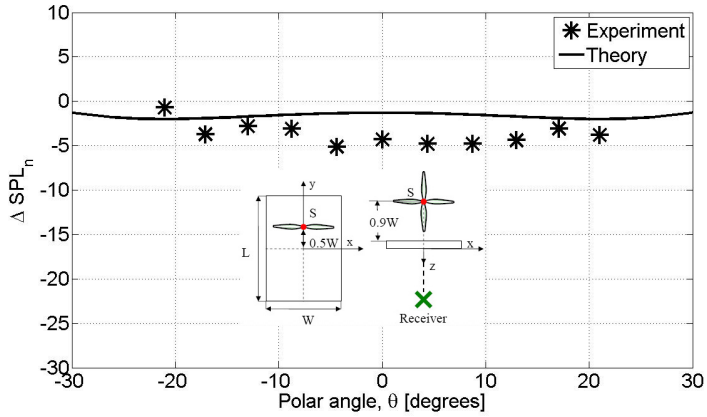

(b)

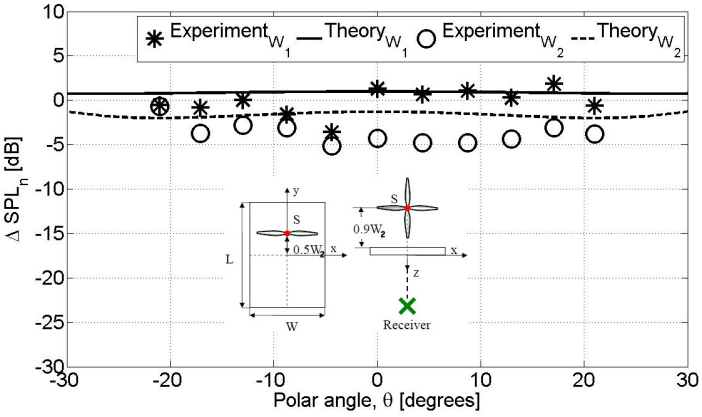

(c)

Figure 128: Effect of shield width for a rotor source, as a function of polar angle, θ. $f = 1100$ Hz, $kz = 39$, $\phi = 13^o$ (a) $kW_1 = 3.13$, $L/W_1 = 3.3$, (b) $kW_2 = 6.5$, $L/W_2 = 1.8$, (c) comparison of W_1 and W_2.

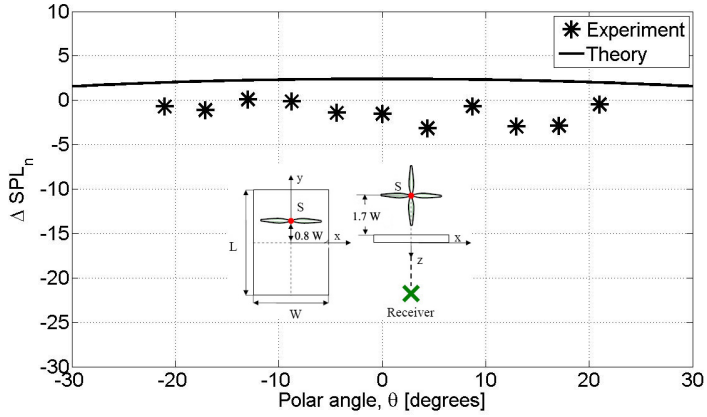

(a)

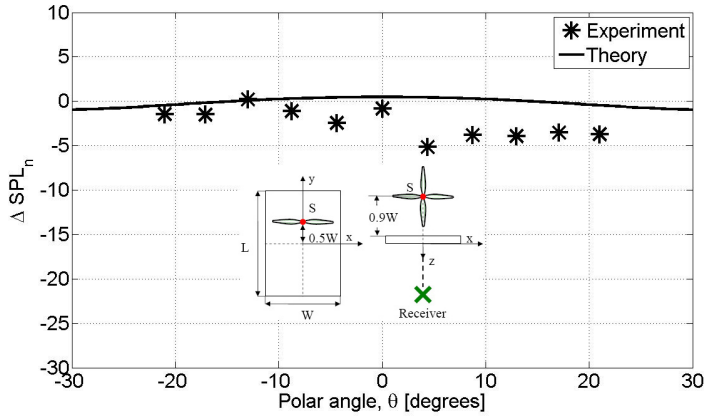

(b)

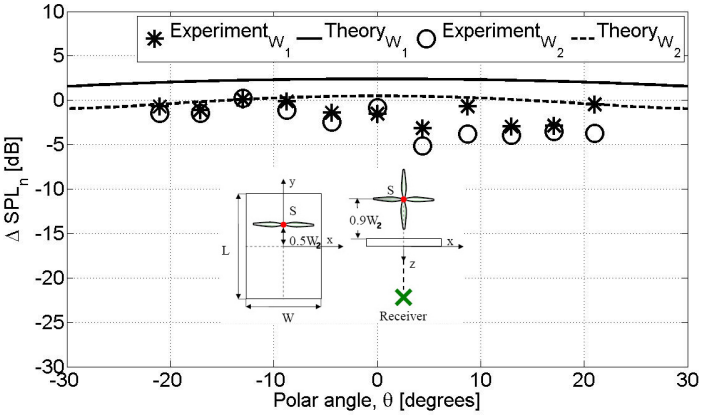

(c)

Figure 129: Effect of shield width for a rotor source, as a function of polar angle, θ. $f = 800$ Hz, $kz = 28.9$, $\phi = 13^o$ (a) $kW_1 = 2.68$, $L/W_1 = 3.3$, (b) $kW_2 = 4.81$, $L/W_2 = 1.8$, (c) comparison of W_1 and W_2.

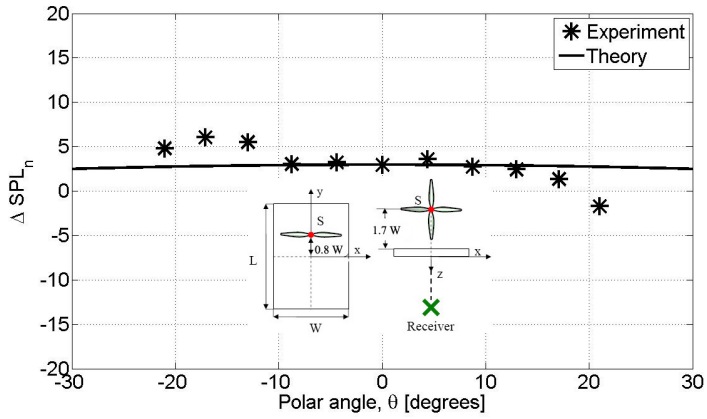

(a)

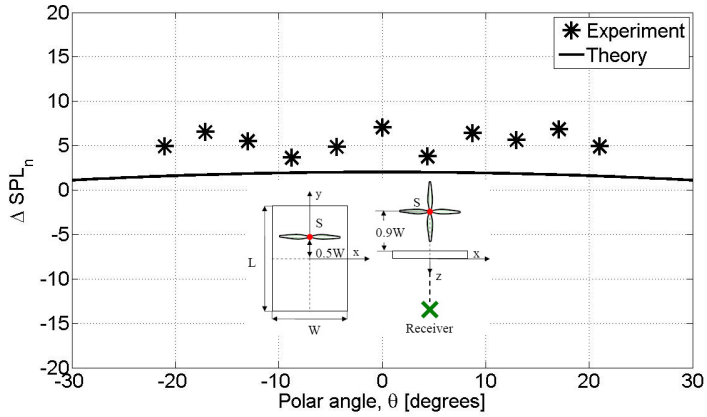

(b)

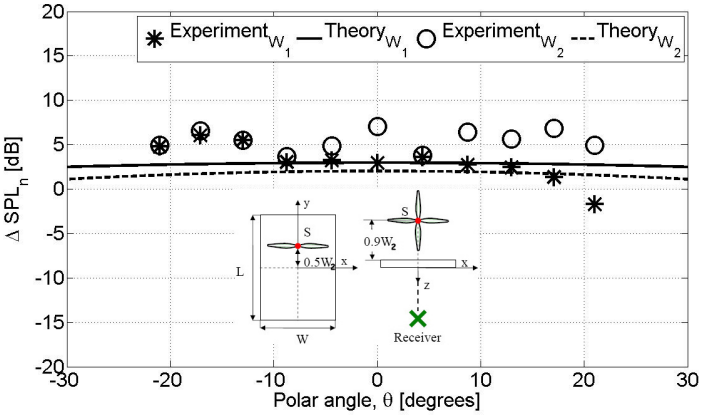

(c)

Figure 130: Effect of shield width for a rotor source, as a function of polar angle, θ. $f = 400$ Hz, $kz = 14.8$, $\phi = 13^o$ (a) $kW_1 = 1.37$, $L/W_1 = 3.3$, (b) $kW_2 = 2.47$, $L/W_2 = 1.8$, (c) comparison of W_1 and W_2.

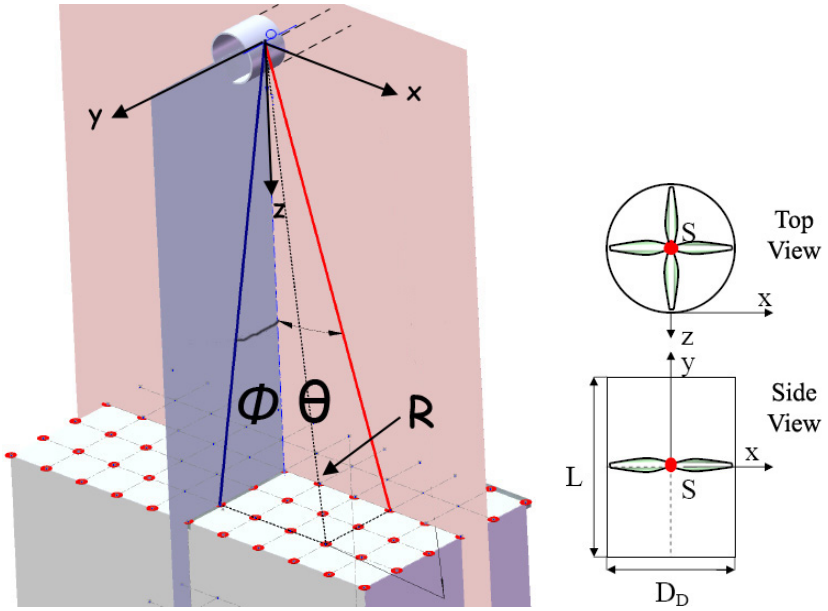

Figure 131: Illustration of ducted rotor configuration, (a) main measurement parameters, (b) rotor placement inside the duct.

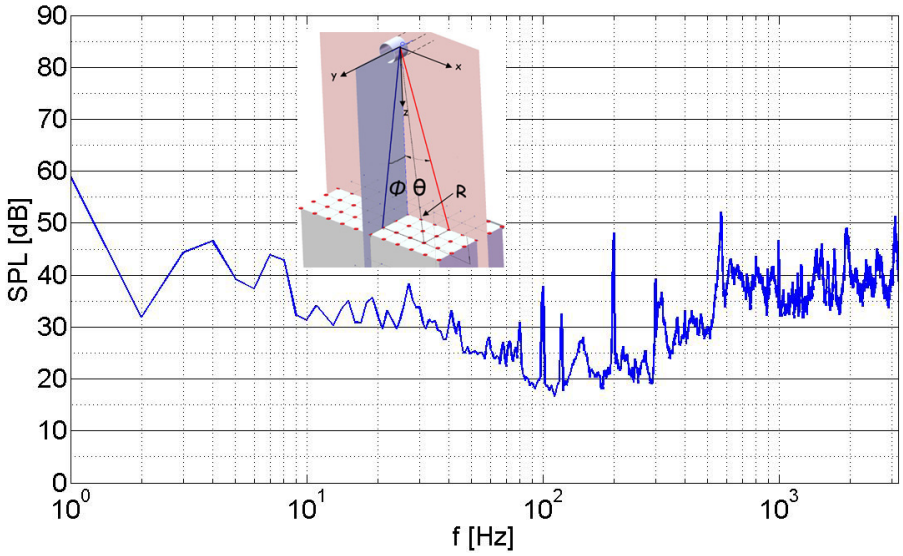

Figure 132: Spectrum of rotor noise shielded by a cylindrical barrier. $D = 6.5''$, $L = 12''$, $z = 87.5''$, $\theta = 0^o$, $\phi = 0^o$, $n_B = 4$, $\Delta f = 1$ Hz.

ducted point source when the receiver is at $\phi = 0^o$, it is not a consistent behavior and does not apply for the higher azimuthal angle. On the other hand, for longer duct, the point source appears to give better estimates to rotor source.

Figure 135 shows the results at the lower frequency of 400 Hz for two different duct lengths when the receiver is at $\phi = 11.8^o$ azimuthal angle. There is 25 to 30 dB difference between the rotor source and the point source in terms of shielding. It appears that shielding levels are much higher for the point source compared to the rotor source.

6.3 Multiple Point Source Simulation for Shielding

In Section 6.2.2, it was found that the shielding produced by the rectangular barrier for the rotor source was much less than that predicted for a point monopole source. In addition, the sharp peaks and valleys calculated for the point source were not so sharp for the rotor source or were almost non-existent. It was hypothesized that this may be a result of the rotor source being made up of a number of point sources over the rotor disc. To test this hypothesis, additional calculations were carried out by placing multiple sources above the rectangular barrier. As shown below, it was indeed found that assuming the rotor to be made up of multiple point sources, reduced magnitude of the peaks and valleys in the shielding curve and also reduced the overall shielding just as observed in the experiments.

The theoretical analysis for this multiple point source simulation is discussed below. Example of application of this analysis to various rotor/shield configurations is then provided and selected comparisons of the measured results with the new calculations are presented.

6.3.1 Theoretical Analysis

The SPL of the center source shown in Figure 137(a), was distributed into n point sources with equal SPL and placed on the circle shown in Figure 137(b). It was assumed that the sum of power levels of each of the n sources was equal to that of the single point source at the center of the rotor. Various multiple point source configurations were tried which included point sources on a circle representing the rotor tip, (Figure 137(b)), point sources on two circles, i.e., rotor tip and the circle passing through the half radius of the blade (Figure 137(c)), and on four circles as shown in Figure 137(d). After many trials it was

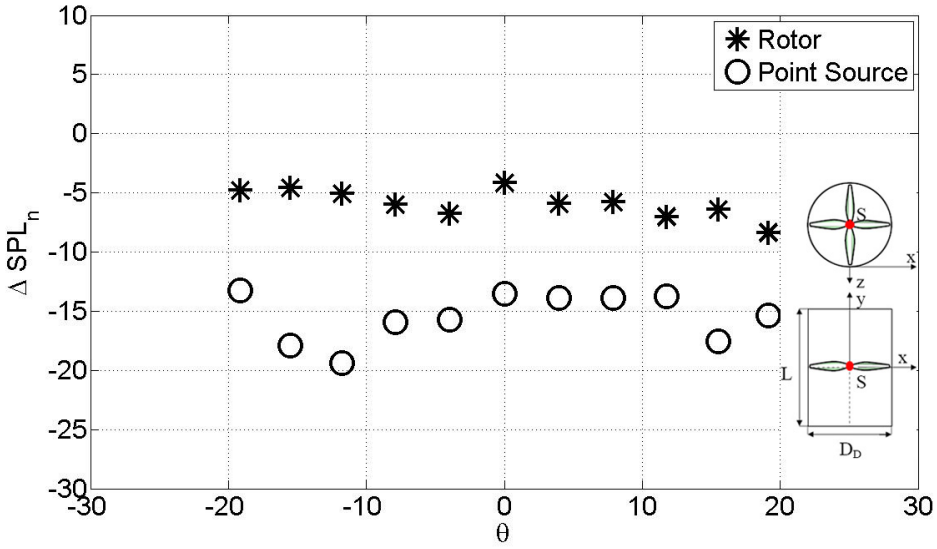

(a)

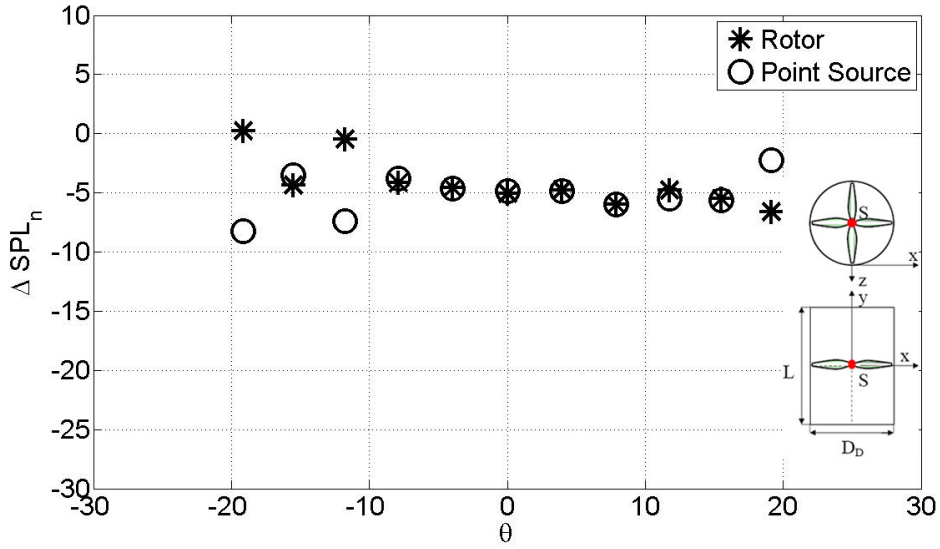

(b)

Figure 133: Comparison of noise shielding for a point source and a rotor placed inside a duct, as a function of polar angle, θ. $f = 1200Hz$, $\phi = 11.8^o$, $kz = 47.6$, (a) $L/D_D = 1.7$, (b) $L/D_D = 3.4$.

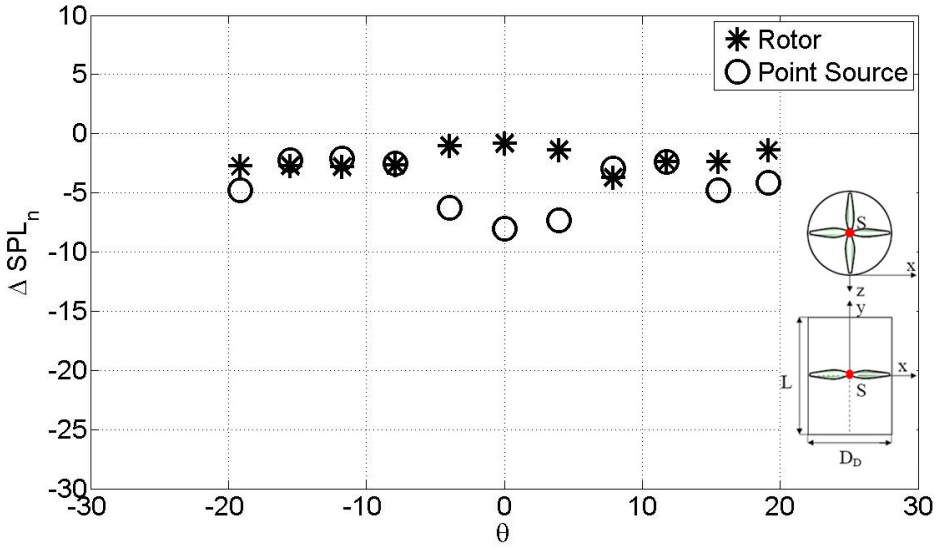

(a)

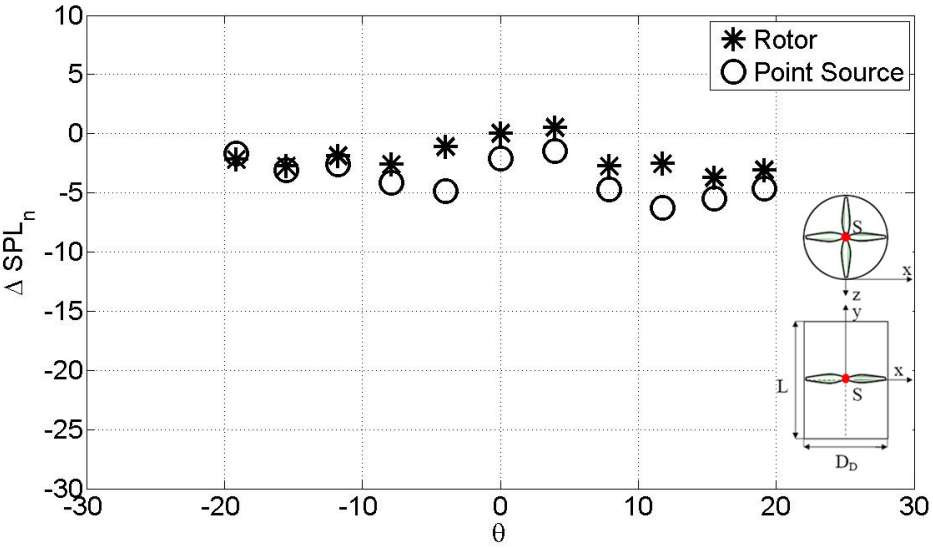

(b)

Figure 134: Comparison of noise shielding for a point source and a rotor placed inside a duct, as a function of polar angle, θ. $f = 1200Hz$, $\phi = 0^o$, $kz = 47.6$, (a) $L/D_D = 1.7$, (b) $L/D_D = 3.4$.

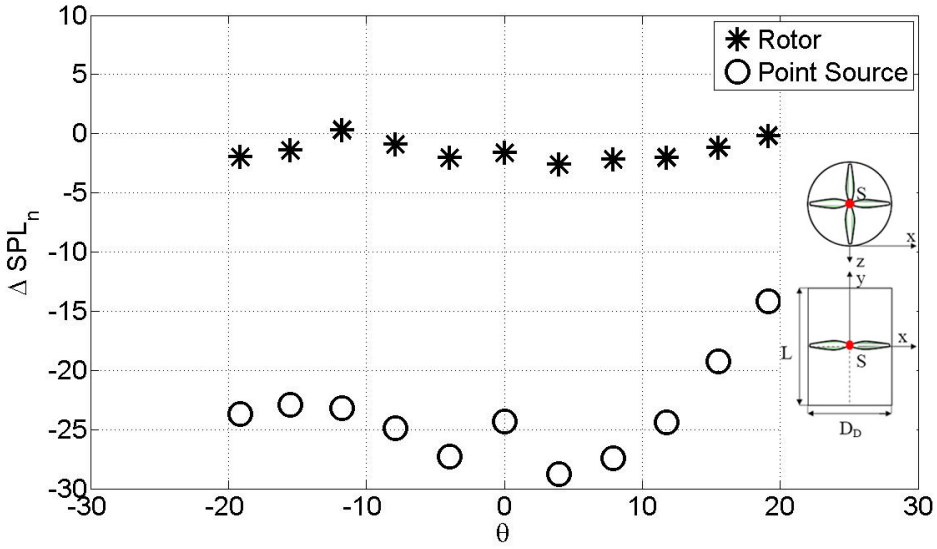

(a)

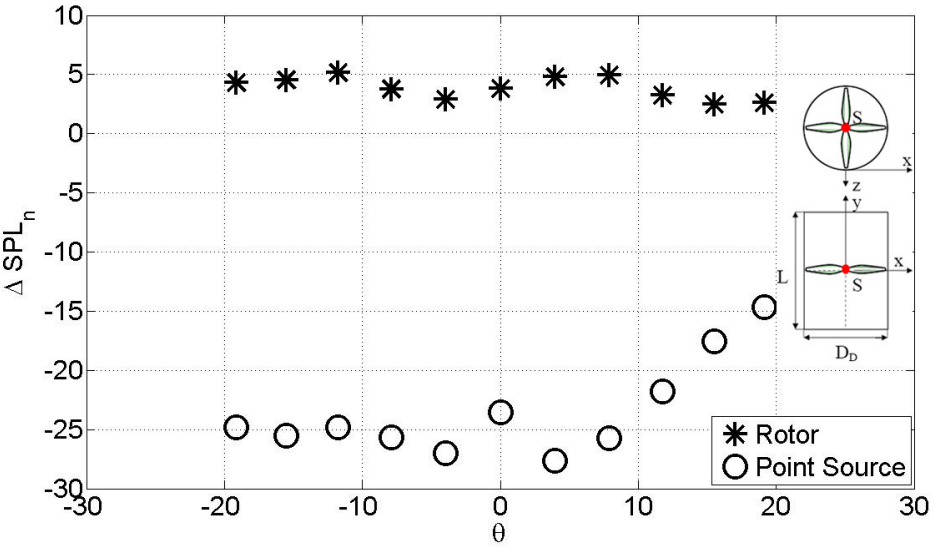

(b)

Figure 135: Comparison of noise shielding for a point source and a rotor placed inside a duct, as a function of polar angle, θ. $f = 400Hz$, $\phi = 11.8^o$, $kz = 16.4$, (a) $L/D_D = 1.7$, (b) $L/D_D = 3.4$.

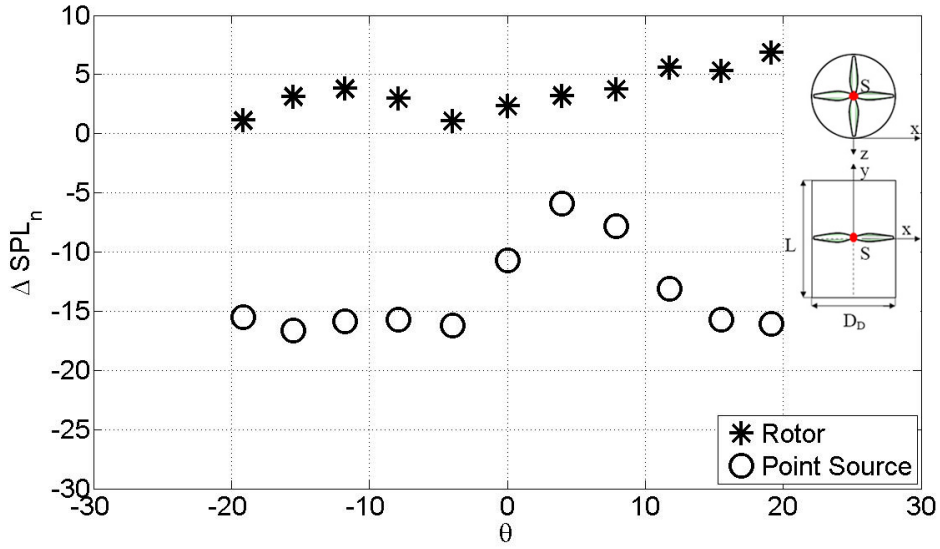

(a)

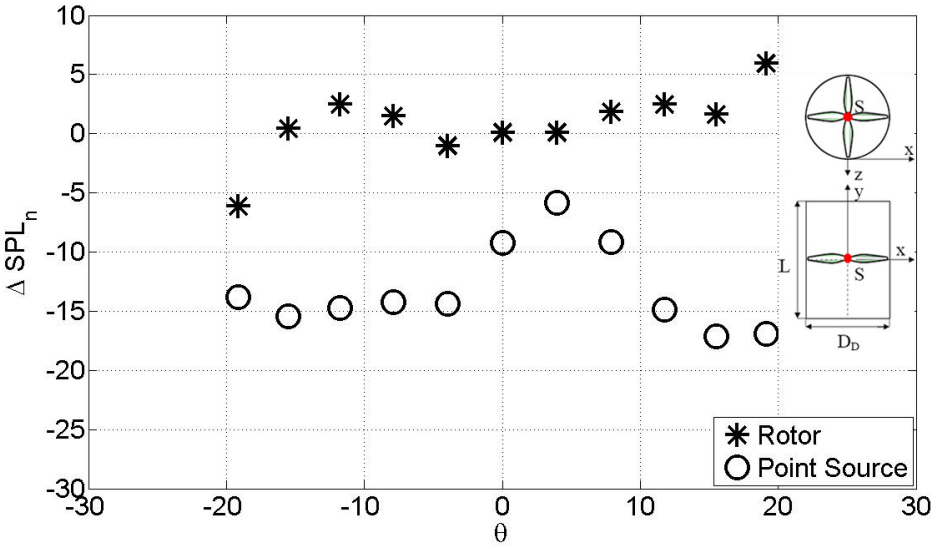

(b)

Figure 136: Comparison of noise shielding for a point source and a rotor placed inside a duct, as a function of polar angle, θ. $f = 400Hz$, $\phi = 0^o$, $kz = 16.4$, (a) $L/D_D = 1.7$, (b) $L/D_D = 3.4$.

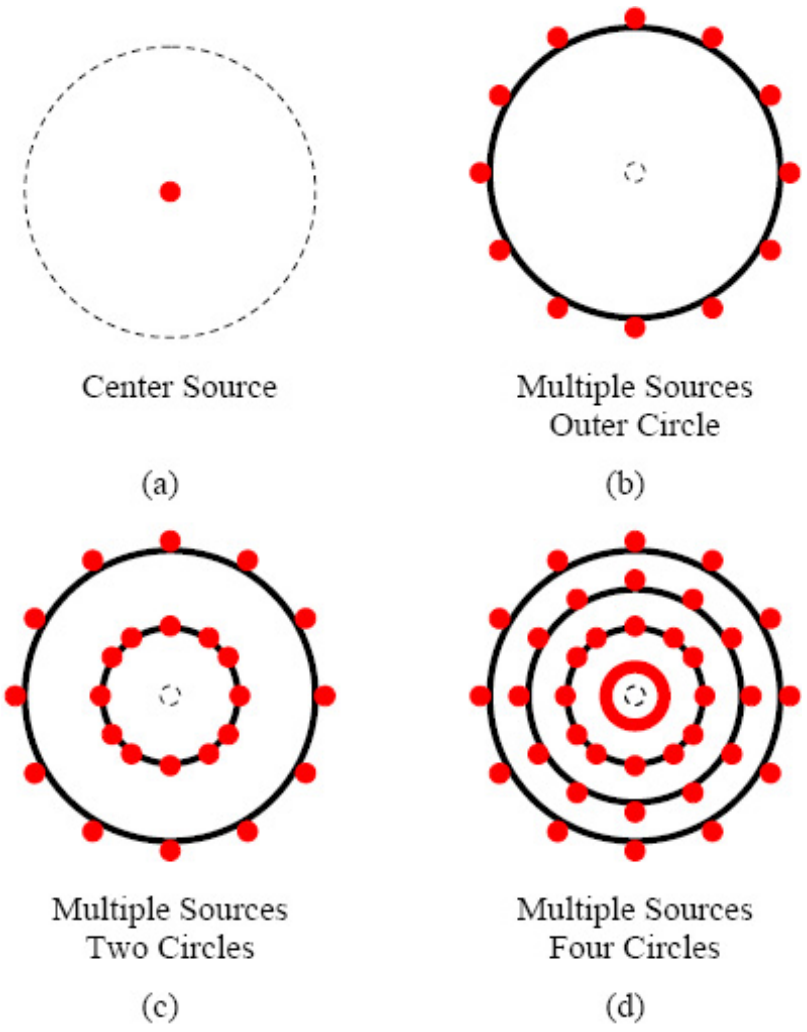

Figure 137: Point source configurations used to simulate rotor noise.

found that the same shielding curve was obtained whenever $n \geq 12$. Since $n = 12$ was found to be the optimal number of sources (in that more sources didn't make difference to the final results), the results presented in this work always employ a total of 12 point sources placed on any circle. In Figure 138, the results of this simulation, for a $6.5''$ diameter rotor, are compared as the 'Center' and 'Outer Circle' cases. The outer circle case had 12 point sources and the 2 circle case had 12 point sources on each of the two circles.

When the source was placed at the center of the rotor, the interferences between the diffracted waves produced significant peaks and valleys. The SPL levels are more likely to oscillate with large differences. This was due to the fact that the phase relationship was well defined for one source, so perfect destructive and constructive interferences occurred.

However when the source was distributed to the periphery the plot obtained was more uniform and smoother. Although the phase relationship between the multiple sources placed at the periphery was neglected in this part work, the interferences between the diffracted waves from multiple sources produced more complicated phase patterns at the receiver. As a result, using one point source at the center to simulate the rotor is clearly, very likely to lead to wrong conclusions as seen in Figure 138 where the point source assumption of a 100 dB source produces a minimum level of 75 dB across the shield compared to about 90 dB when the same sound field is made of 12 equally-spaced point sources each equal to 89 dB.

When the sources were placed at the periphery, it was assumed that the sources at the tip of the rotor were dominant and the inner sources were neglected. What happens if the inner sources over the blade are also taken into account? To answer this question, it was assumed that the rotor noise source was made up of $n = 24$ point sources with equal sound pressure level. Half of them were placed on the outer circle and the others were placed on the inner circle as shown in Figure 137(c). The results are also shown in Figure 138 and labeled as the '2 Circles' case. The results show that less shielding is obtained if the sources are assumed to be located at the outermost periphery of the rotor. This analysis was repeated for a larger diameter rotor of $13''$. In this case the number of circles were increased to four as shown in Figure 137(d) and $n = 48$. Each circle had 12 point sources. The results shown in Figure 139 confirmed the previous conclusion that the sources on the outermost circle produce the least shielding.

To understand the rule of other rotor/shield parameters, effects of tip clearance, d, shield width, W, shield length, L, and rotor diameter, D (see Figure 140) were calculated. Typical results for a frequency of 1200 Hz are described below:

1. Effect of Clearance: In Figure 142, calculated results for varying clearance, d, are given for fixed D, W and L. Figure 141(a) shows the case where one point source was placed at the center. Figure 141(b) shows the case where 12 point source were evenly placed along the periphery. Different clearances are compared for a $6.5''$ rotor. In Figure 143, rotor diameter was doubled and the procedure was repeated. When the clearance is less than half a rotor diameter, the change in this parameter does not

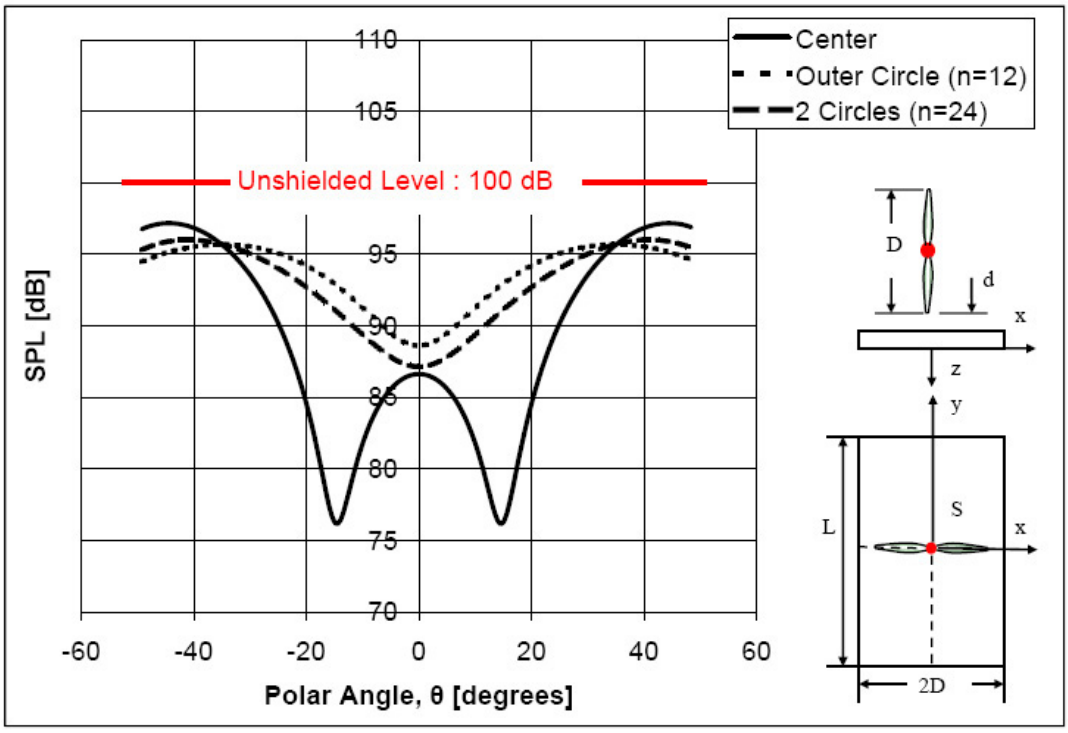

Figure 138: Comparison of using a single point source and multiple point sources to simulate rotor noise. $f = 1200$ Hz, $kW = 7.15$, $kz = 42.9$, $L/W = 2$, $W = 2D$, $d = D/4$, $D = 6.5''$.

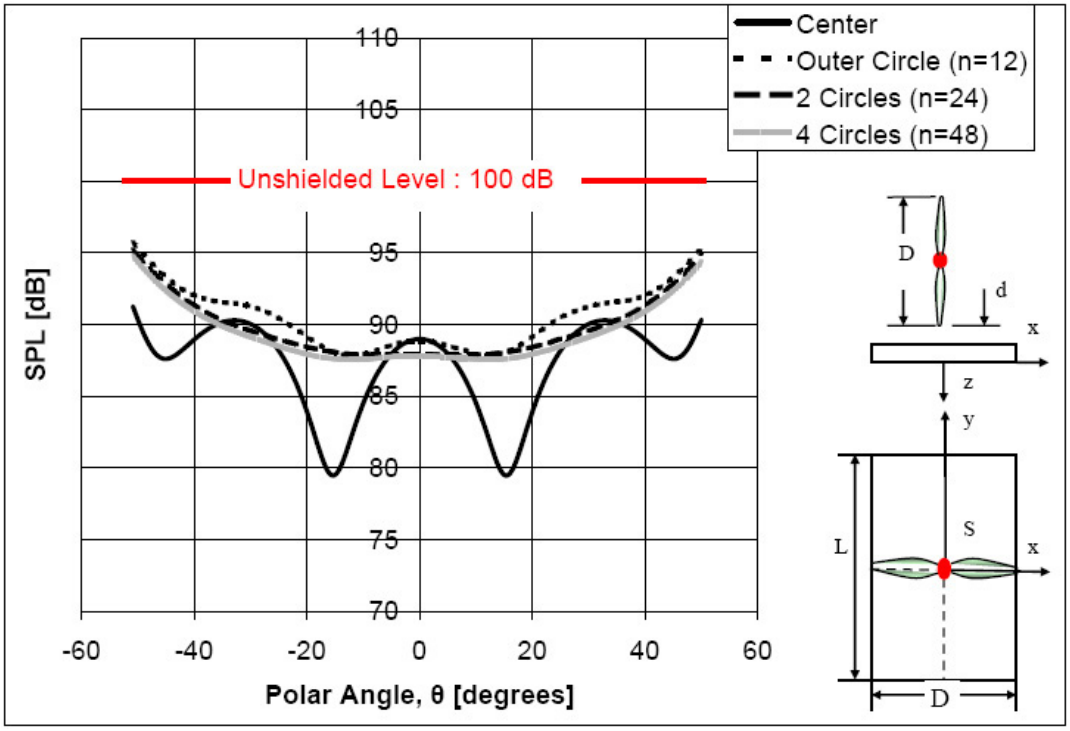

Figure 139: Comparison of using a single point source and multiple point sources to simulate rotor noise. $f = 1200$ Hz, $kW = 7.15$, $kz = 42.9$, $L/W = 2$, $W = D$, $d = D/4$, $D = 13''$.

affect the shielding pattern much. When the clearance is increased above half a rotor diameter, additional shielding is obtained. It appears that appropriate adjustment of the tip clearance can increase the shielding by as much as 5 dB as seen in Figure 141(b) for $D = 6.5''$.

2. Effect of Rotor Diameter: Figure 144 shows calculated results for varying diameter, D, is given while d, W, and L are fixed. Center point source case is shown in Figure 143(a) and multiple point source case in Figure 143(b). It is observed that as the individual sources are spread out with increasing diameter of the rotor, the shielding pattern becomes more uniform and have no similarity with the results for the center point source case. In the analysis presented above, the shield dimensions were kept constant when the rotor diameter was changed. Additional calculations were performed where all shield dimensions were scaled with respect to the rotor diameter. For example assuming a reference diameter of $D = D_1$, calculations were performed for $D = 2D_1$,

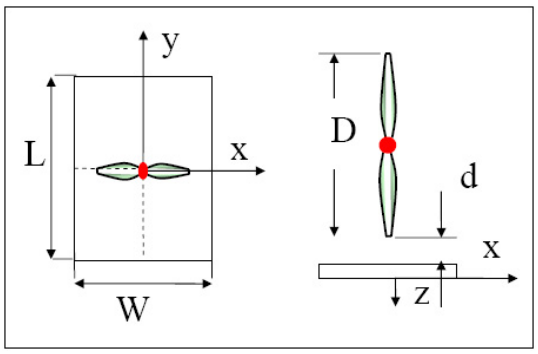

Figure 140: Parameters to be analyzed from Figure 142 to Figure 148.

$4D_1$, $8D_1$ while changing the diameter, shield width was also changed in proportion to the new diameter. In Figure 145 results for varying diameter, D, are given while d is fixed. The shield dimensions W and L are scaled by the diameter of each rotor. Center point source and multi point source cases are shown in Figure 144(a) and 144(b), respectively. So, unlike results in Figure 143(a) and 143(b), the shield dimensions are not constant, as the rotor diameter changes the shield dimensions also change proportional to it. However the clearance was kept constant for all cases. Much larger shielding is obtained as larger shields are used.

Finally, from Figure 146 to Figure 147 the measurement distance R was varied where D, W, L, and d were fixed. Figure 145(a), 146(a), and 147(a) shows the shielding pattern for the single point source assumed to be placed to simulate the rotors with diameters of D, $2D$, and $4D$, respectively. As the diameter of the rotor increases, the measurement distance has more effect on the shielding pattern. However when multiple point sources are placed on the periphery to simulate the same size rotors, the measurement distance is observed to be less important. The multiple point source results are shown in Figure 145(b), 146(b), and 147(b) for rotors of D, $2D$,and $4D$, respectively.

6.3.2 Application of Multiple Point Source Simulation

In this section, a number of calculations to see the differences in the shielded noise pattern for the point source configuration as well as multi-source configuration is presented. Typical results from the present experiments are compared with two sets of calculations are shown

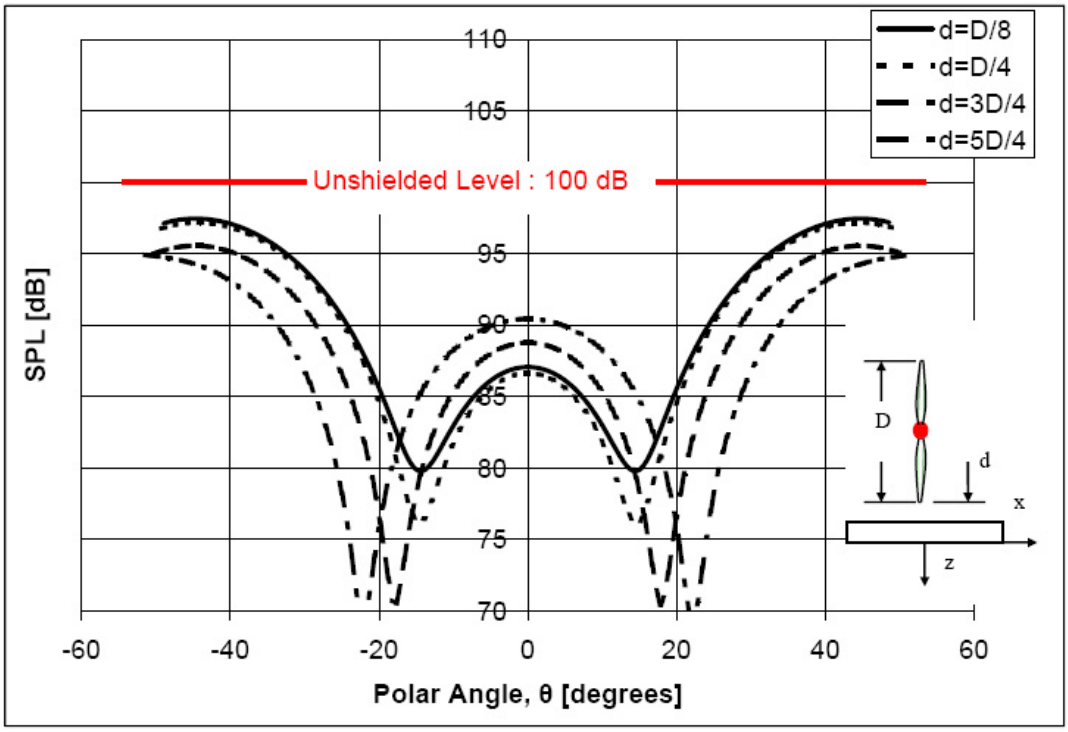

(a)

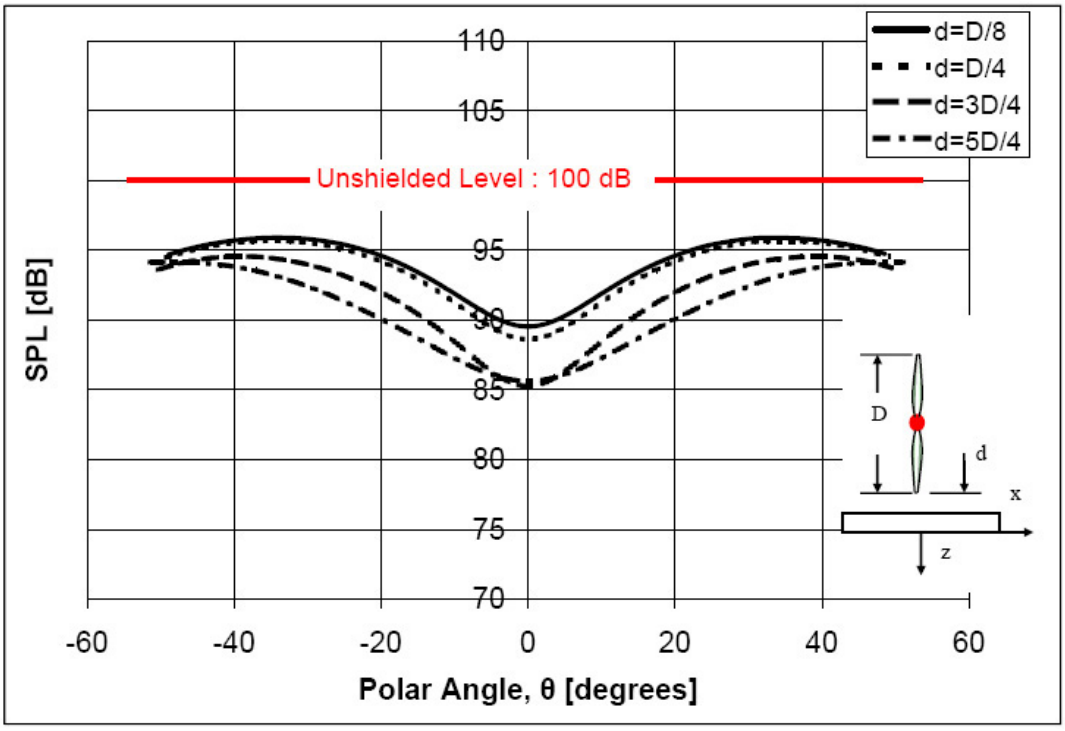

(b)

Figure 141: Effect of clearance; (a) single point source at the center, (b) multiple point sources at the periphery. $n = 12$, $f = 1200$ Hz, $kW = 7.15$, $kz = 42.9$, $L/W = 2$, $W = 2D$, $D = 6.5''$.

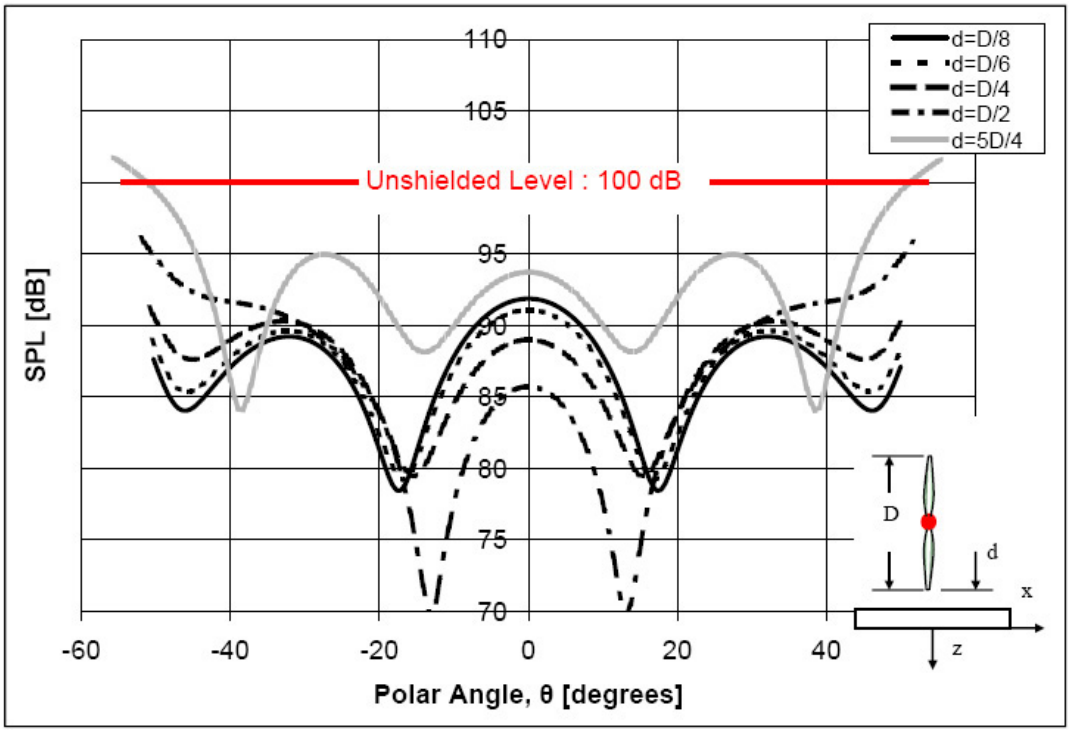

(a)

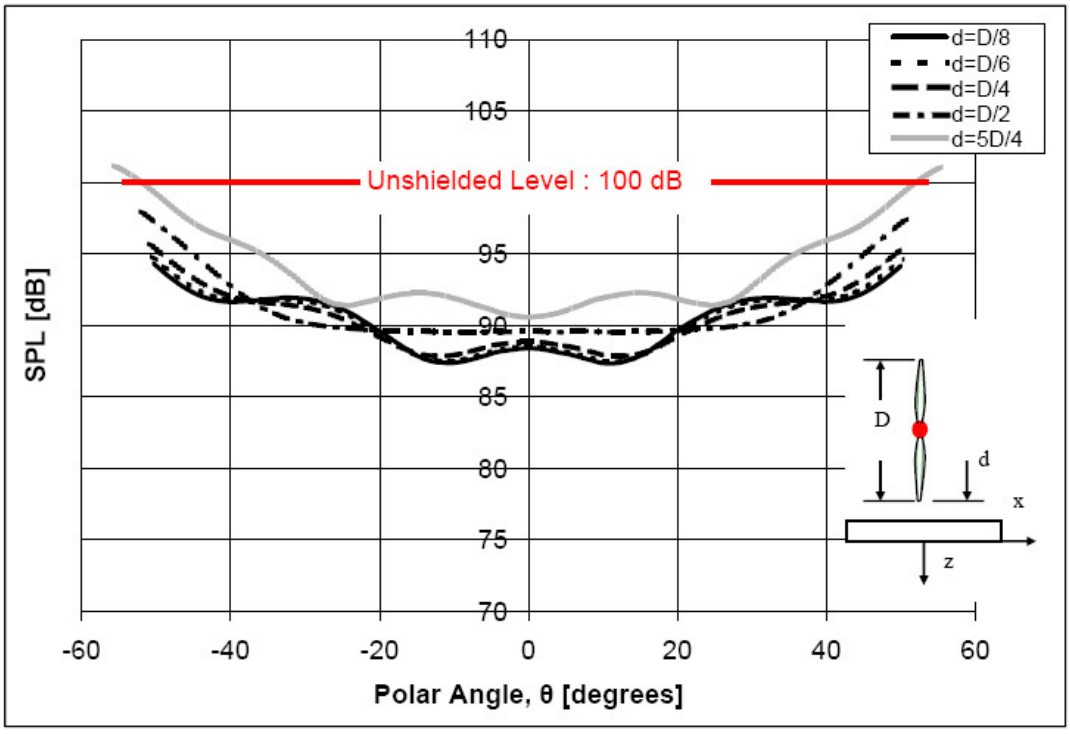

(b)

Figure 142: Effect of clearance; (a) single point source at the center, (b) multiple point sources at the periphery. $n = 12$, $f = 1200$ Hz, $kW = 7.15$, $kz = 42.9$, $L/W = 2$, $W = D$, $D = 13''$.

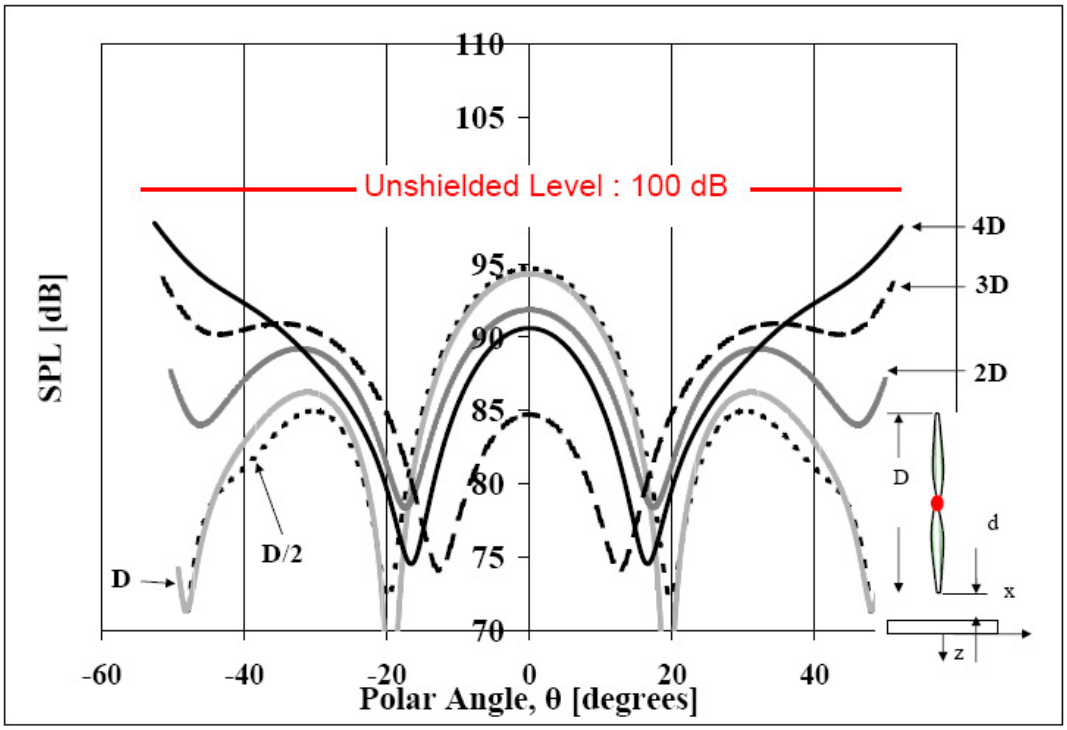

(a)

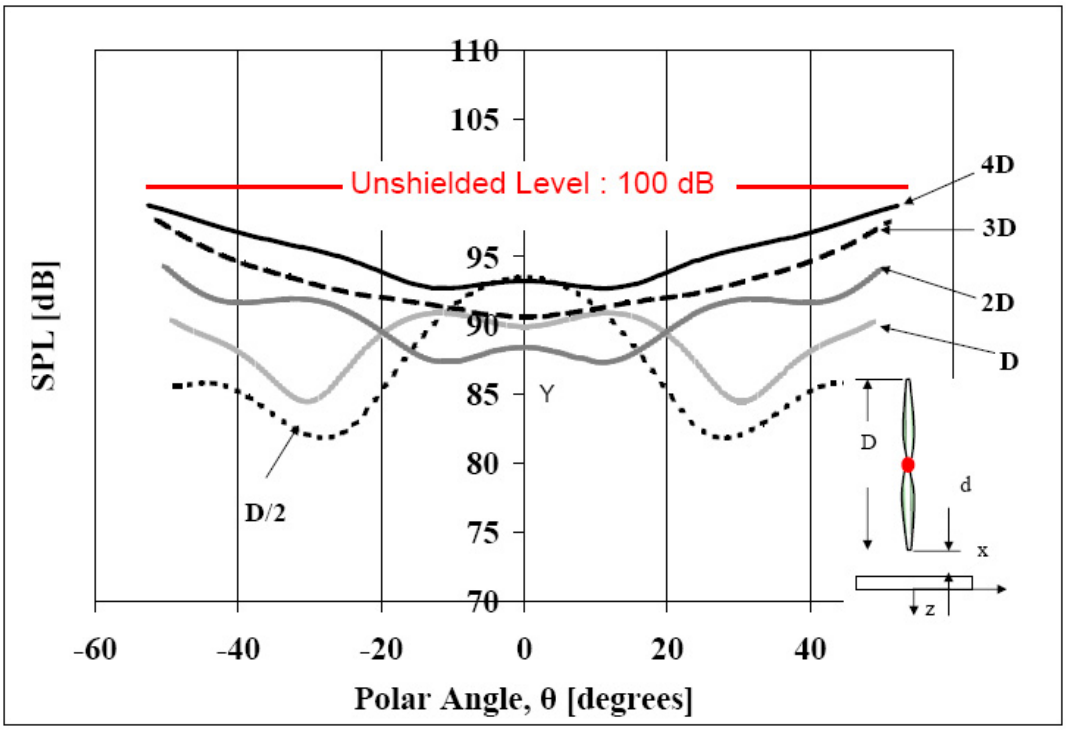

(b)

Figure 143: Effect of rotor diameter, (a) single point source at the center, (b) multiple point sources at the periphery. $n = 12$, $f = 1200$ Hz, $kW = 14.3$, $kz = 42.9$, $L/W = 2$, $W = 4D$, $d = D/4$, $D = 6.5''$.

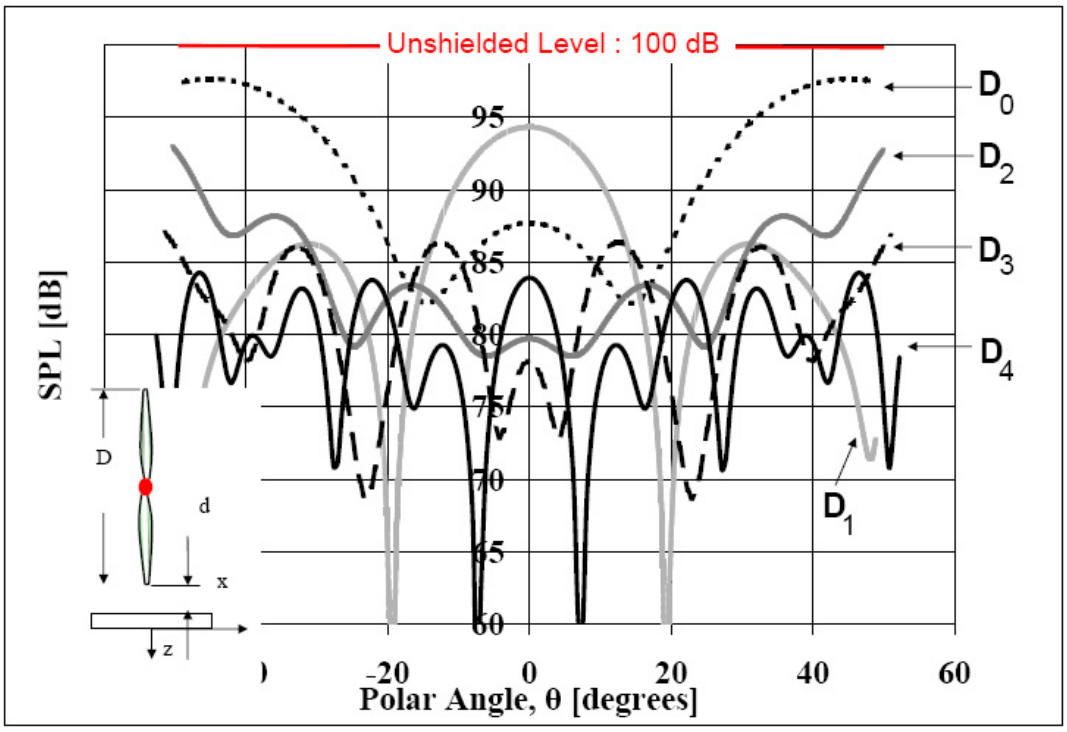

(a)

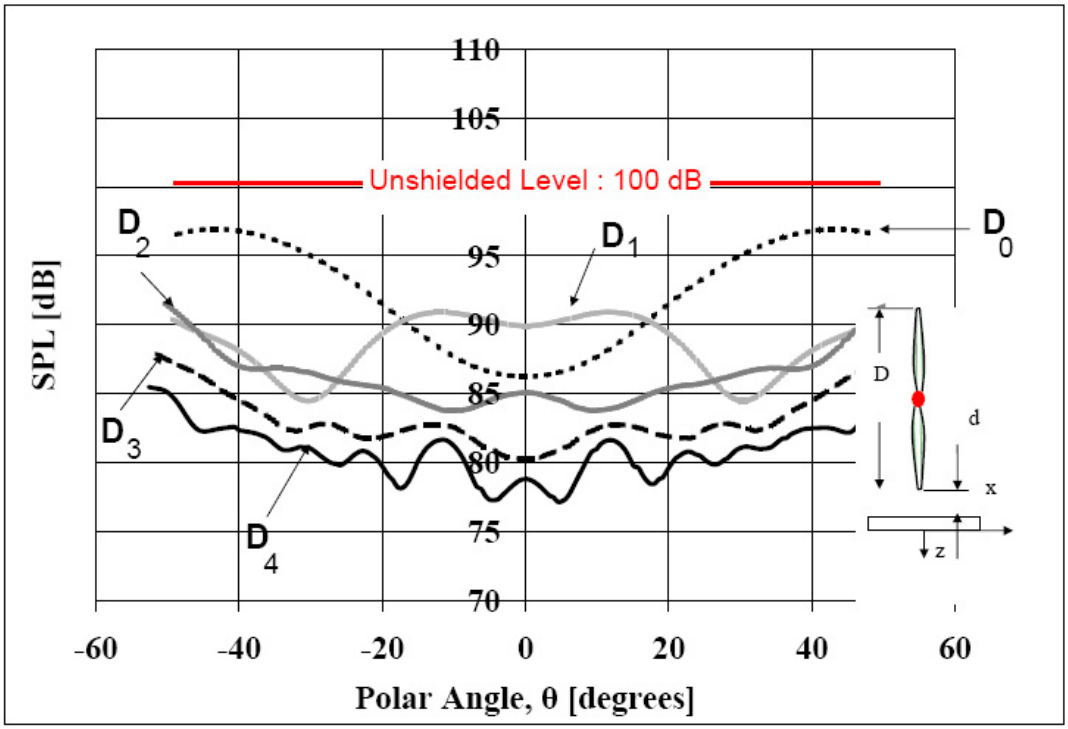

(b)

Figure 144: Effect of rotor diameter, (a) single point source at the center, (b) multiple point sources at the periphery. $n = 12$, $kz = 42.9$, $D_0 = D/2$, $D_1 = D = 6.5''$, $D_2 = 2D$, $D_3 = 4D$, $D_4 = 8D$; $L/W = 2$, $W = 2D_i$, $i = 1, ..., 4$; $d = D/2$.

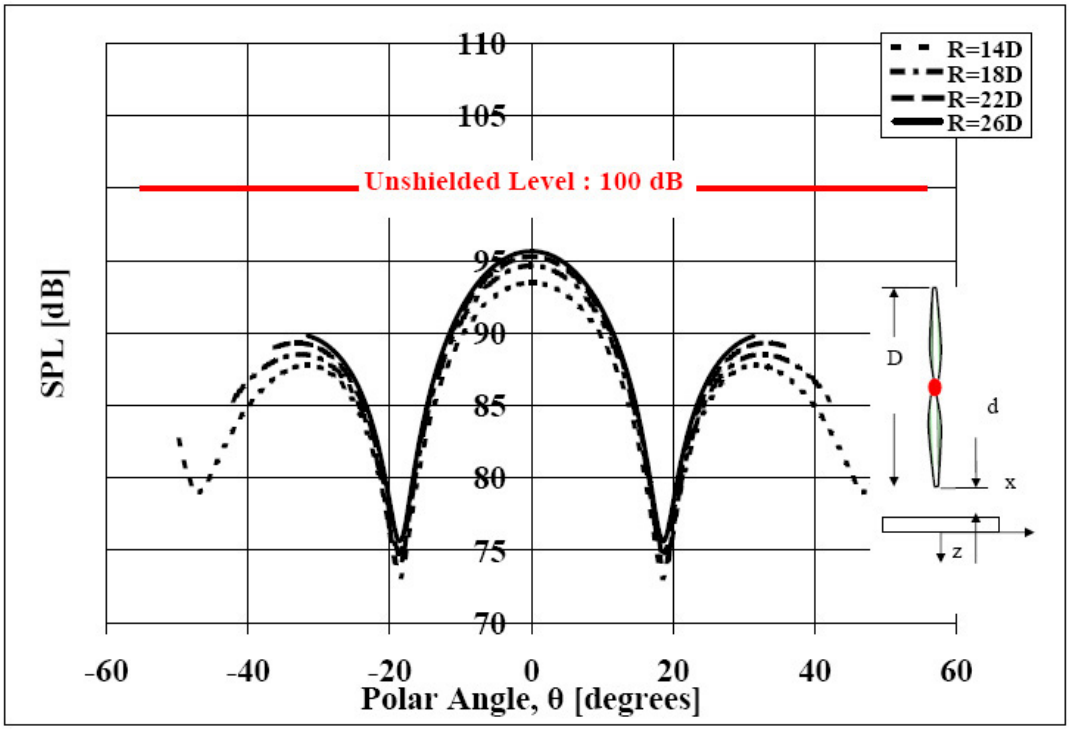

(a)

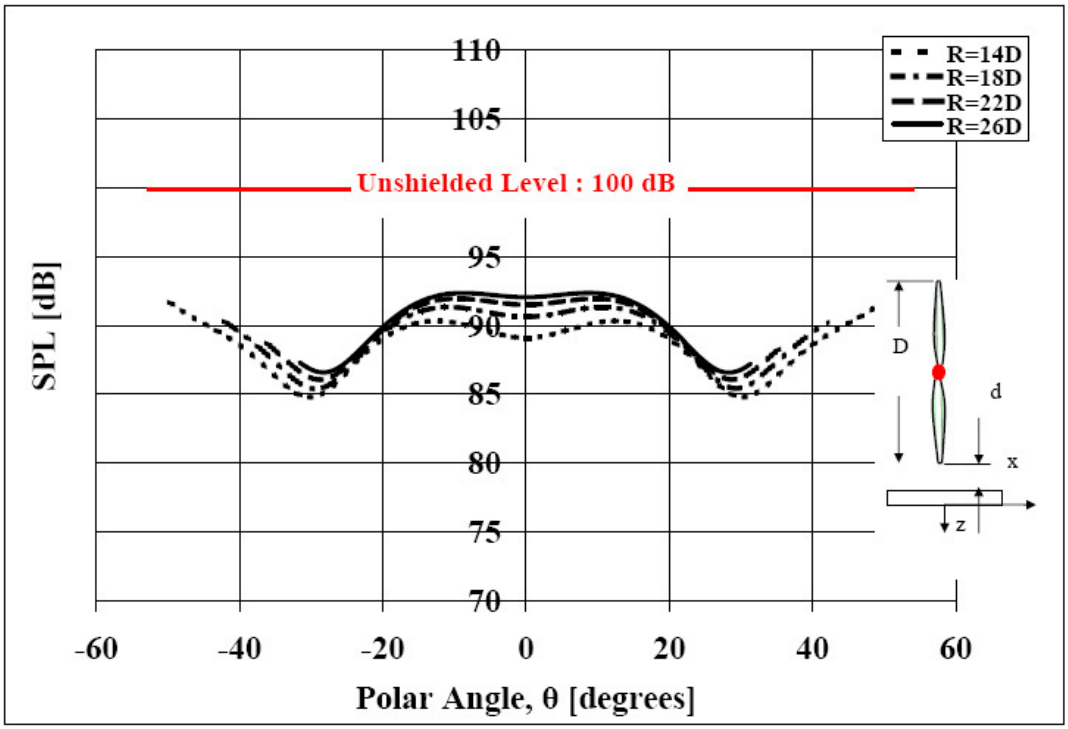

(b)

Figure 145: Effect of measurement distance, (a) single point source at the center, (b) multiple point sources at the periphery. $n = 12$, $f = 1200$ Hz, $kW = 14.3$, $L/W = 2$, $W/D = 4$, $d = D/2$, $D = 6.5''$.

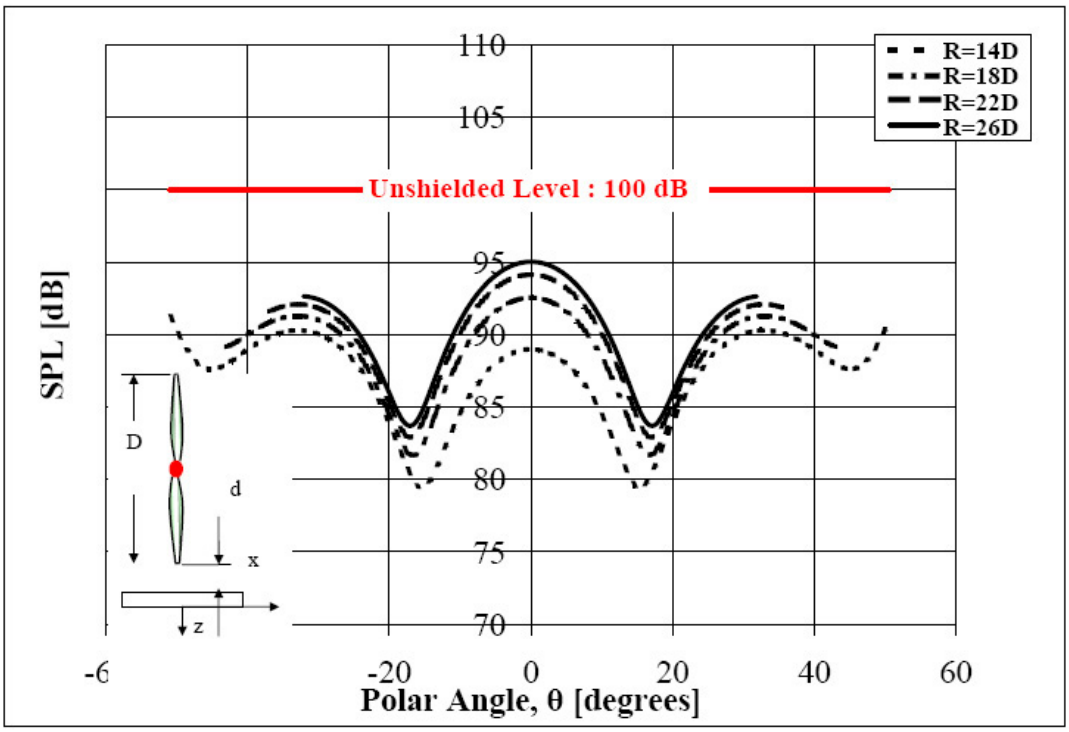

(a)

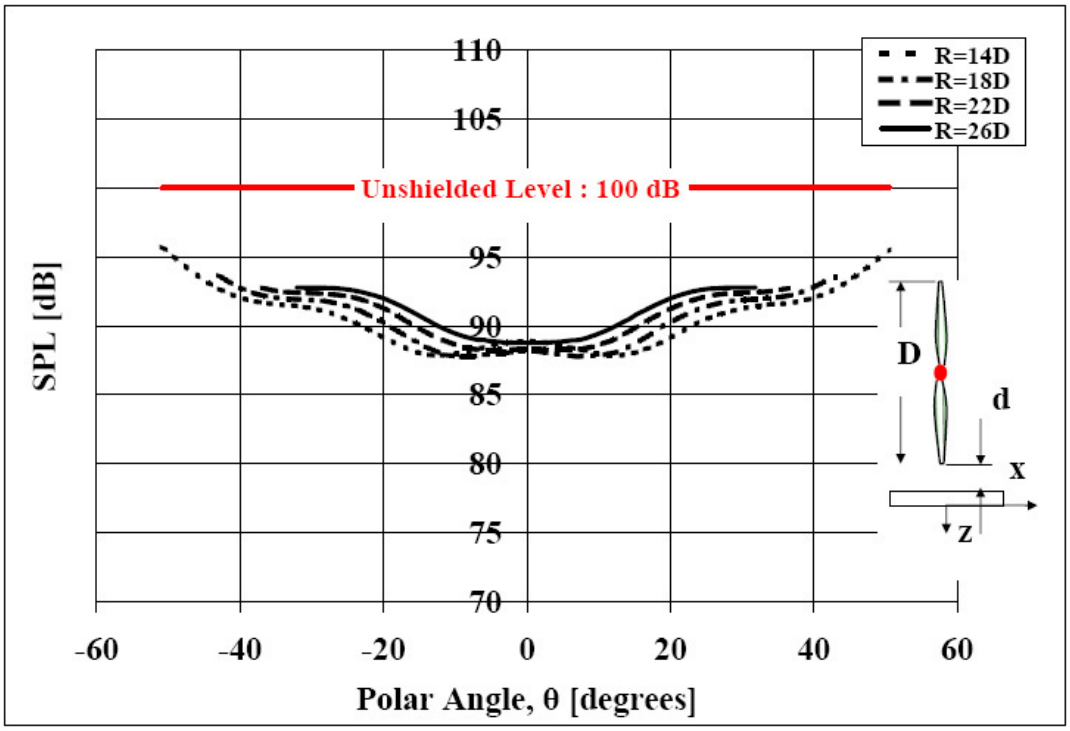

(b)

Figure 146: Effect of measurement distance, (a) single point source at the center, (b) multiple point sources at the periphery. $n = 12$, $f = 1200$ Hz, $kW = 14.3$, $L/W = 2$, $W/D = 4$, $d = D/2$, $D = 13''$.

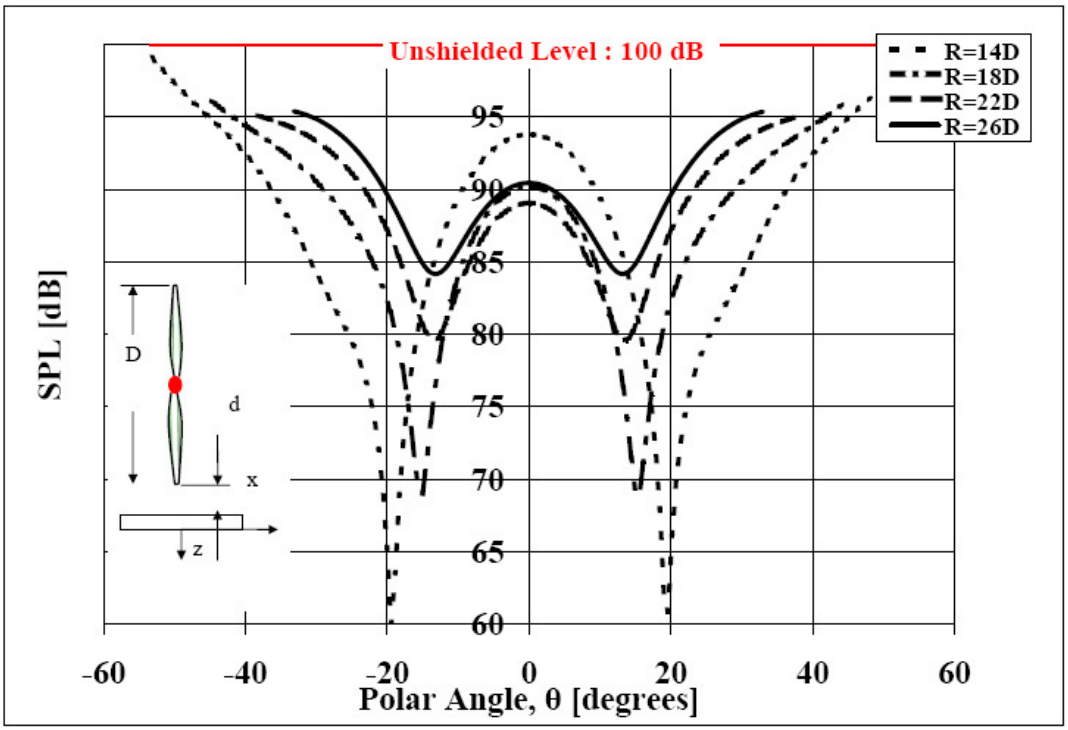

(a)

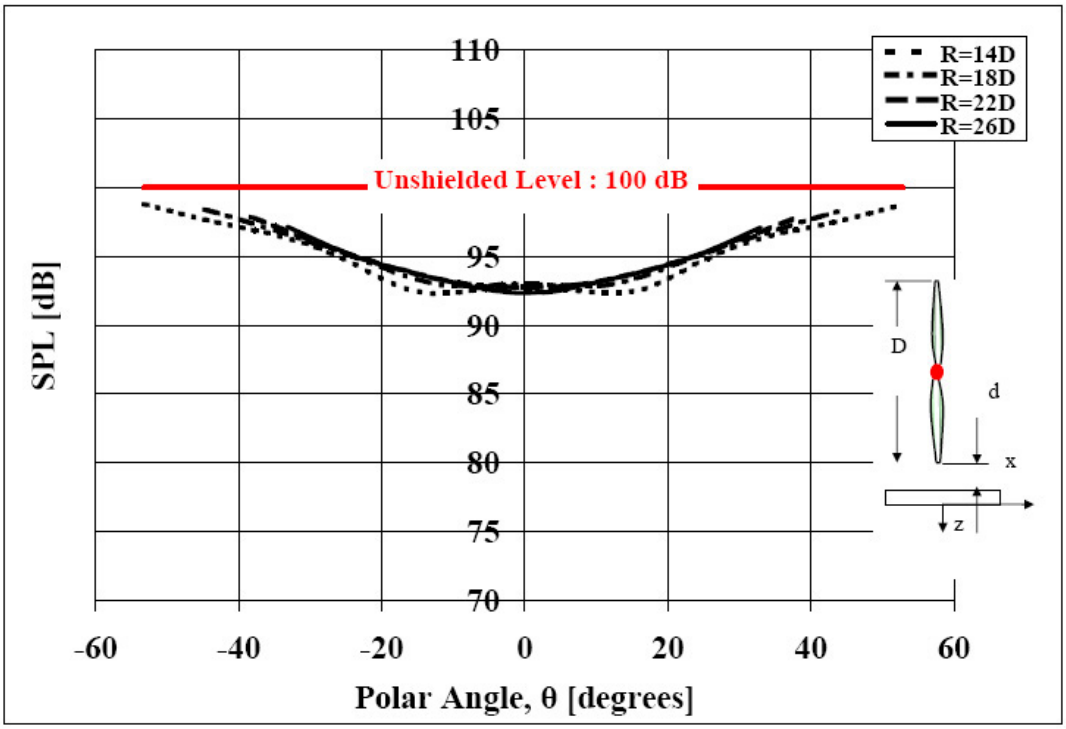

(b)

Figure 147: Effect of measurement distance, (a) single point source at the center, (b) multiple point sources at the periphery. $n = 12$, $f = 1200$ Hz, $kW = 14.3$, $L/W = 2$, $W/D = 4$, $d = D/2$, $D = 26''$.

in Figures 148(a) and 148(b) at 1200 Hz for $\phi = 13^o$, $\phi = 0^o$, respectively. The measured shielding is found to be considerably less than that predicted by calculations using multiple point sources. More importantly, the pattern of the measured shielded noise matches that predicted by the multi-source calculation.

The analysis performed for 1200 Hz frequency in Figure 148 is repeated, first, for 800 Hz in Figure 149, and then, for a narrower rectangular shield at 1200 Hz as shown in Figure 150.

It appears that even after accounting for the multiple point sources over the rotor disc, the measured data shows less shielding than predicted. Yet, the shapes of the measured shielding plots presented here for the rotor are very similar to those predicted using multiple point source assumption. These shapes definitely do not match those predicted by representing the propeller by a single point source (the latter has many peaks and valleys).

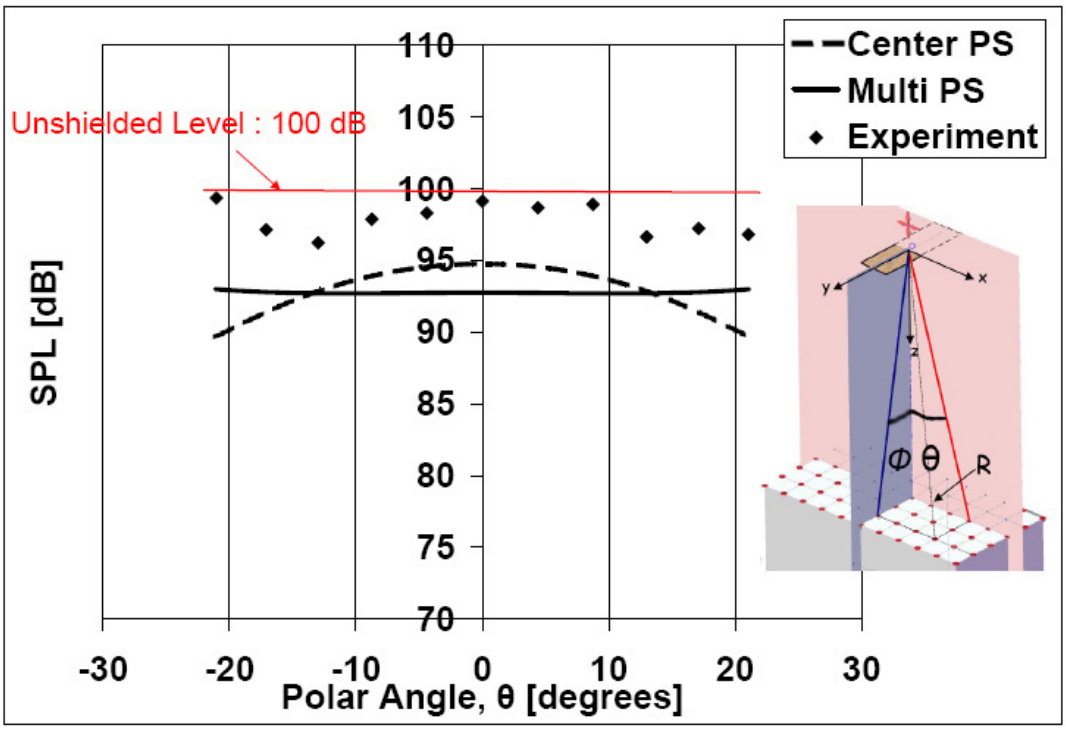

(a)

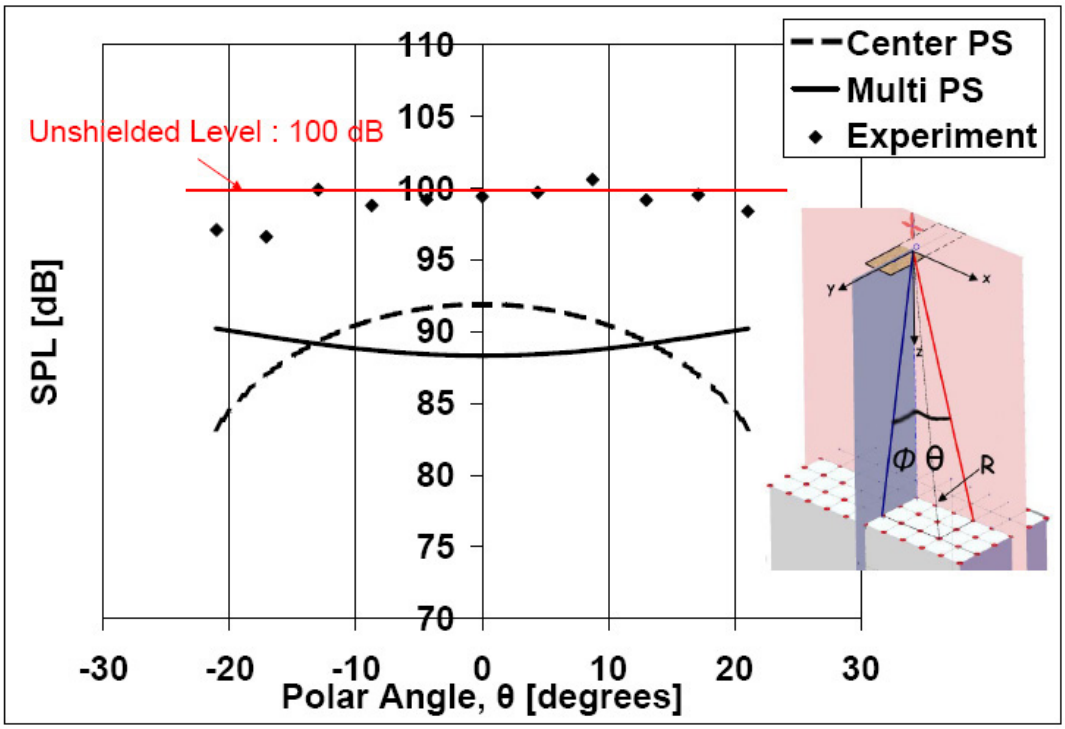

(b)

Figure 148: Experimental shielding of rotor source compared with multi point source simulation, as a function of polar angle, θ. $f = 1200$ Hz, $kW = 7.15$, $kz = 42.9$, $D = W/2$, $L/W = 1.8$, (a) $\phi = 13^o$, (b) $\phi = 0^o$.

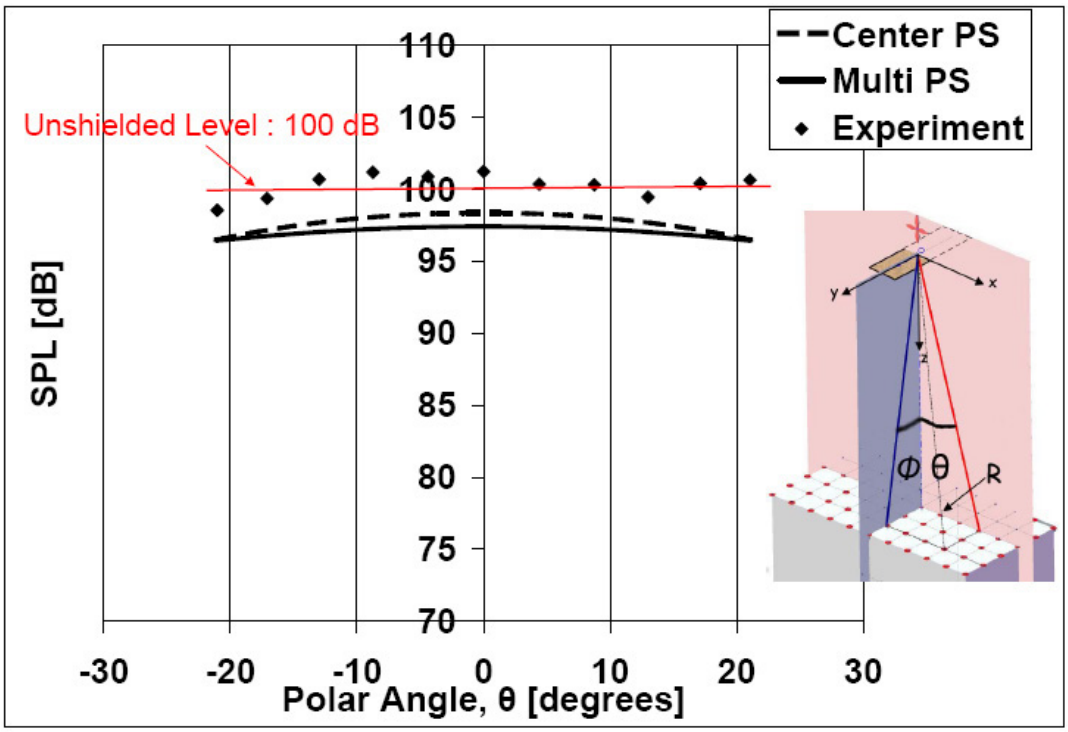

(a)

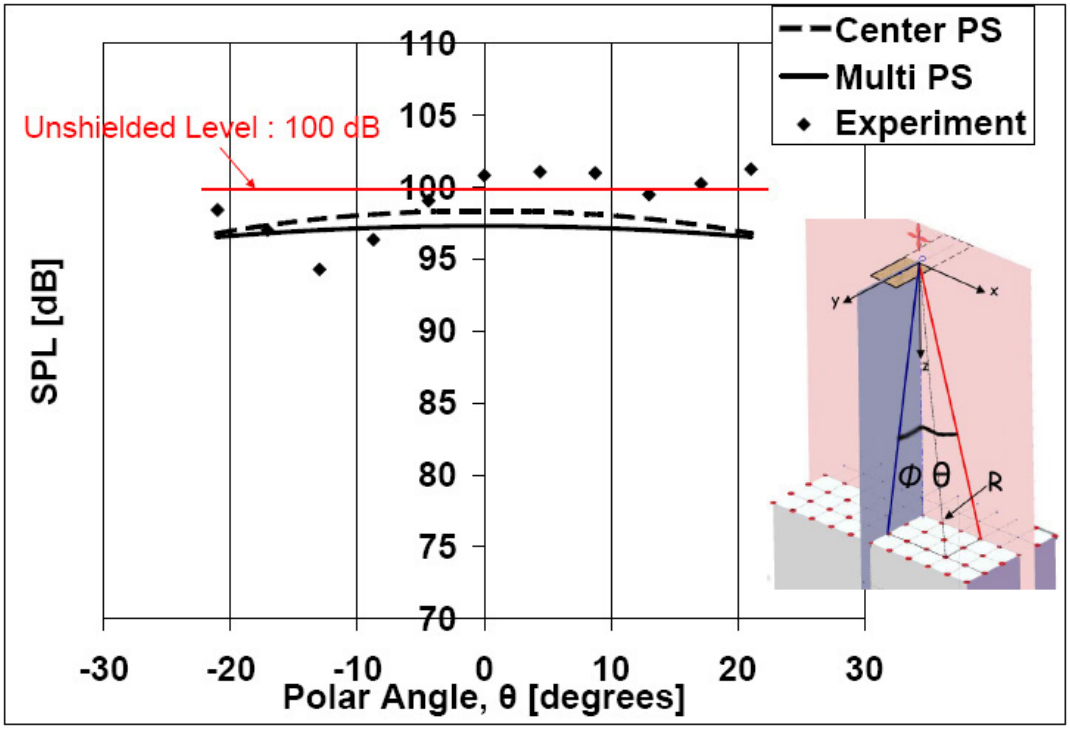

(b)

Figure 149: Experimental shielding of rotor source compared with multi point source simulation, as a function of polar angle, θ. $f = 800$ Hz, $kW = 4.81$, $kz = 28.9$, $D = W/2$, $L/W = 1.8$, (a) $\phi = 13^o$, (b) $\phi = 0^o$.

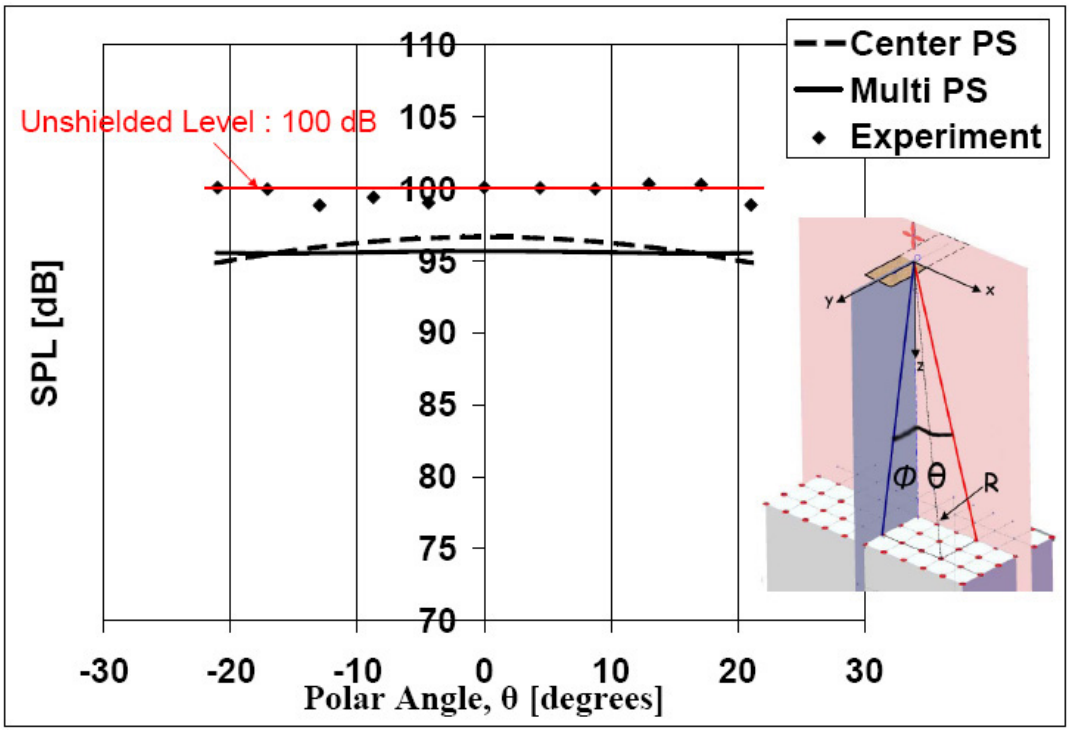

(a)

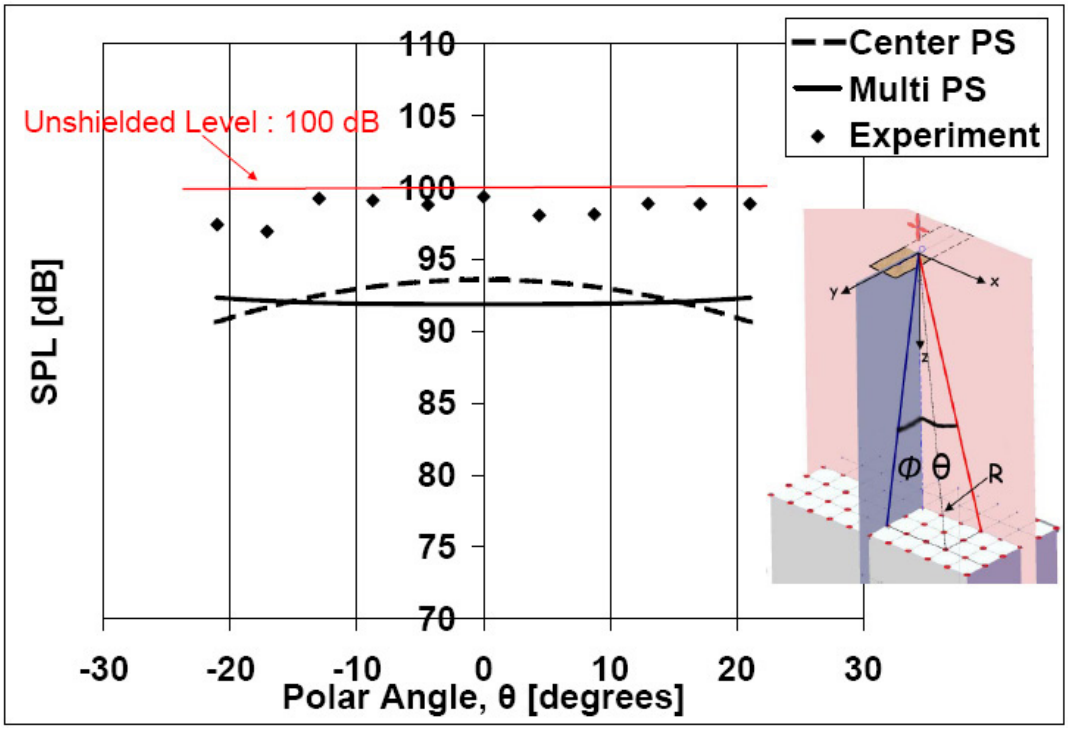

(b)

Figure 150: Experimental shielding of rotor source compared with multi point source simulation, as a function of polar angle, θ. $f = 1200$ Hz, $kW = 7.15$, $kz = 42.9$, $D = 0.9W$, $L/W = 3.6$, (a) $\phi = 13^o$, (b) $\phi = 0^o$.

CHAPTER VII

CONCLUSIONS AND FUTURE WORK

The investigation described in this thesis had two main objectives:

1. To determine the distance at which microphones should be placed for rotor noise measurements so that the rotor can be treated as a point sound source, thus enabling the use of ISL for the purpose of prediction of rotor noise at different distances and for comparing data from different experiments.

2. To determine validity of representing a full rotor by a point sound source for the purpose of calculating shielding of rotor noise.

The research investigated the limits of geometric farfield distance for acquiring acoustic data of model scale ducted and unducted rotors. The measurements performed on several open rotor configurations showed that the open rotors meet the geometric farfield condition for R/D greater than about 10. However, the corresponding R/D for a ducted rotor was found to be greater than 20. These different findings for the ducted and unducted configurations were attributed to the fact that the largest dimension of the ducted rotor was not the radius but the duct length. Interpreting the results according to the duct length parameter showed that R/L should be greater than 15 to satisfy the geometric farfield conditions. For the ducted rotors, it was concluded that as the measurement angle changes from 0^o to 90^o (forward quadrant) the experimental data tends to fit the theoretical ISL range at smaller distances. This appears to be related to the fact that the noise emanates from both openings of the duct. For both openings to appear as a single point source to a microphone the distance would be expected to be larger when the microphone is located along the flow direction or duct axis compared to when the microphone is located at right angles to this direction. Thus both the duct or rotor diameter and the duct length play an important role in determining the distance where the microphones can be said to be in the

geometric farfield.

The geometric farfield experiments were performed in the forward quadrant ($0^o \leq \alpha \leq 90^o$) for both ducted and unducted rotors and also behind the rotor ($\alpha = 180^o$) for ducted rotors. Further investigation is needed draw firm conclusions about the largest microphone distance in the aft angles where the rotor system can be treated as a point source. The geometric farfield distances obtained were close to the experimentation limits of the anechoic chamber for both ducted and unducted cases. In particular, moving the microphones any further would have brought it very close to the tip of anechoic wedges in the test chamber. So, this work needs to be extended by performing the experiments in a larger chamber for larger distances and with more data points especially for the unducted case. Also, the results obtained are for static conditions, flight effects need to be investigated.

This research also investigated the applicability of point source based acoustic shielding models to determine the shielding of real rotor noise sources. Using the point source assumption implies neglecting the character of the original source behind the shield. However, it is obvious that noise from a rotor has a different directivity pattern than a monopole. So the amplitude and the phase of the rays striking on different edges of the shield are not the same for a rotor source as they are for a point source. Also, the rotor noise source may be assumed to be made up of a larger number of point sources, each having its own individual shielding.

The experimental data acquired using rotor sources shielded with rectangular plates and circular ducts showed that the point source theory is not always adequate in estimating the noise shielding in the measurement range of interest. In general, it was found that the shielding produced by the rectangular barrier for the rotor source was much less than that predicted for a point monopole source. In addition, the sharp peaks and valleys calculated for the point source were not so sharp for the rotor source, or were almost non-existent. The shielding curves for rotor sources were found to be more uniform and smoother compared to both experimental results and calculations for the point source.

The calculations based upon a rectangular shield were shown to be inadequate to estimate the shielding by a duct, although they give better fit as the duct length is increased.

Higher shielding was obtained for ducted shielding compared to rectangular shielding. This appears to be related to the combined effect of the propagation of sound through a duct experiencing reflections at the duct opening, and then diffraction around the periphery of the duct exit at both ends as a portion of the sound is transmitted out. (The sound reaching the exit is partly reflected back towards the source and the diffraction is experienced only that portion of sound that is transmitted.) This is expected to show up as reduced acoustic level outside the duct. Likewise, experimental comparisons of a rotor and a point source placed inside a round duct showed that rotor does not always behave the same way as the point source inside a duct.

Using the experimental data acquired for both point source and the rotor source, some design guidelines were established in terms of shielding. Investigation on the source location for point source shielded by a rectangular barrier showed that moving the source closer to the center of the shield increases the shielding, in the $\theta \in [-20^o, +20^o]$ observation range. Comparison of calculations with the experimental data for the point source indicated that the location and magnitude of the peaks and valleys in the shielding curve were quite sensitive to the precision with which the sources are placed with respect to the shield surface. For the rotor source, when the source was shifted away from the center (forward) of the shield, the shielding levels didn't change as much as they did for the point source at high frequencies. Both the experiments and calculations for the point source showed 0-5 dB noise increase with the rectangular shield at the lowest frequency examined ($f = 400Hz$). Even higher increase was found for the rotor source. For better understanding of rotor shielding, further investigation is needed using larger shield dimensions and a larger observation range.

The examination of shielding data can be extended in view of the propagation of duct acoustics in the far field. Both the geometric far field experiments and the shielding experiments were conducted only for static conditions. Flight effects need to be added to the list of future research on this topic. Another possible extension of this work is the investigation of shielding effects on semicircular shielding of rotors as used in the channel wing configurations.

It was hypothesized that the calculations under point source assumption cannot estimate the results of rotor source experiments because of the rotor source being made up of a number of point sources over the rotor disc. To test this hypothesis, additional calculations were carried out by replacing the rotor by multiple point sources at the periphery of the rotor. The rotor was simulated as if it was made up of point sources collectively emanating sound power whose sum is equal to the sound power emanating from a point source located the center of the rotor.

Multiple point source approach was applied for the geometric far field estimations. It was observed that in the application of ISL, the right combination of rotor diameter, frequency, and number of sources with the phase lag between the sources gives a good prediction of the experimental results. It was concluded that the phase relationship between the sources distributed over the rotor disc could be the main reason for the deviations from the ISL in the near field. Further investigation on the effect of phase distribution of rotor noise sources is needed to understand the findings of this research.

The calculations using multiple point source approach for rectangular shielding showed that the interferences between the diffracted waves from multiple sources produced more complicated phase patterns at the receiver than the single source case. When the source was placed at the center of the rotor, the interferences between the diffracted waves produced significant peaks and valleys. This was due to the fact that the phase relationship was well defined for one source, so perfect destructive and constructive interferences occurred. However when the source was distributed on the rotor periphery, the shielding obtained was more uniform and smoother. As a result, using one point source at the center to simulate the rotor is clearly, very likely to lead to wrong conclusions. It was found that assuming the rotor to be made up of multiple point sources, reduced magnitude of the peaks and valleys in the shielding curve and also reduced the overall shielding just as observed in the experiments. Future research should move beyond looking the multiple point sources as stationary monopoles and assume dipoles modeled as rotating sources. Combination of monopoles and dipoles should also be considered to simulate thickness noise as well as loading noise, respectively.

In conclusion, in this dissertation the limitations of rotor noise measurements and solutions for the prediction of SPL in the farfield are discussed for both shielded and unshielded configurations.

APPENDIX A

UNCERTAINTY ANALYSIS

A.1 Basics of the Analysis

In this section, first the terminology and uncertainty analysis procedure is summarized, then the elemental error sources are introduced. Measurement error is the difference between the true value and the measured value. Total measurement error is expressed as the root sum of squares of bias error and precision error. Coleman and Steele [49] define the bias error as the fixed, systematic, or constant component and the precision error as the random component of the total error. In a simpler way, Moffat [50] suggests that latter would change from trial to trial and the the other wouldn't. Additionally, he states that the type of error depends on the intentions of the experimenter, how the experimenter might repeat the experiment. The question to ask to discriminate the precision error from the bias error is to ask whether the error component would change when the measurement was repeated in a specified manner. Once the elemental error sources for each individual measurement variable are defined, their effects are classified as the bias, B_i, and precision, P_i, error limits of the measured value of the variable, X_j. Then the error limits of each individual variable, $X_j, (j = 1, 2..., n)$, are computed and combined in a data reduction equation given by the general formulation,

$$r = r(X_1, X_2, ..., X_n) \tag{53}$$

The propagation of errors through the data reduction equation gives the bias, B_r, and precision, P_r, errors in the experimental result. Finally, the total error of the experiment is expressed as

$$U_r = \sqrt{B_r^2 + P_r^2} \tag{54}$$

The elemental error sources and the tolerances related to them are defined below.

- Motor Speed: The electric motor was operated with an uncertainty of ± 5 rpm in

angular speed.

- Frequency: Uncertainty in the frequency due to the computational resolution was kept ± 1 Hz.

- Structural Dimensions: The duct outer diameter tolerances was given as $\pm 0.045''$ and wall thickness as $\pm 15\%$ by the manufacturer. Duct and rectangular shield lengths and rectangular shield width were set as $\pm 0.01''$.

- Source and Receiver Locations: Both the point source and the center of the rotor source were placed at the same point during shielding experiments. Also, during geometric far field experiments the sources were kept at a fixed point. All other placements (placements of the rectangular shields, ducts, microphones) were made assuming the center of the source as the reference point. The error for all placements made with respect to this reference point,i.e. (x,y,z) coordinates of the source and the microphones with respect to the shield were set in a $\pm 0.25''$ error margin. These are considered as the limits of precision error since the configuration was changed from time to time.

- Atmospheric Conditions: The temperature, atmospheric pressure and humidity rate (relative humidity) ranges that the measurement equipment was exposed during the experiments are given in Table 7.

A.2 Uncertainty in the Location Parameters

1. Polar Angle, θ: The elemental error sources are x and z coordinates of the receiver. Data reduction equation is

$$\theta = atan(x/z) \tag{55}$$

The precision limit for θ is found from equation (54) as follows

$$P_\theta^2 = (\frac{\partial \theta}{\partial x} P_x^2 + \frac{\partial \theta}{\partial z} P_z^2) \tag{56}$$

Substituting partial derivatives

$$P_\theta^2 = (\frac{1}{1+(x/z)^2} \frac{1}{z})^2 (P_x^2 + \frac{x^2}{z^2} P_z^2) \tag{57}$$

The experimental values are substituted in equation (57) and the final result for P_θ is obtained to in $\pm 0.02''$ range

2. Azimuthal Angle, ϕ: The elemental error sources are y and z coordinates of the receiver. Data reduction equation is

$$\phi = atan(y/z) \tag{58}$$

The precision limit for ϕ is

$$P_\phi^2 = (\frac{\partial \phi}{\partial y} P_y^2 + \frac{\partial \phi}{\partial z} P_z^2) \tag{59}$$

Substituting partial derivatives

$$P_\phi^2 = (\frac{1}{1+(y/z)^2} \frac{1}{z})^2 (P_y^2 + \frac{y^2}{z^2} P_z^2) \tag{60}$$

Like P_θ, the experimental values are substituted in equation (60) and the final result for P_ϕ is obtained to be in the $\pm 0.02''$ range.

3. Measurement Distance, R: The elemental error sources are x, y and z coordinates of the receiver. Data reduction equation is

$$R = \sqrt{x^2 + y^2 + z^2} \tag{61}$$

The precision limit for ϕ is

$$P_R^2 = (\frac{\partial R}{\partial x} P_x^2 + \frac{\partial R}{\partial y} P_y^2 + \frac{\partial R}{\partial z} P_z^2) \tag{62}$$

Substituting partial derivatives

$$P_R^2 = \frac{1}{x^2 + y^2 + z^2} ((xP_x)^2 + (yP_y)^2 + (zP_z)^2) \tag{63}$$

Since the error range for $P_x, P_y, and P_z$ is chosen to be $\pm 0.25''$, equation (63) reduces to

$$P_R^2 = \frac{1}{x^2 + y^2 + z^2} \frac{x^2 + y^2 + z^2}{16} \tag{64}$$

So the error for the distance variable is $P_R = 0.25''$.

A.3 Uncertainty from the Acoustic Pressure Measurement Equipment

The range of ambient atmospheric conditions during the experiments are provided in Table 7. Using these data and the error coefficients provided by the manufacturer for the related instruments (microphones and calibrator), the error ranges due to temperature, pressure and humidity rate are calculated for each experiment. The causes of uncertainty due to the measurement equipment are listed below:

1. Calibrator variability under atmospheric conditions : The sound calibrator bias was given as ±0.2 dB under the reference conditions of $23(\pm 3)^oC$, $101(\pm 4)kPa$ and $50(10, +15)\%$ humidity rate. The estimated values for the precision error limits for the experiments are shown from Table 8 to Table 12 in the 'Calibrator' column. The corresponding error sources due to the atmospheric conditions appear in the rows as 'ΔdB_T', 'ΔdB_P', and 'ΔdB_{HR}' for temperature, pressure and humidity rate, respectively.

2. Microphone variability under atmospheric conditions: The estimated values for the precision error limits corresponding to the atmospheric conditions during the experiments are given in Table 7. The estimated values for the precision error limits for the experiments are shown from Table 8 to Table 12 in the 'Microphones' column.(Reference conditions were specified the same as the calibrator.)

3. Microphone variability in frequency : In the frequency range of interest of this work, it was seen that the variability of free field response of the condenser microphone type used is negligible.

A.4 Uncertainty in the Sound Pressure Levels

The reflections inside the test facility are considered to be sources of precision error. For geometric farfield experiments, the error range allowed for the reflections were ±1 dB. For the shielding experiments, the error range for reflections were ±2 dB as explained in Section 6.1.1 in detail. The uncertainty for the sound pressure levels is the combination

Table 7: Range of atmospheric conditions during the experiments. T : Temperature, P_{atm} : Atmospheric pressure, HR : Humidity Rate.

Experiment Type	**T** $[^oC]$	P_{atm} $[kPa]$	**HR**[%]
Geometric Far Field (Open Rotor)	0-13	101-102	40-90
Geometric Far Field (Ducted Rotor)	7-18	102-102.8	40-90
Rectangular Shielded (Point Source)	10-25	99.6-103.2	40-90
Rectangular Shielded (Rotor Source)	20-30	100.7-102.5	40-90
Circular Shielded	18-26	100.8-102.3	40-90

Table 8: Error limits for geometric farfield experiments for open rotors.

Error Source	**Calibrator**	**Microphones**	**Total**
ΔdB_T	± 0.02	± 0.04	± 0.06
ΔdB_P	± 0.0008	± 0.007	± 0.0078
ΔdB_{HR}	± 0.05	± 0.1	± 0.15

Table 9: Error limits for geometric farfield experiments for ducted rotors.

Error Source	**Calibrator**	**Microphones**	**Total**
ΔdB_T	± 0.017	± 0.033	± 0.017
ΔdB_P	$\pm 6.4e-5$	± 0.006	± 0.0061
ΔdB_{HR}	± 0.05	± 0.1	± 0.15

Table 10: Error limits for rectangular shielded point source.

Error Source	**Calibrator**	**Microphones**	**Total**
ΔdB_T	± 0.02	± 0.04	± 0.06
ΔdB_P	± 0.003	± 0.03	± 0.033
ΔdB_{HR}	± 0.05	± 0.1	± 0.15

Table 11: Error limits for rectangular shielded rotor source.

Error Source	**Calibrator**	**Microphones**	**Total**
ΔdB_T	± 0.015	± 0.03	± 0.045
ΔdB_P	± 0.0014	± 0.013	± 0.0144
ΔdB_{HR}	± 0.05	± 0.1	± 0.15

Table 12: Error limits for experiments with round duct as a shield.

Error Source	**Calibrator**	**Microphones**	**Total**
ΔdB_T	± 0.012	± 0.024	± 0.036
ΔdB_P	± 0.0012	± 0.011	± 0.0122
ΔdB_{HR}	± 0.05	± 0.1	± 0.15

Table 13: Uncertainty in the sound pressure levels.

Source	$\Delta dB_{Instrumentation}$	$\Delta dB_{Reflections}$	ΔdB_{Total}
Geometric Far Field (Open Rotor)	0.2178	± 1	1.2178
Geometric Far Field (Ducted Rotor)	0.1731	± 1	1.1731
Rectangular Shielded (Point Source)	0.243	± 2	2.243
Rectangular Shielded (Rotor Source)	0.2094	± 2	2.2094
Circular Shielded	0.1982	± 2	2.1982

reflection errors and measurement errors. In Table 10 the total error from measurement equipment and error from reflections are listed in column '$\Delta dB_{Instrumentation}$' and in column '$\Delta dB_{Reflections}$', respectively, for each experiment. Finally, in the ΔdB_{Total} column the uncertainty for sound pressure levels are calculated by using equation (54).

APPENDIX B

MATLAB PROGRAMS

B.1 Programs for Geometric Far Field Analysis

In this section the main programs that are used for the geometric far field analysis are presented. These programs apply for Chapter 5.

B.1.1 Program 1

This program computes the SPL of a rotor with given diameter at a distance range using multi point source approach. Then compares the results with the inverse square law. The phase relationship is neglected.

```
clear all
dB_Ref=100;
R_Ref=12;
N_PS=50; %Number of point sources
D_Rotor=6.5;
f=1000;
dB_P=10*log10((10^(dB_Ref/10))/N_PS);
theta_inc=2*pi/N_PS;
m=100;
R=D_Rotor:D_Rotor:m*D_Rotor;
n=length(R);
SPL_center(1)=Apply_ISL(dB_Ref,R_Ref,R(1)) %The SPL measured at first microph
for j=2:n
    SPL_center(j)=Apply_ISL(SPL_center(j-1),R(j-1),R(j));
end
for i=1:N_PS
```

```
    theta(1)=0;
    R_P(1,i)=sqrt((R(1)+(D_Rotor/2)*sin(theta(i)))^2+((D_Rotor/2)*cos(theta(i
    SPL_circ(1,i)=Apply_ISL(dB_P,R_Ref,R_P(1,i));     %The SPL measured at fir
    for j=2:n
        R_P(j,i)=sqrt((R(j)+(D_Rotor/2)*sin(theta(i)))^2+((D_Rotor/2)*cos(the
        SPL_circ(j,i)=Apply_ISL(SPL_circ(j-1,i),R_P(j-1,i),R_P(j,i));
    end
    theta(i+1)= theta(i)+theta_inc ;
end
for j=1:n
SPL(j)=logsum(SPL_circ(j,:),1,N_PS);
end
figure
arg=R./D_Rotor;
semilogx(arg,SPL_center,'-k',arg,SPL,'--k','LineWidth',3,'MarkerSize',22)
grid on
xlabel('R/D','fontsize',18)
ylabel('SPL','fontsize',18)
legend('Center','Circumference',-1)
set(gca,'fontsize',18)
```

B.1.2 Program 2

This program computes the SPL of a rotor with given diameter at a distance range using multi point source approach. Then compares the results with the inverse square law. Phase relationship is included.

```
clear all
A_single=100; %Sound power of a single source
N_multi=50; %Number of point sources
D_Rotor=13; %Rotor Diameter
```

```
%We assume that we placed N_multi number of point sources to
%the circumference of the rotor with equal angular spacing.
theta_inc=2*pi/N_multi;
m=100;
R=D_Rotor:D_Rotor:m*D_Rotor; %Measurement distance range
n=length(R);
f=1000;
c=1140*12;
k=2*pi*f/c;
p_ref=20e-5; %Pa
p_single=(A_single/R(1))*exp(-(1i)*k*R(1));
SPL_single=20*log10(abs(p_single(1))/p_ref);
SPL_center(1)=SPL_single;
for j=2:n
    SPL_center(j)=Apply_ISL(SPL_center(j-1),R(j-1),R(j));
end
for s=1:n
    theta(1)=0;
    phase(1)=0;
    delta_phase=0;
    for j=1:N_multi
        R_multi(j,s)=sqrt((R(s)+(D_Rotor/2)*sin(theta(j)))^2+((D_Rotor/2)
                                                    *cos(theta(j)))^2);
        A_multi(j)=A_single/N_multi;
        p_multi(j,s)=(A_multi(j)/R_multi(j,s))*exp(-(1i)*k*R_multi(j,s)
                                                    -i*phase(j));
        SPL_multi(j,s)=20*log10(abs(p_multi(j,s))/p_ref);
        theta(j+1)= theta(j)+theta_inc;
        phase(j+1)=phase(j)+delta_phase;
```

```
    end
    p_multiple(s)=sum(p_multi(:,s));
    SPL_multiple(s)=20*log10(abs(p_multiple(s))/p_ref);
end
%Comparison Plot
figure
arg=R./D_Rotor;
semilogx(arg,SPL_center,'-k',arg,SPL_multiple,'--k','LineWidth',3)
grid on
base=70;
top=base+30;
ylim([base top])
xlabel('R/D','fontsize',18)
ylabel('SPL','fontsize',18)
legend('Center','Circumference',-1)
set(gca,'fontsize',18)
%Print the results to an excel file
M=[arg' SPL_center' SPL_multiple'];
path_write='C:\PhDThesis\MatlabGenerated\GFF';
sheet_write='13_1000_50_nophase';
xlswrite(path_write, M, sheet_write)
```

B.2 Programs for Shielding Analysis

In this section the main programs that are used for the analysis of shielding experiments and calculation of their theoretical correspondents are presented. These programs apply for Chapter 6.

B.2.1 Program 3

This is the main function that computes the shielding of point source by a rectangular plate.

```
function [x_theory,SPL_theory]= Theory(frequency,ShieldCoord,ShieldDim,
                                       MicInitCoord);
%Only the angular increments are taken from the source coordinate system,
%which is the coordinate system that takes the source as origin.
%General Input
%The center of the source is fixed. Point O is the center of the source.
%ShieldCoord(x,y,z) is the midpoint of the shield w.r.t. point O.
%ShieldDim(L,W) is the the two planer dimensions of the shield.
%MicInitCoord(x,y,z)is the initial coordinates of the microphone w.r.t. O.
c=1130*12; %Speed of Sound[in/sec] %
%c=347.412; %m/sec=1140ft/sec;
eps=0.0001;
%Data based on global coordinate system (GCS)(inch),The center of the GCS
%is always the mid point of the shield!
%The GCS is presented by the right hand rule in the thesis however in the
%code it is used the same as in Ahtye paper! So y and z axis show opposite
%directions. But below all the differences between the coordinate systems
%are compensated. z-axis doesn't make a difference because we always take
%its abs value, z always enters the code positive.
%x_s, y_s, z_s are Source coord on GCS.
x_s= -ShieldCoord(1); %displacement
y_s= -ShieldCoord(2); %displacement
z_s= abs(ShieldCoord(3)); %distance
delta_y=-(ShieldCoord(2)-MicInitCoord(2));
D=abs(MicInitCoord(3)-ShieldCoord(3));%distance
W=ShieldDim(1); %Length of the rectangular shield
L=ShieldDim(2); %Width of the rectangular shield
%Visual Edge coordinates on the microphone traverse axes.
%Right Visual Edge Coordinates
```

```
beta_RVE= atan((W/2-x_s)/z_s); %[rad]
beta_RVE=beta_RVE*180/pi; %Convert radians to degrees
x_RVE=((W/2-x_s)/z_s)*(z_s+D);  %x coordinate of RVE in the microphone
                                %traverse coordinate system
%Left Visual Edge Coordinates
beta_LVE= -atan((W/2+x_s)/z_s); %[rad]
beta_LVE=beta_LVE*180/pi; %Convert radians to degrees
x_LVE=-((W/2+x_s)/z_s)*(z_s+D);  %x coodinate of LVE in the microphone
                                 %traverse coordinate system
%The left and right limits
%x_1=x_LVE+0.05;
%x_lim=(z_s+D)*tan(pi/3);%Limit on the microphone traverse line, right end
%x_1=-5.2;
%x_lim=5.2;  %metric
x_1=-100.05;
x_lim=100.05;  %inch
%Frequency related variables
Lambda=c/frequency; %Wavelength
k=2*pi*frequency/c; %Wave number
kW=k*W; %Dimensionless Wave Number
    x=x_1+0.05; % <0
    n=0;
    while x<x_lim
        n=n+1;
        %Case 1: Bottom Edge
        phi_0b=atan(z_s/(L/2-y_s));
        Denom=(L/2-y_s)-delta_y;
        theta=atan(D/abs(Denom));
        if (Denom<0)
```

```
    phib=pi+theta;
else
    phib=2*pi-theta;
end
rho_0b=z_s/sin(phi_0b);
rhob=D/sin(theta);
[R_b,Rdash_b,R1_b]=Distance (rhob,rho_0b,phib,phi_0b,x,0);
[VG_b]=VelPotGeometric(phib,phi_0b,k,R_b,Rdash_b);
[VD_b]=VelPotDiffracted(rhob,rho_0b,phib,phi_0b,k,R_b,Rdash_b,
                        R1_b,eps);
[VU_b]=VelPotUnshielded(k,R_b);
V_b=(VG_b+VD_b)/VU_b;
%Case 2: Top Edge
phi_0t=atan(z_s/(L/2+y_s));
Denom=(L/2+y_s)+delta_y;
theta=atan(D/abs(Denom));
if (Denom<0)
    phit=pi+theta;
else
    phit=2*pi-theta;
end
rho_0t=z_s/sin(phi_0t);
rhot=D/sin(theta);
[R_t,Rdash_t,R1_t]=Distance (rhot,rho_0t,phit,phi_0t,x,0);
[VG_t]=VelPotGeometric(phit,phi_0t,k,R_t,Rdash_t);
[VD_t]=VelPotDiffracted(rhot,rho_0t,phit,phi_0t,k,R_t,Rdash_t,
                        R1_t,eps);
[VU_t]=VelPotUnshielded(k,R_t);
V_t=(VG_t+VD_t)/VU_t;
```

```
%Case 3: Right Edge
if (W/2-x_s)<0.000000000001
    phi_0r=pi/2;
else
    phi_0r=atan(z_s/(W/2-x_s));
end
alphar=atan((x-(W/2-x_s))/D);
phir=3*pi/2-alphar;
rho_0r=z_s/sin(phi_0r);
rhor=D/cos(alphar);
[R_r,Rdash_r,R1_r]=Distance (rhor,rho_0r,phir,phi_0r,delta_y,0);
[VG_r]=VelPotGeometric(phir,phi_0r,k,R_r,Rdash_r);
[VD_r]=VelPotDiffracted(rhor,rho_0r,phir,phi_0r,k,R_r,Rdash_r,
                        R1_r,eps);
[VU_r]=VelPotUnshielded(k,R_r);
V_r=(VG_r+VD_r)/VU_r;
%Case 4: Left Edge
if (W/2+x_s)<0.000000000001
    phi_0l=pi/2;
else
    phi_0l=atan(z_s/(W/2+x_s));
end
alphal=atan((x+(W/2+x_s))/D);
phil=3*pi/2+alphal;
rho_0l=z_s/sin(phi_0l);
rhol=D/cos(alphal);
[R_l,Rdash_l,R1_l]=Distance (rhol,rho_0l,phil,phi_0l,delta_y,0);
[VG_l]=VelPotGeometric(phil,phi_0l,k,R_l,Rdash_l);
[VD_l]=VelPotDiffracted(rhol,rho_0l,phil,phi_0l,k,R_l,Rdash_l,
```

```
                                        R1_l,eps);
        [VU_l]=VelPotUnshielded(k,R_l);
        V_l=(VG_l+VD_l)/VU_l;
        %Total SPL
        V_Total=abs(V_b+V_t+V_r+V_l);
        dB_SPL=20*log10(V_Total);
        SPL_theory(n)=dB_SPL;
        %Calculate the directivity angle
        beta_dir=atan(x/(z_s+D)); %Directivity angle
        %Change receiver place, increase angle by 0.5 deg
        dz=pi/360;
        beta_new=beta_dir+dz;
        x_theory(n)=x;
        x=(z_s+D)*tan(beta_new); %Update x
    end  %End of 'while statement'
```

B.2.2 Program 4

This program compares the experimental shielding with the calculations and plots the results.

```
clear all
%The code is written such that mid point of the shield is the
%origin of the global coordinate system, which means shield is constant and
%source is moving. On the other hand, experiments are done such that the
%source is the origin, which means that shield is moving and source is
%fixed. So the coordinates given in this code are in the latter coordinate
%system, everything is compansated in the theory part.
%p.s. z always should enter the code as a positive number!
%!!!Check the parameters below before you start the code!!!!!!!!!!!!!!!!!
sheet='3'; %common for both cases
```

```
ShieldCoord=[0 0 3.5];
ShieldDim=[7,36];
%Enter unshielded data file path
path_unsh='C:\Shielding_Tests\Duct_Shielding\Data_Unsh\Data10_Unsh1.xls';
data_unsh = xlsread(path_unsh,sheet);
%Enter shielded data file path
path_sh = 'C:\Shielding_Tests\Duct_Shielding\Data10_7x36.xls';
data_sh = xlsread(path_sh,sheet);
%Give the frequency set needed
[row_count,column_count]=size(data_sh);
%frequency =[300,400,600,800,1200];
%frequency =[300,400,600,800,1200,2000,2400,3000];
frequency=[95*4,400,95*5,500,95*6,600,95*7,700,95*8,800,95*9,900,95*10,1000
%,95*11,1100,95*12,1200];
%[f_lower,frequency,f_upper]=ThirdOctaveFreq(34,20,100);
freq_count=length(frequency);
step_count=row_count/freq_count;
%Give the y coordinates of microphone
y_mic=[-18,-12,-6,0,6,12]';
columnsize_y=length(y_mic);
z=abs(data_unsh(1,13))-0;
%Compute the data to plot
[SPL_unsh,SPL_exp,x_exp]=Experiment(data_unsh,data_sh);
%Assign zero to the shielding data that corresponds to unusable unshielded
%data
[r,c]=size(SPL_exp);
for i=1:r
    for j=1:c
        if data_unsh(i,j+2)==0;
```

```
            SPL_unsh(i,j)=0;
            SPL_exp(i,j)=0;
        end
    end
end
%Comparison Plot
i_i=1;
i_f=freq_count;
for i=i_i:i_f
    for j=1:columnsize_y
            if  SPL_exp((i-1)*step_count+1,j)==0
                |SPL_exp((i-1)*step_count+2,j)==0
                |SPL_exp((i-1)*step_count+3,j)==0
                |SPL_exp((i-1)*step_count+4,j)==0 ...
                |SPL_exp((i-1)*step_count+5,j)==0
                |SPL_exp((i-1)*step_count+6,j)==0
                |SPL_exp((i-1)*step_count+7,j)==0
                |SPL_exp((i-1)*step_count+8,j)==0 ...
                |SPL_exp(i*step_count-2,j)==0
                |SPL_exp(i*step_count-1,j)==0
                |SPL_exp(i*step_count,j)==0
                SPL_Exp(:,j)=[0 0 0 0 0 0 0 0 0 0 0]';
            else
                SPL_Exp(:,j)=SPL_exp((i-1)*step_count+1:i*step_count,j);
            end
            y=y_mic(j);
            MicInitCoord=[0 y z];
            ShieldInitCoord=ShieldCoord;
            [x_theory,SPL_theory(:,j)]= Theory(frequency(i),ShieldCoord,
```

```
                                                    ShieldDim,MicInitCoord);
    end
    x=x_exp(1+(i-1)*step_count:i*step_count);
    a=x-ShieldCoord(1)*ones(length(x),1);
    a_theory=x_theory'-ShieldCoord(1)*ones(length(x_theory),1);
    b=z-ShieldCoord(3);
    theta=atan(a/b)*180/pi;
    theta_theory=atan(a_theory/b)*180/pi;
    phi=atan(-(ShieldCoord(2)-y_mic)./b)*180/pi;
    arg=theta;
    arg_theory=theta_theory;
    base=-30;
    top=base+40;
    x_l=-30;
    x_u=30;
    figure
    plot(arg,SPL_Exp(:,1),'*k',arg_theory,SPL_theory(:,1),'-k')
    grid on
    %xlim([-30 30])
    xlim([x_l x_u])
    ylim([base top])
    %xlabel('x_m','fontsize',24)
    xlabel('Polar angle, \theta [degrees]','fontsize',24)
    ylabel('\Delta SPL_n','fontsize',24)
    legend('Experiment','Theory')
    set(gca,'fontsize',24)
end
```

B.2.3 Program 5

This function computes the SPL for a rotor with a given diameter, shielded by a rectangular plate using multi point source approach.

```
function [x_theory_center,SPL_theory_center,SPL,phase]
                =SumPS(frequency,ShieldDim,MicInitCoord,ShieldInitCoord,
                        N_PS,D_Rotor,dB_Ref,Phase)
[x_theory_center,D_SPL_theory_center]
   = Theory(frequency,ShieldInitCoord,ShieldDim,MicInitCoord);
%DeltaSPL=Shielded-Unshielded ==>Shielded=DeltaSPL+Unshielded.
SPL_theory_center=dB_Ref*ones(1,length(D_SPL_theory_center))
                        +D_SPL_theory_center;
dB_P=10*log10((10^(dB_Ref/10))/N_PS);
theta_inc=2*pi/N_PS;
n=length(x_theory_center);
for i=1:(n-1)
    x(1)=x_theory_center(1);
    x(n+1)=-x_theory_center(1);
    dist(i)=(x_theory_center(i+1)-x_theory_center(i))/2;
    x(i+1)=x_theory_center(i)+dist(i);
end
for i=1:N_PS
    phase(1)=0;
    theta(1)=0;
    ShieldCoord(i,:)=[(ShieldInitCoord(1)-D_Rotor/2*sin(theta(i)))
        ShieldInitCoord(2) (ShieldInitCoord(3)-D_Rotor/2*cos(theta(i)))];
    MicCoord(i,:)=[(MicInitCoord(1)-D_Rotor/2*sin(theta(i)))
        MicInitCoord(2) (MicInitCoord(3)-D_Rotor/2*cos(theta(i)))];
    [x_theory,D_SPL_theory]= TheorywPhase(frequency,ShieldCoord(i,:),
```

```
                                        ShieldDim,MicCoord(i,:),phase(i));
j=1;
for k=1:n
    x_l=x(k);
    x_u=x(k+1);
    D_SPL_add=0;
    s=j;
    D_SPL_mean(k)=0;
    while x_theory(j)>=x_l & x_theory(j)<x_u
        D_SPL_midsum=D_SPL_add+D_SPL_theory(j);
        D_SPL_add=D_SPL_midsum;
        D_SPL_mean(k)=D_SPL_midsum/(j-s+1);
        if j<length(x_theory)
            j=j+1;
        else
            break
        end
    end
end
for k=2:n
    if D_SPL_mean(k)==0
        D_SPL_mean(k)=D_SPL_mean(k-1);
    end
end
D_SPL_theory_rotor(:,i)=D_SPL_mean;
SPL_theory_rotor(:,i)=dB_P*ones(1,length(D_SPL_mean))+D_SPL_mean;
clear D_SPL_mean
theta(i+1)= theta(i)+theta_inc ;
phase(i+1)=phase(i)+Phase;
```

```
end
for i=1:n
SPL(i)=logsum(SPL_theory_rotor(i,:),1,N_PS);
end
```

B.2.4 Program 6

This program computes the SPL of a multi point source system using 'SumPS' function and prints the results on an excel file.

```
clear all
frequency=800;
dB_Ref=100; %Reference SPL of a single source
Phase=0; %Phase between the multi sources
D=6.5;    %Rotor diameter [inches]
d=3.25;  %Tip Clearance
MicInitCoord=[0 -18 90]; %Microphone initial coordinates
D_Rotor=D;
ShieldInitCoord=[0 0 D_Rotor/2+d]; %Shield initial coordinates
ShieldDim=[13 24]; %Shield Dimensions
N=12; %Number of point sources
N_PS=N;
dB_P=10*log10((10^(dB_Ref/10))/N);
[x_theory_center,SPL_theory_center,SPL,phase]
=SumPS(frequency,ShieldDim,MicInitCoord,ShieldInitCoord,N_PS,D_Rotor,
        dB_Ref,Phase);
a=x_theory_center-ShieldInitCoord(1)*ones(1,length(x_theory_center));
b=MicInitCoord(3)-ShieldInitCoord(3);
theta=atan(a/b)*180/pi;
arg=theta;
M=[arg' SPL_theory_center' SPL'];
```

```
path_write='C:\PhDThesis\MatlabGenerated\Fix';
sheet_write='-18';
xlswrite(path_write, M, sheet_write)
```

B.3 Additional Functions Used in the Programs

In this section the additional Matlab functions that are found inside the programs in the previous two sections are presented.

Compute the geometric velocity potential:

```
function [VG]=VelPotGeometric(phi,phi0,k,R,Rdash)
VG=heaviside(pi+phi0-phi)*exp(i*k*R)/(k*R)+heaviside(pi-phi0-phi)*exp(i*k*Rda
```

Compute the diffracted velocity potential:

```
function [VD]=VelPotDiffracted(rho,rho0,phi,phi0,k,R,Rdash,R1,eps)
R_Control_1=2*rho*rho0*(1+cos(phi-phi0))/(R1^4);
R_Control_2=2*rho*rho0*(1+cos(phi+phi0))/(R1^4);
if R_Control_1<eps
    Tau=sqrt(k*(rho*rho0*(1+cos(phi-phi0))/R1));
else
    Tau=sqrt(k*(R1-R));
end
if R_Control_2<eps
     Tau_dash=sqrt(k*(rho*rho0*(1+cos(phi+phi0))/R1));
else
    Tau_dash=sqrt(k*(R1-Rdash));
end
VD=-sqrt(2/(pi*k*R1))*exp(-i*pi/4)
    *(sign(pi+phi0-phi)*FresnelIntegral(Tau)*exp(i*k*R)/sqrt(k*(R1+R))
     +sign(pi-phi0-phi)*FresnelIntegral(Tau_dash)*exp(i*k*Rdash)
                                                  /sqrt(k*(R1+Rdash)));
```

Compute the unshielded velocity potential:

```
function [VU]=VelPotUnshielded(k,R)
VU=exp(i*k*R)/(k*R);
```

Using experimental data for shielding form the data matrices to be necessary for the program:

```
function [SPL_unsh,SPL_exp,x_exp]=Experiment(data_unsh,data_sh);
%PS data
%read the excel data file ------
%Final row numbers of the excel file should be adjusted
%Unshielded Data
SPL_reference_unsh = data_unsh(:,2);
SPL_traverse_unsh = data_unsh(:,3:8);
%Shielded Data
SPL_reference_sh = data_sh(:,2);
SPL_traverse_sh = data_sh(:,3:8);
%number of mics on vertical(y) axis
y_mic=[-18,-12,-6,0,6,12];
columnsize_y=length(y_mic);
%Calculate Traverse-Reference
for i=1:columnsize_y
    SPL_unsh (:,i) = Delta(SPL_traverse_unsh(:,i),SPL_reference_unsh);
    SPL_sh (:,i) = Delta(SPL_traverse_sh(:,i),SPL_reference_sh);
    %SPL_unsh (:,i) = SPL_traverse_unsh(:,i);
    %SPL_sh (:,i) = SPL_traverse_sh(:,i);
    SPL_exp (:,i) = Delta(SPL_sh(:,i),SPL_unsh(:,i));
end
%traverse line
n=12;
```

```
x_exp=data_sh(:,n);
```

Do logarithmic summation:

```
%SPL_Vector is the Vector whose elements are the SPL to be summed.
%n_l is the row number of the first element required to be in the sum
%and n_u is the last element's.
function SPL = logsum(SPL_Vector,n_l,n_u)
Exp_sum=0;
for i=n_l:n_u
        Exp_sum=Exp_sum+10^(SPL_Vector(i)/10);
end
SPL = 10*log10(Exp_sum);
```

Apply inverse square law for given distances:

```
% If D2>D1, SPL1>SPL2, If D1>D2, SPL2>SPL1
function [SPL2]=Apply_ISL(SPL1,D1,D2)
SPL2=SPL1-20*log10(D2/D1);
```

Calculate the difference between two numbers:

```
function [delta_SPL] = Delta (x,y)
%x,y are vectors
n=length(x);
for i=1:n
    delta_SPL(i)=x(i)-y(i);
end
```

Calculate distance for given cylindrical coordinates:

```
%R: Source-to-Receiver Distance
%Rdash: Source-to-Image Source Distance
%R1: Characteristic Distance
function [R,Rdash,R1]=Distance (rho,rho0,phi,phi0,z,z0)
```

```
R=sqrt(rho^2+rho0^2-2*rho*rho0*cos(phi-phi0)+(z-z0)^2);
Rdash=sqrt(rho^2+rho0^2-2*rho*rho0*cos(phi+phi0)+(z-z0)^2);
R1=sqrt((rho+rho0)^2+(z-z0)^2);
```

Calculate distance from the source to the microphone:

```
function [distance] = Distance_Meas (x,y,z)
%x,y,z are vectors
n=length(x);
for i=1:n
    distance(i)=sqrt(x(i)^2+y(i)^2+z(i)^2);
end
```

REFERENCES

[1] Ahuja, K., "Designing clean jet noise facilities and making accurate jet noise measurements," *International Journal of Aeroacoustics*, vol. 2, no. 3, 2003.

[2] Wilson, C., *Noise Control-Measurement, Analysis and Control of Sound and Vibration*, ch. 2. Florida: Krieger Publishing, 1994.

[3] Marte, J. and Kurtz, D., "A review of aerodynamic noise from propellers, rotors, and lift fans," *NASA CR 107568*, Jan. 1970.

[4] Sharland, I., "Sources of noise in axial flow fans," *J. Sound Vib.*, 1964.

[5] Blake, W., *Mechanics of Flow Induced Sound and Vibration*. New York: Academic Press Inc, 1986.

[6] Hubbard, H., *Aeroacoustics of Flight Vehicles*, vol. 1, ch. 1. New York: Acoustical Society of America, 1995.

[7] Pierce, A., *Acoustics - An Introduction to Physical Principles and Applications*. New York: Acoustical Society of America, 1996.

[8] Blackstock, D., *Fundamentals of Physical Acoustics*. New York: Wiley, 2000.

[9] Nallasamy, N., "Noise radiation from fan inlet and aft ducts," *AIAA Paper 96-1769*, May 1996.

[10] Koch, L. D., Bridges, J., Brown, C., and Kharavan, A., "Experimental and analytical determination of geometric far field for round jets," *Noise Control Engineering Journal*, vol. 53, no. 1, pp. 20–28, 2005.

[11] Ahuja, K. K., Milway, S. K., and Churney, A., "Potential errors introduced in the use of static engine noise data not acquired in geometric farfield," *AIAA 2006-2553, 12th AIAA/CEAS Aeroacoustics Conference, Cambridge, Massachusetts*, July 2006.

[12] Rayleigh, J., *The Theory of Sound*, vol. 2. New York: Dover Publications, 1945. Publication date of the original copy is 1877.

[13] Kirchhoff, G., *Vorlesungen uber Mathematische Optik*. Vorlesungen uber Mathematische Physik, 1891.

[14] Sommerfeld, A., "Mathematische theorie der diffraction," *Mathematische Annalen*, vol. 47, no. 2, 1896.

[15] MacDonald, H., "Diffraction at a straight edge," in *Proceedings of the London Mathematical Society*, no. 14 in All ACM Conferences, (London), pp. 103–105, LONDON MATH SOC, 1915.

[16] Primakoff, H., Kelin, M., Keller, J., and Carstensen, E., "Diffraction of sound around a circular disk," *J. Acoust. Soc. Am.*, vol. 19, no. 1, pp. 132–142, 1947.

[17] Maekawa, Z., "Noise reduction by screens," *Applied Acoustics*, vol. 1, pp. 157–173, July 1968.

[18] Bowman, J., Senior, T., and Uslenghi, P., *Electromagnetic and Acoustic Scattering by Simple Shapes*, ch. 8, pp. 308–345. Amsterdam: North Holand Publishing Company, 1969.

[19] Broadbent, E. G., "Noise shielding for aircraft," *Prog. Aerospace Sci.*, vol. 17, pp. 231–268, 1977.

[20] Ahtye, W. and McCulley, W., "Evaluation of approximate methods for prediction of noise shielding by airframe components," *NASA TP 1004*, 1980.

[21] Keller, J., "One hundred years of diffraction theory," *IEEE Transactions on Antennas and Propagation*, no. 2, 1985.

[22] Whitfield, C. E., Gliebe, P. R., Mani, R., and Mungur, P., "High speed turboprop aeroacoustic study (single rotation) volume 1: Model development," *GE Aircraft Engines, Cincinnatti, Ohio*, May 1989. NASA CR-182257.

[23] Whitfield, C. E., Mani, R., and Gliebe, P. R., "High speed turboprop aeroacoustic study (counterrotation) volume 1: Model development," *GE Aircraft Engines, Cincinnatti, Ohio*, 1990. NASA CR-185241.

[24] Amiet, R., "Unified aeroacoustics for high speed turboprop aerodynamics and noise v2 - development of theory for wing shielding," *NASA CR 185192*, May 1991.

[25] Hanson, D., McColgan, C., Ladden, R., and Klatte, R., "Unified aeroacoustics for high speed turboprop aerodynamics and noise v3 - application of theory for blade loading, wakes, noise and wing shielding," *NASA CR 185193*, May 1991.

[26] Dunn, M. H., "Tbiem3d - a computer program for predicting ducted fan engine noise," *NASA/CR-97-206232*, Sept. 1997.

[27] Clark, L. and Gerhold, C., "Inlet noise reduction by shielding for the blended wing airplane," *AIAA-99-1937*, 1999.

[28] Stanescu, D., Hussaini, M. Y., and Farassat, F., "Aircraft engine noise scattering - a discontinuous spectral element approach," *40th AIAA Aerospace Sciences Meeting and Exhibit, Reno, Nevada*, Jan. 2002. AIAA-2002-800.

[29] Stanescu, D., Hussaini, M. Y., and Farassat, F., "Large scale frequency domain numerical simulation of aircraft engine tone noise radiation and scattering," *8th AIAA/CEAS Aeroacoustics COnference and Exhibit, Breckenridge, Colorado*, 2002. AIAA-2002-2586.

[30] Xu, J., Stanescu, D., Hussaini, M. Y., and Farassat, F., "Computation of engine noise propagation and scattering off an aircraft," *41th AIAA Aerospace Sciences Meeting and Exhibit, Reno, Nevada*, Jan. 2003. AIAA-2003-542.

[31] Dunn, M. H. and Tinetti, A., "Aeroacoustic scattering via the equivalent source method," *10th AIAA/CEAS Aeroacoustics Conference, Manchester, Great Britain*, May 2004.

[32] Gerhold, C., Clark, L., Dunn, M., and Tweed, J., "Investigation of acoustical shielding by a wedge shaped airframe," *AIAA 2004-2867*, 2004.

[33] Ricouard, J., Davy, R., Loheac, P., Moorea, A., and Piccin, O., "Rosas wind tunnel test campaign dedicated to unconventional concepts study," *AIAA 2004-2867*, 2004.

[34] Tinetti, A. and Dunn, M. H., "Aeroacoustic noise prediction using the fast scattering code," *11th AIAA/CEAS Aeroacoustics Conference, Monterey, California*, May 2005.

[35] Reimann, C., Tinetti, A., and Dunn, M. H., "Noise prediction studies for blended wing body using the fast scattering code," *11th AIAA/CEAS Aeroacoustics Conference, Monterey, California*, May 2005.

[36] Reimann, C., Tinetti, A., and Dunn, M. H., "Noise scattering by the blended wing body airplane : Measurements and prediction," *12th AIAA/CEAS Aeroacoustics Conference, Cambridge, Massachusetts*, May 2006.

[37] Reimann, C., Tinetti, A., and Dunn, M. H., "Engine liner optimization using the fast scattering code," *13th AIAA/CEAS Aeroacoustics Conference, Rome, Italy*, May 2007.

[38] Chappius, J., Ricouard, J., and Roger, M., "Aft fan noise shielding by a lifting surface: Analytical, numerical and experimental results," *AIAA 2006-2617, 12th AIAA/CEAS Aeroacoustics Conference, Cambridge, Massachusetts*, May 2006.

[39] Agarwal, A. and Dowling, A., "Low-frequency acoustic shielding by silent aircraft airframe," *AIAA Journal*, vol. 45, no. 2, 2007.

[40] Agarwal, A., Dowling, A., Shin, H., Graham, W., and Sefi, S., "Ray tracing approach to calculate acoustic shielding by a flying wing airframe," *AIAA Journal*, vol. 45, May 2007.

[41] Nark, D., Burley, C., Rawls, J., Tinetti, A., and Dunn, M. H., "Initial integration of noise prediction tools for acoustic scattering effects," *14th AIAA/CEAS Aeroacoustics Conference, Vancouver, British Columbia*, May 2008.

[42] Tinetti, A. and Dunn, M. H., "Scattering of high frequency duct noise by full scale hybrid wing body configurations," *15th AIAA/CEAS Aeroacoustics Conference, Miami, Florida*, May 2009.

[43] Papamoschou, D., "Prediction of jet noise shielding," *AIAA 2010-653, 48th AIAA Aerospace Sciences Meeting, Orlando, Florida*, 2010.

[44] Bowman, J. and Senior, T., "Diffraction of a dipole field by a perfectly conducting half plane," *Radio Science*, vol. 2, pp. 1339–1345, 1967.

[45] Ahuja, K., "Laboratory simulation of point monopole and point dipole sound sources," *2nd International Congress on Recent Developments in Air- and Structure-Borne Sound and Vibration, Auburn University, AL*, 1992.

[46] Turkdogru, N., Ahuja, K., and Churney, A., "Geometric farfield conditions for reliable acoustic measurements of ducted and unducted rotors," *Internoise 2007, Istanbul, Turkey*, 2007.

[47] Sijtsma, P., Oerlemans, S., and Holthusen, H., "Location of rotating sources by phased array measurements," *AIAA Paper 2001-2167*, 2001.

[48] Turkdogru, N., Ahuja, K., and Gaeta, R., "Validity of the point source assumption in rotor noise measurements with shielding," *16th AIAA/CEAS Aeroacoustics Conference, Stockholm, Sweden*, 2010.

[49] Coleman, H. and W.G. Steele, J., *Experimentation and Uncertainty Analysis for Engineers*. New York: John Wiley & Sons, 1989.

[50] Moffat, R., "Contributions to the theory of single-sample uncertainty analysis," *Journal of Fluid Engineering*, vol. 104, pp. 250–260, June 1982.

VITA

Nurkan Turkdogru was born in Izmir, Turkey. She attended public schools in Manisa, Turkey, received a B.S. in Mathematics from Istanbul Technical University in 1999 and an M.S. in Mechanical Engineering from Istanbul Technical University in 2002 before coming to Georgia Tech, where she received another M.S. in Aerospace Engineering.